



TECHNISCHE  
UNIVERSITÄT  
WIEN  
Vienna University of Technology

## DISSERTATION

# Micro- and nanostructured surfaces for studying T cell activation

Ausgeführt zum Zwecke der Erlangung des akademischen Grades eines  
Doktors der technischen Wissenschaften

unter der Leitung von

Univ. Prof. Dr. Gerhard J. Schütz

und

Dr. Eva Sevcsik

E134

Institut für Angewandte Physik

eingereicht an der

Technischen Universität Wien

Fakultät für Physik

von

Dipl.-Ing. **Viktoria Motsch**, BSc

Matr.Nr.: 0625440

Nordbahngasse 17c/1/4

2253 Weikendorf

Wien, im Mai 2019



Die approbierte gedruckte Originalversion dieser Dissertation ist an der TU Wien Bibliothek verfügbar.  
The approved original version of this doctoral thesis is available in print at TU Wien Bibliothek.

# Kurzfassung

Die räumliche Anordnung funktionaler Komponenten ist eines der grundlegenden Konzepte auf zellulärer Ebene. Obwohl es eine Vielzahl von Methoden gibt, die räumliche Verteilung von Biomolekülen in Zellen abzubilden, sollte Observation durch Interaktion ergänzt werden, um biologische Systeme vollständig zu verstehen. Hier wurden unterschiedliche Mikro- und Nanostrukturierungstechniken eingesetzt, um verschiedene Aspekte der T-Zell-Aktivierung zu untersuchen.

Die DNA-Origami-Technik ermöglicht es, Liganden präzise im Nanometerbereich zu positionieren. In dieser Arbeit wird eine DNA-Origami-Nanoplatte als Interaktionsplattform mit verschiedenen Funktionalitäten konzipiert, um den Einfluss unterschiedlicher räumlicher Anordnungen von Liganden auf die Aktivierung von T-Zellen zu untersuchen. Weiters wird durch die Bindung dieser Nanoplatte zusammen mit kostimulatorischen Proteinen an ein Lipid-Doppelschicht eine mobile Interaktionsplattform gebildet, die einer antigenpräsentierenden Zelle ähnelt.

Fluorescence recovery after photobleaching (FRAP) ist eine häufig verwendete Methode zur Erfassung kinetischer Parameter bei Proteininteraktionen in lebenden Zellen. Dennoch werden FRAP-Experimente oft durch unspezifische Beiträge bei der Regeneration des Fluoreszenzsignals behindert. Protein-Mikrostrukturierung ermöglicht die Eliminierung solcher unspezifischen Beiträge und vereinfacht die Analyse von FRAP-Daten erheblich. Dieser Ansatz wird am Beispiel der Interaktion zwischen dem T-Zell-Rezeptor und der Syk-Kinase ZAP70 demonstriert.

Electron-beam-induced deposition (EBID) ermöglicht eine maßgeschneiderte Oberflächenstrukturierung mit einer Auflösung unter 10 nm. Durch den geringen Durchsatz begrenzt, ist die Produktion von großformatigen EBID-Strukturen in angemessener Zeit nicht möglich. Daher implementieren wir einen Pick-and-Place-Manipulationsansatz, bei dem eine einzelne Zelle an einem beschichteten AFM-Cantilever befestigt und auf dem strukturierten Bereich positioniert wird. Weiters wird erörtert, wie EBID-Strukturierung mit dem DNA-Origami-Ansatz kombiniert werden kann.



Die approbierte gedruckte Originalversion dieser Dissertation ist an der TU Wien Bibliothek verfügbar.  
The approved original version of this doctoral thesis is available in print at TU Wien Bibliothek.

# Abstract

Spatial organization of functional components is one of the fundamental concepts at the cellular level. Although a vast number of methods exists to visualize the spatial organization of biomolecules in cells, observation should be augmented by interaction in order to fully understand biological systems. Here, several micro- and nanostructuring techniques were implemented in order to investigate different aspects of T cell activation on the respective length scales.

The DNA origami technique offers the possibility to position ligands precisely at the nanometer scale. In this thesis, a DNA origami nanoplate is designed to serve as an interaction platform featuring multiple functionalities. These platforms can be used to probe the effect of different spatial arrangements of ligands on T cell activation. Further, by attaching the DNA origami nanoplates and co-stimulatory proteins to a lipid bilayer system, a mobile interaction platform is formed which closely resembles an antigen presenting cell.

Fluorescence recovery after photobleaching (FRAP) is a commonly used technique to acquire kinetic parameters on protein interactions in living cells. Still, FRAP experiments are often hampered by non-specific contributions to the fluorescence recovery signal. Protein micropatterning, the second approach used in this thesis to achieve spatial organization, allows for the elimination of such non-specific contributions and considerably simplifies the analysis of FRAP data. This approach is demonstrated on the example of the interaction between the T cell receptor and the Syk kinase ZAP70.

Electron-beam-induced deposition (EBID) allows for custom designed surface structuring with sub-10 nm resolution. Still, this method is limited by its low throughput and production of large scale EBID structures is not feasible in a reasonable amount of time. Here, we implement a pick-and-place manipulation approach in which a single cell is attached to a coated AFM cantilever and positioned on the structured area. Further, it is discussed how EBID structuring can be combined with the DNA origami approach.



Die approbierte gedruckte Originalversion dieser Dissertation ist an der TU Wien Bibliothek verfügbar.  
The approved original version of this doctoral thesis is available in print at TU Wien Bibliothek.

# Eidesstattliche Erklärung

Ich erkläre an Eides statt, dass ich die vorliegende Arbeit selbstständig verfasst, andere als die angegebenen Quellen/Hilfsmittel nicht benutzt, und die den benutzten Quellen wörtlich und inhaltlich entnommenen Stellen als solche kenntlich gemacht habe. Das in TISS der TU Wien hochgeladene Textdokument ist mit der vorliegenden Dissertation identisch.

Datum

Unterschrift



Die approbierte gedruckte Originalversion dieser Dissertation ist an der TU Wien Bibliothek verfügbar.  
The approved original version of this doctoral thesis is available in print at TU Wien Bibliothek.



*The woods are lovely dark and deep.  
But I have promises to keep,  
And miles to go before I sleep,  
And miles to go before I sleep.*

Robert Frost



Die approbierte gedruckte Originalversion dieser Dissertation ist an der TU Wien Bibliothek verfügbar.  
The approved original version of this doctoral thesis is available in print at TU Wien Bibliothek.

# Contents

<b>I</b>	<b>Introduction and fundamentals</b>	<b>1</b>
<b>1</b>	<b>Introduction</b>	<b>3</b>
<b>2</b>	<b>Immunobiology</b>	<b>11</b>
2.1	Cells of the immune system . . . . .	11
2.1.1	T cells . . . . .	12
2.1.2	Antigen presenting cells . . . . .	13
2.1.3	B and NK cells . . . . .	14
2.2	Antigen recognition by T cell receptors . . . . .	14
2.2.1	Key players in T cell activation . . . . .	15
2.2.2	The immunological synapse . . . . .	22
2.3	Signaling pathways . . . . .	25
<b>3</b>	<b>Microscopy techniques</b>	<b>29</b>
3.1	Fluorescence microscopy . . . . .	29
3.1.1	Photophysical principles of fluorescence . . . . .	29
3.1.2	Microscopy setup . . . . .	31
3.1.3	Total internal reflection fluorescence microscopy . . . . .	33
3.1.4	Fluorescence recovery after photobleaching . . . . .	34
3.1.5	Single molecule fluorescence microscopy . . . . .	37
3.2	Atomic force microscopy . . . . .	44
3.2.1	Fundamentals of atomic force microscopy . . . . .	45
3.2.2	Different modes of the atomic force microscope . . . . .	47
3.2.3	AFM measurements in liquid . . . . .	50
3.2.4	Image processing . . . . .	50
3.2.5	Imaging artifacts . . . . .	51
3.2.6	Combining AFM with fluorescence microscopy . . . . .	52

3.2.7	Single cell force spectroscopy . . . . .	52
3.3	Electron microscopy . . . . .	54
3.3.1	Electron-beam lithography . . . . .	54

## **II DNA origami nanostructuring 57**

### **4 Introduction 59**

### **5 Theoretical background 63**

5.1	DNA structure . . . . .	63
5.2	Thermodynamic considerations of DNA duplex formation . . . . .	69
5.2.1	Kinetics of DNA dissociation and hybridization processes	71
5.3	Optical properties of DNA . . . . .	74
5.4	dsDNA as a secondary structure unit . . . . .	75
5.5	DNA nanoconstructs interacting with lipid bilayers . . . . .	77
5.5.1	Lipid bilayer systems . . . . .	77
5.5.2	Attachment of DNA structures to lipid bilayers . . . . .	79

### **6 Self-assembled DNA nanostructures 83**

6.1	Principles of DNA origami . . . . .	83
6.2	DNA nanoconstruct design . . . . .	85
6.2.1	Strand routing and breaking . . . . .	87
6.2.2	Computer aided design process . . . . .	89
6.2.3	Attachment position for modified strands . . . . .	90
6.2.4	Base stacking, end passivation and polymerization . . . . .	92
6.3	Molecular self-assembly of DNA nanostructures . . . . .	93
6.3.1	Thermal annealing procedure . . . . .	93
6.3.2	Scaffold and staple concentrations . . . . .	95
6.3.3	Buffer conditions . . . . .	95
6.4	Purification methods . . . . .	97
6.4.1	The need for purification . . . . .	97
6.4.2	Agarose-gel electrophoresis . . . . .	97
6.4.3	Spin column filtration . . . . .	99
6.4.4	Polyethylene glycol precipitation . . . . .	101
6.4.5	Purification Conclusion . . . . .	102

<b>7</b>	<b>A nanostructuring DNA origami platform</b>	<b>105</b>
7.1	Introduction . . . . .	105
7.2	DNA platform design and synthesis . . . . .	106
7.2.1	DNA templated design . . . . .	106
7.2.2	Model generation . . . . .	108
7.2.3	DNA platform synthesis, purification and labeling . . . . .	110
7.3	Characterization . . . . .	111
7.3.1	Agarose gel electrophoresis analysis . . . . .	112
7.3.2	AFM analysis of DNA origami platform . . . . .	114
7.3.3	Diffusion analysis of DNA structures . . . . .	116
7.4	T cell interaction platform . . . . .	119
7.4.1	Attachment strategies . . . . .	121
7.4.2	Modification with antibodies . . . . .	124
7.4.3	Modification with the single chain antibody fragment . . . . .	126
<b>8</b>	<b>Conclusion and outlook</b>	<b>131</b>
<b>9</b>	<b>Materials and methods</b>	<b>133</b>
9.1	DNA-templated design . . . . .	133
9.2	Folding, purification and labeling . . . . .	134
9.2.1	Folding protocol . . . . .	134
9.2.2	Folding mix . . . . .	134
9.2.3	Purification of DNA origami structures . . . . .	136
9.2.4	Labeling of DNA origami structures . . . . .	136
9.3	Characterization of the DNA origami platform . . . . .	137
9.3.1	Agarose gel electrophoresis . . . . .	137
9.3.2	Atomic force microscopy . . . . .	137
9.3.3	Diffusion analysis . . . . .	138
9.3.4	Antibody modification setup . . . . .	140
9.3.5	Single chain antibody fragment modification setup . . . . .	140
<b>III</b>	<b>TCR micropatterning to study ZAP70 kinetics</b>	<b>143</b>
<b>10</b>	<b>Introduction</b>	<b>145</b>

<b>11 Theoretical background</b>	<b>147</b>
11.1 Fluorescence recovery after photobleaching . . . . .	147
11.1.1 The influence of diffusion and binding . . . . .	148
11.1.2 Diffusion-uncoupled FRAP . . . . .	150
11.1.3 Diffusion-coupled FRAP . . . . .	150
11.1.4 Fitting FRAP recovery curves . . . . .	151
11.2 Protein micropatterning . . . . .	154
11.2.1 Types of immobilization . . . . .	154
11.2.2 Lithography techniques . . . . .	156
11.2.3 Soft lithography . . . . .	158
11.2.4 Application in cell biology . . . . .	162
11.3 ZAP70 . . . . .	162
11.3.1 Discovery of ZAP70 . . . . .	162
11.3.2 Structure of ZAP70 . . . . .	163
11.3.3 ZAP70 in the TCR pathway . . . . .	165
11.3.4 The dynamics of signaling complexes . . . . .	166
<b>12 Results</b>	<b>169</b>
12.1 Jurkat T cell activation on OKT3 micropatterns . . . . .	169
12.2 Complex recovery behavior of ZAP70-GFP in non-activated Jurkat T cells . . . . .	176
12.3 Micropatterning to specifically probe ZAP70-TCR binding kinetics	179
12.4 Mobile fraction . . . . .	184
12.5 Interaction times . . . . .	185
<b>13 Conclusion and outlook</b>	<b>189</b>
<b>14 Materials and methods</b>	<b>191</b>
14.1 Cells and reagents . . . . .	191
14.2 Surface preparation . . . . .	192
14.3 Total internal reflection fluorescence microscopy . . . . .	192
14.4 Ratiometric Ca <sup>2+</sup> Imaging . . . . .	193
14.5 FRAP experimental procedure . . . . .	193
14.6 FRAP analysis . . . . .	195

<b>IV</b>	<b>EBID nanostructuring</b>	<b>197</b>
<b>15</b>	<b>Introduction</b>	<b>199</b>
<b>16</b>	<b>The generation of carbon nanostructures</b>	<b>201</b>
<b>17</b>	<b>Pick-and-place manipulation</b>	<b>205</b>
17.1	Attaching cells to the cantilever . . . . .	206
17.1.1	Cantilever choice . . . . .	206
17.1.2	Cantilever modification . . . . .	206
17.1.3	Harvesting cells . . . . .	207
17.1.4	Attaching cells by performing a force curve . . . . .	207
17.2	Cell transfer . . . . .	208
17.3	Single cell delivery . . . . .	210
17.4	Results . . . . .	211
17.4.1	Micropatterned surfaces . . . . .	211
17.4.2	EBID structures . . . . .	214
<b>18</b>	<b>DNA origami on EBID structures</b>	<b>217</b>
18.1	Results . . . . .	218
18.1.1	Stepwise photobleaching . . . . .	219
18.2	Quenching effects of ITO . . . . .	220
<b>19</b>	<b>Conclusion and outlook</b>	<b>221</b>
<b>20</b>	<b>Materials and methods</b>	<b>223</b>
20.1	Sample preparation . . . . .	223
20.1.1	PEG-Silanization . . . . .	223
20.1.2	Electron-beam-induced deposition . . . . .	223
20.1.3	Biomolecule adsorption . . . . .	224
20.2	Atomic Force Microscopy . . . . .	224
20.3	Chamber design . . . . .	225
20.4	Stepwise photobleaching . . . . .	226

<b>V</b>	<b>Outlook and Conclusions</b>	<b>227</b>
<b>VI</b>	<b>Appendix</b>	<b>231</b>
<b>A</b>	<b>Sequences</b>	<b>233</b>
A.1	Modification strands . . . . .	233
A.2	Staple strand mixes . . . . .	234
A.3	M13mp18 . . . . .	238
	<b>List of Abbreviations</b>	<b>241</b>
	<b>List of Figures</b>	<b>245</b>
	<b>List of Tables</b>	<b>249</b>
	<b>Bibliography</b>	<b>250</b>
	<b>Danksagung</b>	<b>281</b>
	<b>Curriculum Vitae</b>	<b>283</b>



# Part I

## Introduction and fundamentals



Die approbierte gedruckte Originalversion dieser Dissertation ist an der TU Wien Bibliothek verfügbar.  
The approved original version of this doctoral thesis is available in print at TU Wien Bibliothek.

# Chapter 1

## Introduction

Cells, the fundamental functional and structural units of all living organisms, are complex machineries containing many biomolecules, mainly proteins, in their cytoplasm. Although the cytoplasm is densely filled with proteins, it is still a highly ordered assembly. Spatial organization of functional components is one of the general concepts at the cellular level with complex geometries being directly linked to function. As the number of different proteins in a typical human cell is estimated to be  $10^5$  [1] and the total number of proteins in a single cell is estimated to be as large as  $10^9$  [2], spatial organization is a feasible approach for proteins to serve their many tasks in living cells. This involves not only the location of proteins relative to cellular components, but also with respect to other proteins. Cells have different mechanisms to control spatial organization of their components, these include compartmentalization, the cytoskeleton, membrane anchoring and higher ordered protein assemblies [3]. In contrast to bacterial cells, eukaryotic cells are subdivided into functionally distinct, membrane-enclosed compartments. Each of these so called organelles contains a distinct chemical environment with its own set of specialized molecules. The cytoskeleton consists of a network of protein filaments in the cytoplasm which supports and moves the plasma membrane. Besides giving the cell its shape, providing mechanical strength and being responsible for cell motion, the cytoskeleton is involved in connectivity, internal organization, cellular dynamics and molecular transport. The importance of structure to a cell is reflected in the energy consumption of the maintenance of the actin network. With actin being one of the major components of the cytoskeleton, the actin network uses up to 50 % of a cells adenosine triphosphate (ATP) [4]. The plasma membrane and

its components can serve as scaffold to confine diffusion and flatten a 3D to a 2D system and about 30% of the proteins encoded in a mammalian genome are membrane proteins [3]. It is possible that the accumulation and colocalization of certain proteins is facilitated by the local lipid composition of the membrane. This highly controversial topic of membrane rafts is currently one of the most heatedly discussed in membrane biology [5–7]. Spatial organization of cell surface receptors and ligands can strongly influence the interaction between cells [8, 9]. Surface-surface interactions can trigger the self assembly of many proteins into multifunctional higher order complexes. These complexes often colocalize proteins and enzymes which belong to the same pathway, and influence enzyme activity by recruitment or exclusion of regulatory elements.

At the present day, a wide range of methods exists to study spatial organization in biomolecules in cells. Especially, the recent development of superresolution microscopy brought optical microscopy into the nanodimension and led to a vast number of newly available techniques and insights [10, 11]. But in order to fully investigate and understand biological systems, observation should be augmented by interaction. Controlling spatial arrangement to correlate structural variations to functional differences might help to gain insights in the purpose of specific arrangements. But so far, available methods to manipulate the positioning or arrangement of biomolecules lack some desirable features. Cellular processes happen on different length scales, a general method would therefore allow to control the relative or absolute position of proteins over a range of length scales starting from the size of a molecule up to the size of a cell, i.e. the nano- to micrometer range.

Communication of cells with either other cells or their environment happens with the use of ligands, which bind to transmembrane proteins referred to as receptors. In general, ligands are small, external molecules which can be immobilized on a surface, such as the plasma membrane of a cell, or be present in solution. If a surface receptor is engaged by a ligand, it may transmit a signal causing, among other things, conformational changes. These physical changes can then further induce chemical or biological changes in the system. Furthermore, the spatial organization of membrane-bound ligands has profound influence on receptor-mediated signaling. Investigation of receptor-ligand interactions has had a vast impact on biomedicine including drug-target interactions. [12]

Because of its central importance in adaptive immunity, the interaction of the

T cell receptor (TCR), present on the surface of T cells, with antigen presented by the peptide major histocompatibility complex (pMHC) is one of the most intensely studied receptor-ligand systems known. T cells are a major player in our body's immune system and much effort has been put into their characterization. Although many of the cell-surface and cytoplasmic molecules that are involved in the various forms of T cell recognition, activation and effector function have been identified, some fundamental questions still remain unanswered. It is assumed that next to intrinsic properties of the binding partners also the geometrical constraints in the immunological synapse, i.e. the transient interface between a T cell and an antigen presenting cell (APC), as well as mechanical forces and local molecular crowding influence receptor-ligand interactions. [13, 14]

Further, T cell activation is accompanied by the coordinated rearrangements of receptors, adhesion molecules and signaling proteins [15, 16]. Nevertheless, important insights on the association of the TCR with other co-receptors or membrane proteins are still missing. Pioneering colocalization studies were already performed on the TCR, but the difficulty in data analysis to separate specific interactions from other contributions made definite statements impossible [17, 18]. In particular, measurements of the binding kinetics of the  $\zeta$ -chain-associated protein kinase 70 (ZAP70), a protein present in the cytoplasm of T cells and a key player in T cell signaling, have been influenced by unspecific contributions, e.g. a cytosolic diffusing fraction and/or a membrane diffusing fraction. An improved method for measuring binding kinetics of interaction partners of the TCR would thus aid in elucidating the orchestrated interactions of the manifold of proteins involved in T cell activation.

## Goal of this work

The focus of this work is to establish nanostructuring techniques in the group and to use them together with existing microstructuring techniques to investigate different aspects of T cell activation on the nano- and the micrometer scale. In particular, this thesis will focus on structuring proteins in the plasma membrane. Therefore, the nanostructuring methods should allow a spatial arrangement of proteins on a scale of 10 nm to 100 nm and it should be possible to construct a variety of different geometries. Importantly, all structured surfaces must be compatible with live cell single molecule microscopy.

## Requirements

Probing properties of biological systems at different length scales is best accomplished by using appropriate structures at those length scales. However, it is hard to think of any single method which allows for structuring surfaces on the nano- and the micrometer scale at the same time. Using different surface structuring techniques subsequently, each tailored to probe system properties at a specific length scale, is a more feasible approach in contrast to the combination of different methods into a single approach, for which the individual techniques need to be compatible with each other.

Whereas soft lithography methods which involve printing and stamping of bio-molecules are well established techniques in the micrometer regime, lowering it further to the nanometer scale proved to be challenging [19]. Nonetheless, microstructures can display a large amount of ligands in defined areas and rearrange a large portion of interaction partners in a cell. The generation of interaction areas in a cell is a well suited approach to distinguish specific interactions of the patterned ligand with its interaction partner from unspecific interactions. Still, moving from bulk to single molecule experiments is not feasible in this approach.

In contrast to soft lithography techniques, methods for the organization of proteins on the nanometer scale often rely on hierarchical self-assembly based on pairwise interactions. This can be found in the sequence-specific hybridization of complementary strands of deoxyribonucleic acid (DNA). The specificity and predictability of these interactions together with being independent of the structural context, makes DNA an interesting candidate for the generation of structures on the nanoscale. In general, single DNA strands self-assemble in a conformation which minimizes the global free energy of the system by maximizing the number of possible base pairs between different strands or within a single strand. These properties of DNA have led to a variety of different methods for the design of nanostructures by self-assembly of single-stranded DNA (ssDNA) [20]. The most widely used approach known as DNA origami was first introduced in 2006 and involves the binding of a set of short, linear ssDNA “staples” to a long, circular ssDNA scaffold. The folding into a user-defined shape is accomplished by designing the staple sequences in a way that each staple specifically binds and connects two or more segments of the scaffold [21, 22]. While DNA origami have become a useful tool in the nanostructuring of surfaces, increasing their size and going to longer distances induces problems since global effects come into play.

Electron-beam lithography techniques offer the possibility to create custom patterns with sub-10 nm resolution as well as patterns in the micrometer regime, since electron beams can be focused into spots with diameters varying from micrometers down to the subangstrom level [23]. In electron-beam-induced deposition (EBID), a focused electron beam is scanned over a sample which leads to the localized decomposition of the substrate and the simultaneous deposition of nonvolatile components at the irradiated substrate sites [24, 25]. This method offers a direct-write process in the micro- and nanometer regime but is limited by its low throughput. Since only small areas can be patterned in an acceptable amount of time with this approach, experiments with cells are challenging. Other methods for placing cells on specific sample areas, e.g. using an atomic force microscope (AFM), need to be utilized in order to use this surface modification technique efficiently.

## Approach

Three different approaches to structure surfaces will be used and applied to questions in T cell biology, in order to test the influence of spatial organization on T cell activation or to use spatial organization as a tool to study protein binding kinetics in T cell activation. For this, I use DNA origami, microcontact printing and EBID lithography. A detailed introduction into immunobiology and in particular T cell biology is given in chapter 2. Chapter 3 of this work describes different microscopy techniques, such as single molecule fluorescence microscopy and fluorescence recovery after photobleaching (FRAP).

In order to position ligands precisely at the nanometer scale, DNA origami (Figure 1.1a) were introduced in the research group. With this tool, it is possible to create nanostructured surfaces which can be used to mimic APCs. Using DNA origami to investigate T cell activation requires three main steps:

- design and characterization of a DNA origami base structure
- introduction of multiple functionalities on the DNA origami base structure and subsequent characterization
- exploration of the effects of different designs on T cell activation

For receptor-ligand interactions between two cells, both interaction partners are usually displayed on the plasma membrane and are therefore mobile. Thus, it

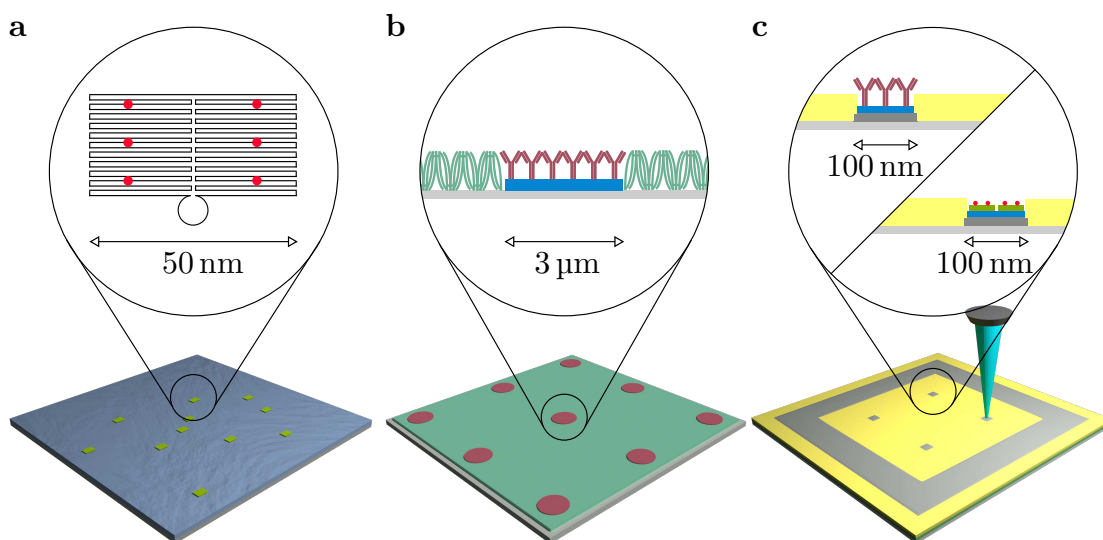


**Figure 1.1:** *Schematic overview of the presented methods for structuring surfaces. (a) DNA origami (green) on a supported lipid bilayer (blue) serve as mobile platforms for presenting ligands in specific configurations to cells. Zoom-in: Individual DNA origami offer attachment sites for ligands which can be positioned on a nanometer scale. (b) Micropatterning offers the possibility to present immobile ligands on a micrometer scale (pink) separated by other proteins like fibronectin (teal) promoting cell adhesion. The zoom-in shows a micropattern decorated with antibodies. Antibodies and fibronectin not drawn to scale. (c) In EBID a focused electron beam produces carbon islands and surfaces (gray) on a polyethylene glycol (PEG)-coated (yellow) indium tin oxide (ITO) layer (green). This technique supports the production of individually designed surfaces on the nano- and micrometer scale. Zoom-in: EBID structures can be decorated with ligands such as antibodies or with DNA origami.*



is desirable to attach DNA origami to lipid bilayers and to thereby generate mobile interaction platforms. Ideally, this approach makes DNA origami compatible with existing procedures in T cell biology. An introduction in the DNA origami technique with a detailed description of DNA origami functionalization and characterization is given in part II.

Soft lithography techniques such as micropatterning (Figure 1.1b) are well established in the research group. Here, the focus lies on its application in T cell biology, in particular on probing the binding kinetics of ZAP70. Micropatterning allows to focus ligand-receptor interactions on defined spots and to separate them from cellular background processes. FRAP is a standard technique to gather information on binding kinetics of proteins. Theoretical and experimental considerations concerning FRAP experiments of T cells on micropatterned surfaces are described in detail in part III.

EBID allows for custom designed surface structuring (Figure 1.1c). This brings some advantages with it, such as the combination of micro- and nanostructuring but also its disadvantages such as low throughput. In part IV, different approaches of applying EBID-structured surfaces on T cell biology are presented. This part is subdivided in two main chapters. Since production of large scale EBID structures is not feasible in a reasonable amount of time, a possibility to circumvent this issue is to use a coated AFM cantilever, attach a single cell to it and position it on the structured area. Further, it is discussed how EBID structuring can be combined with DNA origami to shield the produced nanostructure and place a defined number of ligands at these positions.



# Chapter 2

## Immunobiology

Immunology, the study of the responses we make against infection by potential pathogens, emerged in the late 18<sup>th</sup> century with the development of smallpox vaccine by Edward Jenner. The body's immune responses can be categorized into innate and adaptive responses. An innate immune response is not specific for any individual pathogens, but it occurs rapidly and can combat a wide variety of pathogens. In contrast, the adaptive immune response triggers the production of antibodies against a specific pathogen. This form of responses is developed during the lifetime of an individual as an adaptation to an infection, hence its name. To protect the individual effectively against disease, the immune system consists of a variety of effector cells and molecules which carry out its main tasks: immunological recognition, effector function, regulation and memory. The different cell types involved in the adaptive immune system are introduced in the following section. This chapter is mainly based on [13].

### 2.1 Cells of the immune system

The cells of the innate and adaptive immune system are called leukocytes or white blood cells, which can be grouped into two main categories—the myeloid and lymphoid lineages. In general, leukocytes originate in the bone marrow and most of them also develop and mature there. After maturation, their role is to guard the peripheral tissues, either by residing within tissues or by circulating in the bloodstream or the lymphatic system. The lymphoid cells are the main type of cell found in lymph. They include natural killer (NK) cells of the innate

immune system together with the lymphocytes of the adaptive immune system (T and B cells). Unlike other leukocytes, T and B lymphocytes possess highly specialized antigen receptors on their surface with which they can recognize individual antigens. Further, they are distinguished from each other by their sites of differentiation—the thymus and bone marrow, respectively. For the sake of completeness all types of lymphocytes are described. As the focus of this thesis lies on the interaction of T helper cells with APCs, these cell types are described in greater detail.

### 2.1.1 T cells

T cells (thymus cells) are, together with B cells, the key player in adaptive immunity. Their main job is to recognize infectious agents, which are presented to them by antigen presenting cells. T cells originate—as all other cells of the immune system—in the bone marrow, but unlike other lymphocytes they mature in the thymus before they congregate in lymphoid tissues throughout the body. Prior to the T cells finishing their development and leaving the thymus as naïve T cells, they have to undergo negative selection, in which T cells that are capable of binding too strongly to self antigens expressed on major histocompatibility complex (MHC) molecules are removed. Each individual T cell is specific for exactly one antigen. If a naïve T cell meets its specific antigen presented to it in the form of peptide-loaded MHC molecule on the surface of an APC, it initiates an adaptive immune response. Unlike B cells, T cells cannot recognize and therefore cannot respond to soluble antigens. Antigens have to be processed by professional APCs and presented to them via carrier molecules such as MHC. Following recognition, T cells proliferate and differentiate into several functionally specialized types of effector T cells. Depending on the expression of either CD8 (cluster of differentiation 8) or CD4 (cluster of differentiation 4) on their surface and on the corresponding class of MHC they can interact with, T cells can be categorized into CD8<sup>+</sup> T cells, also called cytotoxic T cells, which recognize antigen peptides presented by MHC class I molecules and CD4<sup>+</sup> T cells, also called helper T cells, which recognize antigen peptides presented by MHC class II molecules. Following antigen recognition, CD8<sup>+</sup> T cells differentiate into cytotoxic effector T cells which recognize and kill cells infected with viruses or other intracellular pathogens. In contrast, CD4<sup>+</sup> T cells can differentiate into distinct effector T cells with different immunological functions such as activa-

tion of target cells by providing additional signals influencing the behavior and activity of other cells of the immune system or regulatory activity to limit the extent of an immune response. In both cases, recognition of hazardous antigen is achieved by TCRs being present on a T cell's surface, which are able to interact with peptide-loaded MHCs and co-stimulatory molecules on the surface of an APC. A more detailed description of the TCR complex, in particular its structure, its function and its interaction with pMHC, is given in section 2.2.1. Some of the T cells involved in the immune response differentiate into memory T cells, which will readily differentiate into effector T cells in the case of a second exposure to their specific antigen, thereby being responsible for long-lasting immunity. Due to their central importance in adaptive immunity, there has been an immense progress in our understanding of how T cells recognize antigen on a molecular scale and T cells are most likely the best-studied cells known to mankind. Still, T cell biology is a complex field and some fundamental questions remain unanswered. [13, 26]

### 2.1.2 Antigen presenting cells

APCs stand at the beginning of an effective adaptive immune response. They take up antigen material at sites of infection, process it and after migration to local lymphoid tissue, they present individual antigens as peptides via MHCs molecules on their cell membrane to other cells of the immune system. These antigens can be recognized by T cells via an interaction of the TCR and the pMHC. In addition to presented antigen, lymphocytes require additional signals to become activated and initiate an immune response. APCs deliver these signals by expressing cell-surface proteins called co-stimulatory molecules, which are also present on their plasma membrane. The cell-surface proteins B7.1 (CD80) and B7.2 (CD86) expressed by APCs can provide co-stimulatory signals to T cells. Further, APCs also express cell-adhesion molecules to control their interactions with leukocytes. This tight adhesion is due to the binding of intercellular adhesion molecules (ICAMs) with proteins of the integrin family on leukocytes [13]. Proteins involved in the activation of T cells will be described in further detail in section 2.2.1. A variety of cells can serve as some form of APC and can present antigen to CD8 cytotoxic T cells [27, 28]. APCs capable of stimulating CD4 helper T cells expressing MHC class II molecules together with co-stimulatory molecules on their plasma membrane are called professional APCs. In general,

macrophages, B cells and dendritic cells (DCs) are regarded as the professional APCs of the immune system. Mainly the highly specialized DCs, which have the broadest range of antigen presentation, are involved in activating T cells [29].

### 2.1.3 B and NK cells

B cells (bone marrow- or bursa-derived cells) are a major cellular component of the adaptive immune response. They express B cell receptors (BCRs) on their cell membrane, which allows them to bind to and recognize specific antigen, which will lead to cell proliferation and differentiation into plasma cells. Antigen recognition by B cells and subsequent activation occurs in the secondary lymphoid organs (SLOs), such as the lymph nodes and spleen, and can happen with or without the help of T cells (T cell-dependent/independent activation). In addition to their role in humoral immunity by the secretion of antibodies, B cells can also present antigen and serve as APCs. [13, 30, 31]

NK cells are part of the innate immune system and lack antigen specificity in contrast to T and B cells. NK cells can recognize and kill some abnormal cells and their main function is to defend from both tumors and intracellular infections. NK cells will not be described in further detail, since they are part of the innate immune system. Unless indicated otherwise, the term lymphocyte refers to antigen-specific lymphocytes only. [13, 32]

## 2.2 Antigen recognition by T cell receptors

T cell activation is a unique process, as T cells have the ability to discriminate between healthy and abnormal cells in the body. Two features are particularly intriguing. First, antigen recognition is highly specific, since a single T cell can recognize only one specific antigen. Second, few—maybe even only one—pMHC are sufficient to activate a T cell, which makes T cell activation a highly sensitive process [33].

## 2.2.1 Key players in T cell activation

### T cell receptor (TCR)

The TCR is the centerpiece of immunological recognition and consequently of adaptive immunity in general. Although being related to immunoglobulins, the TCR is quite distinct in its structure and recognition properties.

The TCR heterodimer consists of two different transmembrane glycoprotein chains, termed TCR $\alpha$  and TCR $\beta$ , linked by a disulfide bond (Figure 2.1a). These  $\alpha$ : $\beta$  heterodimers show close structural similarities to an immunoglobulin molecule, in particular to the Fab fragment, which is the antibody region responsible for the binding of antigens. The extracellular portion of each chain has an amino-terminal variable (V) region with homology to an immunoglobulin V domain, a constant (C) region with homology to an immunoglobulin C domain. These V domains are responsible for antigen recognition in most T cells. A short stalk segment, similar to an immunoglobulin hinge region, contains the cysteine residue that forms the interchain disulfide bond and it connects the other domains to the membrane. The transmembrane helices of both chains span the membrane by a hydrophobic transmembrane segment and end in a short cytoplasmic tail. These transmembrane segments contain positively charged residues, two on the  $\alpha$  chain and one on the  $\beta$  chain.

The TCR $\alpha$ : $\beta$  heterodimer is not sufficient to constitute a complete antigen receptor and other molecules are required for cell surface expression of the full TCR. These molecules are the CD3 $\gamma$ , CD3 $\delta$  and CD3 $\epsilon$  chains, which together form the CD3 complex, and the  $\zeta$  chains, present as a disulfide linked homodimer. In contrast to the  $\zeta$  chains, which have only a short extracellular domain, the CD3 proteins have a extracellular immunoglobulin-like domain. In general, the term TCR refers to the entire complex including all subunits. It is thought, that the interaction between different receptor subunits is mediated by reciprocal charge interactions between basic and acidic intramembrane amino acids of the chains, as indicated in Figure 2.1b. In particular, the two positive charges allow the TCR $\alpha$  transmembrane region to interact with one CD3 $\delta$ :CD3 $\epsilon$  dimer and with one  $\zeta$  dimer, while the single positive charge in the TCR $\beta$  chain allows it to interact with a CD3 $\gamma$ :CD3 $\epsilon$  dimer. Tyrosine phosphorylation on the cytosolic regions of the CD3 $\gamma$ ,  $\delta$ ,  $\epsilon$  and the  $\zeta$  chains initiates TCR signaling. The regions where these phosphorylations occurs are called immunoreceptor tyrosine-based

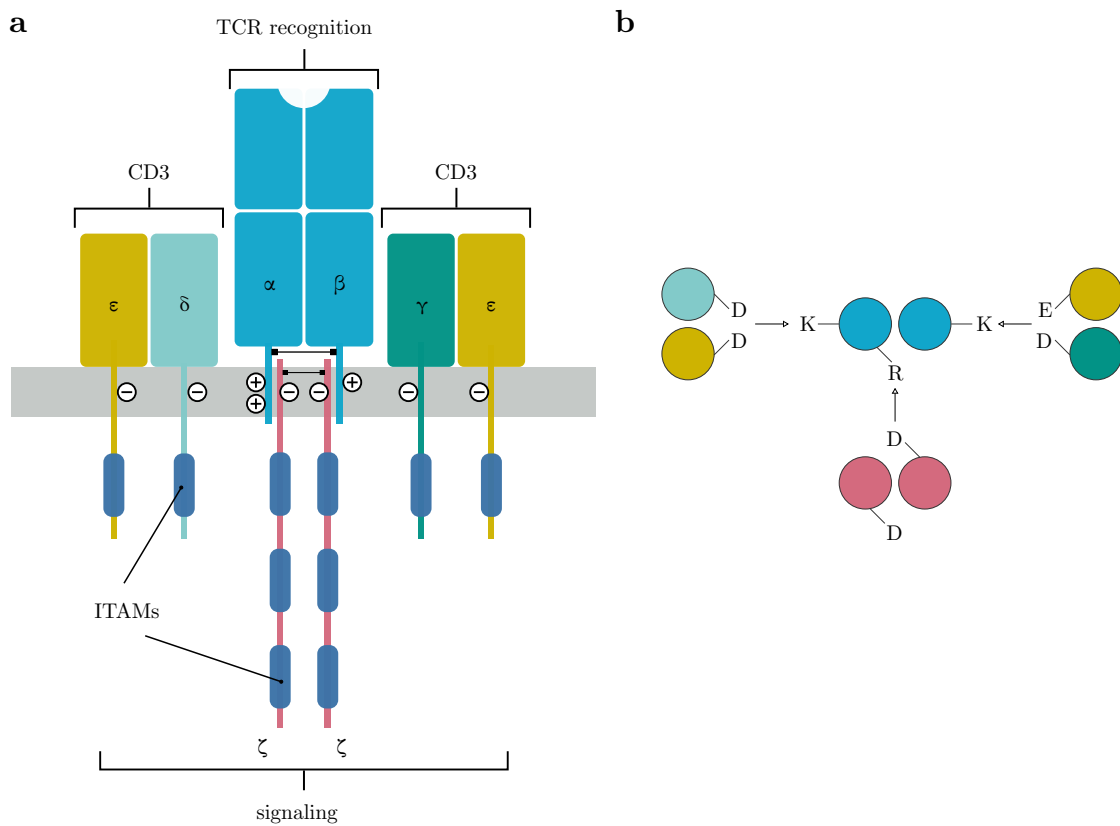


**Figure 2.1: Composition of the T cell receptor complex.** (a) The TCR complex consists of the TCR $\alpha$ : $\beta$  heterodimer, which is responsible for antigen recognition, associated with CD3 with its four signaling chains ( $\gamma$ ,  $\delta$  and two times  $\epsilon$ ). Further, a homodimer of  $\zeta$  chains is associated with the TCR. In total, the TCR complex has ten immunoreceptor tyrosine-based activation motifs (ITAMs), one on each CD3 chain and three on each  $\zeta$  chain. Charges in the transmembrane region of each chain are indicated with plus and minus signs. (b) Transmembrane cross section of the TCR subunits. The positive charges from a lysine (K) of the  $\alpha$  chain attracts the two negatively charged aspartic acids (D) of the CD3 $\delta$ : $\epsilon$  dimer, similar to how the lysine (K) of the  $\beta$  chain attracts the negative charges of aspartic acid (D) and glutamic acid (E) of the CD3 $\gamma$ : $\epsilon$  dimer. Further, the other positive charge of the arginine (R) on the  $\alpha$  chain interacts with the  $\zeta$  homodimer. Illustration adapted from [13].



activation motifs (ITAMs). In total the TCR has 10 ITAMs with each CD3 subunit containing one ITAM and each  $\zeta$  chain containing three ITAMs. [13]

### pMHC and CD4

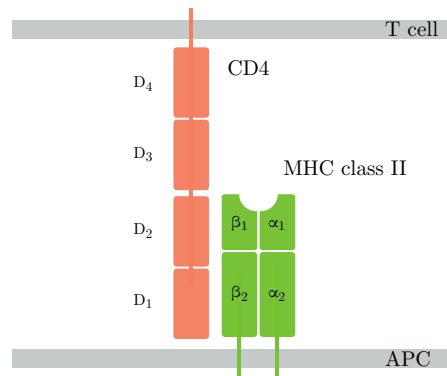


**Figure 2.2:** *The binding of CD4 to an MHC class II molecule. The MHC class II molecule consists of two transmembrane glycoprotein chains with two domains each, shown in green. Together they form a compact four-domain structure. The CD4 molecule consists of four Ig-like domains, shown in red. The binding site for CD4 is at the base of the  $\beta_2$  domain on the MHC class II, nearest to the membrane and distant from the peptide-binding cleft. Illustration adapted from [13].*

pMHC molecules play an as important role in the recognition of antigen as the TCR itself, since T cells can only recognize stimulating peptides when bound to an MHC molecule. Thus, the peptide together with the MHC molecule make up the ligand recognized by the T cell. Two distinct types of MHC molecules—MHC class I and MHC class II—are known. Although showing similarities, they differ in their structure as well as their expression pattern in the tissues of the body. As the focus of this thesis lies on CD4<sup>+</sup> helper T cells, only MHC class II molecules, which can be recognized by those cells, will be discussed. MHC class II molecules consist of two membrane spanning chains,  $\alpha$  and  $\beta$ . This four-domain structure can also be seen as two paired protein domains close to the plasma membrane, resembling immunoglobulin domains, and as two domains furthest away from the membrane,  $\alpha_1$  and  $\beta_1$ . These two domains from different chains fold together the peptide binding site (Figure 2.2).

The CD4 molecule is composed of four immunoglobulin-like domains ( $D_1$  to  $D_4$ ). The two tightly packed amino-terminal domains  $D_1$  and  $D_2$  form a rigid structure and are connected by a flexible hinge to the two carboxy-terminal domains  $D_3$  and  $D_4$ . The amino-terminal domain  $D_1$ , structurally similar to an immunoglobulin V domain, is thought to be the binding site for MHC class II molecules. Both CD4 and the TCR can bind simultaneously to the same pMHC complex without spatially blocking each other. Moreover, binding of CD4 to the pMHC is necessary for an effective response and increases the sensitivity to antigen. CD4 is therefore called a co-receptor. Still, cell-based assays suggest only a weak interaction between CD4 and pMHC with affinities  $K_d > 100 \mu\text{M}$  [34, 35]. As a comparison, affinities ( $K_d$ ) in the range of  $1 \mu\text{M}$  to  $100 \mu\text{M}$  have been found for TCR-pMHC binding [36–38].

CD4 can strongly interact with the tyrosine kinase Lck via its cytoplasmic tail. Binding to the pMHC complex results in CD4 recruiting Lck in close proximity to the TCR and other associated signaling components. This leads to the propagation and enhancement of the intracellular signal generated when the TCR binds its ligand. Further details of the intracellular signaling pathway are discussed in section 2.3.

### Cell-adhesion molecules

During migration through the cortical region of the lymph node, transient binding of T cells to APCs allows them to sample a large number of MHC molecules in search of a specific peptide. If a T cell recognizes a pMHC molecule, binding of ICAMs on the APC to proteins of the integrin family on T cells leads to tighter adhesion. More precisely, T cell signaling results in a conformational change in leukocyte function-associated antigen 1 (LFA1), thereby greatly increasing its affinity for ICAM-1. The integrin molecule LFA1 consists of two transmembrane protein chains, a large  $\alpha$  chain that pairs noncovalently with a smaller  $\beta$  chain (Figure 2.3a). All T cells express LFA1, which is composed of the  $\alpha_L:\beta_2$  chains and is also known as CD11a:CD18. ICAM-1, the ligand of LFA1, is a single-pass membrane protein and its extracellular domain is composed of several immunoglobulin-like domains.

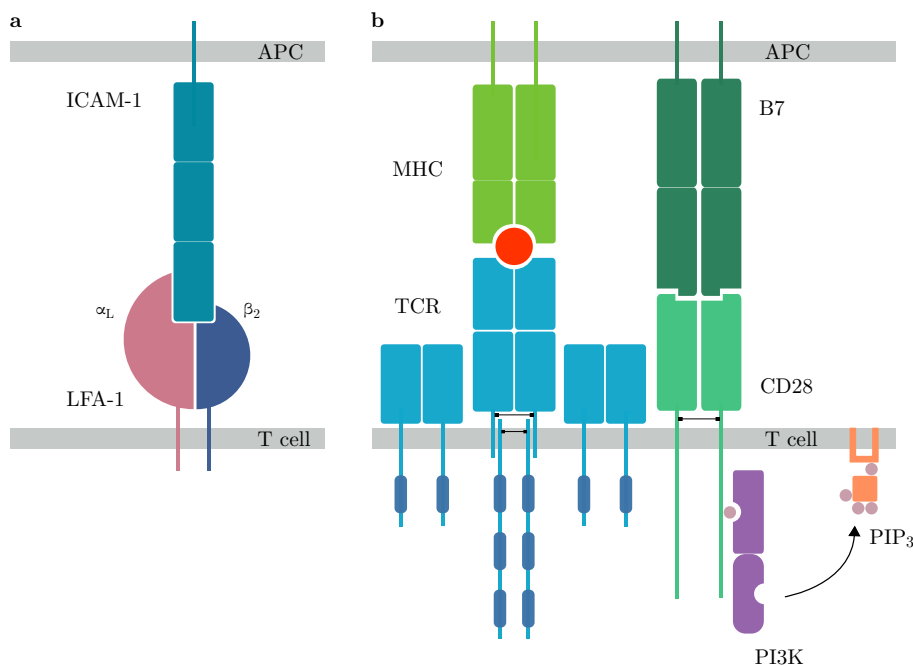


**Figure 2.3: Binding of adhesion and co-stimulatory molecules to their ligands.** (a) Binding of integrins on the T cell to adhesion molecules on the APC stabilizes cell-cell interactions. LFA1, member of the integrin family, consists of an  $\alpha$  chain paired noncovalently to a  $\beta$  chain. (b) T cell engagement to both antigen and a co-stimulatory ligand on the same APC is necessary for sustained T cell activation. Specialized APCs present co-stimulatory molecules such as B7 to T cells. B7 can interact with CD28, which results in the tyrosine phosphorylation of the cytoplasmic domain of CD28. This leads to the activation of PI 3-kinase and to the generation of PIP<sub>3</sub>. Illustration adapted from [13].

### Co-stimulatory molecules

Binding of the TCR complex to MHC molecules displaying antigenic peptides is not sufficient for the sustained activation of naïve T cells. Interaction of cell-surface receptors on the T cell with co-stimulatory ligands on the APC provides an additional signal necessary for T cell activation and most adaptive immune responses. The co-stimulatory ligands B7.1 and B7.2, also known as CD80 and CD86 respectively, are cell-surface proteins mainly expressed on professional APCs. They bind to the CD28 receptor that is present on the surface of all naïve T cells (Figure 2.3b). The interaction of CD28 with B7 leads to the tyrosine phosphorylation of the cytoplasmic domain of CD28 by Lck. This results in the activation of the phosphoinositide 3-kinase (PI 3-kinase) to generate phosphatidylinositol (3,4,5)-trisphosphate (PIP<sub>3</sub>), which then is responsible for the recruitment of several enzymes important in downstream signaling.

### ζ-chain-associated protein kinase 70 (ZAP-70)

Recruitment of Lck via CD4 to the TCR leads to the phosphorylation of ITAMs located on the intracellular chains of the TCR complex (Figure 2.4a). These doubly phosphorylated ITAMs serve as binding sites for signaling proteins that have a tandem SH2 (Src homology 2) domain, in particular for the tyrosine kinase ZAP70 (ζ-chain-associated protein kinase 70), which promotes downstream signaling [39]. This rapid translocation of cytosolic ZAP70 to the plasma membrane during TCR activation was first shown in HeLa cells using ZAP70 fused to a Green fluorescent protein (GFP) [40]. The two SH2 domains of ZAP70 can be simultaneously engaged by two phosphorylated tyrosines on an ITAM (Figure 2.4b). To ensure this binding, precise spacing of the tyrosine residues on the ITAM is of importance. Further, simultaneous binding of both SH2 domains improves the affinity and thereby provides specificity to ZAP70 binding [41–43]. In addition, also lipids influence SH2 domain mediated cellular protein-protein interaction networks. In the case of ZAP70, the C-terminal SH2 domain can simultaneously bind multiple plasma membrane lipids and a phosphorylated tyrosine residue [44]. ZAP70 association to the TCR is a highly dynamic process, involving binding and release of ZAP70 [45]. ZAP70 recruitment to the active TCR complex leads to the phosphorylation of ZAP70, either by Lck or by autophosphorylation. As a result of this phosphorylation, ZAP70 becomes an active

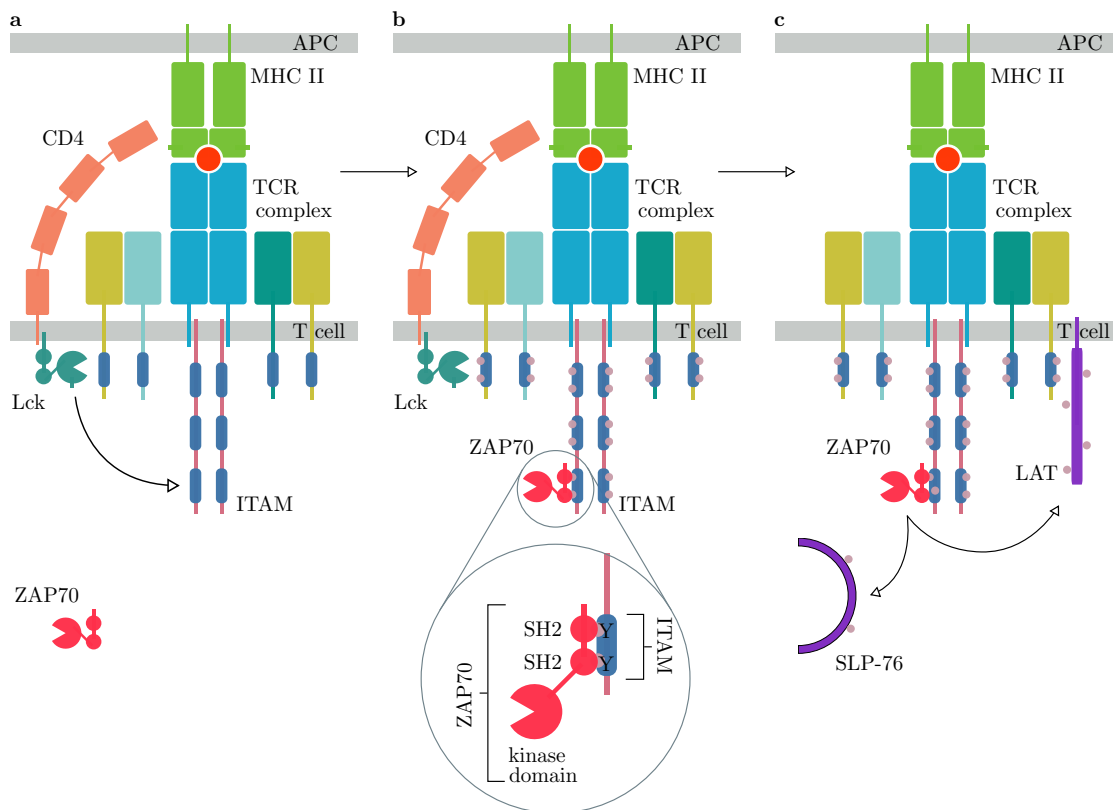


**Figure 2.4: ITAM phosphorylation is responsible for the recruitment of ZAP70 to the TCR.** (a) Upon engagement of CD4 with the pMHC, the co-receptor-associated kinase Lck phosphorylates the ITAMs in the TCR complex. (b) Following this process, the tyrosine kinase ZAP70 binds to phosphorylated ITAMs via its tandem SH2 domain. Thereby ZAP70 can be phosphorylated and activated by Lck. Lower panel: The ITAMs of the TCR contain tyrosine residues (Y) with a specific spacing in between, which is important in binding proteins such as ZAP70 that contain a tandem SH2 domain. When both tyrosine residues are phosphorylated, ZAP70 can dock cooperatively to both phosphotyrosines. (c) After recruitment into the active signaling complex, ZAP70 phosphorylates and recruits the scaffold protein LAT and SLP-76 to the activated TCR complex. Illustration adapted from [13].

kinase whereupon it is able to phosphorylate its substrates. These substrates include the scaffold protein linker of activated T cells (LAT), a transmembrane protein, and another adaptor protein called SLP-76. The adaptor protein Gads links LAT and SLP-76, which is the next step in the signaling pathway.

Further details on ZAP70 can be found in section 11.3.

## 2.2.2 The immunological synapse

T cell antigen recognition takes place within the immunological synapse (IS), i.e. the contact area between an APC and a T cell (Figure 2.5a). Originally, the term immunological synapse was chosen to highlight the structural similarities with the neurological synapse, the contact between neurons in the central nervous system. The synapse nature of this complex cellular structure that forms at the interface of a T cell and an APC was first proposed by M. Norcross in 1984 [46], although the term immunological synapse was first used by W. Paul and colleagues in 1994 [47]. Besides this first description in terms of directed secretion of cytokines between T cells and APCs, it was the groundbreaking discovery of molecular segregation of proteins into activation clusters [15, 16, 48] that led to the conjoined concept of the immunological synapse as the physical manifestation of T cell activation, and molecular segregation as its functional reflection [49].

The bimembrane structure of the IS lays the foundation for antigen-binding and subsequent molecular recognition events, which emphasizes its central importance in T cell activation. This synapse shows a complex, still highly organized and dynamic distribution of molecules, composing typical pattern-activation clusters, that allow for a bidirectional and cell-specific flow of information. This molecular redistribution is highly dependent on antigen, requiring the interaction of a TCR with a peptide-loaded MHC molecule. Still, there is growing evidence that the interaction between receptors and ligands in the IS is not only dependent on the intrinsic properties of the binding partners, but also local molecular crowding and geometrical constraints within the IS as well as mechanical forces play an important role. Depending on the type of T cell and APC forming the IS, its outcome and features will differ. For CD4<sup>+</sup> helper T cells, the interaction with an APC loaded with a specific antigen will lead to antigen recognition and T cell activation. Despite ongoing findings, further research is needed to advance our understanding of the IS. [26, 50]

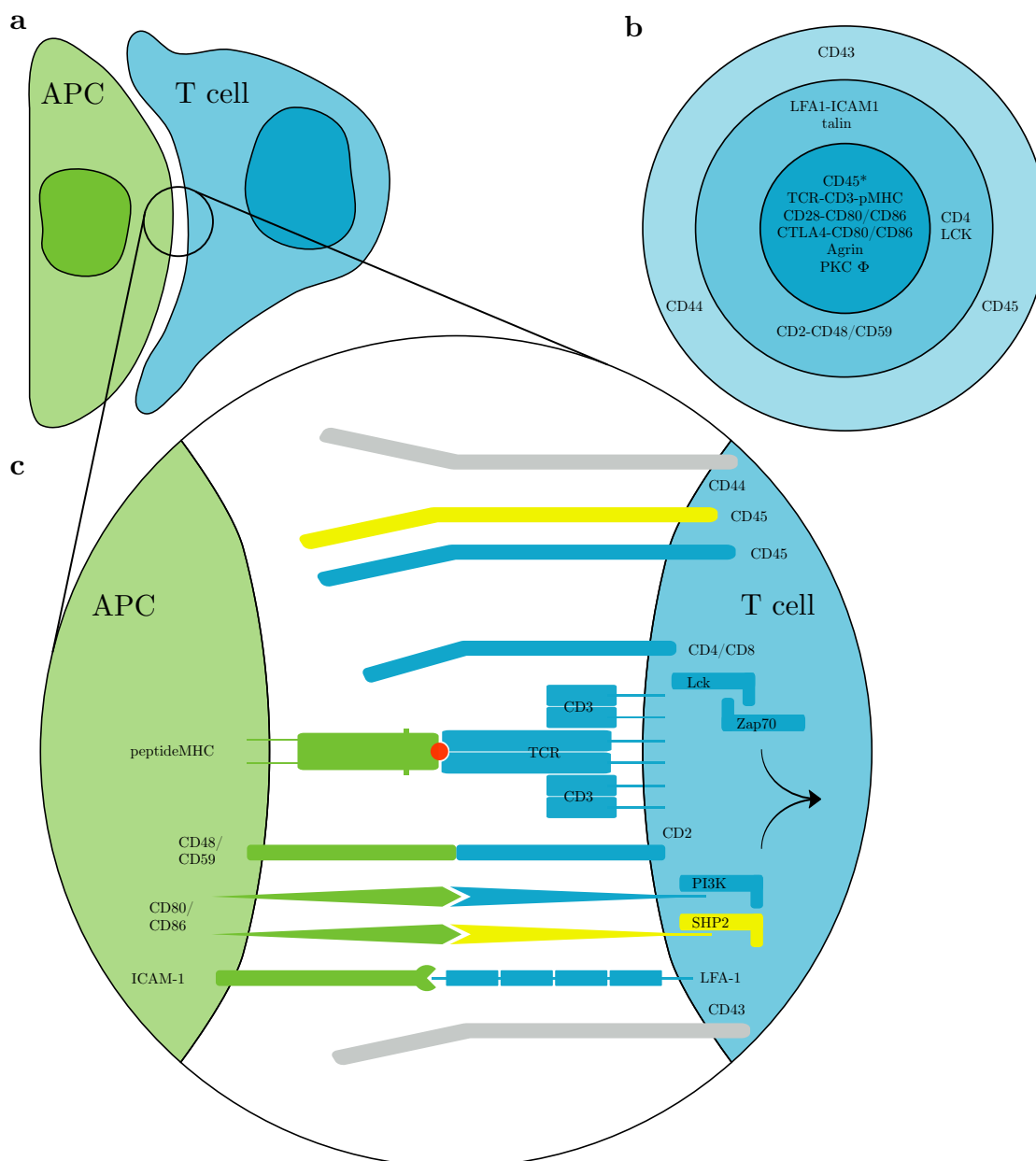


**Figure 2.5: Overview of an immunological synapse (IS).** (a) The IS is the interaction site between a T cell and an APC. (b) Top view of the IS showing the characteristic "bull's eye" pattern consisting of a central region of the supramolecular activation complex (cSMAC), a peripheral ring called pSMAC, and the outmost distal region being the dSMAC. (c) Profile view of the IS with a selection of signaling molecules and ligand pairs important for T cell activation (arrow). Blue indicates activating/co-stimulatory molecules, yellow indicates inhibitor molecules and gray indicates molecules which are not contributing to signaling. The pMHC is shown in green. Illustration adapted from [14, 26].

## Structure

Initial findings describe the structure of an IS as concentric rings containing segregated clusters of proteins (see Figure 2.5b). Key molecules such as the TCR and the adhesion integrin LFA1 are organized in these distinct areas termed supramolecular activation complexes (SMACs). The presence of these SMACs within the IS was first reported by Abraham Kupfer and co-workers, who visualized T cell–APC conjugates in 3D. [16]

However, depending on cell type and stimulation conditions, IS formation was found to be rather variable [51, 52]. Further, the generation of the central supramolecular activation complex (cSMAC) takes several minutes after interaction of the TCR and the pMHC on a supported lipid bilayer which would be too late for triggering the initial TCR signals [53]. Indeed, it was revealed that prior to mature IS formation, the TCR begins clustering immediately after T cells recognize pMHC on the bilayer. These initial TCR microclusters mediate both initial and sustained TCR signaling [54–58] and are described as units of CD3 $\zeta$ , accumulating at the center of the interface upon stimulation [59, 60]. Quantification analysis showed that each TCR microcluster contains up to several hundred TCR molecules. Initially, microclusters are generated at the center of the IS and then, as the T cell spreads, are increased over the entire interface. After maximum cellular spreading, these microclusters move toward the center of the interface and accumulate to generate the cSMAC of the IS. It has been noticed that only strong antigen stimulation induces cSMAC formation. [61]

## Formation

Synapse formation begins with the establishment of initial contacts between a T cell and an APC by interactions between LFA1 present on the T cell and adhesion molecules such as ICAM on the target cell. Recognition of agonist pMHC causes the T cell to form a stable cell contact with the corresponding APC and the recruitment of receptors and signaling molecules to the resulting IS (Figure 2.5c). Initial membrane proximal TCR signaling proceeds during the formation of a mature IS. Thus, a mature immunological synapse is not a necessity to initiate T cell activation, but forms as a consequence of initial signals. [14, 49, 53]



## Artificial APCs

To elucidate mechanisms explaining molecular segregation of proteins within the IS, specific proteins in the T cell junction need to be visualized in detail. Grakoui and coworkers were the first to replace the APC with a planar lipid bilayer containing fluorescently labeled pMHC and ICAM to monitor their spatiotemporal redistribution upon interactions with cellular receptors during the development of the IS. As long as adhesion through ICAM is provided, T cells form synapses with such antigen-bearing artificial membranes and proliferate. [15]

## 2.3 Signaling pathways

While the previous sections provides a detailed description of important proteins involved in T cell activation, this section closes the chapter on immunology by summarizing the T cell signaling pathway. It thereby gives an overview of how the different components involved in T cell activation interact with each other and how this leads to activation. It also describes the release of calcium into the cytosol, which is regularly used as an indicator of lymphocyte activation.

The TCR $\alpha$ : $\beta$  heterodimer has excellent specificity for antigen, but lacks the intrinsic signaling capacity. Only the association of the antigen-binding chains with additional proteins forms a fully functional antigen receptor complex. These signal transduction subunits are responsible for the translation of the initial external signal into biochemical signals within the cell. [62, 63] The proteins composing this subunit are the CD3  $\gamma$ ,  $\delta$ ,  $\epsilon$  chains together with the TCR $\zeta$  chains, which cytoplasmic regions contain signaling motifs known as ITAMs (Figure 2.1a). Activation of the receptors by antigen recognition and co-receptor binding to the pMHC complex allows Lck to phosphorylate those ITAMs (Figure 2.2). The phosphorylated ITAMs then recruit and activate the tyrosine kinase ZAP70, which is responsible for phosphorylation of the scaffold protein LAT—a transmembrane protein with a large cytoplasmic domain—and the adaptor protein SLP-76. Then, these proteins recruit the key signaling protein PLC- $\gamma$  to the membrane. The additional co-stimulatory signal required for PLC- $\gamma$  activation is delivered through the cell-surface receptor CD28. Activated PLC- $\gamma$  cleaves PIP2 to generate the second messengers DAG and IP3. Activated PLC- $\gamma$  initiates three distinct terminal TCR signaling pathways—a cytosolic Ca<sup>2+</sup> increase and the activation of both Ras and PKC- $\theta$ —that culminate in the activation

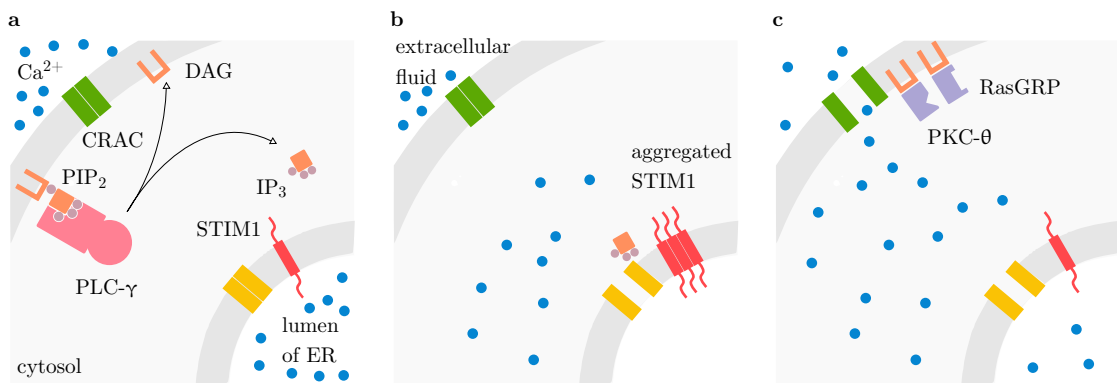


**Figure 2.6:**  $Ca^{2+}$  entry activates the nuclear factor of activated T cells (NFAT). (a) When phospholipase C- $\gamma$  (PLC- $\gamma$ ) is activated by phosphorylation, it cleaves phosphatidylinositol bisphosphate (PIP<sub>2</sub>) into two important signaling molecules, inositol trisphosphate (IP<sub>3</sub>) and diacylglycerol (DAG). (b) Binding of IP<sub>3</sub> to a receptor in the endoplasmic reticulum (ER) membrane opens the calcium channels (yellow) and allows calcium ions to enter the cytosol from the ER. This depletion of  $Ca^{2+}$  stores causes the aggregation of the ER sensor STIM1. (c) Aggregation of STIM1 leads to the opening of calcium channels in the plasma membrane called CRAC, allowing the entry of extracellular calcium. This results in a further increased calcium concentration and a restoration of ER  $Ca^{2+}$  stores. Further, the signaling proteins RasGRP and protein kinase C- $\theta$  (PKC- $\theta$ ) are recruited to the membrane. Illustration adapted from [13].

of nuclear transcription factors (see Figure 2.6). IP<sub>3</sub> induces an increase in the intracellular Ca<sup>2+</sup> concentration by opening Ca<sup>2+</sup> channels on the ER membrane and releasing the stored calcium into the cytosol. Entry of extracellular calcium further increases cytosolic Ca<sup>2+</sup> concentration and restores ER Ca<sup>2+</sup> stores. The increased cytosolic Ca<sup>2+</sup> results in the activation of a transcription factor called nuclear factor of activated T cells (NFAT). DAG is involved in the activation of the small GTPase Ras, which stimulates the mitogen-activated protein kinase (MAPK) relay and leads to the expression of the transcription factor AP-1. DAG is also responsible for the recruitment of PKC-θ, which leads to the activation of NFκ B. The transcription factors NFκ B, NFAT, and AP-1 initiate gene transcription of the cytokine interleukin-2 (IL-2) in the nucleus, resulting in differentiation and proliferation of the activated lymphocyte.



# Chapter 3

## Microscopy techniques

Microscopy is the art of imaging small objects that are not within the resolution limit of the human eye. Optical microscopy techniques enabled early progress in cell biology and—together with the development of other microscopy techniques—revolutionized the life sciences. While optical microscopy still is an essential technique, other branches of microscopy evolved, in particular electron microscopy and scanning probe microscopy. In this section, the fundamental principles of these microscopy techniques are described, with particular focus on the techniques used in this thesis.

### 3.1 Fluorescence microscopy

In this section, fundamental concepts of fluorescence microscopy are described. First, general physical concepts of fluorescence will be introduced. Then, the working principles of fluorescence microscopes will be discussed, particularly with regard to total internal reflection fluorescence (TIRF) microscopy. Further, single-molecule microscopy and specialized microscopy techniques will be described. This section is mainly based on [64].

#### 3.1.1 Photophysical principles of fluorescence

Fluorescence is the relaxation from an excited state via the emission of light by atoms or molecules, that have previously been excited by the absorption of light. The time interval between absorption and emission is called fluorescence lifetime. In general, the emitted light has a lower energy, i.e. a longer wavelength,

than the absorbed light. This difference in energy is called Stokes shift. Typical fluorescence processes happen in a wavelength range of 250 nm to 700 nm. The physical systems in which fluorescence occurs are called fluorophores.

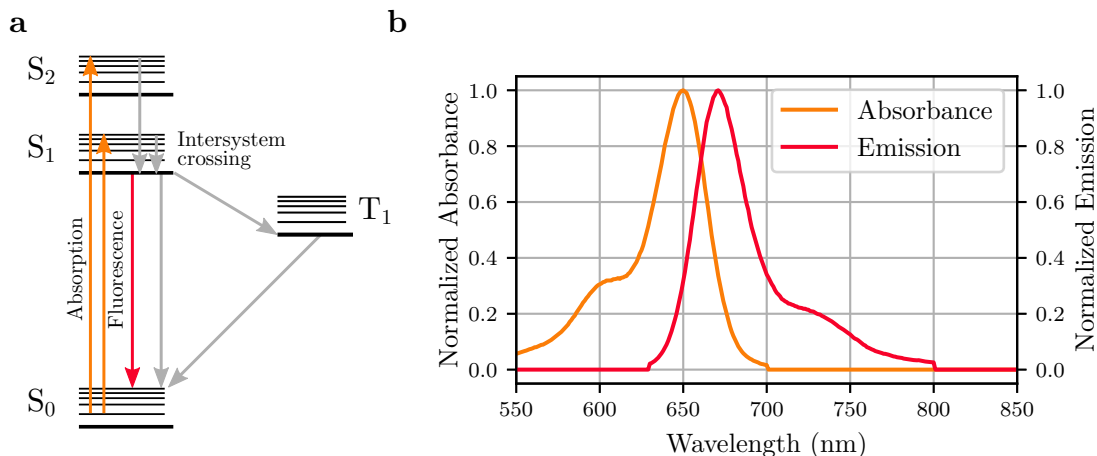


**Figure 3.1: The physical basis of fluorescence.** (a) A Jablonski diagram showing the excitation and relaxation of a fluorescent molecule.  $S_0$ ,  $S_1$  and  $S_2$  are the singlet ground state and the first and second excited singlet states, respectively.  $T_1$  is a triplet state. Thick lines indicate the vibrational ground state of each electronic state, whereas thin lines indicate higher vibrational states. Colored arrows indicate radiative transitions between different states, gray arrows indicate non-radiative transitions. (b) The normalized absorption and emission spectrum of the Alexa Fluor 647 dye. Alexa Fluor 647 has an absorption peak at 650 nm and fluoresces at a range of higher wavelengths with a peak at 665 nm. The energy difference between absorption and emission is called Stokes shift.

Different electronic states called  $S_0$ ,  $S_1$ ,  $S_2$  etc. exist for each molecule (Figure 3.1a). In general, excitation happens starting from the ground state  $S_0$ , since only few molecules have enough energy to populate a different state at room temperature. Absorption of UV- or visible light leads to the excitation into higher vibrational levels of the singlet states  $S_1$  or  $S_2$ . In a typical excitation process with light of a broad wavelength range, many different vibrational states of the excited states will be occupied with different probabilities. Their combination gives rise to the absorption spectrum of a fluorophore (Figure 3.1b). Directly after the absorption of a photon, relaxation to the lowest vibrational level of the excited state  $S_1$  happens via the dissipation of energy from the molecule to

its surroundings. The relaxation to the ground state coupled with the emission of a photon is called fluorescence. Densely packed vibrational levels of the ground state lead to a broad emission spectrum of the fluorophore. Most fluorophores run through this cycle several hundred to thousand times—depending on the fluorophore—until they photobleach in the excited state. Photobleaching leads to the irreversible destruction of the fluorophore by photochemical alteration. Besides fluorescence, also other possibilities exist for the relaxation of the excited state. The excited fluorophore can collide with a different molecule, leading to a non-radiative energy transfer like quenching. A different transition type is intersystem crossing to the lowest electronic triplet state. Since direct transitions from the excited triplet state to the singlet ground state are forbidden, this either leads to phosphorescence or to a transition back to an excited state, resulting in delayed fluorescence. This effect can be used to deliberately put a fluorophore in a dark state. Molecules in the triplet state have a high chemical reactivity, leading to photobleaching of fluorophores and to phototoxic effects in living cells by the generation of free radicals.

### 3.1.2 Microscopy setup

Fluorescence microscopy experiments were performed on a Zeiss Axiovert 200 inverted microscope (see Figure 3.2). Three different laser lines were used for fluorophore excitation, a 647 nm diode laser (Toptica iBeam smart 200 mW) which was later replaced by a 640 nm diode laser (Coherent OBIS LX FP 75 mW), a 488 nm diode laser (Toptica iBeam smart 200 mW) and a 532 nm diode-pumped solid state laser (Spectra physics Millennia 6s). All diode lasers could be directly modulated, whereas the green laser was attenuated via an acousto optic modulator (AOM). Spatial filters are used to improve the beam shape and to adjust the diameter of each individual laser. After spatial filtering, the different laser lines are combined. This is either done by using multiple dichroic mirrors or by using an OBIS Galaxy Laser Beam Combiner. The laser beam is focused into the back focal plane of the objective ( $\alpha$  Plan-Apochromat 100 $\times$ /1.46 Oil DIC (UV) VIS-IR) via a telescope. A periscope is used to couple the lasers into the microscope. Moving the bottom mirror of the periscope parallel shifts the laser beam and enables TIRF microscopy (see also section 3.1.3). Both excitation and emission light passes through the objective, which is located at the bottom of the sample. Dichroic mirrors together with emission filters were used to separate the

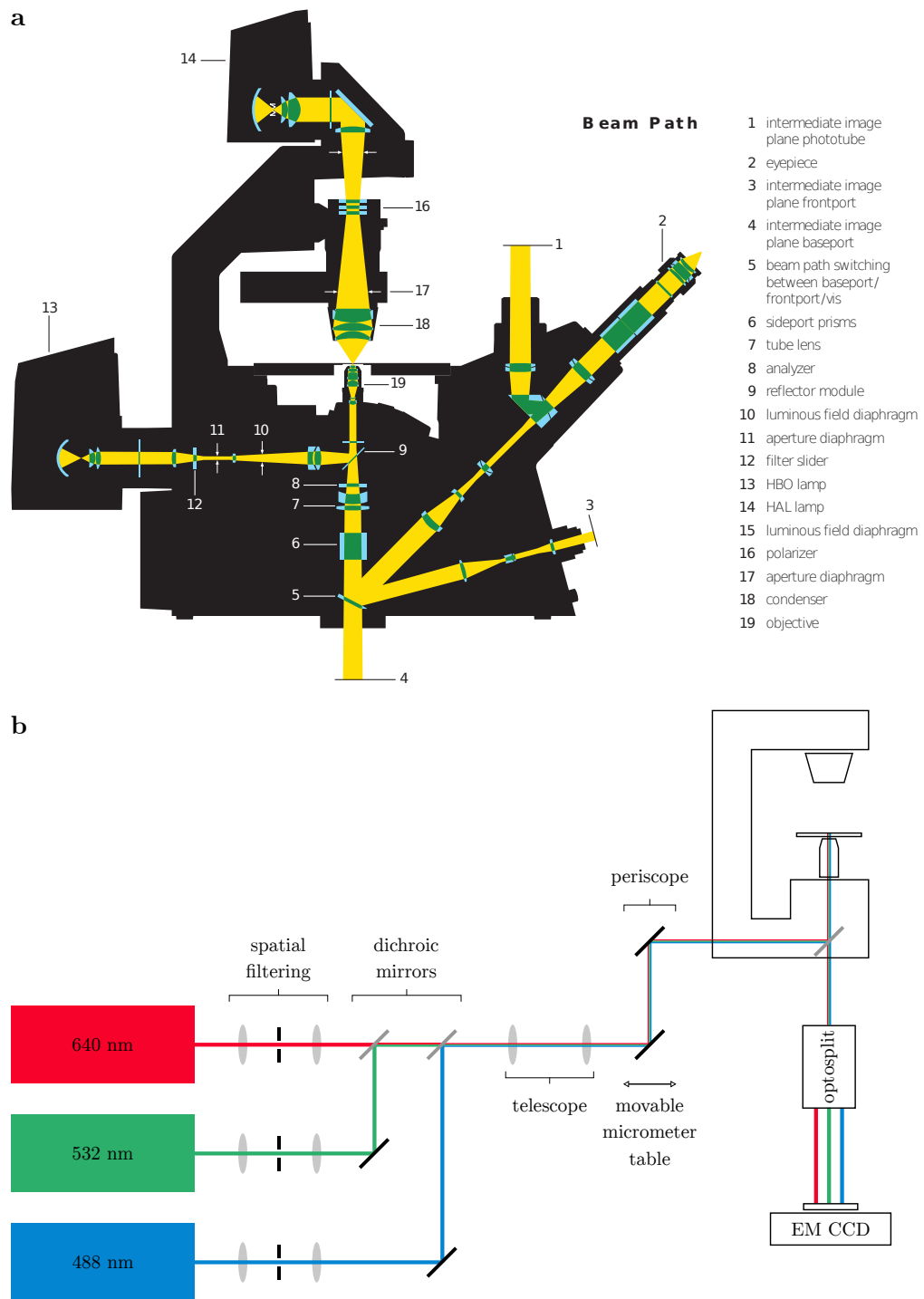


**Figure 3.2:** *Schematic overview of an inverted microscope and the microscopy setup. (a) Beam path in an Zeiss Axiovert 200 inverted microscope. Image taken from [65] (b) Beam path of the microscopy setup.*



excitation from the emission light. A set of filters and dichroic mirrors (Cairn Research Optosplit) can be used to split the emission light of distinct spectral channels on different regions of the camera chip, thereby enabling simultaneous multicolor imaging.

### 3.1.3 Total internal reflection fluorescence microscopy

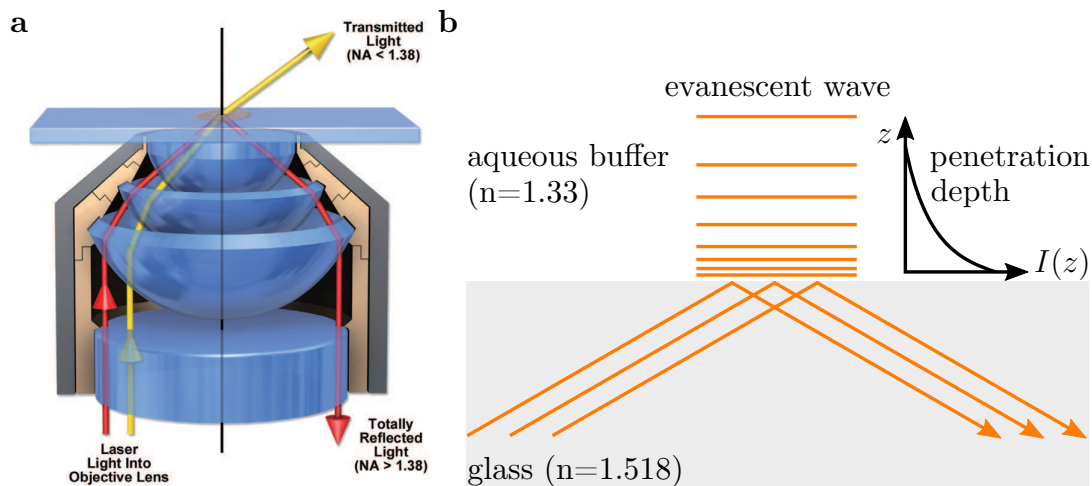


**Figure 3.3:** *TIRF microscopy allows for the observation of single molecule fluorescence at surfaces and interfaces. (a) Schematic illustration of an objective-based TIRF setup. The laser beam is moved to one edge of the objective's rear aperture and TIRF illumination is obtained when the incident angle at the specimen is greater than the critical angle. Image taken from [64] (b) The evanescent wave exponentially decays at the interface of the glass-water surface. Illustration adapted from [64].*

Conventional wide field microscopy and laser scanning confocal microscopy are the most common imaging techniques based on the illumination of a fluorescently labeled specimen with a broad cone of light. A large number of cellular events happen at cellular surfaces like the plasma membrane. When using conventional microscopy techniques, the signals from these events cannot be distinguished from the fluorescent background in other focal planes. TIRF microscopy solves this problem by inducing an evanescent wave to selectively excite fluorophores close to the glass-water or glass-buffer interface. [66, 67]

The behavior of light rays upon reflection and refraction from a planar surface

is an essential concept for TIRF microscopy. A collimated beam of light passing between two media of varying refractive indices is either refracted or reflected at their interface, depending on the difference in refractive index between the two media and on the incident beam angle. If the incident angle is above a certain critical angle, the total incident light is reflected and no significant amount is refracted into the medium of lesser refractive index. According to Snell's law, the relation between the refractive indices of the two media  $n_1$  and  $n_2$ , and the critical angle  $\theta_c$  reads

$$\sin \theta_c = \frac{n_1}{n_2}. \quad (3.1)$$

In the case of total internal reflection, a small fraction of the incident light can penetrate the specimen and propagate parallel to the surface in the plane of incidence, resulting in an electromagnetic field close to the interface (see Figure 3.3). This field is also called evanescent wave and  $I(z)$ , the intensity at a distance  $z$  along the optical axis, decays exponentially with distance to the interface

$$I(z) = I_0 e^{-z/d} \quad (3.2)$$

with  $I_0$  representing the intensity at the interface and  $d$  being the characteristic penetration depth. The penetration depth  $d$  at the wavelength of incident light in vacuum  $\lambda_0$  reads

$$d = \frac{\lambda_0}{4\pi n_2 \sqrt{(\sin \theta_1 / \sin \theta_c)^2 - 1}}. \quad (3.3)$$

In biological systems,  $n_1$  is the refractive index of the coverslip ( $n = 1.518$ ) and  $n_2$  is the refractive index of the buffer solution or the internal cellular components ( $n = 1.33$  to  $1.37$ ). Since  $n_1 > n_2$ , total internal reflection occurs when the incident angle is larger than the critical angle  $\theta_c$ . Usually, the penetration depth is from 30 nm to 300 nm, independent of the incident light polarization direction. It decreases as the reflection angle becomes larger. Fluorophores close to the interface of glass and liquid will be excited in the evanescent field but due to the exponential decay of this field, fluorophores at larger distances will not be excited. This leads to a drastic reduction of background fluorescence from molecules not in the focal plane.

### 3.1.4 Fluorescence recovery after photobleaching

Fluorescence recovery after photobleaching (FRAP) is a method to study the chemical equilibrium between mobile and immobile states of molecular assemblies

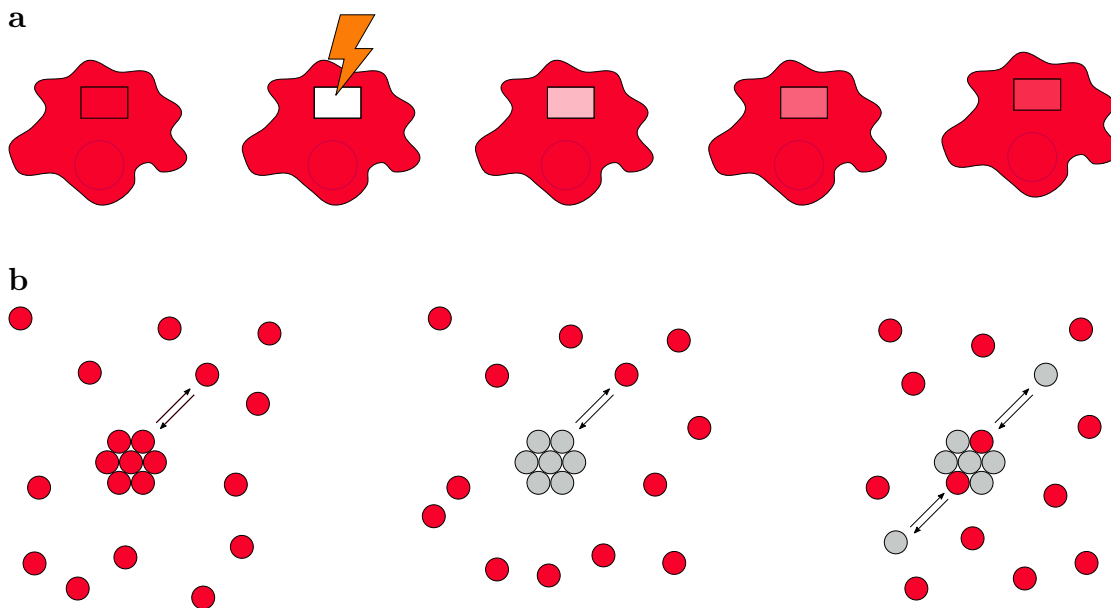


**Figure 3.4:** *Fundamental principles of a FRAP experiment.* (a) In a small region of a cell, fluorescently tagged molecules at equilibrium are photobleached with a brief and intense bleach pulse. Fluorescence recovery in this region is monitored to determine important kinetic parameters, e.g. the half-time of recovery and the fraction that does recovery. The orange lightning bolt represents high intensity laser excitation. (b) The subunits in a supramolecular structure, previously fluorescent, get photobleached by an intense bleach pulse. When bleached molecules dissociated from the structure, they can be replaced by soluble non-bleached subunits. Illustration adapted from [64].

in cells, i.e. probing the rates of association and dissociation of molecules to organized subcellular structures. These structures usually consist of subunits, which exist in a dynamic equilibrium with unbound molecules in the cytoplasm or in the plasma membrane. In the FRAP technique, fluorescently tagged molecules in a defined sample area are photobleached by a brief exposure to an intense beam of light. The recovery of non-bleached molecules to this area is monitored by time-lapse microscopy (see Figure 3.4). Analysis of this recovery curve provides the half-time of fluorescence recovery, which can be related to the half-time for molecular exchange under certain assumptions and controls. Further, the fraction of molecules participating in the recovery can be determined. Ideally, the bleach pulse in a FRAP measurement only alters the fluorescence equilibrium without disturbing the cell and is of infinitely small duration.

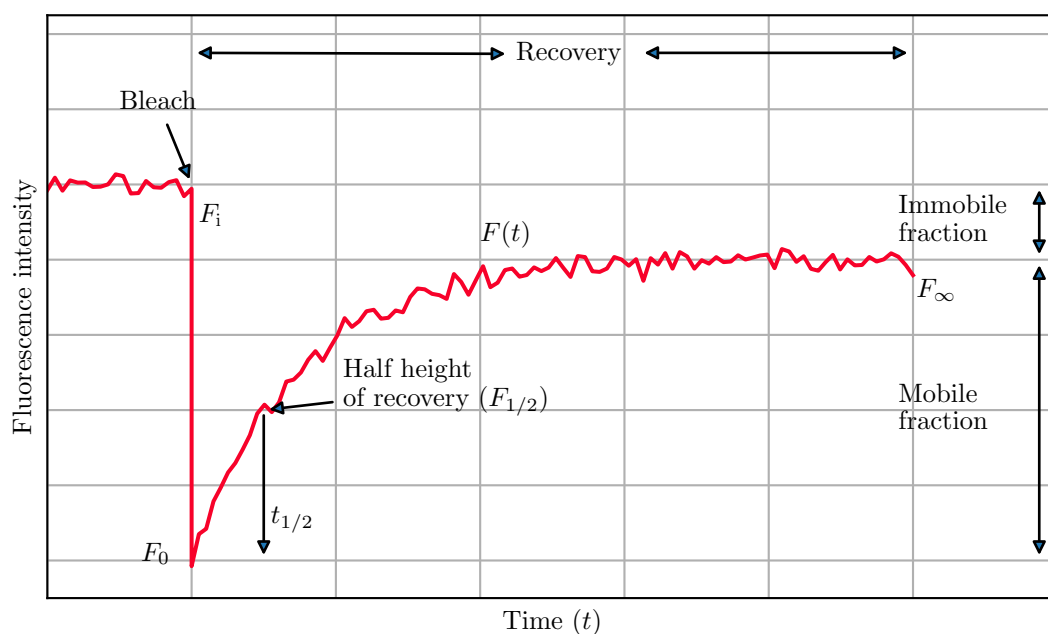


**Figure 3.5:** *Fluorescence intensity of a structure in a typical FRAP experiment.* The initial intensity ( $F_i$ ) drops after a photobleach pulse to  $F_0$  and recovers over time ( $F(t)$ ). Further indicated are the half-time of recovery ( $F_{1/2}$ ) and the fluorescence equilibrium ( $F_\infty$ ), as well as the percent mobile and immobile fraction. Illustration adapted from [64].

The half-time of recovery is mainly determined by the rate at which bleached

molecules dissociate from a structure, which is dependent on the bond-strength between molecules in this structure. In the simplest case, the association rate is primarily diffusion limited and therefore not rate-limiting. More detailed information on the influence of diffusion and binding can be found in section 11.1.1. In general, fluorescence recovery can be separated into two overlapping phases:

- In the first part, bleached soluble molecules are rapidly replaced with fluorescent molecules by diffusion.
- In the second phase, recovery of the bleached structure is determined by the replacement of bleached molecules in a structure by fluorescent molecules.

An example fluorescence intensity curve of a FRAP experiment is shown in Figure 3.5. After the initial drop in fluorescence following the bleach pulse, the level of recovered fluorescence ( $F_\infty$ ) usually reaches a stable plateau, which is less than the initial level before photobleaching ( $F_i$ ). The ratio of the molecules recovering  $F_\infty/F_i$  is called the mobile fraction, whereas the balance is the immobile fraction,  $1 - F_\infty/F_i$ . Less than full recovery can be caused by photobleaching a significant amount of fluorescent molecules in the system or by a fraction of molecules in the structure not recovering at all, or at a much slower rate. The fluorescence intensity immediately after bleaching ( $F_0$ ) accounts for incomplete photobleaching and for molecules already recovered after the bleach pulse, but before the first image was recorded. For the analysis of most photobleach-recovery events, the perturbation-relaxation theory is used and the monitored fluorescence recovery curve is fit by an exponential function.

Further details on performing FRAP experiments and subsequent data analysis is discussed in section 11.1.

### 3.1.5 Single molecule fluorescence microscopy

Ernst Abbé observed the diffraction pattern produced from a periodic specimen in the rear focal plane of the objective and developed the theory for image formation in the light microscope. This theory states that the microscopy image is the interference effect of a diffraction phenomenon. This section is mainly based on [64].

Diffraction, the scattering of light, is one of the key principles to determine how a microscope forms an image. In fluorescence imaging, light emitted from

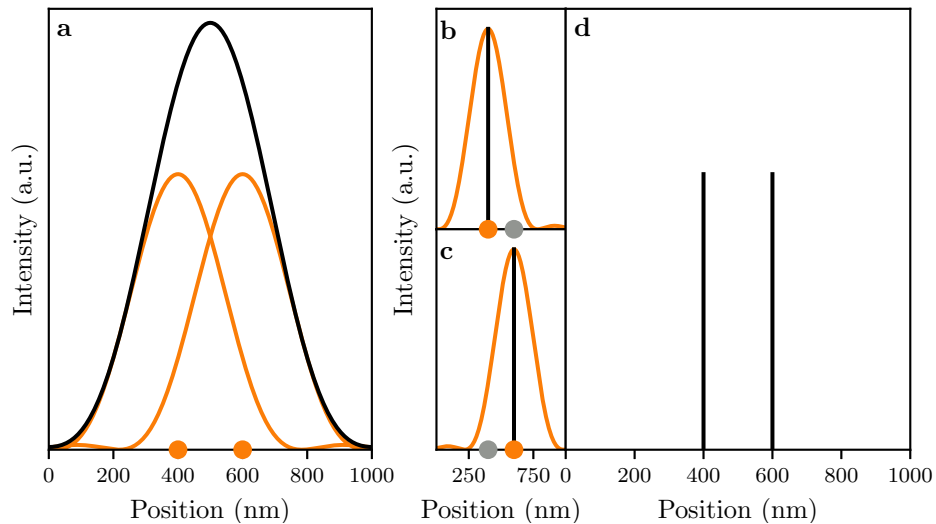


**Figure 3.6:** *The central diffraction spot of a point source is called Airy disk. (a) Profile of the Airy disks of two emitters (orange dots), which are fluorescent at the same time. Due to their small separation distance, their photon distributions (orange curves) overlap (black curve) and their exact position cannot be determined using conventional microscopy. (b) If only one emitter is fluorescent, it can be localized with high precision (black bar). (c) In superresolution microscopy, this situation is artificially created by stochastic or targeted switching processes, such that each emitter can be localized precisely, although not at the same time. (d) Once the positions of both emitters are obtained they can be used for reconstruction. Illustration adapted from [68].*

a point source in the object plane experiences diffraction in the front aperture of the objective. This causes the image of a point to consist of a central disk of finite diameter surrounded by a series of diffraction rings. Since diffraction is the reason why a real object is never perfectly represented, it sets a limit beyond which an optical system cannot resolve fine spatial details. The central diffraction spot, containing roughly 84% of the light from the point source, is called Airy disk (see Figure 3.6). The radius of the central disk in an Airy pattern is determined by the wavelength  $\lambda$  and the aperture angle of the lens. The aperture angle in a microscope is given by the numerical aperture (NA). The radius  $d$  of the diffraction spot for a point light source in the image plane is given by

$$d = \frac{1.22\lambda}{2\text{NA}} \quad (3.4)$$

with the NA being defined as

$$\text{NA} = n \sin \theta \quad (3.5)$$

where  $n$  is the refractive index of the medium between the lens and the sample and  $\theta$  is the half-angle over which the objective can collect light. Aberrations influence the imaging behavior of the microscope in such a way, that a point source will be imaged according to the empirical point spread function (PSF). Both fluorophore characteristics and imaging system determine the size of the PSF.

The resolving power of a microscope is defined by equation 3.4 with  $d$  being the minimum resolved distance. This equation describes the Rayleigh criterion, which defines that two adjacent object points can be resolved when the Airy disk of one point coincides with the first diffraction minimum of the other point in the image plane. For high NA oil immersion objectives ( $\text{NA} = 1.4$  or greater) and an excitation wavelength  $\lambda$  in the range of 400 nm to 700 nm, the limit of spatial resolution ranges from 200 nm to 300 nm. This means that two fluorophores spaced less than this distance apart will appear as a single object. Therefore, small cellular structures as well as most molecular processes cannot be resolved with conventional microscopy.

Growing research interest in molecular structures raised the demand for increased resolution and drove the development of new superresolution imaging techniques. These methods offer lateral resolution in the tens of nanometers and even less. Many of these techniques are based on the fact that fluorophores can

be photo-switched on and off and their signal can then be recorded sequentially in time. The most prominent superresolution microscopy techniques are stimulated emission depletion (STED) microscopy, i.e. point scanning microscopy where the Airy disk itself is engineered to smaller physical dimensions, and single-molecule localization microscopy, including photoactivated localization microscopy (PALM) and stochastic optical reconstruction microscopy (STORM).

A central concept in superresolution and single-molecule techniques is the identification and localization of individual molecules. To acquire Airy disk images of individual fluorophores, an array detector with small highly sensitive pixel photosites, like an electron multiplying charge-coupled device (EMCCD) is used. Further, a high contrast mode of fluorescence imaging, such as TIRF is highly recommended. Then, the position of a molecule corresponds to the center of each diffraction-limited spot and can be localized by analyzing its photon distribution on the pixels of the EMCCD. This localization is performed by fitting the single-molecule PSFs to a theoretical Gaussian distribution and mapping the coordinates. Besides the position of the emitter, fitting also yields the intensity in photons. If the density of Airy disks is too high, they overlap and determining the photon distributions of individual disks becomes impossible. The localization precision is dependent on the number of collected photons during image acquisition and is given by

$$\langle(\Delta x)^2\rangle = \frac{s^2}{N} \quad (3.6)$$

with  $\Delta x$  being the error in localization,  $s$  being the standard deviation of the PSF and  $N$  being the number of photons collected. If background noise is sufficiently small and the pixel size  $a \ll s$ , then

$$\Delta x = \frac{s}{\sqrt{N}} \quad (3.7)$$

holds true. Further, also the uncertainty in determining the number of detected photons  $\Delta N$  depends on the total number of collected photons. [69]

Due to its high localization precision, single-molecule fluorescence microscopy can be used for imaging cellular structures or even protein-protein interactions. Further, ensemble measurements mask the distribution of different subfractions and in particular minority fractions can hereby be determined. Single-molecule fluorescence microscopy enables live cell imaging at physiological conditions and can also be used to investigate kinetic processes.



### Single particle tracking (SPT)

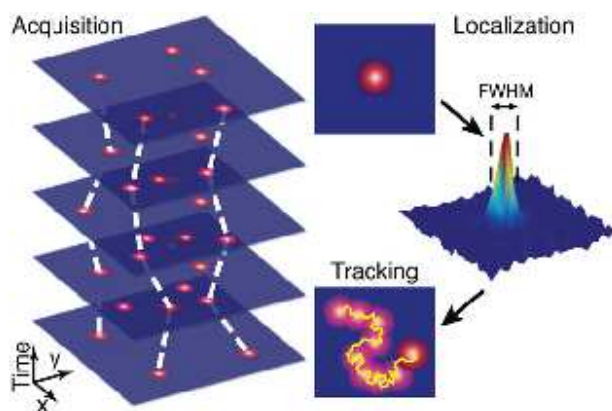


**Figure 3.7:** *The fundamental principle of SPT consists of acquisition, localization and tracking. During acquisition, an image series typically containing hundreds to thousands of images with low molecular density is recorded (red spots). In the localization step, the position of each particle at a given time is obtained. The positional accuracy is determined by the full width at half maximum (FWHM) of the PSF, the number of collected photons and noise due to experimental conditions. The positions at different time points are linked to generate trajectories that track particle motion. Illustration taken from [70]*

The movement of a biomolecule in a lipid bilayer is influenced by unspecific impacts of other molecules, but also by specific interactions. The random motion of molecules resulting from collisions with other molecules due to thermal energy can be described by free Brownian motion. Thus, diffusion is responsible for the distribution of biomolecules over the accessible space without the need for energy. The mobility of a biomolecule is an important parameter for its interaction behavior and in contrast to random collisions, specific interactions with other molecules can strongly influence the diffusion behavior. Although Brownian motion is a fundamental principle in biophysics, almost all single particle tracking (SPT) experiments show that the diffusive motion of molecules in living cells is anomalous.

SPT is a versatile method to investigate a variety of dynamic processes in the life sciences and it provides insights into the single molecule behavior in the natural context of living cells. First, localization algorithms are used to determine the position of each fluorophore in each recorded frame. Then, the fitted single-

molecule positions in consecutive images are compared and linked. In general, nearest-neighbor-algorithms are used for this linking procedure and the reconstruction of the resulting single-molecule trajectories. Diffusion analysis is based on the measurement of the mean square displacement (MSD) for a given time-lag  $t$ . These parameters can then be used to determine the diffusion constant  $D$  and to identify confined or anomalous diffusion. SPT removes ensemble averaging and allows for a complete statistical characterization of the system under study. Temporal-average information of the process can be obtained by following the diffusion of a single molecule for a long time. But at the same time, spatial-average information is also available, since many individual molecules can be analyzed. [70, 71]

### Stepwise photobleaching

Single-molecule fluorescence can be used to analyze complexes in regard to the number of their constituent subunits. Several approaches have been developed to gain information on the stoichiometry of complexes by subunit counting. These approaches include counting the photobleaching steps of fluorescent complexes, the analysis of a histogram of measured spot intensities, and the colocalization of fluorescent tags of multiple colors. The ability to discriminate individual fluorescent complexes requires a low protein density. Further, a high labeling efficiency and specificity are prerequisites for quantitative measurements. This section will focus on counting photobleaching steps, also called stepwise photobleaching, and is mainly based on [73].

Photobleaching is the destruction or alteration of the chemical structure of a fluorophore upon intense illumination, that leads to an irreversible loss of fluorescence. Photobleaching is a stochastic process and is perceived as an exponential decay of sample intensity for bulk experiments. On the single-molecule level, photobleaching is observed by the loss of emission from an individual fluorescent molecule in a stepwise fashion. This behavior is exploited in single-molecule experiments, where the subunits of a complex are labeled with a fluorescent tag. The identification and counting of multiple fluorophores provides a method for counting the subunits of a complex, even those lying within a diffraction-limited spot (see Figure 3.8). Although being a potent method to determine the stoichiometry of complexes, some major drawbacks have to be noted.

- A certain fraction of fluorophores is not functional, resulting in a decrease

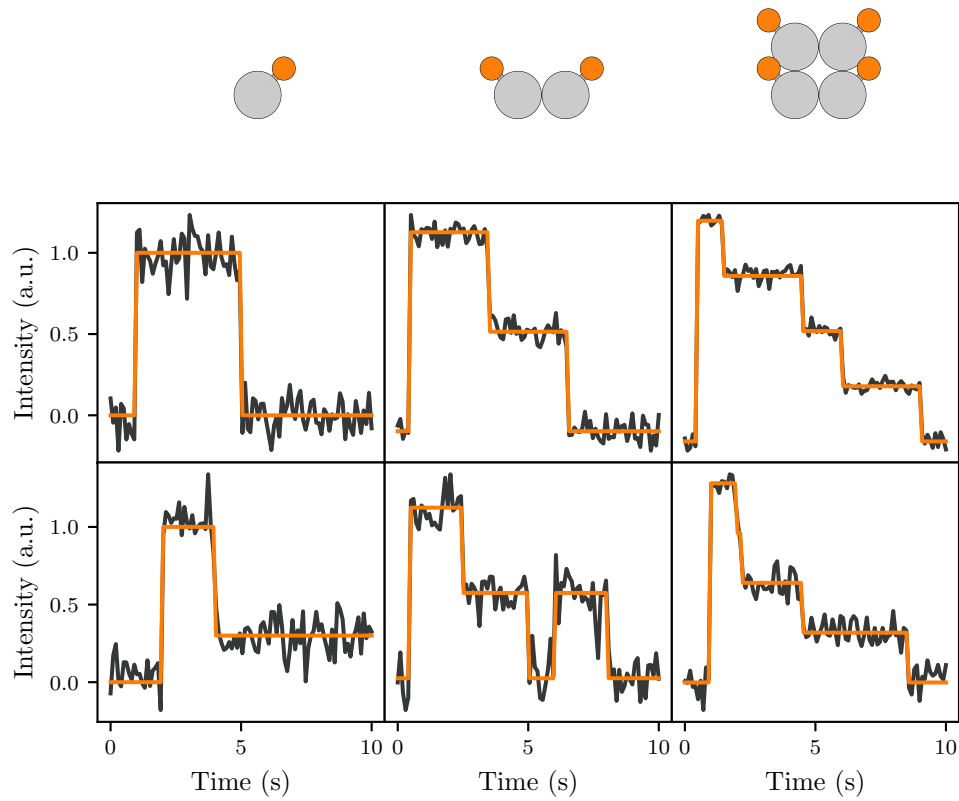


**Figure 3.8:** *Bleaching steps of single fluorescent protein complexes reveal the number of fluorescently labeled subunits. Time courses of fluorescence emission for protein complexes with monomeric, dimeric and tetrameric protein complexes. Two examples for each complex are shown, with the upper row illustrating an ideal case and the lower row indicating possible issues when performing a stepwise photobleaching experiment. These issues include different baselines, blinking and multistep bleaching (left to right). Illustration adapted from [72].*

in the number of bleaching steps counted. This leads to an underestimation of the actual number of components.

- The noise intrinsic to the emission process complicates the discrimination of adjacent bleaching steps and washes out the individual steps. For complexes with a large number of subunits, the average time between steps becomes shorter because the frequency of bleaching events is proportional to the number of fluorophores that are still functional. Further, noise increases with the number of fluorophores and can become large enough to mask the bleaching steps at the beginning of the exposure.
- Although being applicable to dynamic processes in general, movement of the fluorescence signal during image acquisition introduces additional noise and can result in significant brightness fluctuations, making mobile protein complexes harder to access within this method.
- For the investigation of protein complexes in cells, the requirement for well distinguishable fluorescent complexes leads to an upper limit of the expression level. Too high protein densities at the plasma membrane make this method not feasible.

### Colocalization of multiple colors

Especially when the complex of interest is present in variable stoichiometries, two or more fluorescent tags help to discriminate different subpopulations based on the presence, number of bleaching steps, or differential emission intensity of these tags. But also purely homogeneous populations of complexes can be analyzed by the use of multiple colors. A high probability that all subunits are labeled by functional fluorophores is a prerequisite for two-color colocalization analysis of protein complexes. Unspecific binding of labels needs to be minimized for quantitative colocalization analysis.

## 3.2 Atomic force microscopy

Atomic force microscopy is a technique to measure surface structure and was developed by Binnig, Quate and Gerber in 1986 [74]. In contrast to many other scanning probe microscopy techniques, AFM has the advantage that almost any

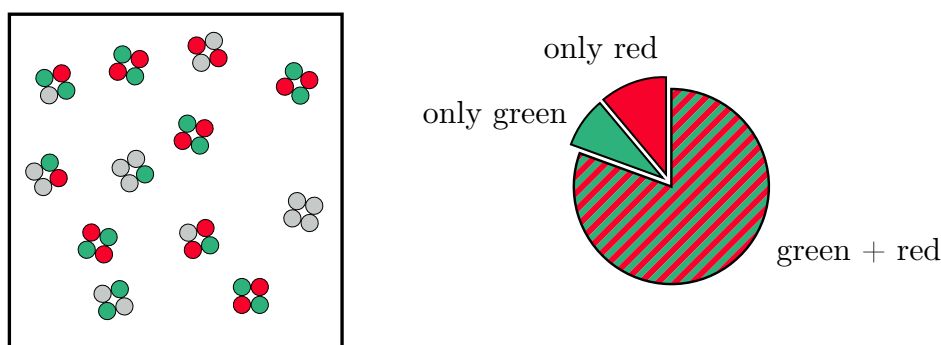


**Figure 3.9:** *Colocalization of spectrally separated fluorophores gives information on the interaction of differentially labeled subunits of complexes. The distribution of localizations with two colors in contrast to single colored localizations leads to insights on complex stoichiometry. For valid implication, the majority of fluorophores must be functional. Red and green colors indicate different fluorophores. Illustration adapted from [73].*

sample can be imaged, be it very hard or soft, conducting or insulating. Further, AFM measurements can be carried out under a vast variety of conditions, including measuring in physiological buffers at 37 °C to monitor biological reactions and even see them occur in real time. In 1994, an AFM was first used for experiments in liquid, clearing the way for imaging biological samples under physiological conditions [75]. In addition to its use as a microscope, AFMs have various other modes enabling it to measure other sample properties and to also manipulate samples at the nanometer scale. This section will focus on the fundamental principles of atomic force microscopy and is mainly based on [76].

### 3.2.1 Fundamentals of atomic force microscopy

The functional principle of an AFM is rather different from optical or electron microscopes that form images by focusing light or electrons onto a surface and basically measure a two-dimensional projection of a sample surface. In an AFM, a sharp probe is scanned across the sample surface, thereby generating a map of the sample height or topography (see Figure 3.10a). Piezoelectric elements are used for moving the AFM tip relative to the sample. This tip (the probe) is integrated in a cantilever, which also functions as an optical lever and together they make up a typical force transducer used in an AFM. Such a force transducer

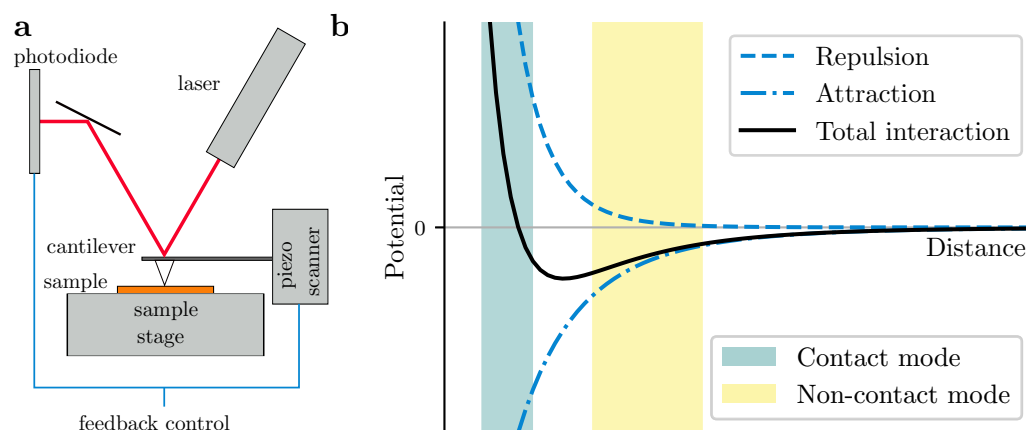


**Figure 3.10: Basic setup and working principle of an AFM.** (a) A tip attached to the end of a cantilever is scanned across the sample surface. Interactions with the surface cause a bending of the cantilever that can be detected by the optical lever principle. For this, a laser beam is focused on the back side of the cantilever, gets reflected and directed to a four-quadrant photodiode. Changes in the cantilever angle are detected as differences in the deflection of the laser beam. The deflection signal can be used as an input signal for the feedback loop guiding the cantilever movement. (b) The Lennard-Jones potential is a model describing the interaction between a pair of neutral atoms or molecules in dependence of their mutual distance. It is composed of a repulsive term, describing the Pauli repulsion, and an attractive term, describing the van der Waals force. Shaded areas indicate different operation modes of the AFM.

measures the weak interactions between the probe and sample surface. These interactions mainly consist of repulsive forces by the atomic shell and attractive van der Waals forces, described by a Lennard-Jones potential (see Figure 3.10b). Upon acting atomic forces, the cantilever is deflected according to Hooke's law

$$F(z) = -kz \quad (3.8)$$

with  $F$  being the force in  $z$  direction,  $k$  being the spring constant of the cantilever and  $z$  being the cantilever deflection. This deflection is measured by the optical lever principle with a laser beam being reflected from the back side of a reflective cantilever onto a four-segment photodiode. The probe is scanned across the surface with x-y piezoelectric elements. For hard samples, contact mode imaging is commonly used, whereas biological samples are mainly imaged with the less invasive tapping mode. In the following section these different imaging modes used in an AFM are described.

### 3.2.2 Different modes of the atomic force microscope

#### Contact mode

First available AFMs were operated in contact mode (see Figure 3.11a). This contact mode imaging is mainly performed in the repulsive regime (see green shaded area in Figure 3.10b). Two main submodes can be distinguished, the constant height and the constant force mode.

In constant height mode, the cantilever height is held at a fixed level when being scanned across the surface. Changes in the surface height lead to a cantilever deflection, which therefore corresponds to the sample topography. For each scanned pixel the cantilever deflection is recorded and used to generate a topography map.

In constant force mode, the force between probe and sample is kept constant by controlling the expansion of the piezoelectric scanner in  $z$  direction via a feedback loop. Keeping the force between the probe and the sample at a set value implies maintaining a constant distance between probe and sample surface. Monitoring  $z$  piezoelectric movement for maintaining a fixed probe-sample distance generates a map of the surface height. By enabling a  $z$  movement of the cantilever, constant force mode extends the vertical imaging range of an AFM by including larger topographic changes.

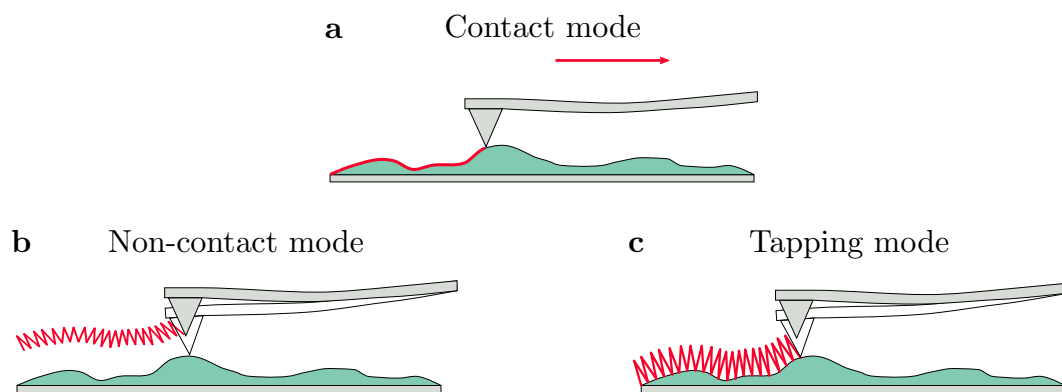


**Figure 3.11: Operating modes in atomic force microscopy.** (a) In contact mode, the cantilever is scanned across the surface at a fixed height. The expansion of the piezoelectric element corresponds to the topography. (b) In non-contact mode, the cantilever oscillates near its resonant frequency and is scanned across the sample without getting in contact. Changes in oscillation due to interactions of the tip with the sample are used to generate a topography map. (c) The tapping mode is an oscillating mode in which the cantilever tip gets in contact with the sample. Again, the altered oscillation is used to map the topography of the sample. Illustration adapted from [77].



In both cases, direct contact of the tip and the sample in contact mode can lead to sample deformations. This causes reduced image quality and also possible sample damage, especially in the case of biological specimens. Further, direct contact can also cause contamination of the tip with sample material which interferes with image quality and reduces resolution. Contact mode is mainly used for hard samples with typical cantilever spring constants ranging from  $0.01 \text{ N m}^{-1}$  to  $1 \text{ N m}^{-1}$  leading to forces in the range of nN to  $\mu\text{N}$ .

### Oscillating modes

Oscillation modes in an AFM are suitable for measuring specimen with a small probe-sample force, because of the signal-to-noise benefits associated with modulated signals. A large number of dynamic operation modes exist, which are basically just variations of a fundamental working principle. By the use of piezoelectric elements, the cantilever is oscillated, typically at its resonant frequency. Due to interactions of the tip and the force field from the sample, this oscillation changes, it gets damped. This damping leads to a reduction of the frequency and the amplitude of the oscillation. Similar to contact mode AFM, this oscillation is monitored and the height of the cantilever is adjusted via a feedback loop to maintain a constant distance between tip and sample. Various oscillating modes differ in the amplitude of the oscillation applied to the probe or in the detection method of changes in oscillation. Long-range interactions, such as the van der Waals force, are mainly responsible for changes in the oscillation frequency. Therefore, oscillating mode imaging is performed in this attractive regime (see yellow shaded area in Figure 3.10b).

The non-contact mode is a dynamic imaging mode introduced to scan soft biological samples and was first used in 1987 [78]. In this mode, the cantilever oscillates near to its resonant frequency, driven by piezoelectric elements in close distance to the sample (1 nm to 10 nm), but without being in contact with the surface (see Figure 3.11b). Using a feedback loop, the frequency of the oscillation, and thereby the tip-sample distance are kept constant. The feedback control signal is used for mapping the surface topography.

The tapping mode is a combination of contact and non-contact mode and was first introduced in 1993 [79]. Similar to contact mode imaging, it is a dynamic imaging mode in which an oscillating cantilever is scanned across the sample surface (see Figure 3.11c). The cantilever oscillates at or around its resonant

frequency with an amplitude of typically 20 nm to 100 nm. During imaging, the probe is allowed to touch the sample surface (that is, to pass into the repulsive regime) at the lower turning point of the oscillation. Due to the increased resolution in tapping mode compared to non-contact mode, it is the preferred mode for imaging soft, biological samples.

In addition to the amplitude signal, also the delay in the phase of the probe oscillation is often recorded and is referred to as phase imaging. This can be useful for distinguishing materials, since the phase of the oscillating cantilever is a measure of the energy dissipation involved in the contact between the tip and the sample, depending on viscoelasticity, adhesion and also contact area. Therefore, phase contrast reflects the material properties in a wide variety of samples, but also topometric differences. Although understanding individual contributions to the phase shift is not trivial, phase imaging is one of the most commonly used techniques for mechanical surface characterization.

### 3.2.3 AFM measurements in liquid

AFM measurements can be carried out in almost any environment, be it vacuum, gas or liquid. In particular the ability to scan in liquid is extremely useful for biological applications to measure samples in their native state. Further, the tip-sample interactions in liquid are much weaker than in air, which allows for applying only a small force to the sample when scanning. The fundamental operation modes are similar in liquid to air with minor adjustments being necessary. Both sample and cantilever are submerged in liquid. This implies that also the laserbeam needs to enter the liquid, leading to minor beam path adjustments to correct for refraction effects. Further, oscillations of the cantilever are coupled to the liquid and the actual cantilever resonance is shifted to lower frequency. Finally, damping reduces the oscillation amplitude.

### 3.2.4 Image processing

Quantitative analysis of AFM data requires different data processing steps, that include functions like filtering and background subtraction. The purpose of data processing is to clarify the data and to make it easier to analyze the features that have been measured. In general, all images need processing and if not mentioned otherwise, all AFM images in this thesis are processed with the techniques

described in this section.

### Leveling

Leveling is usually the first processing operation carried out on the data. It is required in nearly all cases and is therefore considered to be the most important processing step. The reason leveling is required is that height changes of the background, caused by tilt of the substrate in an image, will mask the height changes associated with the sample. Even small tilts in the sample background can have serious effects in measuring samples with very small heights. Further, also scanner bow is a common problem in AFM images and leads to a curve in the image plane. Different methods can be used for image leveling such as polynomial fitting or two-dimensional plane fitting.

### Filtering

Filtering of AFM images is used to remove unwanted high or low-frequency noise. The most commonly used techniques on AFM images are matrix filtering and Fourier filtering. Matrix filters move certain frequency components by averaging adjacent points in the image and can be grouped into low-pass and high-pass filters. Low-pass filters reduce high-frequency components and have a smoothing effect on the data, whereas high-pass filters are usually used for sharpening or edge detection by reducing low-frequency components. In the case of Fourier filtering, the image is transformed from real space into frequency space, certain components are removed and then the image is transformed back into real space. They can achieve similar results to matrix filtering, but are more flexible and offer the possibility to remove or to enhance specific components of an image.

### 3.2.5 Imaging artifacts

In general, all measurement techniques are prone to artifacts. In AFM measurements, tip geometry is the main factor influencing the recorded data, since an actual AFM image is the convolution of tip geometry and sample topography. Often, it is assumed that the tip radius is finer than the image details and the tip opening angle is smaller than the feature angles in the sample. This means that the influences of the tip on the image are negligible. Next to tip artifacts, also scanner artifacts and processing artifacts need to be taken into account.

### 3.2.6 Combining AFM with fluorescence microscopy

Typical bio-AFMs reach a spatial resolution of around 2 nm, roughly hundred times higher than the resolution in conventional fluorescence microscopes, which are limited by diffraction. Recent advances in superresolution microscopy helped closing this gap. Despite having disadvantages in resolution, higher imaging speed, a larger observed area and being less invasive are the main benefits of fluorescence microscopy in contrast to atomic force microscopy. Therefore, combining the advantages of both methods can be useful and typical combination systems consist of an AFM-head on top of an inverted fluorescence microscope. Calibration is necessary to relate the scan areas in both techniques and to overlay obtained images.

### 3.2.7 Single cell force spectroscopy

Investigating the adhesion of cells to surfaces is a challenging task because of cell surface heterogeneity and many different contributions to this complex process. Determining the contribution of individual elements to the total binding proves to be difficult, nevertheless numerous assays have been developed to quantify cell adhesion. SCFS is a ground-breaking technique to quantify single cell-cell and cell-surface interactions, i.e. to measure the interaction forces between a living cell bound to a cantilever and a target cell or a functionalized substrate under physiological conditions. At the same time, other properties of a cell, including stiffness and elasticity, can be determined. AFM force spectroscopy can be used to resolve individual detachment events, as well as to determine the overall force required to detach a cell from a substrate. [80, 81]

#### Principles of force spectroscopy

The cantilever in an AFM can be viewed as a leaf spring in physical terms. Its deflection can therefore be used to derive actual adhesive forces and energies if its spring constant is known. In a force spectroscopy experiment, the cantilever is approached to and retracted from a surface in  $z$  direction by the use of piezoelectric elements. As the cantilever comes in contact with the surface, it deflects and at a given setpoint force its movement stops. After a user-defined time, the cantilever is retracted from the surface and interactions between the cantilever and the surface cause the cantilever to be pulled down until the required disruption

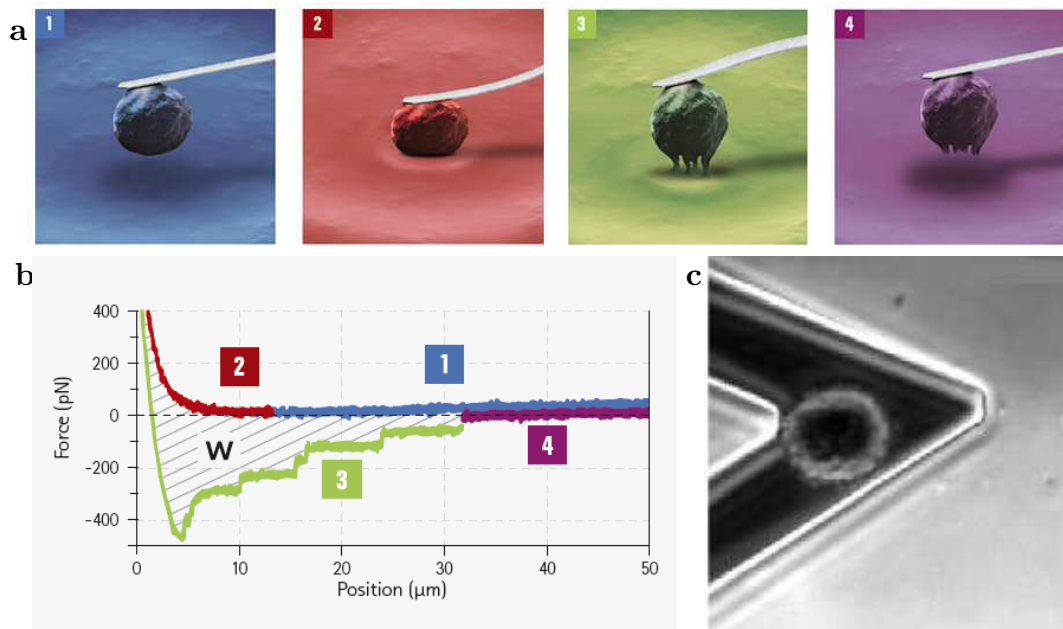


**Figure 3.12: Cell-substrate adhesion operating principle.** (a) A single measurement cycle of a single cell force spectroscopy (SCFS) experiment. Here, a single living cell is bound to a cantilever (1), brought into contact with the substrate (2) and is separated after a user-defined reaction time by retracting the cantilever (3). The cell resists the removal from the substrate, if it adheres to it and therefore bends the cantilever (4) [80]. (b) The force vs. distance curve is the result of a SCFS experiment and allows to determine single molecule events, the work of removal  $W$ , tether formation, the maximum adhesion force and viscoelastic parameters. Numbers and color scheme correlate to the cycle steps described in panel a [80]. (c) Phase contrast image of a cell attached to a tipless cantilever [81].

force is reached. Using this method, also multiple unbinding events, originating from multiple interactions, can be detected.

Spectroscopy experiments can also be used to measure cell detachment, if this measurement cycle is performed with a cell being attached to the cantilever (see Figure 3.12c). In this case, the interaction between the bound cell and either a second cell or a coated surface cause the cantilever to deflect. From these experiments, the maximal force required for detachment can be determined, as well as the unbinding events of single ligand-receptor pairs can be identified (see Figure 3.12a and b). [82]

The implementation of atomic force microscopy for SCFS allows unrivaled spatial and temporal control of cells at near-physiological conditions. For further details, see section 17.

### 3.3 Electron microscopy

Spatial resolution in optical microscopy is limited by diffraction, whereby the wavelength is the most contributing factor. According to de Broglie, quantum objects can be described in terms not only of particles, but also of waves, i.e. all matter has a wave-like nature with a related wavelength depending on the momentum [83]. This wave-particle duality also holds true for electrons and is exploited in electron microscopy. The wavelengths of electrons for acceleration voltages in the regime of kV are in the range of nm to pm and are much smaller than the wavelength of visible light. Therefore electrons can be used to resolve much smaller objects than possible with photons.

Two different types of electron microscopes can be distinguished, a scanning electron microscope (SEM) and a transmission electron microscope (TEM). In a SEM, an electron-beam is scanned across the sample surface and the back-scattered electrons are detected. In a TEM, the original form of an electron microscope, electrons pass through a very thin specimen and get detected by a camera. [84]

#### 3.3.1 Electron-beam lithography

The techniques presented so far focus on imaging small structures, in particular biological samples. Energetic beams of electrons can also be utilized to fabri-

cate structures on the micro- and nanometer scale for such diverse applications as microelectronics, nanophysics, and molecular biology. Conventional electron lithography, based on the interaction of electrons with a polymethylmethacrylate resist, has reached its resolution limit at around 10 nm, mainly influenced by molecular size and resist development mechanisms. Electron-beam-induced deposition (EBID) is a resistless deposition technique which can be used to construct three-dimensional nanostructures in the presence of carbonaceous gasses in the SEM chamber and might overcome the present resolution limits.

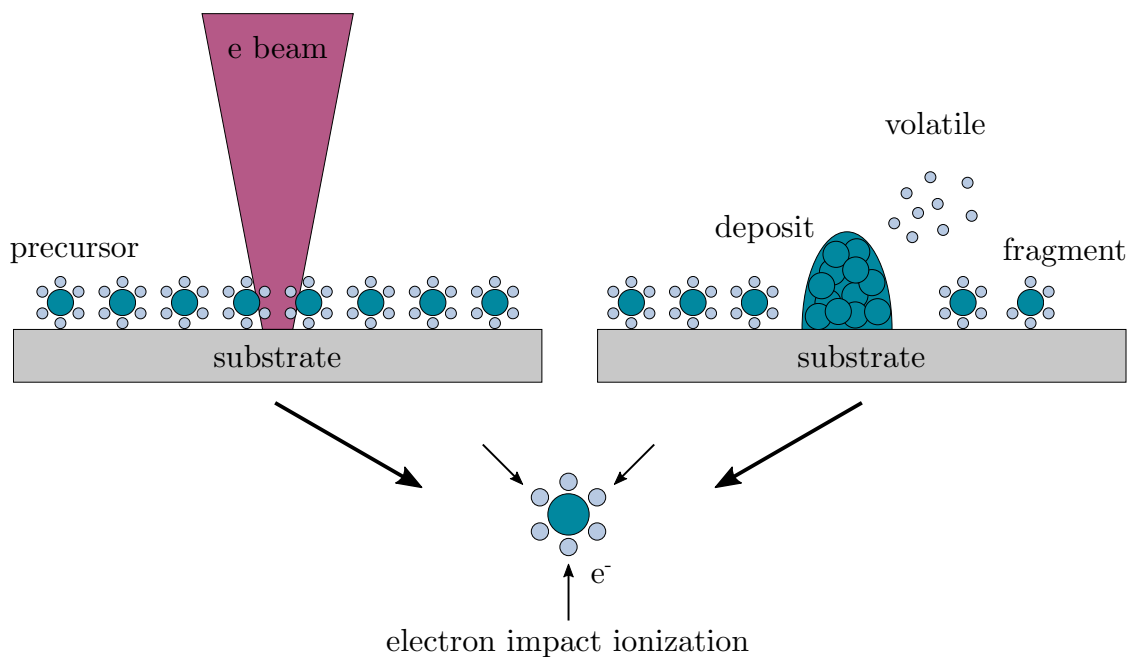


**Figure 3.13:** *EBID is a resistless deposition technique practiced mainly in SEMs. A highly focused electron-beam interacts with a substrate, where the precursor gas molecules are adsorbed. High energetic electrons dissociate the adsorbed molecules, leading to the formation of a deposit on the substrate. Volatile fragments are pumped away. Illustration adapted from [85].*

Already in the first electron microscopes, it was observed that the presence of an electron-beam slowly coats the sample with a carbonaceous substance [86] and initially, EBID was used to generate contamination grown patterns in an electron microscope as an etching mask [24]. Only recently, EBID was used as a tool for additive lithography mainly in SEMs [87]. In this technique, an electron-beam is focused in a high vacuum chamber onto a substrate surface on which



precursor gas molecules are adsorbed, which contain the element to be deposited (most often carbon). Various ionization and dissociation processes lead to the decomposition of adsorbed precursor molecules by high energy electrons in the irradiated area into nonvolatile and volatile fragments. The nonvolatile fragments form a solid amorphous carbon deposit with properties ranging from diamond-like-carbon to polymers, depending on the exact deposition conditions. [88] The volatile fragments are re-emitted and evacuated from the deposition chamber (see Figure 3.13). In contrast to conventional lithography techniques, EBID is a one-step method where structures are patterned and deposited simultaneously. [85] Still, the dissociation mechanism is a complex process and not well understood, since even for small molecules a large number of excitation channels is available. Ionization and dissociation are both expected to contribute to the deposition process. For both processes, the cross-section peaks at low electron energies around 50 eV, indicating that secondary electrons are mainly responsible for the deposition, with primary electrons only playing a minor role. [89]

Specific parameters and further details on EBID that are applied in this thesis can be found in part IV.



## Part II

# DNA origami nanostructuring



Die approbierte gedruckte Originalversion dieser Dissertation ist an der TU Wien Bibliothek verfügbar.  
The approved original version of this doctoral thesis is available in print at TU Wien Bibliothek.

# Chapter 4

## Introduction

DNA nanotechnology is based on the design and fabrication of artificial DNA-based structures and their application in a biotechnological context. In nature, deoxyribonucleic acid (DNA) can be found in any living cell and serves not as structural component, but as a molecule responsible for information storage. Its physical and chemical properties are well known and its double helical geometry offers a very defined shape. Due to the fact that complementary strand sequences hybridize into a stable duplex following simple base-pairing rules, interactions between strands can be easily designed. Further, custom DNA oligonucleotide sequences can be easily synthesized and their robustness to temperature changes together with the ability to not degrade under common experimental conditions, make them a versatile and easy to handle material.

The first developments in the field of DNA nanotechnology were the assembly of small discrete objects such as a DNA cube and extended periodic lattices made from DNA tiles by Seeman and coworkers [90, 91], already based on the concept that structural information is transformed and encoded into the sequences of DNA. The breakthrough in the development of DNA-based nanostructures can be attributed to Paul Rothemund, who developed the concept of one long scaffold strand interconnected by small elements, i.e. the DNA origami technique, in 2006 [21]. This method exploits the predictability and chemical stability of base pairing and allows for the production of custom designed objects at the nanometer scale. In this method, one  $\sim 7000$  bases long scaffold strand is folded into an arbitrary geometry with the help of about 200 short staple oligonucleotides (15 bases to 60 bases long) in a one pot reaction. The sequence of the short staple strand is designed in such a way, that it is complementary to at least two

different specific sections of the scaffold strand, thereby forming crossovers between two parallel double helical domains. The fundamental concept of the DNA origami technique is molecular self-assembly, which allows for the simultaneous production of the desired structures. Although this technique was originally developed for two-dimensional shapes, it was soon extended to enable the folding of complex three-dimensional shapes [22, 92, 93].

Different elementary functions of DNA structures can be distinguished, which make this technology a prime candidate to create sophisticated objects. These unique features include

- providing a basic shape, with a vast space of achievable three-dimensional shapes [22, 93–96],
- having an intrinsic function, e.g. integrating flexible parts, such as joints or hinges, that enable the design of conformational changes [92, 97–100] or
- chemical modifications of individual nucleotides to generate a platform for the precise placement of functional components like proteins, nanoparticles or hydrophobic moieties on the nanometer scale [101–103].

These functions make DNA nanostructuring a versatile tool for studying biological systems, e.g. as a frame shaped pattern for the direct observation and regulation of DNA-protein interactions [104, 105], as a molecular rope for studying tug-of-war behavior between motor proteins [106] and as a structural template to study the effect of the distance of binding sites on multivalent ligand-protein binding [107]. Due to the tunable interaction strength and sequence orthogonality of DNA, it can also be used as a functional component within other nano assemblies and be applied to control dynamic processes. This includes the super-resolution technique DNA-PAINT, which is based on adjustable transient binding kinetics of DNA coupled imager dyes [108]. Strand displacement reactions induce reversible conformational changes of nanoscale machines such as DNA tweezers [109]. These reactions are fueled by the energy stored in unpaired bases of single stranded DNA. This principle is also applied to various other nano-machines, to perform directed and controlled transport along a track in a synthetic bipedal DNA walker system [110, 111]. Even autonomous motion—without the external input of fuel strands— can be achieved by powering DNA walkers with hairpin fuels [112].

Currently, research on DNA nanostructures pursues in several distinct directions.

- The development of novel design methods extends the space of potential shapes and conformations that can be made from DNA. [113, 114]
- The fabrication of nanometer-sized tools with positioning capabilities to study certain biological objects and processes. [101, 106, 115]
- The examination of DNA nanostructures for in-vivo applications such as targeted drug delivery. [116]
- The exploration of novel inter-disciplinary applications in e.g. semiconductor research [117–119] or plasmonics [102, 120].

### Structure of this part

DNA nanostructures are the fundamental element in this part of the thesis and will be discussed in regard to form, function and application with particular focus on DNA origami as a molecular platform for T cell activation.

In chapter 5, the properties of DNA as the central building block for DNA nanostructures will be described. This includes its biochemical and mechanical properties as well as thermodynamic considerations.

In chapter 6, the DNA origami method will be introduced. It will focus in particular on the design process together with the assembly procedure. Further, external labeling strategies and purification methods will be described. For a general overview of the production process, see upper section of the flowchart in Figure 4.1.

Chapter 7 focuses on the design and synthesis of the platform used in this thesis and further includes quality control and characterization of the obtained DNA nanostructures by the use of atomic force microscopy and single molecule imaging techniques, giving the needed resolution on the nanometer scale. This chapter also includes the description of immobilization techniques necessary for subsequent characterization (see central section of Figure 4.1).

Section 7.4 shows the actual usage of DNA origami in the field of T cell biology. This includes the description of the performed experiments together with the analysis of the results (see lower section of Figure 4.1).

Finally, chapter 8 gives an outlook on subsequent projects.

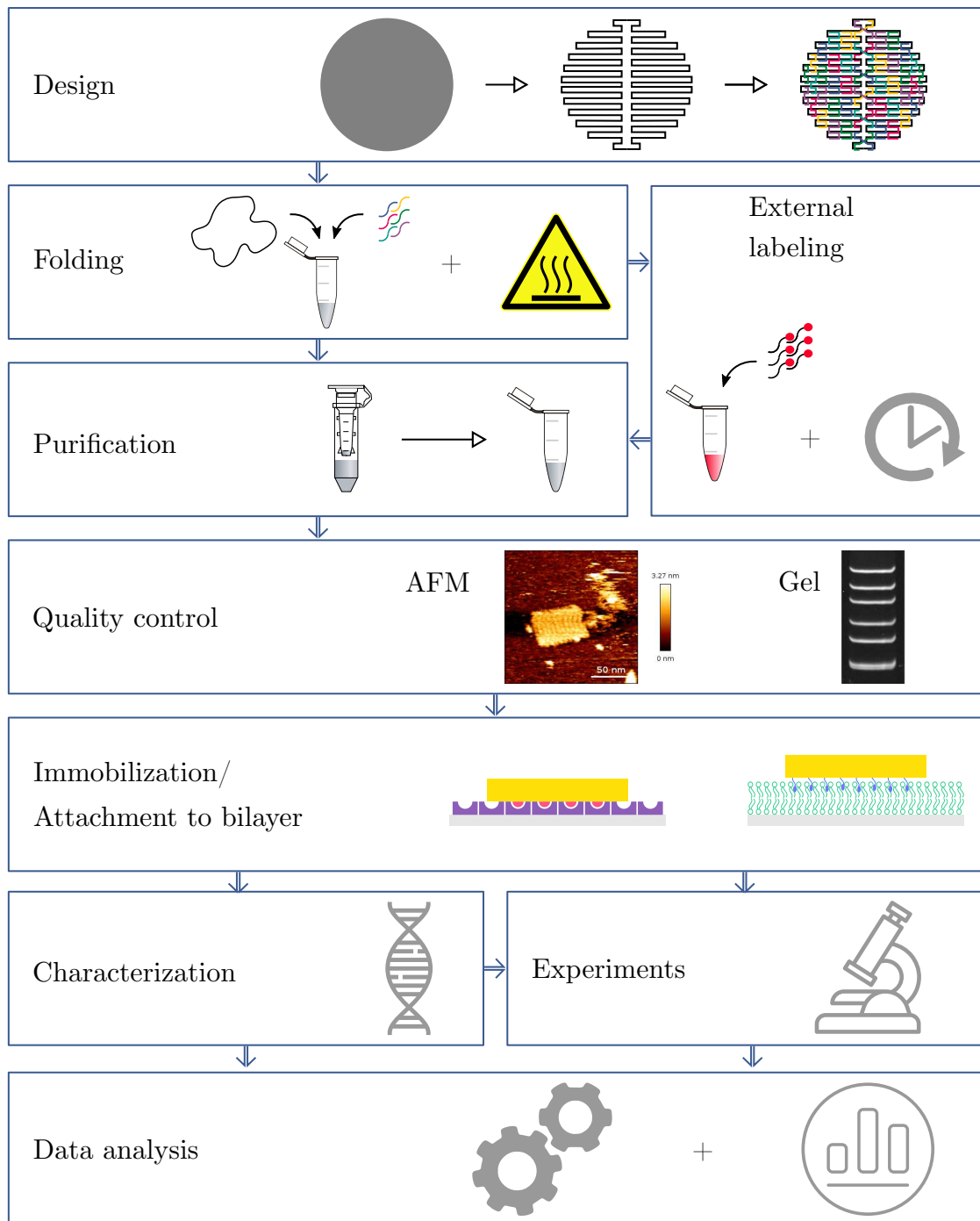


**Figure 4.1:** *This flowchart schematically shows the individual steps of the DNA origami nanostructuring procedure. Each step is described in detail in the following chapters in this part of the thesis.*

# Chapter 5

## Theoretical background

Deoxyribonucleic acid (DNA) is the central biomolecule for living organisms as it is nature's long-term information storage molecule. It contains the blueprint of a cell by encoding the amino acid sequence of proteins with its four bases. Nevertheless, many regions of the genome have regulatory function, necessary to control gene expression, and do not code for specific proteins. Its extraordinary biochemical and biophysical properties, like a high chemical and mechanical stability, make DNA—besides its actual biological function—an ideal building block for complex nanostructures. Further, the ability to chemically synthesize short DNA strands with custom sequences is utilized by DNA nanotechnology as strands with predictable specific base pairing, encoded by the four bases, can be used to design structures that assemble with nanometer precision.

This chapter gives an overview of the basic biochemical properties of DNA limited to the most relevant aspects for DNA nanotechnology. This includes a theoretical overview of DNA, from its structure over hybridization energies to secondary structures. Further, DNA will be examined from a biophysical standpoint with focus on mechanical properties of single and double stranded DNA as well as optical and electrical properties, and the thermodynamics of double-stranded DNA (dsDNA) formation are presented.

### 5.1 DNA structure

dsDNA is composed of two polynucleotide chains twisted around each other in the form of a double helix. Each chain is made up from four types of nucleotide

subunits, each consisting of a sugar (deoxyribose) with a phosphate group attached to it and a nitrogen-containing side group, the base. Four different nucleotides (adenine, guanine, cytosine, thymine, abbreviated by their initial letter A, G, C, T, respectively)—derivatives of either purine or pyrimidine—can be distinguished (see Figure 5.1a). By linking each sugar to the next sugar via the phosphate group, a polymer chain is created. More precisely, the 3'-hydroxyl of one 2'-deoxyribose is attached via a phosphate to the 5'-hydroxyl of another 2'-deoxyribose (see Figure 5.1b). Each resulting DNA strand consists of a regular phosphate sugar backbone with an irregular attachment of the four bases. This specific sequence of bases contains the information content of DNA. Due to the chemical structure of its backbone, DNA has an inherent polarity and by convention DNA sequences are written from the 5'-end (portrayed as a blunt end) to the 3'-end (portrayed as a pointed end). The phosphor group is deprotonated under physiological conditions, resulting in a negatively charged backbone. [3]

### Single-stranded DNA

A chain of single-stranded DNA (ssDNA) is a relatively flexible structure with each nucleotide being almost freely connected to the next nucleotide. ssDNA has a contour length of 0.5 nm to 0.7 nm per nucleotide [122, 123] and a salt dependent persistence length ranging from 0.5 nm to 5 nm, which can be approximated with its contour length in the case of high salt concentrations [124]. Therefore ssDNA can be approximated with a freely-jointed chain model. In this model, the  $n$  nucleotides of the chain are treated as stiff rods with an inter-nucleotide distance  $l$ . These segments are flexibly connected and randomly oriented relative to each other. For this model, the contour length, i.e. the length of the chain when completely stretched, is given by  $r = n \cdot l$  and the mean square end-to-end distance  $r$  of a random coil of ssDNA chain can be calculated by [125]

$$\langle \bar{r}^2 \rangle = n \cdot l^2. \quad (5.1)$$

Further, the radius of gyration  $r_G$  can be calculated [125]:

$$r_G = \sqrt{\frac{n}{6}} \cdot l. \quad (5.2)$$

An extension or compression of a ssDNA chain will result in a nonlinear entropic force, that can be approximated using a worm-like chain model [126]. The



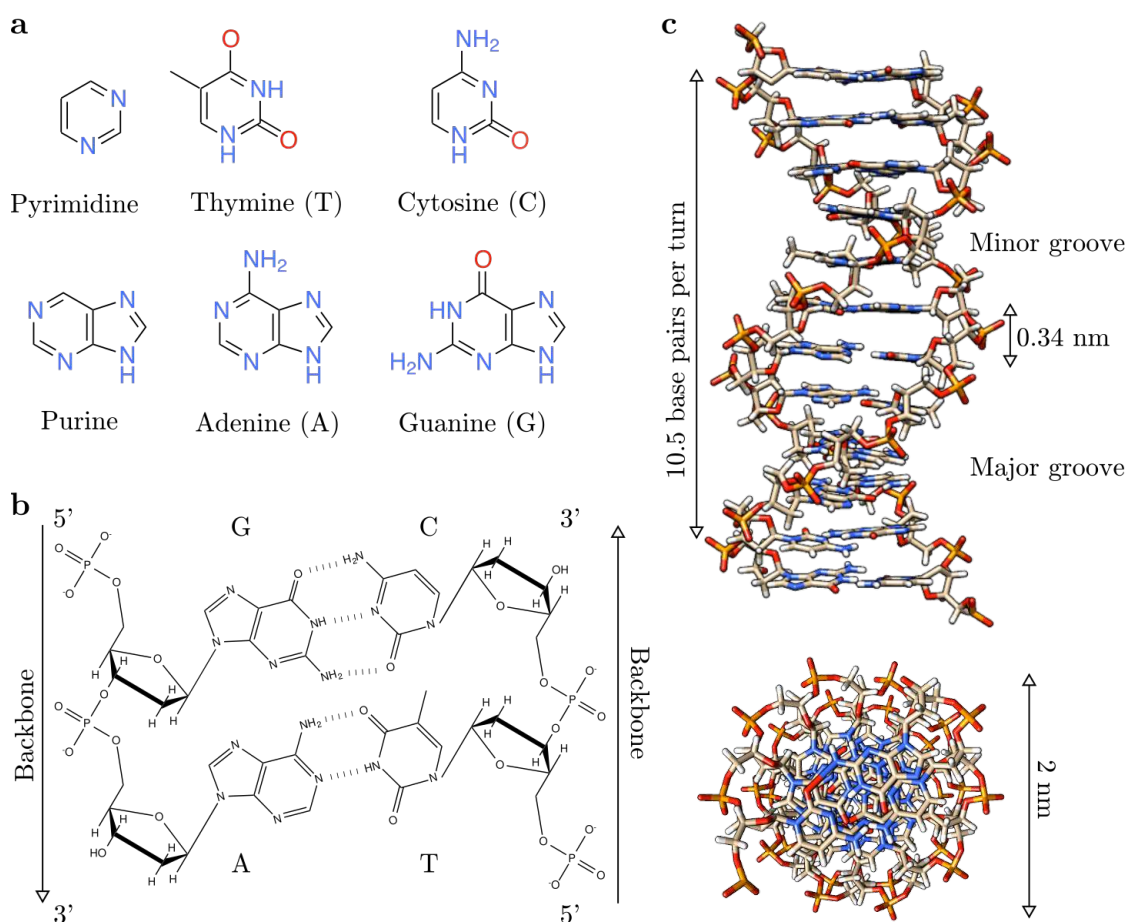


**Figure 5.1: Individual components of DNA and their composition forming a double helix structure.** (a) The heterocyclic molecules purine and pyrimidine are the building blocks of nucleic acids. Thymine (T) and cytosine (C) are pyrimidine derivatives and adenine (A) and guanine (G) are purine derivatives. (b) Watson-Crick base pairing between A and T is established by two hydrogen bonds (dotted lines) and between C and G by three hydrogen bonds. Each base is connected to a 2'-deoxyribose and different nucleotides are joined by a phosphate, linking the 3'-hydroxyl of one 2'-deoxyribose to the 5'-hydroxyl of another nucleotide 2'-deoxyribose. (c) Structural model of a right handed B-form DNA double helix, which is the most prominent form. The diameter is 2 nm with a helical pitch of 10.5 base pairs per turn. Each base pair is separated by 0.34 nm on average. Major and minor groove result of the angle between the paired nucleotides. Atoms are color-coded by type (C = gray, H = white, O = red, P = orange, N = blue). [121]

property of ssDNA of having a high flexibility comes along with a likelihood to undergo backbone strand breaks due to thermal fluctuations. Thermal stability and information redundancy are the main reasons why information is stored in double helical DNA form in the genome.

### Double-stranded DNA

Two complementary strands of ssDNA can hybridize in an anti-parallel fashion through specific base pairing, resulting in a double-stranded DNA (dsDNA) form with double helical structure. X-Ray diffraction pattern by R. E. Franklin and R. G. Gosling [127] played a crucial part in the discovery of DNA's structure. Along with subsequent related work, it led to the determination of the helical structure of DNA by J. D. Watson and F. H. C. Crick in 1953 [128]. The right-handed double helical structure is commonly known as B-form DNA and most abundant under the conditions found in cells [129] (see Figure 5.1c). Besides the B-form, different double helical conformations like the right-handed A-form DNA, found in crystallized DNA, [130] or the left-handed Z-form DNA [131] are known. This thesis deals only with B-form DNA, if not specified otherwise.

The formation of helical dsDNA results from the weak non-covalent base complementarity of opposing nucleotides. The bases are equipped with amino and (except for adenine) ketone groups, with which they interact via hydrogen bonding. Adenine and guanine are both purine derivatives, whereas thymine and cytosine are derived from pyrimidine (see Figure 5.1a). Canonical Watson-Crick base pairing consists of two hydrogen bonds between adenine (A) and thymine (T), and of three hydrogen bonds between cytosine (C) and guanine (G) (indicated by the dotted lines in Figure 5.1b). Because of this difference in hydrogen bonds, G-C pairs are more stable compared to A-T pairs. Further, base pairs are horizontally aligned in the double helix, allowing their  $\pi$ -electrons to interact and for hydrophobic interactions between bases. These stacking energies between neighboring bases stabilize dsDNA duplex [132, 133]. In contrast to popular belief, this base stacking between neighboring bases is mainly responsible for the hybridization energy of a DNA duplex. Base pairing energies are in the range of 13 kJ/mol to 25 kJ/mol, i.e. 130 meV to 240 meV per hydrogen bond, and contribute primarily by aligning the bases to facilitate optimal base stacking [132].

For successful duplex formation, complementary sequences according to the

Watson-Crick base pairing rules are required. Further, two single strands can only hybridize in an antiparallel fashion, that is if the strands have inverse polarity (see Figure 5.1b). DNA nucleotides are negatively charged at neutral pH values, leading to the electrostatic repulsion of different DNA strands. Repulsive interactions are screened at high ionic strength, facilitating DNA duplex formation, especially in densely packed DNA nanostructures. Addition of divalent cations like magnesium leads to the screening of repulsive interactions and even introduces an attractive force between negatively charged DNA strands. As a result of this reduction of the electrostatic repulsion, the mechanical properties of a DNA duplex change like a reduction in bending stiffness and in persistence length. [134]

Hybridization and dissociation of complementary DNA strands can take place at a critical melting temperature. Using a nearest neighbor model, thermodynamic properties of the strand hybridization process, melting temperatures and the energy associated with the hybridization of DNA strands can be calculated [135, 136]. In summary, four factors influencing hybridization reactions can be emphasized.

- Hydrogen bonding between complementary bases of opposing strands
- Base stacking interactions between bases of the same strand
- Electrostatic interactions between the negatively charged DNA backbones
- Entropic effects

In general, neighboring base pairs in a dsDNA duplex are spaced 0.34 nm apart [127, 128] and include an angle of  $34.3^\circ$ . The double helix has a diameter of 2 nm and an approximate pitch of 10.5 base pairs or 3.57 nm [137]. The sugar residues in the backbone are diametrically opposed. The major and minor grooves of the DNA double helix are the consequence of this  $120^\circ$  angle between backbones of complementary nucleotides (see Figure 5.1c). DNA nanotechnology often makes the simplification of a  $180^\circ$  angle between backbones, working reasonably well in most cases. Although the overall shape of the double helical structure is sequence dependent [138], sequence independence is assumed in DNA nanotechnology. Since local DNA conformations are often forced to conform to the overall structure, this is a valid approximation.

	ssDNA	dsDNA
<b>contour length</b>	0.5 nm to 0.7 nm per base	0.34 nm per base pair
<b>persistence length</b>	0.5 nm to 5 nm [124]	40 nm to 50 nm [139]
<b>diameter</b>	1 nm	2 nm
<b>shape</b>	random chain	right-handed double-helix with major and minor groove
<b>model</b>	freely-jointed chain, worm-like chain	worm-like chain
<b>interbase angle</b>	nearly arbitrary	34.3°

**Table 5.1: Properties of ssDNA and dsDNA.** The properties of dsDNA are remarkably different in comparison to ssDNA, which is one of the many reasons why DNA is so attractive as a building material.

dsDNA and ssDNA have remarkable differences in their properties and structural parameters, as can be seen in Table 5.1, which makes DNA an attractive building block for nanotechnology. dsDNA has a contour length  $l$  of 0.34 nm per base pair and a salt dependent persistence length  $l_p$  of 40 nm to 50 nm [139], and it can no longer be modeled as a freely-jointed chain. Instead, the worm-like chain model can be used [139, 140]. In this model, dsDNA is considered as a continuous, flexible, one dimensional object with the persistence length  $l_p$  as a central parameter. Then, the end-to-end distance  $r$  of a dsDNA chain reads

$$\langle r^2 \rangle = 2l_p l \left[ 1 - \frac{l_p}{l} (1 - e^{-l/l_p}) \right]. \quad (5.3)$$

This reduces to  $\langle r^2 \rangle = r^2$  for short strands, which can be treated as stiff rods. For long strands ( $l \gg l_p$ ) this relation can be simplified to

$$\langle r^2 \rangle = 2l_p l \quad (5.4)$$

which is equivalent to the freely jointed chain model when substituting  $l = 2l_p$  [134]. dsDNA is rather stiff in comparison to ssDNA. By either using single or double stranded components, DNA nanostructures can be designed to behave like flexible or rigid elements, respectively. Bending behavior of DNA origami constructs can be predicted using elasticity values for dsDNA.

## 5.2 Thermodynamic considerations of DNA duplex formation

As mentioned in the previous section, the main interactions contributing to the total hybridization energy—base pairing, base stacking and entropic effects—are well known. Still, it is not possible to calculate exact hybridization energies of the DNA duplex formation. But in contrast to many other biological systems, such as proteins, it is possible to make sophisticated predictions using the nearest neighbor model [141]. This ability to predict the accompanied hybridization energies for DNA duplex formation is of huge biological and technological importance. In particular, possible secondary structures of ssDNA can be predicted, which might carry biological function [142, 143] or be responsible for diseases [144]. Further, many biotechnological applications, like polymerase chain reaction (PCR), use predicted hybridization energies to design primer sequences with low secondary structures [145, 146].

The standard Gibbs free energy of DNA hybridization  $\Delta G^\circ$  for a given temperature  $T$  can be expressed as the difference between the enthalpy  $\Delta H^\circ$ , i.e. the thermodynamic measure of the total energy, and the temperature times the entropy  $\Delta S^\circ$ , which is a measure of possible states a system can assume.

$$\Delta G^\circ(T) = \Delta H^\circ - T\Delta S^\circ \quad (5.5)$$

Once  $\Delta H^\circ$  and  $\Delta S^\circ$  are known,  $\Delta G^\circ$  can be calculated for any temperature. Table 5.2 shows the set of nearest neighbor thermodynamic parameters—enthalpy, entropy and free energy—for Watson-Crick base pairs in 1 mol NaCl as generated by J. SantaLucia and D. Hicks in 2004 [141]. Different salt concentrations influence these parameters, and they need to be corrected accordingly. Further, correction factors for the initiation of the hybridization, the ends of a duplex strand and symmetry correction of a DNA sequence, accounting for self-dimerization, need to be considered. Including all those contributions, the total free energy can be calculated [141] and reads

$$\Delta G_{\text{total}}^\circ(T) = \Delta G_{\text{init}}^\circ(T) + \Delta G_{\text{sym}}^\circ(T) + \sum \Delta G_{\text{stack}}^\circ(T) + \Delta G_{\text{terminalAT}}^\circ(T). \quad (5.6)$$

$\Delta G_{\text{init}}^\circ$  accounts for the initialization phase and also includes corrections for the ends of a duplex and the contributions of terminal bases which only have one neighboring base.  $\Delta G_{\text{terminalAT}}^\circ$  takes differences in the terminal correction for CG

and AT pairs into account and  $\Delta G_{\text{stack}}^{\circ}$  accounts for the stacking interactions of different bases. The GC content of a DNA duplex is often used as an approximate measure for DNA duplex stability, since CG pairs have the highest free energy (see Table 5.2).

Propagation sequence	$dH[\frac{\text{kcal}}{\text{mol}}]$	$dS[\frac{\text{kcalK}}{\text{mol}}]$	$dG[\frac{\text{kcal}}{\text{mol}}]$
GG/CC	-8.0	-19.9	-1.84
AA/TT	-7.6	-21.3	-1.00
GC	-9.8	-24.4	-2.24
CG	-10.6	-27.2	-2.17
AT	-7.2	-20.4	-0.88
TA	-7.2	-21.3	-0.58
GA/TC	-8.2	-22.2	-1.30
GT/AC	-8.4	-22.4	-1.44
CA/TG	-8.5	-22.7	-1.45
CT/AG	-7.8	-21.0	-1.28
Initiation	+0.2	-5.7	-1.96
Terminal A/T penalty	+2.2	+6.9	+0.05
Symmetry correction	0.0	-1.4	+0.43

**Table 5.2:** *The thermodynamic parameters for DNA duplex formation at 1 M NaCl. Using a nearest neighbor model the enthalpy, entropy and free energy can be calculated. Sequences to the left and to the right of the slash are given in anti-parallel orientation [141]. Empirical salt-correction equations have been derived such that this data can be used for a variety of solution conditions [135].*

Distinguishing the influence of Watson-Crick base pairing and the influence of base pair stacking on DNA hybridization is not easily accomplished. In particular, it is difficult to measure the influence and energy of a single stack of two neighboring base pairs. Data based on a gel shift assay suggest that base stacking is the main contribution for DNA hybridization and base pairing is mainly responsible for the alignment of the bases [132]. Since ssDNA does not show a strong stacking behavior, this alignment is thought to be crucial for stable duplex formation. Table 5.3 shows a set of experimentally substantiated stacking energies for base pairs

	A	T	G	C
A	-1.11	-1.34	-1.06	-1.81
T	-0.19	-1.11	-0.55	-1.43
G	-1.43	-1.81	-1.44	-2.17
C	-0.55	-1.06	-0.91	-1.44

**Table 5.3:** *Base pair stacking free energy parameters for  $\Delta G$  in  $\text{kcal mol}^{-1}$ . The DNA stacking free energy depends on the involved bases [132].*

### 5.2.1 Kinetics of DNA dissociation and hybridization processes

The disintegration of a DNA duplex  $D$  into the single strands  $S$  and  $\bar{S}$  is a reversible process and can be written as



The melting temperature  $T_m$  is defined as the temperature at which half of all DNA duplexes are melted and reads

$$T_m = \frac{\Delta H^\circ}{\Delta S^\circ + R \ln[D]_0/2} \quad (5.8)$$

with  $[D]_0$  being the initial duplex concentration.

For DNA nanotechnology, the kinetics of duplex formation are of particular importance. The duplex formation is a second-order reaction and the dissociation process is a first-order reaction. Therefore the rate equation according to Eq. 5.7 reads

$$\frac{d[D]}{dt} = -k_- [D] + k_+ [S] \cdot [S] \quad (5.9)$$

with relaxation times  $\tau$  of

$$\tau^{-1} = k_+ ([S] + [S]) + k_-. \quad (5.10)$$

Actual values for  $k_+$  are dependent on salt concentration, temperature and sequence but typically are in the range of  $10^5 \text{ mol}^{-1} \text{ s}^{-1}$  to  $10^7 \text{ mol}^{-1} \text{ s}^{-1}$ .

These considerations have important implications for DNA nanotechnology, as the duration of hybridization and dissociation reactions are critical for the



assembly speed of DNA nanostructures. Hybridization on-rates are mainly dominated by diffusion and thereby by strand concentration. Strand blockage and secondary structures can reduce the effective reaction speed. Hybridization off-rates are determined by the hybridization energies of a duplex. At room temperature, long DNA duplex structures have a half-life orders of magnitude higher than typical experimental timescales. Therefore they can be considered a stable structure.

### Branch migration

Besides the described hybridization process, also branch migration—a process in which one strand, partially paired with its complement, extends its pairing—and strand displacement reactions can take place in which hybridized strands are exchanged or released. These reactions are often utilized in logic gated DNA nanotechnology [109] and might play an important role in the assembly process of DNA nanostructures. In these structures, staple oligonucleotides are designed in such a way that several segments bind to different positions of a scaffold strand (as described in detail in chapter 6). Very likely, several staples of the same type will initially bind to one scaffold strand. By branch migration, identical staples can be removed, thereby being an essential concept in the assembly process.

In a toehold mediated strand displacement system, a single-stranded “invader”, fully complementary to a substrate strand including the toehold, replaces a shorter incumbent strand, partially bound to the substrate (see Figure 5.2). First, the invader strand attaches to the toehold. Then, the invader strand and incumbent strand compete for bases paired with the substrate strand, thereby performing a one dimensional random walk. When the invader strand is fully paired to the substrate strand, the incumbent strand falls off and is released. In contrast, the invader strand can hardly fall off completely because of its attachment to the toehold. The displacement reaction is thermodynamically driven by the net gain in base pairs due to the toehold [147]. These strand replacement reactions take place during the assembly of a DNA origami structure or during the targeted detachment of a DNA strand from a duplex. Strand replacement reactions are typically slower in comparison to the previously mentioned association reactions.



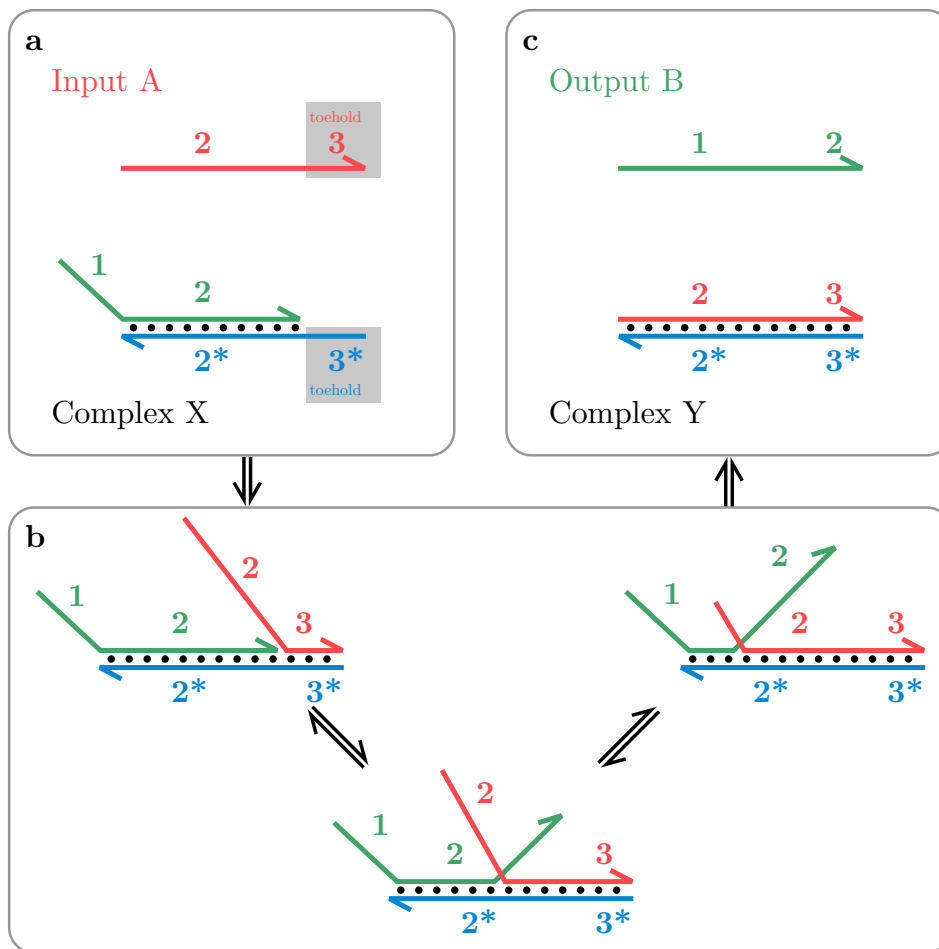


**Figure 5.2:** A toehold mediated strand displacement reaction is an example for a branch migration process. (a) In a dsDNA duplex, the substrate strand (blue) is extended with an additional toehold (3\*). Initially, this substrate strand forms a duplex with an incumbent strand (green), with a partially complementary sequence to the substrate (region 2). An invader strand (red), which is complementary to both, the longer region (2\*) and the toehold region (3\*) of the substrate strand, is added to the mixture and can react with the duplex. (b) Via the toehold region, this strand can attach to the duplex. The two competing strands complementary to the long region perform a one dimensional random walk. This branch migration process is reversible, as long as both strands are partly bound to their complement. (c) Once the invading strand fully displaced the shorter strand, it is released and very unlikely to bind again.

### 5.3 Optical properties of DNA

The melting procedure of a DNA duplex, i.e. the transition from dsDNA to ssDNA, can be monitored experimentally using absorption measurements. DNA bases absorb UV light with an absorption maximum around 260 nm, depending on the sequence length, the types of bases in the sequence and its conformation (ssDNA or dsDNA). This absorption maximum is a result of transitions between  $\pi$ -electrons of bases in a certain plane. In contrast, absorption of the sugar-phosphate backbone takes place mainly at wavelengths lower than 190 nm. The extinction coefficient is an intrinsic property, measuring how strongly light at a given wavelength is attenuated for a chemical species. For calculating this extinction coefficient, the fact that light absorption leads to an electric transition dipole moment which induces a transition dipole in the opposing and the neighboring base, has to be considered. The induced dipole in the opposing base implies that the extinction coefficient of dsDNA is not equal to the sum of the extinction coefficients of both ssDNA strands. The induced dipole in the neighboring base is in the opposite direction and thereby reduces the total dipole moment, leading to a reduced absorption. This effect is called hypochromicity and by monitoring the absorption at a wavelength of 260 nm it allows for the determination of the transition from double-stranded to single-stranded DNA during the melting process.

These optical properties of DNA are heavily used in the quantitation of nucleic acids, i.e. the determination of average DNA concentrations as well as their purity. Commonly, a spectrophotometer is used for this analysis in combination with the Beer-Lambert law to determine unknown concentrations without the need for standard curves. The Beer-Lambert law relates the amount of light absorbed to the concentration of the absorbing molecule and is given by

$$A = \epsilon(\lambda) \cdot c \cdot l \quad (5.11)$$

with the absorption  $A$ , the extinction coefficient  $\epsilon(\lambda)$ , the molar concentration  $c$  and the path length  $l$ . Commonly, an average extinction coefficient at a wavelength of 260 nm is used ( $0.020 \text{ (}\mu\text{g/ml)}^{-1} \text{ cm}^{-1}$  for dsDNA and  $0.027 \text{ (}\mu\text{g/ml)}^{-1} \text{ cm}^{-1}$  for ssDNA), but by using the nearest neighbor model, a more accurate extinction coefficient can be calculated. [148, 149]

## 5.4 dsDNA as a secondary structure unit

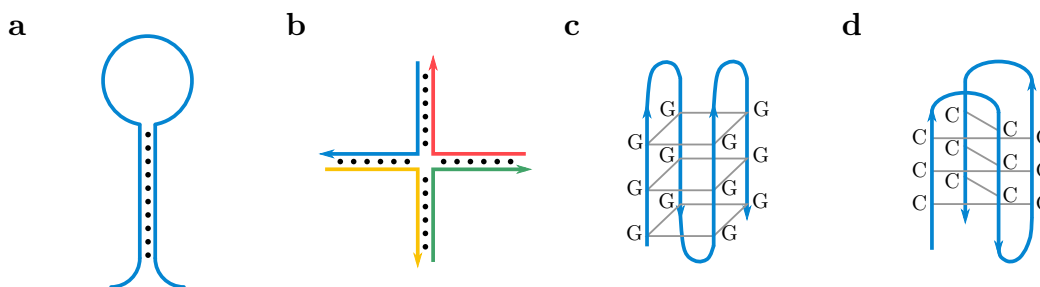


**Figure 5.3: DNA motifs and secondary structure.** (a) Schematic representation of a hairpin motif that can occur in ssDNA, but is more commonly found in RNA. In a DNA hairpin, two regions of a strand base pair to form a double helix that ends in an unpaired loop. (b) Motif of a DNA Holliday junction, also called four way junction, with the four strands colored independently. (c) The G-quadruplex motif is based on Hoogsteen interactions between the guanine bases to form a square planar structure called a guanine tetrad. (d) The DNA i-motif, an abbreviation of intercalated motif, is a quadruplex structure made up of two parallel duplexes and is rich in unusual cytosine-cytosine bonds.

Besides the regular double helical formation of DNA, several other secondary structures exist (see Figure 5.3). While some of these motifs rely on Watson-Crick base pairing, others are able to form without it. In the most simple case, DNA secondary structures consist only of a single strand interacting with itself, but also multiple strands can fold onto each other into a defined secondary structure. Although computationally demanding for long sequences, the predictability of DNA allows for the a priori design of secondary structures, thereby making these structures a versatile tool in DNA nanotechnology, similar to aptamers. Software tools like NUPACK and Mfold allow the prediction of secondary structures for DNA strands with a given sequence at defined conditions [150, 151] NUPACK considers hybridization according to a nearest neighbor model and it therefore does not cover additional motifs like the G-quadruplex or the i-motif. In general, these complex structures based on other interactions than Watson-Crick base pairing are not considered for DNA nanostructure design, but rod like duplexes are used as the main structural components. Four common secondary structure motifs will be described in this section.

### DNA hairpin motif

The DNA hairpin, also called stem-loop, is the most fundamental secondary structure motif (see Figure 5.3a). It consists of a double-stranded stem region and a connecting single-stranded loop. Even though the small loop region of the hairpin is single-stranded, its sequence is less accessible for hybridization reactions. Although occurring in DNA, the hairpin motif is more commonly found in ribonucleic acid (RNA). [152]

### Holliday junction

Another well known structural motif of DNA, based on Watson-Crick base pairing, is the Holliday junction, also referred to as four way junction. In a Holliday junction, four strands of DNA are connected at a single crossover, forming a recombination of two double helices (see Figure 5.3b). A strand is composed of two domains. The second domain of the first strand binds to the first domain of the second strand. This principle continues until the fourth strand binds to the first strand. A  $Mg^{2+}$  ion in the center is assumed to stabilize the junction. For this reason, solutions containing  $Mg^{2+}$  ions might be beneficial for the assembly of DNA nanostructures based on Holliday junctions. Further, Holliday junctions are known to switch between an antiparallel and a parallel state, with transitions being strongly salt dependent [153]. In the context of DNA nanotechnology, Holliday junctions can be used to connect two adjacent double helical DNA strands and are often referred to as crossovers. Nadrian Seeman adopted this motif for DNA nanoconstruct design, allowing also for the formation of larger structures [154].

### DNA G-quadruplex

A G-quadruplex is a complex natural occurring secondary structure element based on non Watson-Crick base pairing interactions (see Figure 5.3c). Instead, Hoogsteen hydrogen bonds connect four guanines within each segment of this motif. Several guanine tetrads can stack on top of each other thereby forming a G-quadruplex. In contrast to previously described secondary structures, the four strand segments align parallel to each other and do not form a double helix. The incorporation of central monovalent ions can stabilize the quadruplex. [155–157]

## DNA i-motif

The i-motif is another complex DNA motif which is not based on Watson-Crick base pairing. This pH switchable motif is similar to the G-quadruplex, as again four segments align parallel to each other and do not form a double helix structure (see Figure 5.3d). But in contrast to the G-quadruplex, cytosine-cytosine bonds are responsible for the formation of this structure. [158–160]

## 5.5 DNA nanoconstructs interacting with lipid bilayers

### 5.5.1 Lipid bilayer systems

Lipid membranes in living organisms form a continuous barrier around all cells. Further, different sub-cellular structures and compartments like organelles or the nucleus are surrounded and thereby separated from each other by membranes. In general, these membranes consist of mostly phospholipids, amphiphilic molecules with a hydrophilic head group and two hydrophobic fatty acids connected by glycerol backbone (see Figure 5.4a). However, also other types of lipids like cholesterol and glycolipids are frequently included in membranes, as are various membrane proteins. Diffusion of membrane proteins and other membrane components and the confinement of these components to a 2D surface are important characteristics of lipid membranes. While some of the proteins act as mechanical anchors, others form pores and act as active transporters and pumps. Membrane-associated proteins are often considered to be essential in signal processing cascades, as mentioned in chapter 2. [3]

The behavior of lipid molecules in aqueous solution can be explained with their amphiphilic properties. Hydrophobic molecules arrange themselves in order to reduce exposed surface area from their aqueous surroundings. Therefore, lipids often form micelles in aqueous solution in order to shield their hydrophobic components and expose their hydrophilic headgroups to their surroundings (Figure 5.4b). Another possible arrangement is a planar lipid bilayer, in which the hydrophobic fatty acid chains are located in the center of the bilayer. If such bilayer close upon themselves, they form a spherical lipid vesicle. Lipid geometry influences lipid arrangement and also membrane curvature. [3]

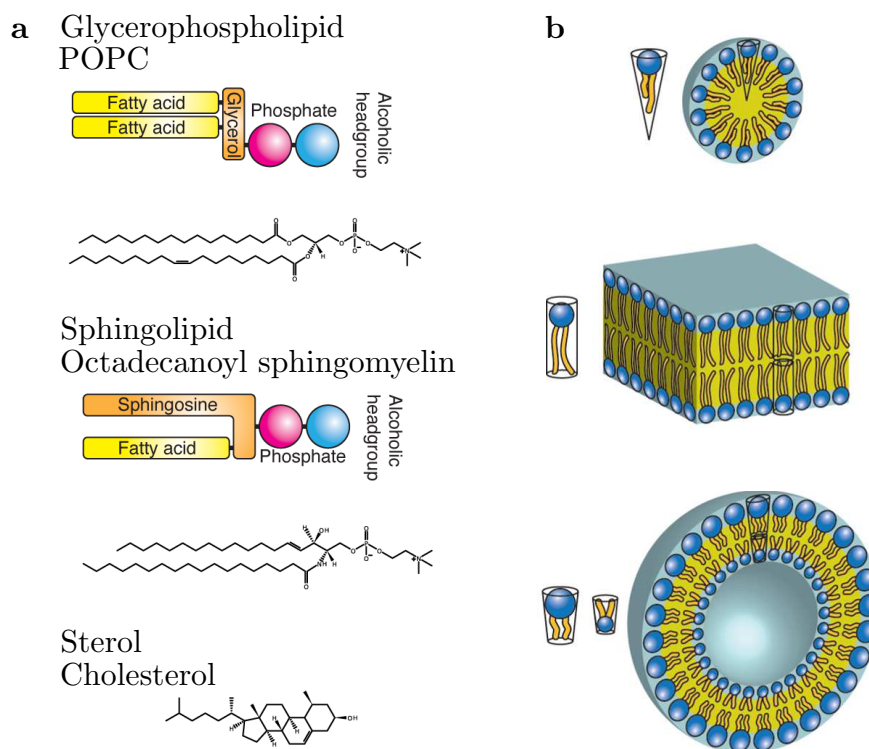


**Figure 5.4: Structures of lipid types and lipid assemblies.** (a) Glycerophospholipids are made up of a glycerol, attached to a polar headgroup, and two fatty acid chains. The molecular structure of POPC, a typical phospholipid, of a sphingolipid and of cholesterol, the most common sterol are shown (top to bottom). (b) Schematic of a micelle (top), formed by lipids with an inverted conical shape, a planar lipid bilayer (center), formed by lipids with a more cylindrical shape, and a lipid vesicle (bottom), that are spherical lipid bilayers with a water core. Images taken from [103].

Artificial lipid bilayers and vesicles are versatile tools to study membrane-related phenomena. Several different model systems of lipid vesicles of different sizes or supported lipid bilayers (SLBs) are commonly used. Here, we will focus on planar supported lipid bilayers (SLBs), which are bilayers formed on hard, hydrophilic substrates like glass or mica. These systems are particularly suited for light microscopy, in particular they are compatible with TIRF microscopy and AFM measurements due to their 2D character. Moreover, they allow for cell attachment without imposing constraints on the cell surface organization or interfering with the physiology of their plasma membrane. Different methods for the formation of supported bilayers exist. Here, we utilize the adsorption and fusion of small unilamellar vesicles (SUVs) from an aqueous suspension to the substrate surface. While SLBs can be functionalized with appropriate ligands, there is no unspecific binding of proteins. Further, SLBs can compensate irregularities within the glass support to a certain degree. The fluidity of the resulting bilayer depends highly on the used lipids, e.g. 1-palmitoyl-2-oleoyl-sn-glycero-3-phosphocholine (POPC) forms lipid bilayers of high fluidity, even at room temperature. [161]

### 5.5.2 Attachment of DNA structures to lipid bilayers

DNA nanostructures attached to lipid bilayers can serve to artificially mimic the function of membrane-associated protein [103, 162], membrane spanning pores [163–168] or to sculpture lipid vesicles [169, 170]. In contrast to vesicles, SLB systems present a 2D substrate allowing for diffusion of DNA nanoconstructs within the bilayer plane [171–173].

A variety of methods exist to attach DNA nanostructures to lipid bilayer systems. DNA constructs conjugated to hydrophobic anchor moieties can be specifically attached to lipid bilayers (see Figure 5.5a). Cholesterol modifications on DNA strands are commercially available and are widely used for this purpose [167, 168, 174–176]. Since cholesterol moieties show only weak binding to lipid bilayers in comparison to other modifications, multiple cholesterol modifications per construct are used for bilayer attachment. Further, for cholesterol a strong influence of linker chemistry was reported [174].

Other methods to attach DNA nanostructures to lipid bilayers either use different DNA conjugated lipids [177, 178] or other hydrophobic moieties like polypropylene oxide (PPO) [179] or porphyrin [163]. Hydrophobic modifications not







located at the end of oligonucleotides but placed at the DNA backbone can be used for the insertion of nanopores into lipid bilayers [164]. In order to prevent clustering of DNA nanostructures in solution, DNA or biotin functionalized cholesterol and phospholipids are first integrated in the membrane and then used to attach nanostructures to the membrane [167, 171]. This strategy can also be used by antibody or aptamer conjugates, which bind to membrane proteins [97, 180, 181]. Further, DNA nanostructures partition in different phases on phase separated lipid vesicles (see Figure 5.5c), depending on the used binding strategy [174]. Membrane binding efficiency of certain attachment methods is therefore thought to be strongly dependent on lipid composition. Diffusion of membrane bound DNA nanostructures on lipid bilayers has been observed by SPT and fluorescence correlation spectroscopy (FCS) [171, 174].

In contrast to specific attachment strategies, electrostatic interactions can be used for the attachment of DNA nanostructures to lipid bilayers without the need for additional modifications (see Figure 5.5b). The negatively charged DNA binds readily to membranes composed of lipids with positively charged head groups [182, 183]. A similar behavior can be observed for zwitterionic lipids in the presence of divalent cations [184, 185]. The absence of mediating divalent cations leads to a reduction of the interactions between DNA and zwitterionic lipids [186]. Since the electrostatic binding of DNA nanostructures to lipid bilayers is unspecific, binding orientation of the structures to the membrane cannot be controlled and specific attachment methods are preferred. However, even when using specific interactions, unspecific binding via electrostatic interactions can lead to incorrect orientations of the structures. This effect can be avoided by excluding divalent cations or by the use of high concentrations of monovalent ions to screen the electrostatic interactions.



## Chapter 6

# Self-assembled DNA nanostructures

Besides its actual function—the capability for biological information storage—DNA has proven to be an extremely useful material for the design of artificial nanostructures. Its remarkable properties described in the previous chapter allow for the construction of DNA structures with nanometer precision. Molecular self assembly is a common way for biological objects to arrange themselves and is utilized in the creation of DNA nanostructures. It allows for the generation of countless copies of the same object in a one pot reaction. Progress in recent years made the design and assembly of custom shapes tailored for very different, specific applications possible. [21, 22, 93, 187–189]

Nadrian Seeman performed pioneering work on utilizing the potential of DNA as a material for building nanostructures. He used Holliday junctions to cross-link different DNA double helices, thereby creating artificial higher ordered structures [154]. This principle still is the foundation of state of the art DNA nanotechnology. Further, by using short synthetic DNA oligonucleotides with custom overlapping sequences, he could create 2D meshes [190] and 3D crystals [191] (see Figure 6.1a and b, respectively).

### 6.1 Principles of DNA origami

In 2006 Paul Rothemund developed the DNA origami technique to create custom shapes and exact dimension on the nanometer scale [21]. In contrast to previous

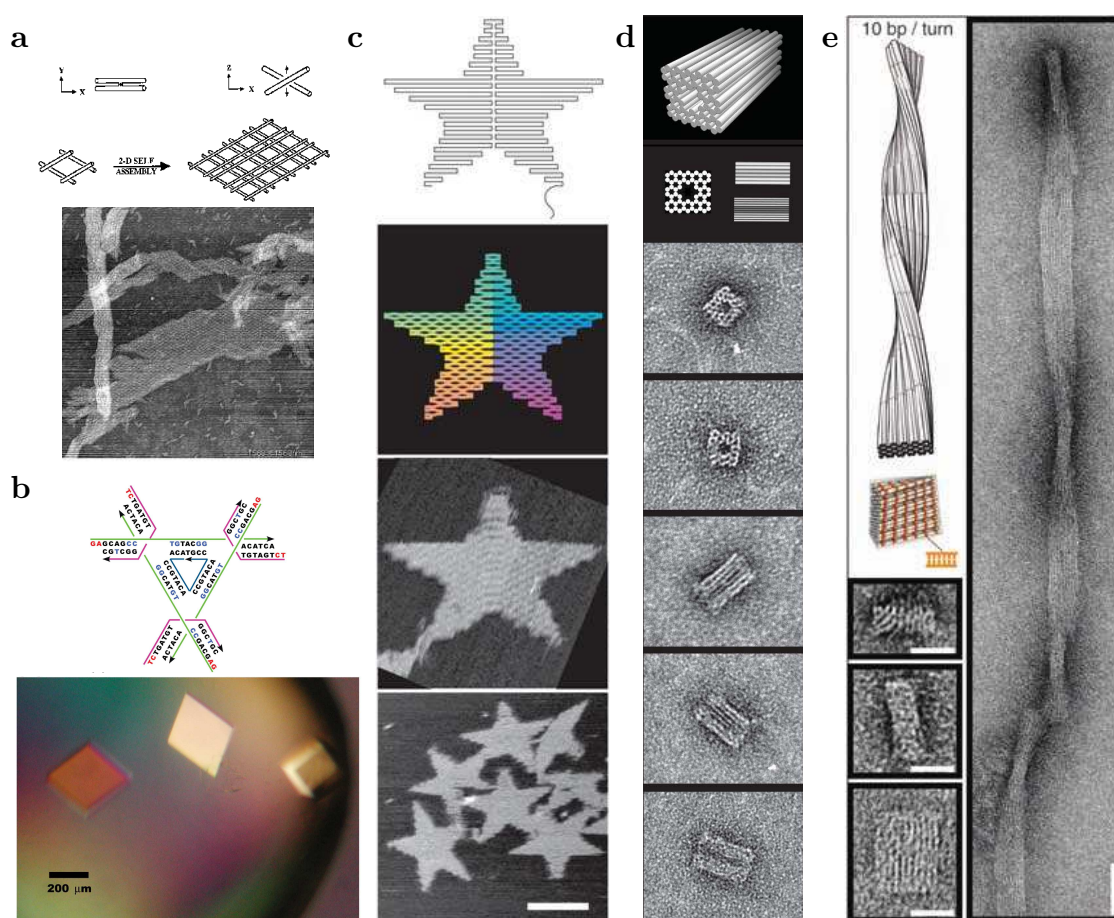


**Figure 6.1: Various examples for DNA nanostructures.** (a) Scheme (top) and AFM image (bottom) of a 2D crystal formed of DNA Holliday junctions. Image width and height: 1568 nm. Image taken from [190]. (b) Schematic (top) and optical image (bottom) of a self assembled 3D DNA crystal. The red bases in the tensegrity triangle form the connections to shape a 3D crystal. The scale bar is 200  $\mu\text{m}$ . Image taken from [191]. (c) Design (upper panels) and AFM images (lower panels) of a DNA origami structure, formed by short oligonucleotides interconnecting different parts of a long DNA scaffold with Holliday junctions. Images without scale bar are 165 nm in width and height. The scale bar is 100 nm. Image taken from [21]. (d) Design (upper panels) and negative stain TEM images (lower panels) of a 3D DNA origami brick structure on a honeycomb lattice formed by Holliday junctions every 7 bases, equivalent to  $240^\circ$ , to neighboring helices. The scale bar is 20 nm. Image taken from [22]. (e) Twisted or bent 3D DNA origami structures can be created by removing or adding base pairs from the standard crossovers in a honeycomb lattice. Design and negative stain TEM images of a monomeric block (left, scale bar 20 nm) and an image of a polymerized structure formed of these blocks (right, scale bar 50 nm) shown. Image taken from [93].

methods for the creation of DNA nanostructures, he used a second and longer type of DNA as a complement to short synthetic DNA oligonucleotides. This technique uses a long circular ssDNA molecule as a scaffold, which is pinched together with short synthetic oligonucleotides termed staple strands, to form a predetermined shape (see Figure 6.1c). Holliday junctions are used to form crossovers between different double helical domains, thereby connecting them. One major advantage to previously used methods is that the same scaffold strand can be used to create different structures by appropriate sequence design of the staple strands, leading to a reduction of the costs of DNA structures since this scaffold strand can be biologically produced. It is generally derived from the m13mp18 phage genome and its sequence is given in Appendix A.3. Soon after its first introduction, the DNA origami technique was extended to the design of 3D structures [22], with the intrinsic ability to include twists and bents (see Figure 6.1d and e, respectively) [93].

DNA is an excellent tool for the development of nanostructures, and its applications range from help in single molecule techniques [168, 192–196] over nuclear magnetic resonance (NMR) [133] to the medical field [97] (see Figure 6.2). Combining scaffold based designs with design strategies that do not use a scaffold strand [197, 198] allow for additional design variability. These strategies come with more flexibility, but with a higher cost in contrast to scaffold based designs. Further, designs without a scaffold strand might be more error prone, since with only short staple strands, no strand can serve as a template for a possible DNA branch migration process.

In this thesis only scaffold based designs are used. The following sections describe the design process in general and details of the specific designs used in this thesis.

## 6.2 DNA nanoconstruct design

Several simplifications on the structure of dsDNA are made when designing scaffolded DNA nanostructures.

- For helical pitch and base-to-base distance, no sequence dependence is taken into account, but a general pitch of 10.5 base pairs per turn is assumed. A standardized value for the base-to-base distance of 3.4 Å, according to TEM measurements, is sufficient for most designs.



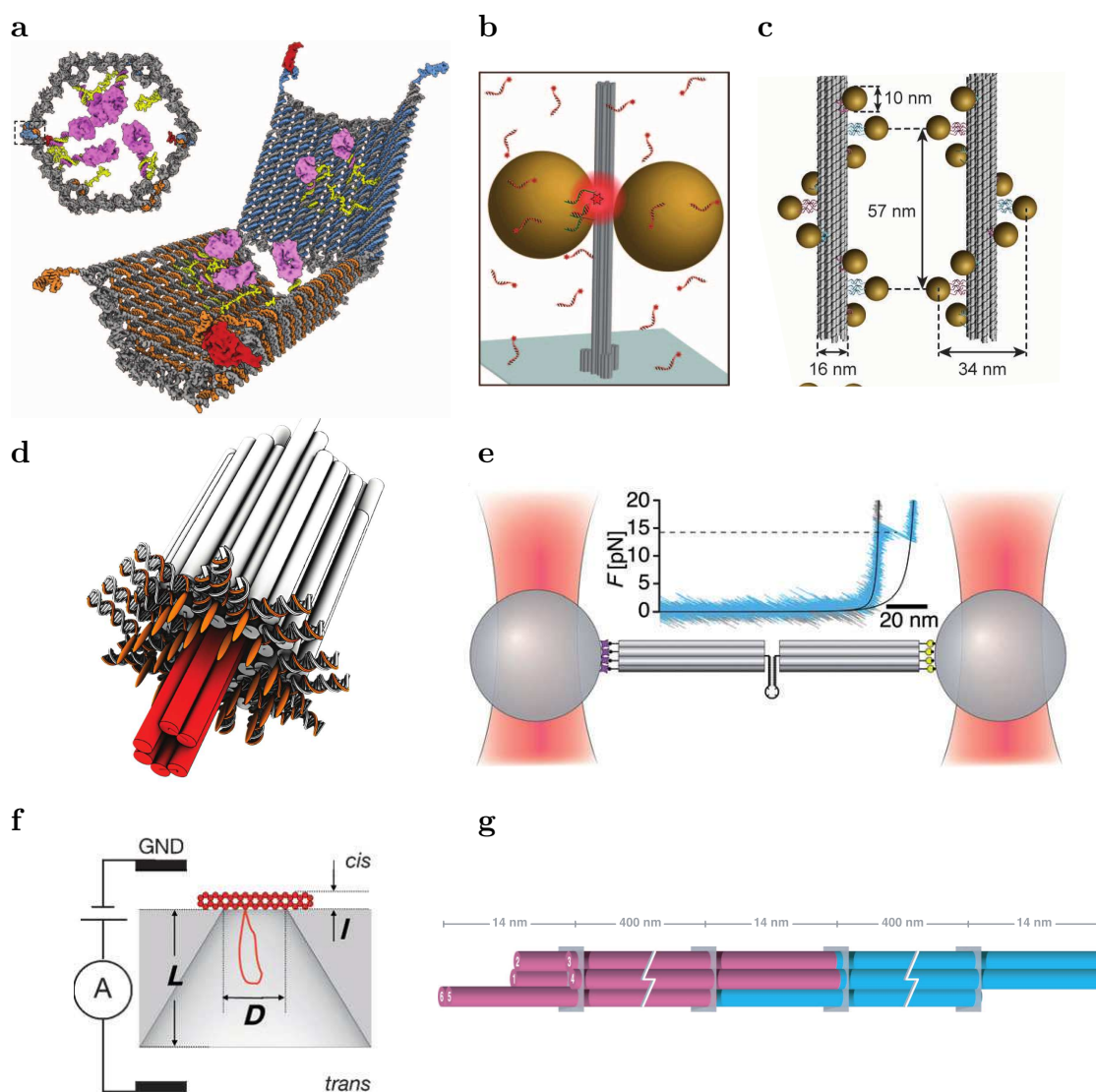


**Figure 6.2: Overview of various DNA origami applications.** (a) A logic-gated DNA nanorobot can release molecular payloads at cell contact. Image taken from [97]. (b) Precisely attached gold particles on a DNA rod can be used for local fluorescent enhancement. Image taken from [192]. (c) DNA bricks are used to make chiral plasmonic nanostructures specifically conjugated with gold nanoparticles. Image taken from [102]. (d) A synthetic lipid membrane channel made from DNA. Hydrophobic cholesterol anchors are used for the incorporation in the lipid bilayer. Image taken from [168]. (e) In optical trapping applications, rigid DNA rods can be used to enhance the resolution. Image taken from [193]. (f) DNA origami gatekeepers on solid-state nanopores. Image taken from [194]. (g) DNA structures can be used for membrane protein alignment in NMR based structural biology. Image taken from [133].

- Major and minor groves are not considered, resulting in opposing backbone positions of scaffold and staple strands at  $180^\circ$  compared to a more accurate  $120^\circ$ . This simplification facilitates crossovers between scaffold and staple strands and is therefore necessary when designing anti-parallel DNA nanostructures, in particular for scaffolded DNA nanostructures. However, close proximity of staple and scaffold crossovers induces mechanical stress in the structure. Therefore, the amount of scaffold crossovers needed to route the scaffold through a structure is kept to a minimum for most structures.

To summarize, several structural features of dsDNA are simplified and no sequence dependence is considered for the design of DNA nanostructures.

### 6.2.1 Strand routing and breaking

#### Crossover selection

Selecting a suitable cross-section with an even number of helices to be able to route a circular scaffold is the first step in the design process of a general DNA nanostructure. As illustrated in Figure 6.3, helices need to come in pairs with one pair being equal to one scaffold loop.

#### Scaffold routing

The next step in the design process is scaffold routing (see Figure 6.3c). Normally, a minimal number of scaffold crossovers is used to reduce mechanical stress in the structure. In general, all crossovers should be placed at such backbone positions of the scaffold which would allow for naturally occurring connections. Backbone position does not need to be considered if single-stranded scaffold loops are used for the passivation of blunt ends.

#### Staple routing

Staple routing and breaking is the last and most crucial design step. To prevent internal stress, crossovers of the same type and in the same direction should be placed 21 bp apart for honeycomb lattice designs, and 32 bp apart for square lattice designs. Further, crossover positions in close proximity ( $<5$  bp) of scaffold crossovers between the same helices should be avoided to minimize possible folding traps and to reduce internal stress.

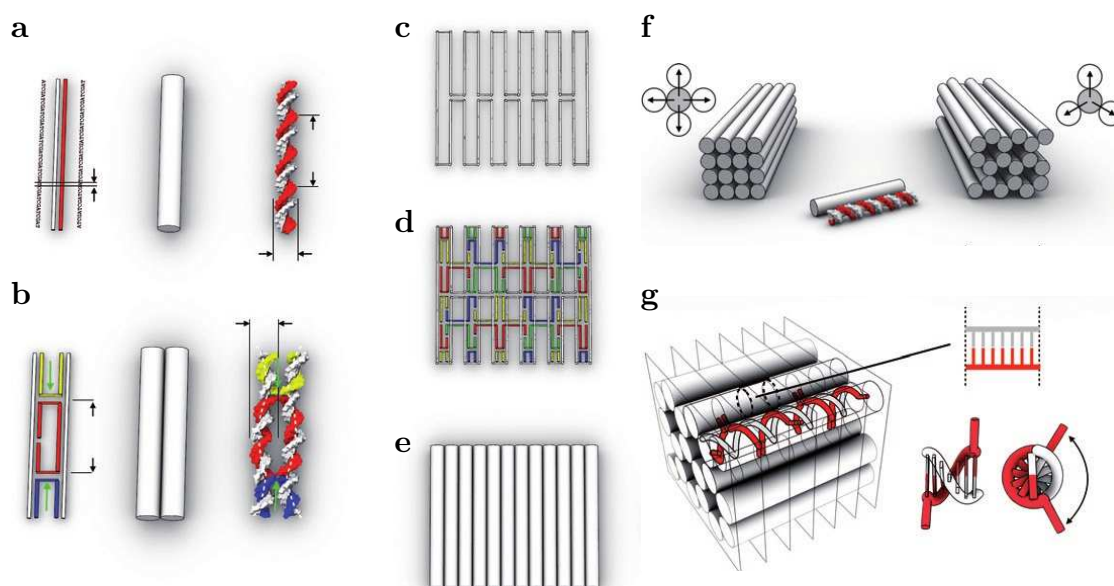


**Figure 6.3: Scaffolded DNA origami design concepts.** (a) DNA double helices are schematically represented as two parallel lines (left), as a cylinder (center) and by a detailed rendering (right). In design illustrations, the white line represents the scaffold strand and the colored line the staple strand. Whereas the two line model is used for the design schematics, the cylinder model is particularly useful for 3D illustrations. (b) Interhelical crossovers (arrows) connect two individual, adjacent DNA double-helical domains. Crossovers are not drawn in cylinder representation. (c) Scaffold routing of an exemplary single-layer DNA nanostructure. (d) A complete scaffold-staple layout, with staples colored differently. (e) Exemplary DNA nanostructure in cylinder representation. (f) A multi-layer DNA origami object with a square lattice cross-section (left) and a honeycomb lattice cross-section (right). (g) For a honeycomb lattice packing, crossovers are spaced in constant intervals of 7bp along the helical axis. This spacing complies with the natural B-form DNA twist density of 10.5 bp per turn, corresponding to an average backbone rotation of  $240^\circ$ . Images taken from [199].



The length of staples should neither be too short nor too long, and is dependent on the individual sequence and the amount of crossover facilitated. For most designs, staples containing crossovers should not be shorter than 30 bases long. Structural designs with average staple strand lengths up to 100 bases are possible [187], but long staple strands possibly reduce folding speed and might increase synthesis costs. In general, an average staple length of 40 bases to 50 bases should be targeted.

The breaking strategy of staple strands has strong influences on annealing speed, yield and quality. In general, the best practice is to keep domains intact, in particular long domains. The placement of backbone nicks can either be directly at crossover positions, leaving all segments intact, but resulting in just one crossover strand, or 3 bp to 4 bp away from crossovers. Both design strategies result in a similar folding success and structural stability.

### Twists, bents and angles

While simple sheets and bricks can serve as basic structural units, scaffolded DNA nanostructures are not limited to these designs. Varying the number of base pairs between crossovers leads to a twisted or bent structure [93]. While inherent bending can only be achieved for multi-layer structures, single-layer structures can still be used to create closed boxes [92] or curved shapes [94].

Alternation of the crossover pattern creates a local tension, which leads to a global deformation, ultimately resulting in a bent shape. Global deformation as the result of local changes is hard to predict and in general, structure prediction tools, as described in the following section, are used.

Further, introducing local tension to create bent shapes reduces the overall folding quality [187] and small bending radii are often not functional [93]. By using angled in contrast to bent structures, these problems can be circumvented and even small angles are possible as no inherent tension is required.

## 6.2.2 Computer aided design process

### caDNAno

caDNAno is a free and open source design tool for the rapid prototyping of DNA nanostructures and was developed by Shawn M. Douglas [200]. Its interface consists of a cross-section design area, in which helices can be added to

the structure, and a design area in which scaffold and staple routing can be performed. Its most versatile features include indications for the placement of crossover between neighboring helices, automatic staple routing and also automatic staple breaking. Further, caDNAno also works as a plugin for Maya, so an interactive 3D geometry can be displayed. caDNAno was used in the design process of structures presented in this thesis.

### CanDo

Estimating the resulting shape of a designed DNA nanostructure is an important but challenging task. Even for simple objects such as bricks or sheets, inherent local tension, resulting from a  $4^\circ$  discrepancy between the intended and the actual crossover position, leads to an overall right-handed twist. Further, objects with an alternating pattern of crossovers due to insertions or deletions are even harder to predict.

CanDo is a DNA nanostructure shape prediction tool using finite element based simulations to offer rapid computational feedback on the 3D structure of programmed DNA assemblies [199, 201]. This free online resource works well for twisted and bent structures, in which curvature is caused by inherent tension. However, angled structures, forced crossovers of distant parts and collision detection are not handled well or not implemented yet. Further, the electrostatic repulsion between helices is currently not modeled. CanDo was used in this thesis to process and model the designs created by caDNAno.

### 6.2.3 Attachment position for modified strands

For the functionalization of DNA nanostructures, off the shelf chemical modifications of oligonucleotides offer an efficient way to add different molecules and nanoparticles in a specific arrangement to these structures. Custom synthesized oligonucleotides are commercially available with a vast variety of modifications such as dye molecules, hydrophobic or biotin modifications. Further, click chemistry can be used to attach proteins or commercially non available modifications to DNA strands.

Two main methods for the introduction of modifications to DNA nanostructures can be distinguished.

- A normal staple strand is replaced by a modified version which directly carries the desired modification.
- A normal staple strand is replaced with a modified version of itself with an extended sequence. In this case, the modified oligonucleotide can hybridize onto the extension sequence.

While the first method is more straight forward, it requires the modifications to undergo the folding process, including the heating step, and not all modifications can tolerate high temperatures up to 90 °C without degradation. Further, introduction of modifications to different position requires the synthesis of individual modified oligonucleotides with the respective staple sequence, which is expensive compared to the synthesis of unmodified staple strands. In the second method, one modified oligonucleotide sequence can be used for multiple different attachment positions. In this case, the length of the hybridized sequence is chosen in a way to generate a thermodynamically stable duplex, typically about 20 basepairs. Modified strands can either be added directly after the folding procedure or after the purification of the folded structures from excess staple strands. If the strands are added directly after folding, one purification step can be omitted, but since unbound staple strands which carry the extension are still in solution, a higher excess of modified strands is required for successful labeling. Attachment of modifications to DNA nanostructures can be applied in proximal or distal configuration, depending on which end of the oligonucleotide is labeled (see Figure 6.4).

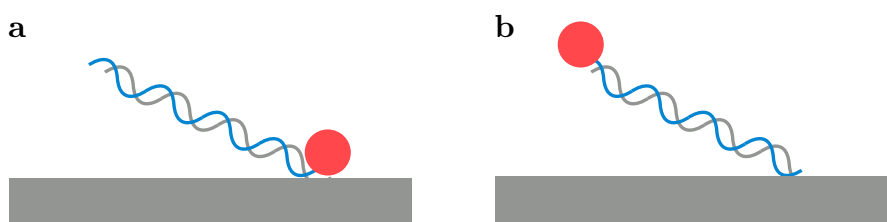


**Figure 6.4:** *Hybridization strategies for modified oligonucleotides to DNA nanoconstructs. (a) Staple strand extension in proximal configuration. (b) Staple strand extension in distal configuration.*

For positioning the modification at the correct side of a 2D nanostructure, the helical orientation of the staple strand bases at the modification positions needs to be considered. Still, for thin constructs extension threading, i.e. staple

extensions protruding temporarily from the opposite side of the DNA construct, can be observed.

In general, functional groups and strand extensions for hybridization are placed at the end of strands. Therefore, possible modification positions are pre-defined by the pattern of the staple breaks. This pattern can only be changed to a certain degree and limits the design freedom for positioning of modifications. A more flexible placement of modifications can be obtained by internal labeling of strands. The introduction of thymine spacers, acting as flexible hinges, leads to an increased mechanical flexibility of the attached functional groups, which is necessary for example for biotin or cholesterol anchors. Further, direct contact of guanine bases to fluorescent dye modifications can lead to quenching effects and should therefore be avoided [146].

#### 6.2.4 Base stacking, end passivation and polymerization

Base stacking interactions at the blunt ends of the DNA double helix lead to a strong but unspecific aggregation of DNA nanostructures into long chains along the helical axis [21]. These chains can be several micrometers long and can—after some time—lead to aggregates. The resulting 1D bandstructures often show dislocations around 75 nm. Depending on the application, this unspecific multimerization might be an advantage, if monomers are assembled into a larger supramolecular structure, or, in the case of single molecule fluorescence techniques, which typically require structure separations in the range of several hundred nanometers, a disadvantage. In both cases, unspecific multimerization should be avoided and specific and therefore controllable interactions should be used for the generation of large assemblies.

Passivating helical ends with ssDNA excludes unspecific base stacking interactions, either by using scaffold loops, i.e. remove the last column of staple strands, or by using few nucleotide long staple extensions with well defined, rarely occurring and inert sequences such as poly-T.

For the deliberate assembly of multi-component structures using non base pairing interactions, complementary shapes at the interfaces are often used [202, 203]. Further, unspecific base stacking interactions are very sensitive to buffer conditions, and changing buffers can therefore induce dynamical switching of structures [204]. In contrast to using unspecific interactions, connection strands are frequently used for the specific formation of multimer constructs [205].

## 6.3 Molecular self-assembly of DNA nanostructures

The ability to form structures following a specific design through self-assembly has made DNA to a popular building material. In general, a one-pot mixture containing all required DNA strands undergoes a thermal annealing procedure to synthesize the designed DNA nanostructures (see Figure 6.5a). However, unwanted byproducts such as aggregates, unfolded, partially folded or miss-folded structures need to be considered in self-assembly reactions [22]. Further, many factors such as structural details, the choice of co-factors, the choice of sequences, the choice of DNA concentrations and the choice of annealing protocol influence the success of the assembly process. In this section, thermal annealing reactions and the composition of scaffold and staple strands for the assembly of scaffolded DNA nanostructures will be discussed.

### 6.3.1 Thermal annealing procedure

In general, DNA nanostructures are formed in a thermal annealing process which involves cooling the sample from about 90 °C to room temperature. Folding times vary from less than an hour for simple 2D structures, to several days for densely packed 3D constructs (see Figure 6.5b). Such long annealing protocols, together with low yields, have challenged the usefulness of scaffolded 3D DNA constructs [207]. It has been found that the folding process happens within a very small temperature window, and by limiting the thermal annealing reaction only to these temperatures, assembly time can be drastically reduced and the yield can be increased close to 100 % [187]. Molecular dynamics simulations also demonstrate that folding of constructs within a small temperature window is possible, showing parallel assembly of the staple strands [208].

While almost all scaffolded DNA nanostructures assemble in trishydroxymethylaminomethane (Tris)-base based buffers containing 20 mM MgCl<sub>2</sub> or less [22, 93, 168, 187, 189, 194, 209], thermal annealing protocols and the scaffold and staple concentrations are highly dependent on the structure and application. For successful folding, a denaturation step is required at the beginning of the folding procedure, which typically implies 15 min incubation at 65 °C to 90 °C prior to the actual annealing process. In general, assembling temperatures of 60 °C to 40 °C

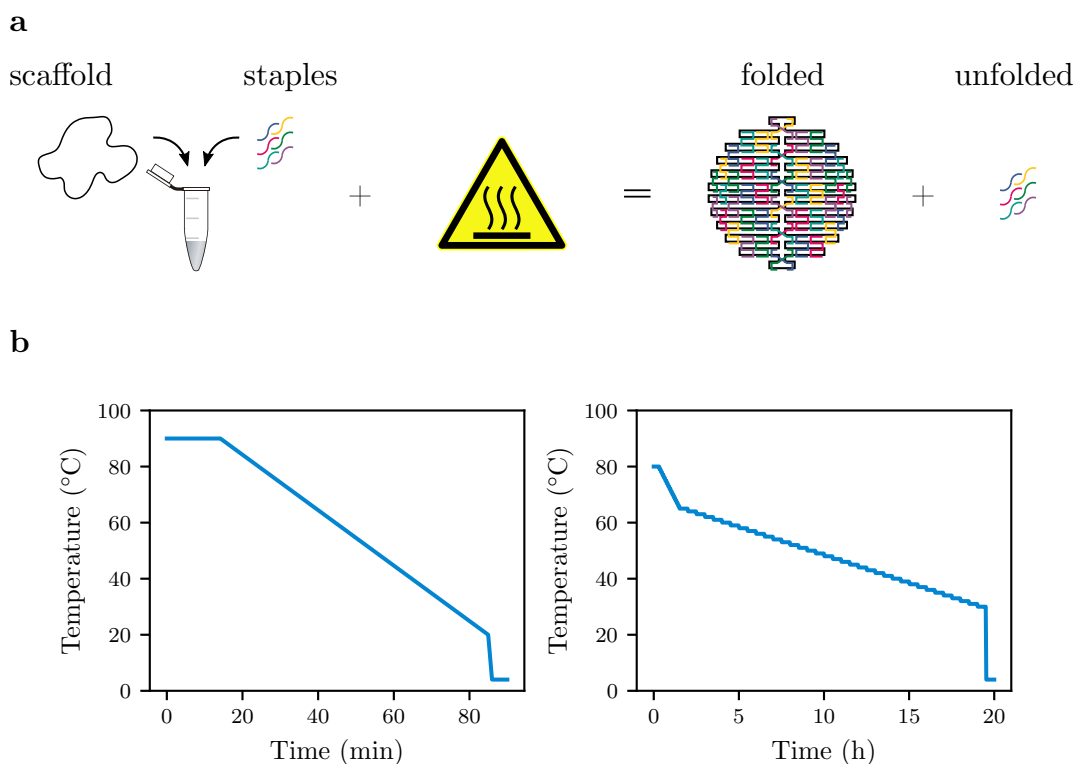


**Figure 6.5: Thermal annealing of scaffolded DNA nanostructures.** (a) Schematic of the folding process. After mixing the scaffold and staple strands with buffer containing cations, the mixture is subjected to a thermal annealing reaction. After this reaction, the products can be categorized in folded and unfolded objects. (b) Two example folding ramps are shown. A 90 min folding ramp from  $89^{\circ}\text{C}$  to  $20^{\circ}\text{C}$  with  $1\text{ min}^{\circ}\text{C}^{-1}$  (left) and a 20 h folding ramp from  $80^{\circ}\text{C}$  to  $66^{\circ}\text{C}$  with  $5\text{ min per }^{\circ}\text{C}$  and from  $65^{\circ}\text{C}$  to  $30^{\circ}\text{C}$  with  $3\text{ min per }^{\circ}\text{C}$  (right). After the annealing process the structures are kept at  $4^{\circ}\text{C}$ . [206]

have been observed. A main factor influencing folding temperatures is supposed to be staple segment stability which in turn is influenced by staple breaking, crossover density, scaffold routing/permutation, shape specific cooperativeness and internal stress [187].

Further, the secondary structure of the scaffold strand increases with decreasing temperatures, explaining why structures which fold at higher temperatures fold faster and with less byproducts. The main purpose of the initial denaturation step is to open up any secondary structure of the scaffold. In general, 15 min incubation at 65 °C are sufficient. Longer durations and higher temperatures seem to induce strand breaks in the scaffold, resulting in a reduced yield.

Screening experiments such as gel migration based assays can be used to optimize the thermal annealing protocol of a given construct. In such assays, different compositions of reaction products can easily be detected.

### 6.3.2 Scaffold and staple concentrations

Next to thermal annealing conditions, the composition of scaffold and staple strands in the folding mixture has important implications for the folding success. In general, an excess of staples of at least four fold over the scaffold concentration is used. Decreasing staple concentrations drastically increases the number of byproducts of the reaction. Further, this results in a slower assembly process, limited by the diffusion of the staple strands. In case of high scaffold concentrations, crowding effects—one staple might bind to two scaffolds at the same time—may reduce the folding efficiency.

### 6.3.3 Buffer conditions

The most commonly used folding buffer is a 1×TAE buffer (40 mM Tris, 20 mM acetic acid, 1 mM EDTA) containing 10 mM to 20 mM MgCl<sub>2</sub>. In this section, the commonly used components of typical folding buffer solutions are described.

- Tris base stabilizes the pH value around 8, an almost neutral value, which is in a suitable range for working with DNA [210].
- Ethylenediaminetetraacetic acid (EDTA) is added to buffers to avoid enzymatic digestion of nucleic acids by removing divalent and trivalent cations [211]. EDTA has a high affinity to metal ions such as Ca<sup>2+</sup> and Fe<sup>3+</sup>, but



also magnesium ions. In principle, the stabilizing properties are only effective in magnesium free buffers, e.g. when using high concentrations of monovalent salts, however, if the concentration of EDTA is much lower than the magnesium concentration, the significant part of the magnesium ions remain unbound. Since other undesirable metal ions present in the buffer have much higher affinity to EDTA than magnesium, even trace amounts of such contaminant metal ions will be chelated by EDTA and thereby replace magnesium as EDTA ligand.

- Acetic acid is often used in folding buffers as the large ions promote the migration of DNA in electric fields, while only weakly increasing the buffer conductivity which is particularly useful in gel electrophoresis. Since acetic acid can lead to impurities and is not necessary for successful folding, TAE buffer can be replaced with TE buffer [212].
- Monovalent cations, e.g. sodium ions, screen charges but do not cause attractive electrostatic interactions between DNA molecules. While most DNA nanostructures are formed in the presence of divalent cations, high concentrations of monovalent cations in the range of mM to M can screen charges enough to allow for folding [189]. Since some samples like lipid bilayers are destabilized in the presence of divalent cations, sometimes magnesium free buffers are used. Further, monovalent ions are often added additionally to magnesium to compensate for adhesion and aggregation caused by magnesium.
- Divalent cations, in particular magnesium, strongly reduce the electrostatic repulsion of neighboring DNA strands and are used to compensate these repulsion effects. Further, they are often used to induce adhesion of DNA constructs to negatively charged surfaces like glass, mica or carbon supported TEM grids.
- Trivalent cations like spermidine have similar effects as monovalent or divalent cations, i.e. mediating the electrostatic attraction of DNA strands, but at much lower concentrations. Even a few hundred  $\mu\text{M}$  are sufficient to keep DNA origami structures in a folded state [213].
- Surfactants, e.g. Tween 80 or sodium dodecyl sulfate (SDS), are used to avoid aggregation and unspecific binding by reducing the adhesion of DNA.



## 6.4 Purification methods

In general, self-assembly reactions are accompanied by unwanted byproducts. In the case of DNA nanostructures, these byproducts are aggregates, unfolded, partially folded or miss-folded structures [22]. These byproducts and residual unbound staple strands need to be removed in order to exclude interference with further assembly steps or experiments. This section will provide an overview of the purification methods to remove these unwanted byproducts.

### 6.4.1 The need for purification

The removal of unwanted byproducts and residual unbound staple strands, i.e. the purification process, is an obligatory step in the generation of DNA nanostructures. Various purification methods have been developed with different applications in mind. While some methods offer close to 100% yield, other methods like agarose-gel electrophoresis (AGE) allow for the separation of a single structural species at the expense of recovery yield.

New purification strategies and methods, such as purification by rate-zonal centrifugation offering high separability and yield with the possibility of an easy volume upscale [214], are constantly developed.

Further, purification methods can also be used for buffer exchange or for concentrating samples. For optimal results, different purification methods can be combined.

### 6.4.2 Agarose-gel electrophoresis

The most common method for the purification of DNA nanostructures is AGE, mainly because of its simplicity and grade of purity. Although it is limited to relatively small initial sample volumes and has low recovery yields. Next to purification, gel electrophoresis is a commonly used tool for quality control.

By applying a voltage potential between both ends of a gel matrix, different species inside a sample are separated by their charge and size. For DNA structures, the gel buffer usually contains a lot of cations. In this case, the applied voltages of 70 V induces enough heat to melt the gel matrix. Therefore, the gel can be placed in an ice bath to counteract the arising heat. The migration speed in the gel matrix depends strongly on the size and shape of the object, with small

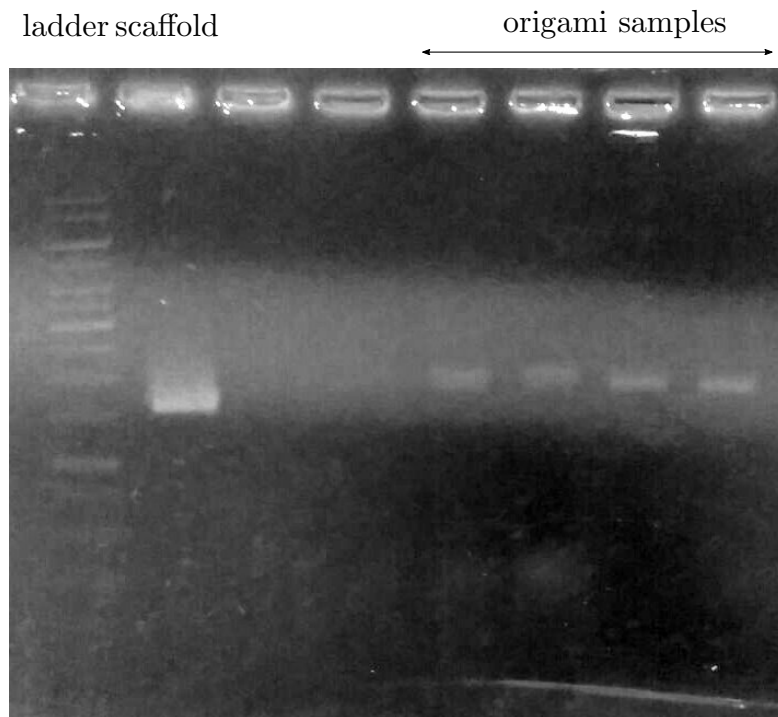


**Figure 6.6:** *Gel electrophoresis purification.* Commonly a DNA ladder, *i.e.* a molecular-weight size marker, and the scaffold strand are loaded together in the gel for comparison with the DNA nanostructure sample. After gel-staining using *EtBr*, a UV lamp is used for visualization.

and compact objects migrating faster compared to larger structures. The migration speed for DNA origami structures is determined by the geometrical shape. Although folded structures are comprised of about twice as many bases, these compact objects will run faster compared to the unstructured scaffold. At the same time, only partly folded objects will run slower compared to the scaffold. Hence, the scaffold strand is often used as a reference point in AGE.

Different methods for labeling the DNA nanostructures in the agarose-gel include using intercalators such as EtBr, which bind DNA and exhibit a strong fluorescence in their bound state, or the direct labeling with fluorescent dyes (see Figure 6.6). While the usage of EtBr allows the simple and direct visualization of DNA samples on a UV screen, it contaminates the sample with molecules which are able to deform DNA [188]. Further, the quantum yield of intercalators strongly depends on their target, heavily favoring dsDNA compared to ssDNA. In contrast, for the direct labeling using fluorescent dyes, the gel slice can only be performed in direct comparison and alignment of the scanned image with the gel. Using a scalpel, the desired band can be extracted from the gel and can be processed by different methods, e.g. Freeze & Squeeze filtration or electrocution. To optimize purification yield and concentration, a narrow and accurate cut is desirable. EtBr or dyes can influence absorbance measurements and absorbance values need to be corrected for this influence. Further, heat generation during the electrophoresis process can impact DNA nanostructure quality. Running the agarose-gel on ice can counteract the build up of heat.

Protocols can be found in the Materials and Methods section 9.

### 6.4.3 Spin column filtration

Purification through spin column filtration is mainly used to separate 2D DNA nanostructures from excess staple strands [21]. Only when the assembly yields of 3D DNA nanostructures increased through recent developments [187, 189], gel electrophoresis was replaced by spin column filtration as the method of choice for these structures [168, 194, 209].

Spin column filtration uses filter units of 100 kDa, which are small enough for most DNA nanostructures and allow for the effective removal of staple strands (see Figure 6.7). Using smaller filter sizes leads to clogging of the filter pores caused by the staples. Several purification rounds are necessary to remove most excess staples.

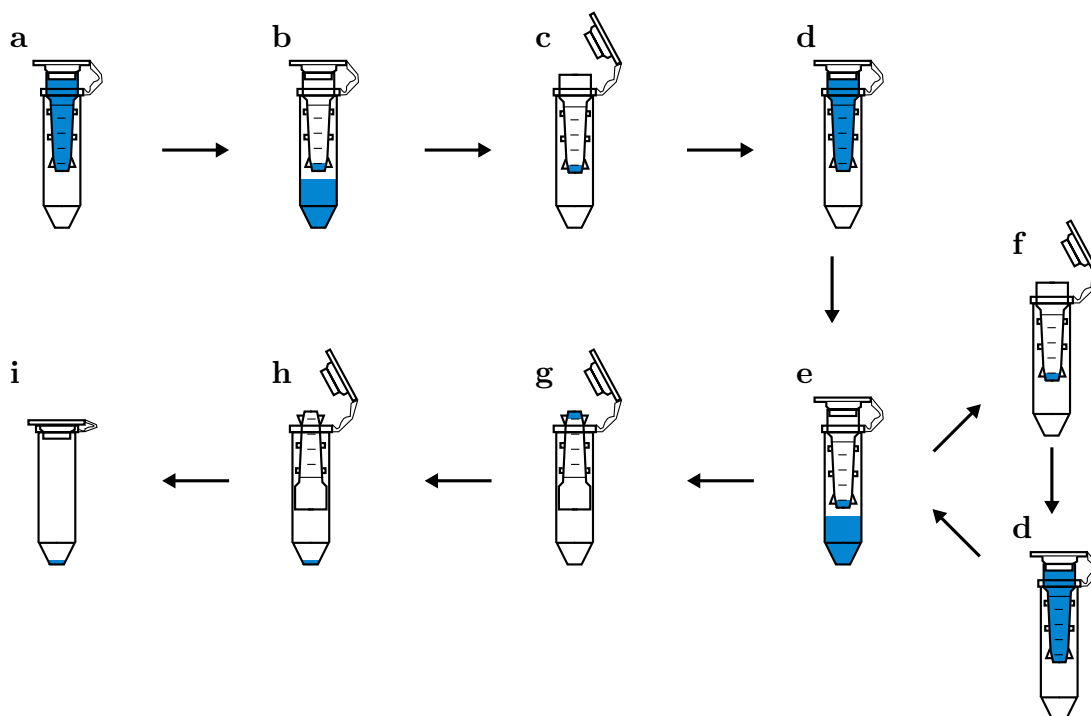


**Figure 6.7: DNA origami purification using Amicon Ultra 100K centrifugal filters.** (a-c) Equilibration with the purification buffer containing low amounts of  $MgCl_2$ . The filter is filled with  $500\ \mu\text{l}$  purification buffer and centrifuged at  $15\ 000\ g$  for  $10\ \text{min}$ . The solution that passed the filter is discarded. (d-f) The purification process itself can be repeated several times, depending on the desired purity. The sample is loaded into the filter and is centrifuged for  $10\ \text{min}$  at  $15\ 000\ g$  and  $4^\circ\text{C}$ . Again, solution that passed the filter is discarded. (g-i) For sample recovery, the filter is flipped and placed in a new tube and spinned for  $2\ \text{min}$  at  $1000\ g$  and at  $4^\circ\text{C}$ . After recovery of the sample, the filter unit can be removed. Illustration adapted from [215].

If suitable buffers are used, spin column filtration gives relatively high yields. Further, it is an easy to use method in contrast to gel electrophoresis and has a high reproducibility. Spin columns can also be used for buffer exchange and for the concentration of samples. Still, spin column filtration offers only staple strand removal and cannot separate misfolded from correctly folded structures. Further, centrifugation can lead to sample aggregation if the centrifugation speed is too high. In general, high concentrations and volumes should be used to keep the material losses at the filter membrane minimal.

#### 6.4.4 Polyethylene glycol precipitation

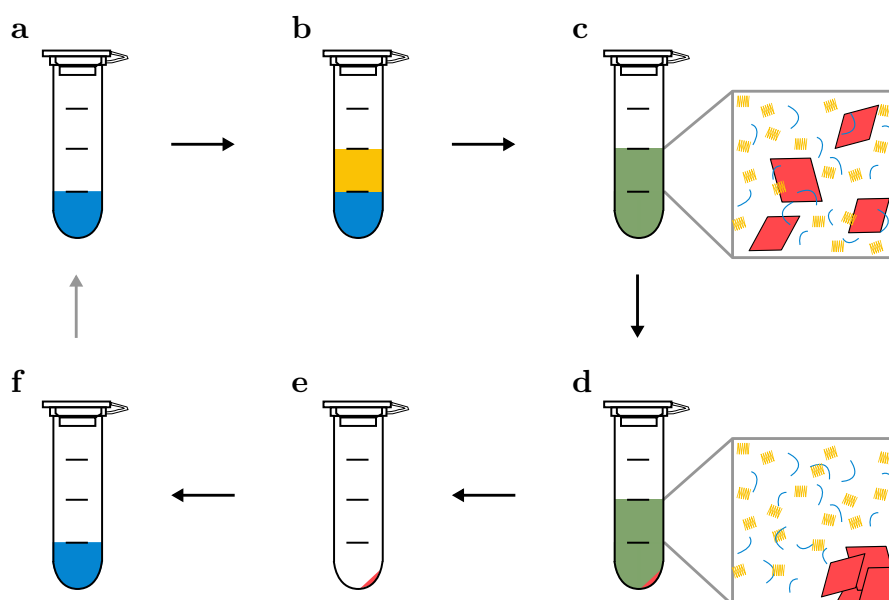


**Figure 6.8: DNA origami purification using PEG precipitation.** (a) Add the sample to a fresh tube. (b-c) Mix sample 1:1 (vol) with PEG purification buffer. (d) Spin for 25 min at 16 000 g. Mark tube position for better localization of the pellet. (e) Carefully remove the supernatant without touching the pellet. (f) Resuspend in the desired buffer. This process can be repeated if necessary. Illustration adapted from [215].

PEG precipitation is a suitable method for purifying greater amounts of DNA nanostructures at a lower cost compared to gel electrophoresis and spin filtration. While already being used in the biochemical field, this method was first used for

DNA nanostructures for creating a high concentrated sample of nanotubes for NMR alignment of membrane proteins [133].

In this purification method, the DNA sample is mixed with PEG precipitation buffer and centrifuged for the separation of the structures from the excess staple strands (see Figure 6.8). Yield and selectivity of this process are dependent on PEG concentration, buffer conditions, temperature, as well as speed and duration of centrifugation.

PEG precipitation is mainly used for the removal of excess staple strands with the advantage of high yields and concentrations at low costs as well as low time expenditure. However, it is not the method of choice for the separation of different folded species. Further, residual amounts of PEG can be present in the sample after this process.

### 6.4.5 Purification Conclusion

	Agarose gel electrophoresis	Amicon spin filtration	PEG precipitation
Volume [μl]	5 - 1000	50 - 100 500 - 2000	≤ 50
$c_{\text{initial}}$ [nM]	gel and imager dependent	20 - 50	arbitrary
Relative $c_{\text{final}}$	40% ± 10%	161% ± 11%	adjustable
Yield	34% ± 7%	88% ± 3%	97% ± 2%
Duration [h]	2	3	0.5
Purity	desired fraction	staple separation	staple separation
Side products	agarose	none	PEG
Labeling	EtBr fluorophores	none	none
Reproducibility	difficult filter dependent	easy filter dependent	moderate
Buffer exchange	running buffer	low MgCl <sub>2</sub> buffer	various buffers
Concentratability	no	yes	yes

**Table 6.1:** *Comparison of different purification methods for DNA origami. The main characteristics of the three predominant methods in DNA origami purification. Table taken from [215].*

Agarose gel purification, spin filtration and PEG precipitation are the three main methods for the purification of DNA nanostructures. Each method has its advantages and disadvantages, and none fulfills all possible requirements. Table 6.1 comprises the characteristics of these methods in order to select the most suitable method for a desired task.

While all presented methods remove excess staple strands, only gel purification can remove unwanted reaction byproducts and guarantee absolute folding correctness. Still, purification yield is relatively low for this method. PEG precipitation is the method best suited for obtaining high yields. On the downside, residual amounts of PEG in the sample may hamper experiments. If this is the case, filter purification is the method of choice.

The subsequent use of purification methods makes it possible to combine the advantages of each individual method. First, an agarose gel purification can be performed in order to obtain a single folded species. Sequential PEG precipitation then allows for an increase in sample concentration and for the removal of residual amounts of agarose, which is not precipitating.





# Chapter 7

## A nanostructuring DNA origami platform

DNA-based nanostructures have—besides their biological compatibility—a vast myriad of properties, making them interesting objects for a wide field of biological and physical applications. Thereby, these synthetic objects may imitate functionalities known today only from natural macromolecular complexes. In particular, the possibility to modify specific staple strands to precisely position modifications allows for the generation of new synthetic structural combinations. Still, the fact that DNA origami nanostructures are limited to sizes in the order of 100 nm, together with the problem of specific positioning of single structures in an ensemble, limit the production of widespread hierarchical arrangements with addressability on the nanoscale. However, the combination of molecular self-assembly techniques with polymerization or electron-beam lithography can be used to generate patterns at a higher level. Such nanosystems are described in part IV.

### 7.1 Introduction

DNA nanostructures offer control over the position of each single staple strand. Therefore, they are a versatile tool for the precise arrangement of small molecules [216–218], proteins [107, 219, 220] or nanoparticles [102, 192]. Here, we report the design of a DNA origami platform of  $60\text{ nm} \times 45\text{ nm} \times 2\text{ nm}$ , featuring up to 44 engineered capture sites for a target protein at the top side at well-defined

positions. The number of capture sites, their functionalization, their orientation and their distance can be adjusted at will. At the bottom side (opposite of the protein capture sites), the employed DNA rectangles can be functionalized with cholesterol moieties which serve as membrane anchors. The DNA constructs adhere to a lipid bilayer mediated by the cholesterol anchors and serve as mobile platforms for protein recruitment. The diffusion behavior of this platform on a lipid bilayer system was investigated using fluorophore modifications. Further, different possibilities for adding functional modifications have been studied.

The coordinated rearrangement of receptors, adhesion molecules and signaling proteins in the immunological synapse plays a key role in the initiation of the immune response. Despite extensive studies, the quantitative molecular details of complex formation, as well as the kinetics, are still poorly understood. Here, DNA origami are decorated with recombinant and site-specifically labeled TCR $\beta$ -reactive single chain antibody fragment (scFv) and embedded on planar glass-supported lipid bilayers, which harbors co-stimulatory molecules and adhesion proteins. This system is used to closely imitate the APC, allowing to re-organize the TCR in living T cells according to the pattern given by the scFv template on the origami. This system can be used to address and answer central questions in T cell immunology: the role of TCR clustering in T cell activation, the unknown composition of protein complexes in the T cell plasma membrane, as well as the mechanisms of their cohesion.

This chapter is structured as follows. At first, the initial concept of a DNA origami platform is introduced with the general design and synthesis of the platform, followed by a thorough analysis of the obtained structures. Then, as a proof of concept, the diffusion behavior of the platform on a lipid bilayer is described. Finally, different possibilities for the attachment of functional modifications are discussed and first experimental results for the application in T cell biology are presented.

## 7.2 DNA platform design and synthesis

### 7.2.1 DNA templated design

The DNA nanostructure was designed to control the position and the number of ligands on a rigid DNA platform interacting with cells (see Figure 7.1). The

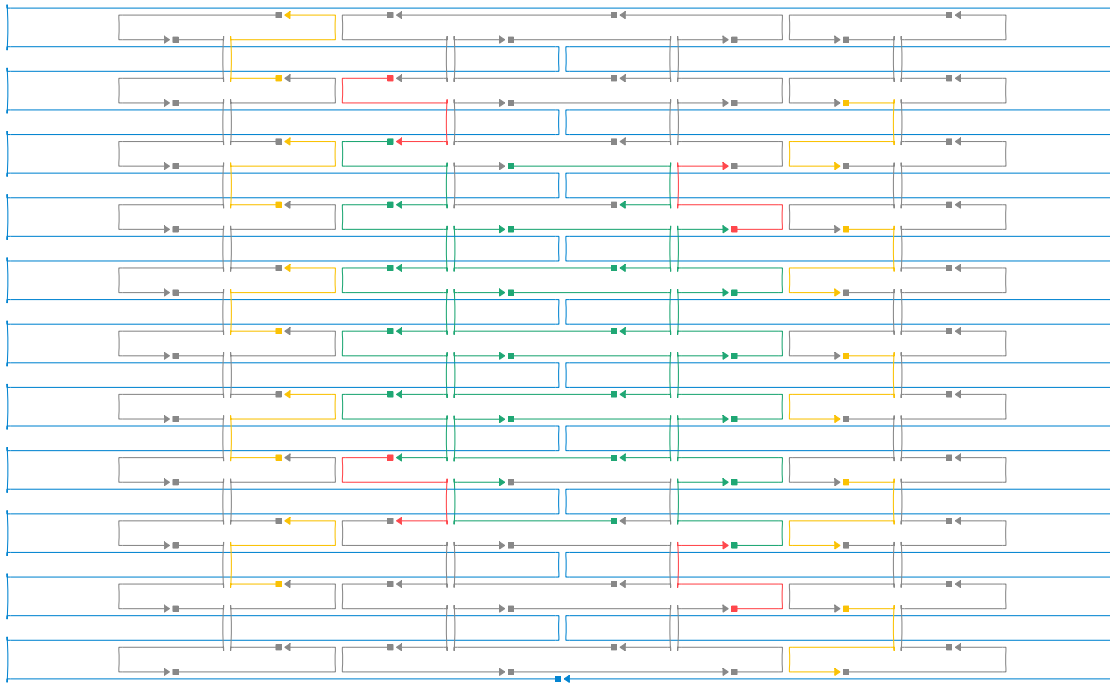


**Figure 7.1:** *Design of the rectangular DNA origami platform.* A schematic representation of the lattice comprising 22 parallel dsDNA helices. Each line represents a single DNA strand with the colors indicating the function of each strand in the design. The blue strand is the scaffold, gray strands are general staples, yellow strands can be extended with the Z'-sequence for the attachment of cholesterol strands, red strands can be extended with the X'-sequence, mainly used for the attachment of fluorophore modifications and green strands can be extended with the Y'-sequence to serve as attachment sites for a different modification, e.g. another fluorophore or biotin. A square and a triangle are used as markers for the 5'- and the 3'-end, respectively, resulting in an arrow indicating the 5'-to-3' direction of each strand.

spatial registry of staple strands in DNA origami makes them a suitable candidate for this task. Using the software caDNAno [200], the platform was designed to assemble as 22 parallel dsDNA helices of the same length in a single plane and comprising a total of 10 065 nt with a molecular mass of 3.3 MDa. These nucleotides form a total of 2816 basepairs, while 704 unpaired nucleotides form loops connecting two helices, and 3729 unpaired nucleotides result from the scaffold remainder. Flexible loops at the ends of the helices are unpaired in order to prevent aggregation by blunt-end stacking [202]. Synthesis of the platform was based on templated molecular self-assembly, in particular it is a modification of one of the DNA origami structures presented in Rothemund's original publication [21] with the M13mp18 scaffold, a 7249 nt long single stranded, circular viral DNA strand derived from the M13 bacteriophage (see section A.3) and 88 shorter staple strands (see section A.2). By exchanging specified staple strands with an extended version of themselves with a unique binding sequence added, desired positions were selected to serve as binding sites for cholesterol moieties or other ligands (see Figure 7.2). Depending on the specific design, different staple strands end at different sides of the platform. The batch-platform offers 20 ligand attachment sites together with four additional fluorophore attachment sites (see Figure 7.2d), whereas in the individual-platform design the number of available ligand attachment sites is reduced to four (see Figure 7.2c). We have taken care that in this design the cholesterol modifications are placed on the opposite side of all other modifications. A poly-T region serves as a spacer and at the same time as a flexible hinge region. Sequences of the different binding region can be found in Table A.1.

## 7.2.2 Model generation

The online platform CanDo [199, 201] was used to predict the 3D equilibrium structure of the designed DNA origami platform based on the caDNAno file. The results of this analysis, shown in Figure 7.3, give the anticipated result of a simple DNA platform of the right dimensions. However, the side view of the structure shows bending caused by internal strain. This results from a difference in the helical twist of B-form DNA of 10.4 bp/turn and in the helical twist of the designed nanostructure of 10.67 bp/turn. This bending effect can be reduced by introducing deletions at specific positions, e.g. deleting one base from every third column of the staples [221, 222]. Further, the mechanical stability of the

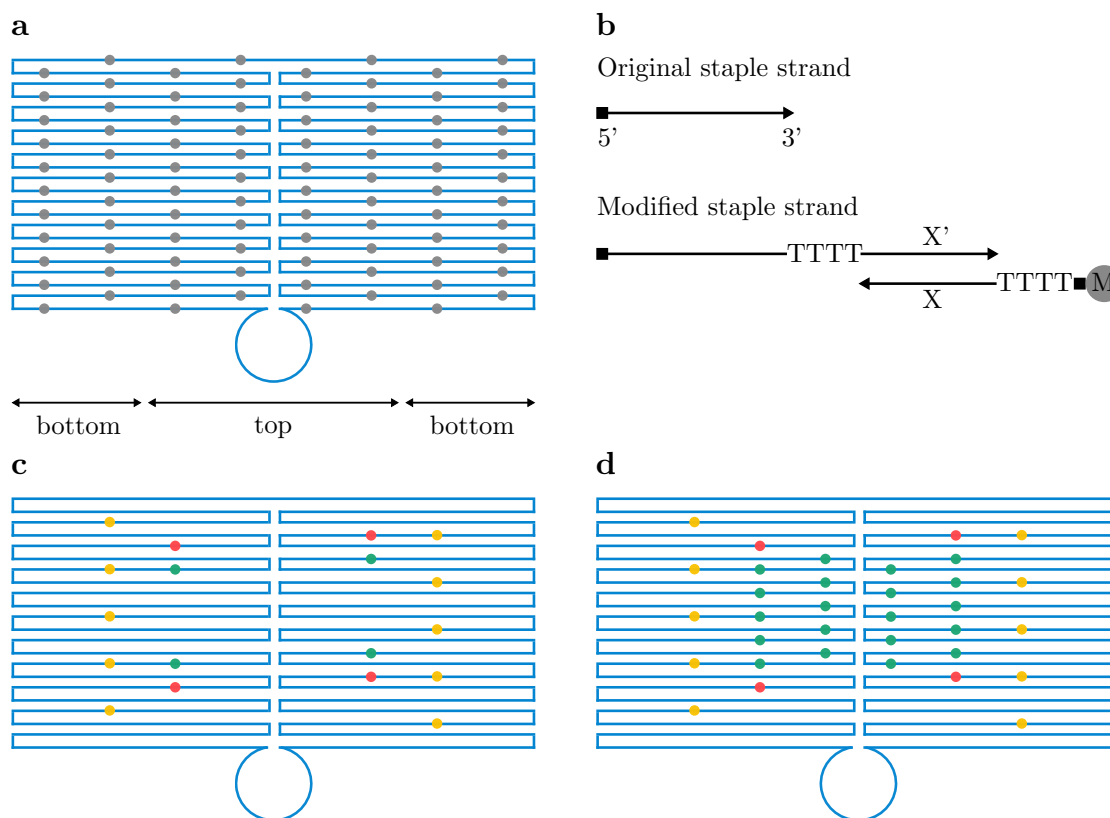


**Figure 7.2: Possible positions of modifications on the DNA origami platform.** (a) A schematic representation of the DNA platform with the scaffold strand in blue and all start and end positions of staple strands marked in gray. These positions may be located at different sides of the platform due to the helical nature of dsDNA. (b) For external labeling, a binding sequence is attached to the staple strand to hybridize a complementary labeling strand with the respective modification (M). (c) Schematic of the individual-platform with the chosen positions for modifications being indicated. Colors indicate different available modifications (yellow = cholesterol, red = fluorophores, green = functional modification). (d) Schematic of the batch-platform. In comparison to the individual-platform, 16 extended strands (green) are added in this design to form a cluster of functional modifications.

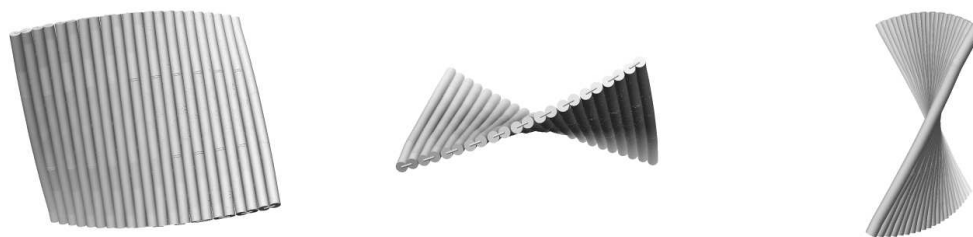


**Figure 7.3: Bending of the DNA origami platform.** Top and side views from the DNA origami platform obtained from CanDo simulations showing its bent shape.

submitted structures in solution is also calculated by CanDo and is found to be sufficient for all planned experiments. Therefore, the design was chosen to be experimentally implemented. The submission parameters can be found in the Methods section 9.1.

### 7.2.3 DNA platform synthesis, purification and labeling

#### Folding

Following theoretical confirmation of the design, the DNA origami platform was folded in a one-pot reaction with high yield and few byproducts, such as higher-molecular-weight aggregates. The folding procedure followed closely the protocol described by Schmied et al. [206].

To facilitate the repeated production of the DNA origami platform, a master mix, i.e. a mix that pools different staple strands into one tube, was used. In particular, four master mixes of oligonucleotides—according to the color coding in the design—need to be combined for the folding mixture. These master mixes are a mix of all unmodified oligonucleotides and three mixes with the three individual groups of oligonucleotides with the same binding sequence attached to them. By keeping them in separate master mixes, it is possible to produce the DNA platform with either all modifications or just with some. The folding mix is prepared in a PCR tube and placed in a PCR machine to run the specific folding program. For details on the folding mix and the folding procedure see

section 9.2.

### Purification

Following the folding procedure, the DNA origami structures need to be separated from the excess of staple strands. Especially for applications on surfaces other than supported lipid bilayers, unspecific binding of strands with fluorophore modifications, which are not attached to the DNA structure, would result in a high background signal and thus impair measurements. General principles of purification methods were already presented in section 6.4. Although the use of centrifugal filters has proven to be a fast and robust purification method, it causes high material losses. PEG precipitation on the other hand has the advantage of high yields and concentrations. Still, DNA nanostructures purified with PEG precipitation often exhibit some kind of smear in the agarose gel (see also section 7.3.1). However, the reason for this seems to be an interaction of the PEG with the agarose gel, as analysis of the DNA origami structures on lipid bilayers with the AFM showed correctly folded structures and they further showed the expected diffusion behavior. Therefore, PEG purification was used unless stated otherwise. For purification protocols see section 9.2.3.

### Labeling

An external labeling strategy is applied to attach modifications to the DNA origami platform, where modified labeling strands are hybridized to the nanostructure, which presents the complementary binding sequence. For adding cholesterol moieties to DNA nanostructures, external labeling is inevitable, as an internal labeling strategy would lead to clustering of the assembled nanostructures in solution. The labeling strands used in this thesis are listed in Table 7.1. For details on the labeling protocol see section 9.2.4.

## 7.3 Characterization

A thorough characterization of the obtained DNA origami platform was performed to ensure proper folding and subsequent behavior. This includes an analysis of the platform itself using gel electrophoresis and AFM measurements,

Modification	Name	Sequence
Dy549	Dy549-4T-X	/Dy549/TTTTCTTCTGTCTATCTTGGC
Abb635	Abb635-4T-X	/Abb635/TTTTCTTCTGTCTATCTTGGC
Abb635	Abb635-4T-Y	/Abb635/TTTTACATTAGGCTAGTCCAC
Cholesterol	Z-TEG-Chol	GGCTAAATATGCTAGGACTCT/CholTEG/
Biotin	Biotin-TEG-Y	/BiotinTEG/TTTTACATTAGGCTAGTCCAC
Click chemistry	Click-TCO-PEG-Y	/TCOPEG/TTTTACATTAGGCTAGTCCAC

**Table 7.1:** *A listing of the labeling strands for the DNA origami platform used in this thesis.*

as well as an analysis of platform mobility on lipid bilayer systems. Unless stated otherwise, the unmodified platform is used.

### 7.3.1 Agarose gel electrophoresis analysis

AGE is not only used for the purification of DNA nanostructures, but can also be used to ensure a proper folding state of the DNA origami structure. Figure 7.4 shows two exemplary gels for the folded DNA platform containing two standard references, a ladder (GeneRuler 1kb DNA ladder), i.e. a mixture of DNA strands with various length, and the scaffold strand. In each gel three sample bands are shown. In both cases, the unpurified platform has been loaded in the gel and the bands consists of a slow migration species, containing the folded structures, and a fast migrating species, containing excess staple strands. The DNA platform purified using centrifugal filters shows a band at the desired position, but this band is either barely visible (Figure 7.4a), or—as most of the time—not present at all (Figure 7.4b). This low yield after spin column filtration is consistent with origami density observations on lipid bilayer systems. For this reason, the DNA origami platform was purified using PEG precipitation. However, AGE of PEG purified structures was inconclusive as these bands exhibit stripes and smears (see Figure 7.4b). Still, subsequent analysis of the DNA platform using atomic force microscopy showed the correctly folded object with a low number of byproducts. Further, analysis on lipid bilayers showed a high DNA origami density and the expected diffusion behavior. For details on the AGE protocol see section 9.3.1.



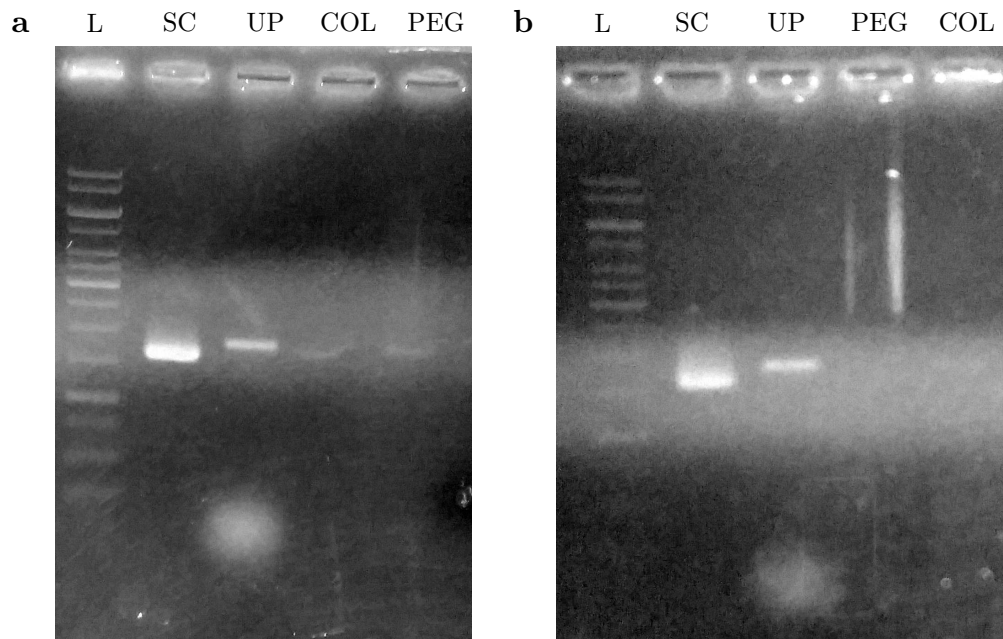


**Figure 7.4:** *Gel electrophoresis of the DNA origami platform.* In both gels, a DNA ladder (*L*) and the scaffold strand (*SC*) are loaded as reference markers. Next to the unpurified (*UP*), two types of purified DNA platforms are shown, after spin column filtration (*COL*) and after PEG precipitation (*PEG*). In both cases, the gel was run for 2 h at 70 V and room temperature.

### 7.3.2 AFM analysis of DNA origami platform

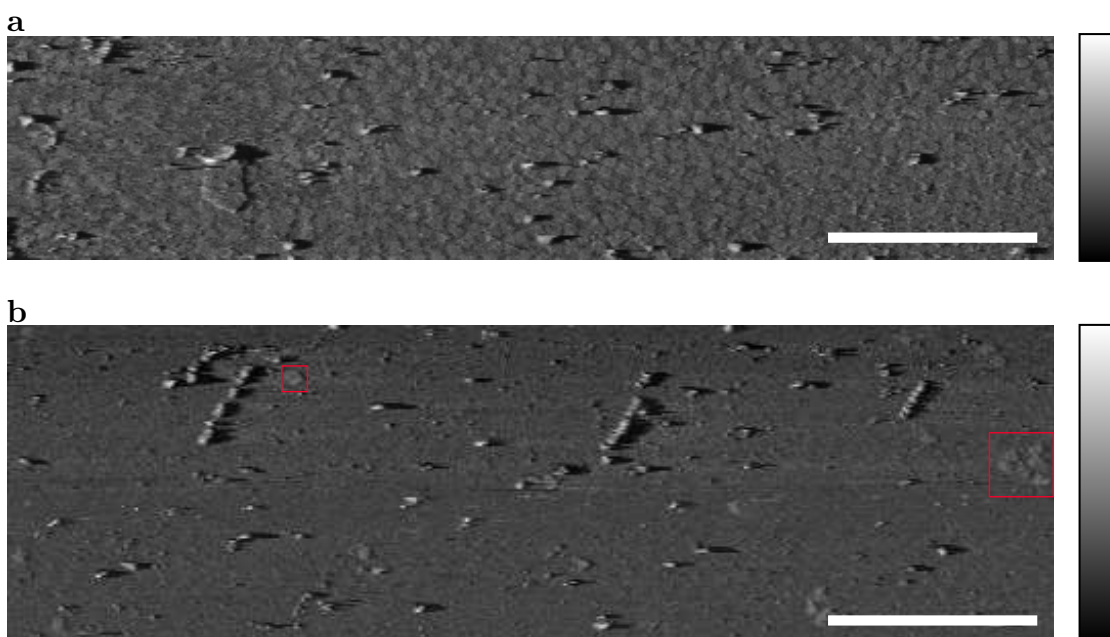


**Figure 7.5:** *AFM overview images of DNA platforms on mica. (a) The lock-in phase image shows a high density of homogeneously formed DNA platforms measured in liquid (AFM imaging buffer, see methods section 9.3.2). Structures clearly higher than the origami structures are thought to be either dirt or accumulations of several folded or partly folded DNA origami structures. (b) A lower density of DNA origami platform allows for singling out individual platforms for a separate scan. Again, origami stacks significantly higher than the single origami platforms can be seen. A single origami platform, as well as a cluster of origami are highlighted using red boxes. Altitude scale in both images is 0 deg to 18.5 deg. Scalebar is 1  $\mu\text{m}$ .*

AFM is a suitable tool for imaging two dimensional DNA origami structures, as it gives a high resolution image with relatively simple sample preparation and by measuring biological samples in a liquid environment, it allows for a native environment [223] (compare section 3.2).

In general, DNA based nanostructures are applied to a freshly cleaved mica surface for AFM imaging, since mica gives an atomically flat substrate over large areas. Although being heavily used, the phenomenon leading to the adsorption of DNA on these surfaces is not fully understood yet. It is postulated that DNA

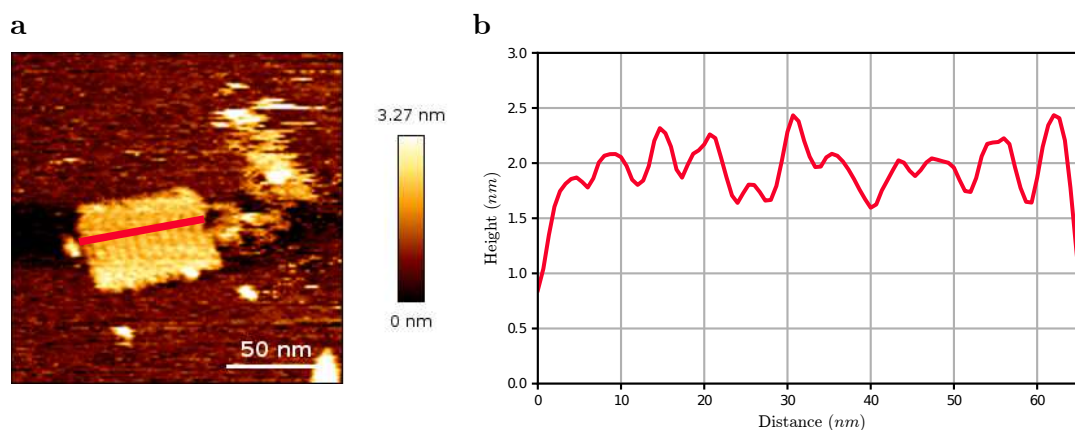


**Figure 7.6:** *AFM image of a single DNA origami platform on a mica surface measured in liquid. (a) The DNA origami platform forms correctly with the desired dimensions. The unpaired remainder of the scaffold strand can be seen on the right. (b) A linescan along the red line is depicted in panel a. The substructure shows eleven peaks, each corresponding to two neighboring DNA double-helices.*

can bind to mica surfaces by sharing counterions [224]. The interaction of divalent counterions such as  $\text{Mg}^{2+}$  with the mica surface and the DNA leads to a net attraction, whereas the interaction with monovalent ions does not lead to adsorption. Imaging quality depends strongly on the used AFM tip and its quality. High quality tips enable imaging of single staple strand defects in an origami structure. For details on sample preparation and AFM imaging parameters see section 9.3.2.

Figure 7.5 shows a typical AFM image in tapping mode with the lock-in phase being depicted. The overview image shows many similarly folded DNA origami structures on an atomically flat mica surface. The DNA structures are flat on the surface since this position maximizes the contact area between the DNA structure and the mica surface, thereby being the energetically favorable state. A high density of DNA origami structures on the mica surface (Figure 7.5a) gives the possibility to examine many structures at once, thereby getting a general overview of the obtained dimensions, the yield and the folding state of the DNA origami structure. Only a low density of DNA structures on the mica surface (Figure 7.5b) allows to zoom in on a single DNA origami structure and to image specific substructural features.

A single rectangular DNA origami structure is shown in Figure 7.6a with an approximate size of  $60 \times 45 \times 2$  nm. The substructure formed by the individual helices can be clearly seen. The remainder of the scaffold strand attached to the origami structure can be seen on the right side of the image, since not all bases of the scaffold strand are used to form the DNA origami structure. In principle, the scaffold can be cut using restriction enzymes with several restriction sites located in the unused part of the scaffold strand. The DNA origami structure consists of 22 helices which leads to 11 peaks in the origami structure, which can be seen in the line scan in Figure 7.6b.

AFM imaging shows that most of the DNA origami structures are folded correctly according to the design presented in section 7.2.1, and are ready to be used in further experiments.

### 7.3.3 Diffusion analysis of DNA structures

To generate a mobile interaction platform, the DNA origami structure can be attached to a SLB. Thereby, these nanostructures can artificially mimic the function of membrane-associated proteins. See also section 5.5.2 for more information on the attachment of DNA origami structures on lipid bilayer systems. In order to characterize the behavior of the DNA platform, it was attached to a lipid bilayer using cholesterol moieties, and labeled with two different fluorophores. Using this system, colocalization analysis as well as diffusion analysis were performed.

The DNA platform modified with ten Z'-strands suitable for hybridizing to the Z-TEG-Cholesterol anchor, and with 9 X'- and 9 Y'-strands suitable for binding two different fluorophores, AbberiorStar635 (STAR635) and Dye 549 (DYE549), was used in these experiments. In contrast to the platform described earlier, the fluorophores in this version are located in the leftmost and rightmost columns (see Figure 7.7d). After synthesis, the structures were purified using PEG precipitation, labeled with the fluorophore strands and purified again. Following this process, they were added to a POPC bilayer and imaged directly after washing. As a control experiment, DNA origami platforms folded without the attachment sites for the cholesterol anchor were incubated. Also, DNA origami platform with the attachment sites were incubated on a bilayer without cholesterol strands. In both cases, no signal of the DNA origami platform could be detected, and it is assumed that the DNA origami platform was unable to bind

to the bilayer and was removed in the washing step. For a detailed description of the sample preparation, the measurement parameters used and the data analysis see section 9.3.3.

### Colocalization

Colocalization analysis (see also section 3.1.5) was performed in order to check for labeling efficiency and to distinguish fully formed DNA origami structures from unbound fluorophores or fluorescent dirt. Only if signals are present in both fluorophore channels, they are considered to be a DNA origami platform. Further, only these colocalized signals were used for SPT to obtain diffusion parameters.

For the colocalization analysis, the sample was simultaneously illuminated by the red and the green laser. All single molecule signals of an image were localized using the 3D-DAOSTORM algorithm [225], and the corresponding regions of interest (ROIs) in both color channels were selected (see Figure 7.7a).

Chromatic aberration can pose a problem when doing multi-color single molecule microscopy. In order to correct for abbe rations, an image of beads is recorded, then the localizations of the two channels are matched and an affine transformation for the x and y coordinates is determined.

After transformation of one color channel to correct for chromatic abbe rations, the positions of all single molecule signals in one channel are matched with all positions of all single molecule signals in the other channel. An exemplary overlay of the DNA origami platform on a POPC bilayer is shown in Figure 7.7b.

In general, more signals in the green channel (DYE549) are present compared to the signals in the red channels (STAR635). The reasons for this can be a reduced labeling efficiency of the STAR635-strand compared to the DYE549-strand, or differences in the characteristics of the different fluorophores such as photobleaching. Further, it is possible that these signals are not DNA origami platforms, but fluorophores which have not been removed in the washing step or dirt on the lipid bilayer. In principle, it is possible that some DNA origami platforms are not detected at all, either by having no fluorophores attached to them or by only having inactive fluorophores attached. However, this scenario seems rather unlikely.

For colocalization analysis, the arithmetic mean of all colocalized signals of the first 15 recorded frames of each tracking movie were considered. After pro-



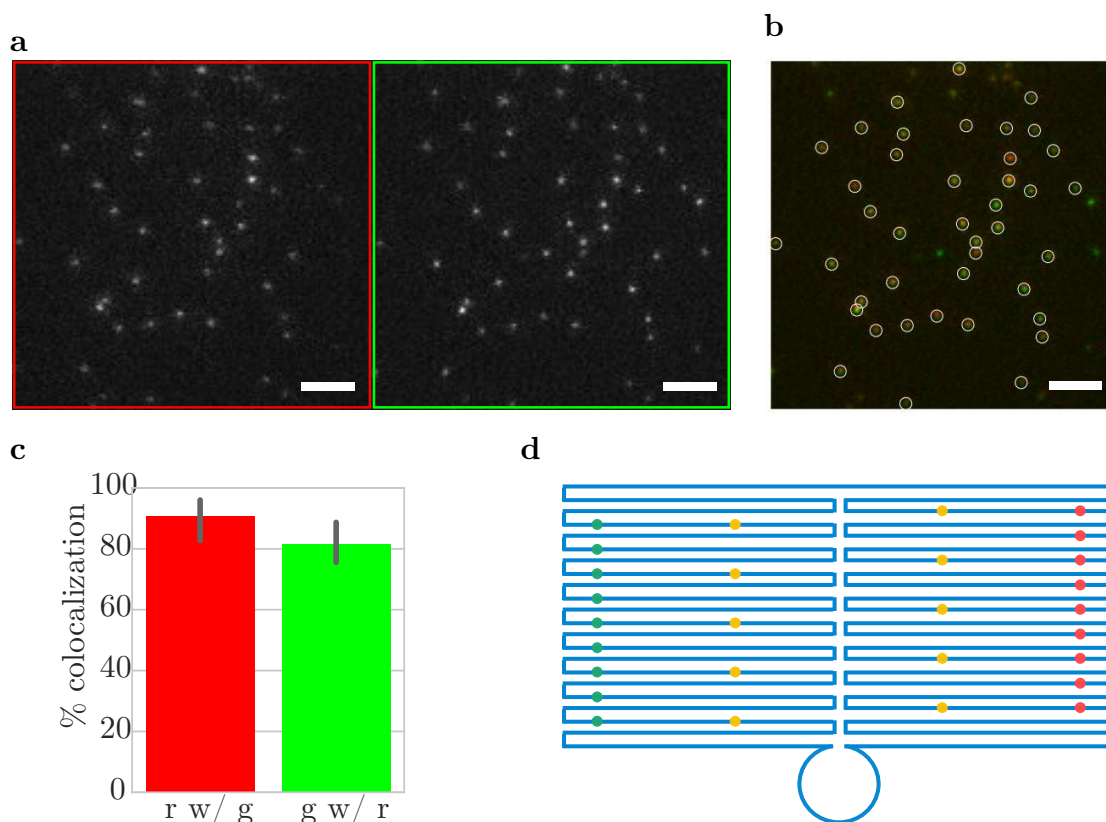


**Figure 7.7: Colocalization analysis of the DNA origami platform.** (a) A fluorescence image of single DNA origami platforms diffusing on a POPC bilayer that are simultaneously excited by the red and green laser. The signals from the two channels are separated spectrally and spatially using appropriate filter sets and the optosplit, respectively (red and green box). (b) In the overlay, red and green signals correspond to the signals from the two channels shown in panel a. Each determined colocalization is highlighted with a white circle. In the shown experiment 98% of all red signals colocalize with a green signal and 80% of all green signals colocalize with a red signal. Scalebars are  $1\ \mu\text{m}$ . (c) Percentage of colocalization from the red channel with the green channel, and vice versa, were determined from three independent experiments.  $r\ w/\ g: 90.85 \pm 6.36\%$ ,  $g\ w/\ r: 81.42 \pm 5.46\%$  (mean  $\pm$  SD). (d) A sketch of the modified DNA platform with colors indicating different modifications (yellow = cholesterol, red = STAR635, green = DYE549).

longed illumination, more fluorophores undergo photobleaching and the number of colocalized platforms drops. Three independent experiments are included in the analysis.  $90.85 \pm 6.36\%$  of all red signals are colocalized with a green signal. Since there are more signals in the green channel than in the red channel, only  $81.42 \pm 5.46\%$  of all green signals are colocalized with a red signal. In principle, this could be because these signals do not come from DNA origami platforms. However, the diffusion behavior of these unpaired signals is similar to the colocalized signals. Therefore, it is plausible that this imbalance is caused by labeling issues.

### Single particle tracking

MSD analysis is a widely used tool in biophysics and can be used to determine the diffusion constant  $D$  (see also section 3.1.5). To select for the DNA origami platform, only colocalized signals were considered in the analysis. First, the tracks for each pair were identified. Then, the mean square displacement and the standard error for each lag time were calculated. By fitting a linear function to the timelag-vs.-MSD graph, the diffusion coefficient and the positional accuracy were calculated. Only the first two lag times were used for fitting.

Figure 7.8a shows an exemplary track of a single DNA origami platform attached to a POPC bilayer in both color channels. The track in the green channel is slightly longer than the track in the red channel, since the red signal undergoes photobleaching earlier than the green signal. Performing MSD analysis on the DNA origami platform in three independent experiments results in a diffusion coefficient  $D$  of  $1.6 \pm 0.2 \mu\text{m}^2/\text{s}$  and a positional accuracy  $PA$  of  $34 \pm 3 \text{ nm}$  (see also Figure 7.8b for the MSD plot of one experiment). The value obtained for the diffusion coefficient is comparable to others reported previously in the literature, considering that—next to the lipid composition—the number and the position of the cholesterol attachment sites strongly influences the diffusion behavior [171, 174, 226].

## 7.4 T cell interaction platform

Following successful characterization, the DNA origami platform is ready to be utilized as a tool to imitate biological systems. Here, the SLB-DNA origami system is used to closely imitate an APC, in order to study the influence of

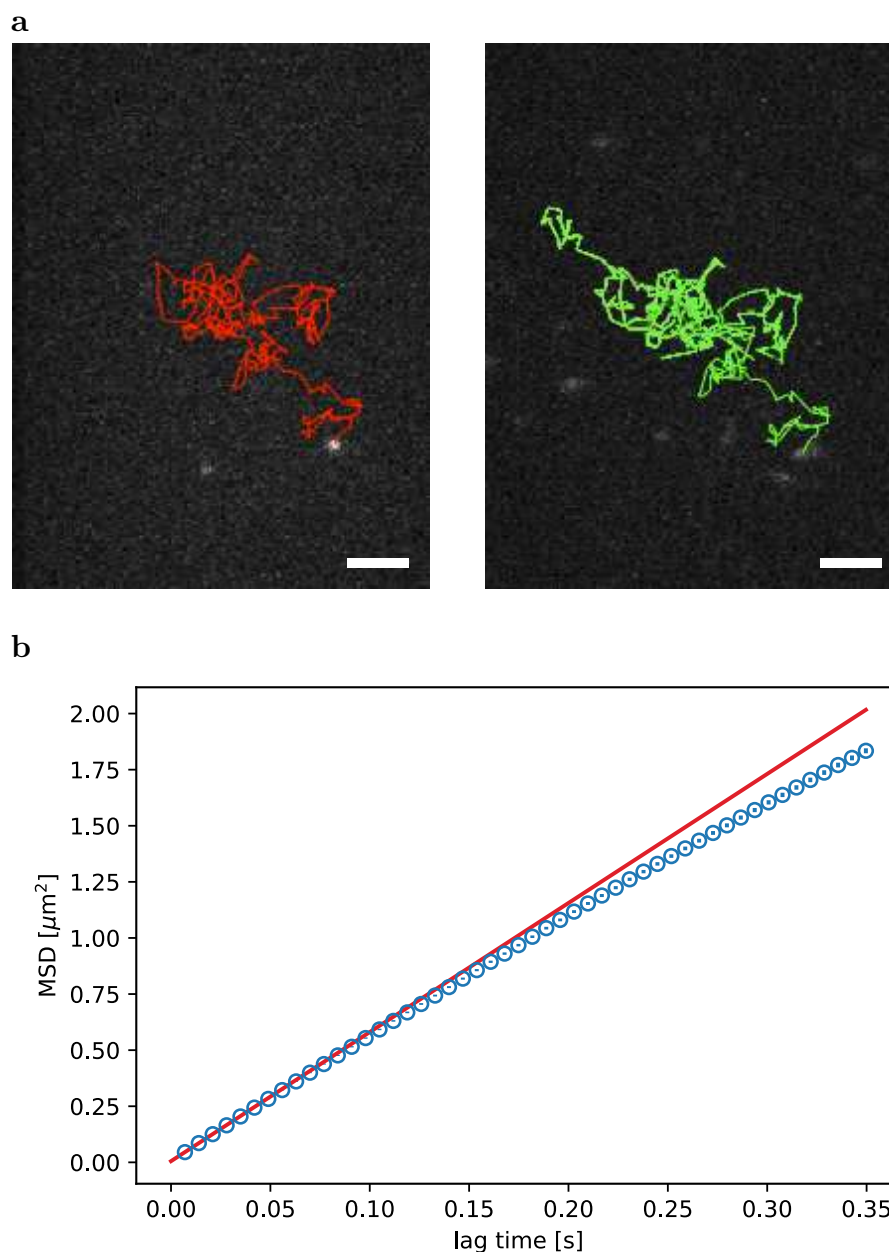


**Figure 7.8:** *Single particle tracking analysis of the DNA origami platform.* (a) An exemplary track of a DNA origami platform can be seen in both color channels. Since the red fluorophores bleach earlier, the track in this channel is shorter. Scalebars are  $5\ \mu\text{m}$ . (b) The MSD plot of the DNA origami platform allows for the derivation of an estimate of the parameters of the movement, such as the diffusion coefficient. Data points are shown in blue, a linear fit using the first two data points is shown in red. For the DNA origami platform, the diffusion coefficient  $D$  in this experiment is  $1.44\ \mu\text{m}^2/\text{s}$  and the positional accuracy  $PA$  is  $36\ \text{nm}$ .



nanoscale spatial organization of the scFv on T cell activation. Therefore, it is necessary to attach other ligands than fluorophores or cholesterol to the DNA origami platform. In this section, the decoration of the DNA origami platform with functional modifications will be described. As a proof of principle, the attachment of an antibody against GFP to the DNA origami platform will be shown. Further, a possible experimental procedure for probing the influence of spatial organization of the scFv on T cell activation will be described.

### 7.4.1 Attachment strategies

The general principle to attach ligands to DNA is by the hybridization of a modified strand to the DNA structure. A wide variety of modifications can be incorporated into an oligo at the time of synthesis. Strands with modifications, such as fluorophores or cholesterols can be used directly and have already been introduced. Other modifications such as biotin can be used to mediate the attachment of specific ligands which are not directly commercially available. Hence, ligands are modified in order to bind to the modification present on the DNA origami platform. Here, different modification possibilities, which can be used for the attachment of ligands, will be discussed.

#### Biotin modifications

Biotin is one of the most useful protein tags and often used in various biochemical applications. The binding of biotin to the tetrameric protein avidin and its variants streptavidin and neutravidin is one of the strongest known protein-ligand interactions with a dissociation constant  $K_d$  on the order of  $10^{-15}$  M [227].

Biotinylation, i.e. the process of covalently attaching biotin to a specific molecule, is a specific way to tag a protein of interest. Due to the small size of biotin, it is unlikely to affect the natural function of the protein of interest. The high affinity and stability of biotin binding to streptavidin makes biotinylation a versatile tool in molecular biology and a vast number of biotinylation reagents are readily available.

Biotin-modified oligos are commercially available with biotin being added to the 5'- or 3'-ends of an oligo. Further, a tetraethylene glycol (TEG) spacer is often introduced between biotin and the oligo, as it allows for an increase in binding to the streptavidin deep-binding pocket. Using an external labeling

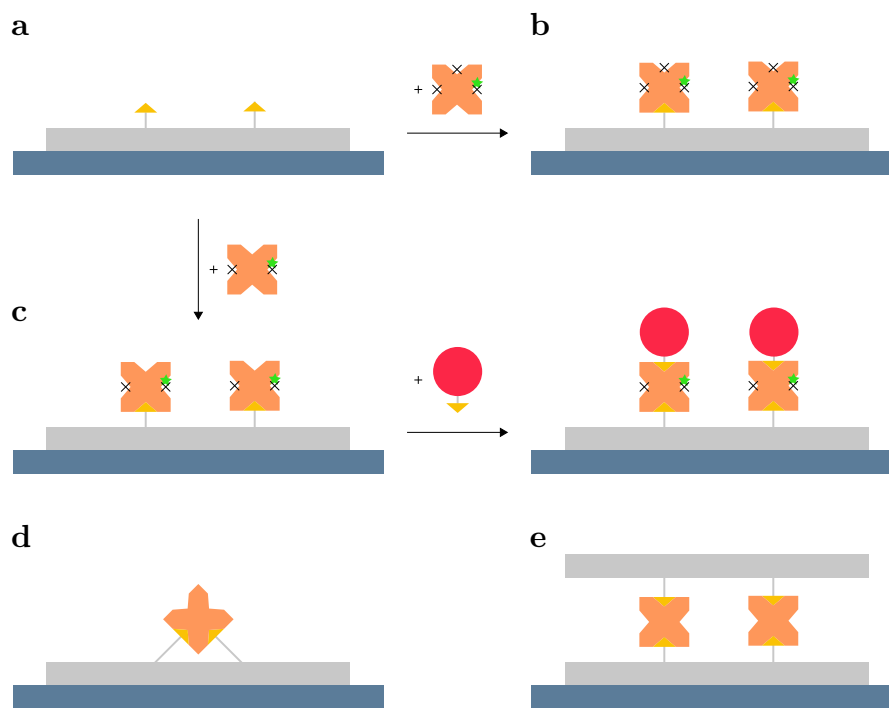


**Figure 7.9:** *Biotin-modified oligos serve as a suitable tool for the attachment of a protein of interest to a DNA origami structure. (a) Initially, a DNA origami platform (gray) is attached to a lipid bilayer (blue) with its biotin modifications (yellow) facing upwards. (b) Fluorescently labeled monovalent streptavidin (orange) is able to bind to the DNA origami platform. (c) Addition of fluorescently labeled divalent streptavidin allows for the attachment of the biotinylated protein of interest (red). (d) Using low amounts of streptavidin in the labeling process can lead to a single streptavidin binding to more than one biotin on the platform. Usage of regular streptavidin increases the likelihood of this configuration. (e) Further, low amounts of streptavidin during labeling can also result in several platforms being attached to each other, especially when the labeling process is performed prior to bilayer attachment.*

strategy, these biotin modified oligos can be hybridized to the complementary oligos on the DNA platform. Then, streptavidin can serve as a linker between the biotinylated DNA origami platform and the biotinylated protein of interest.

Although seeming simple, certain points need to be considered for a successful labeling procedure (see also Figure 7.9).

- A high excess of streptavidin is of utmost importance when labeling the DNA origami platforms. A low amount of streptavidin can lead to the aggregation of two platforms forming a sandwich-like structure. Further, it can result in binding of several biotin molecules that are present on the same platform to a single streptavidin, leading to a reduced total number of streptavidins bound to the platform.
- Performing the labeling process on DNA origami platforms already attached to a lipid bilayer can circumvent some of these problems, as these platforms are unable to form sandwich-like structures, as depicted in Figure 7.9e. However, a single streptavidin protein binding multiple biotins is still possible, if the amount of streptavidin present during the labeling process is too low.
- Modified versions of the tetrameric protein streptavidin can further improve the outcome of the labeling procedure. A monovalent streptavidin protein has only one active binding site together with three dead sites. Using a site-specifically fluorescently labeled monovalent streptavidin should in principle give the same outcome as a fluorophore directly attached to an oligo. By comparing these two systems, the binding of streptavidin to the DNA origami can be validated. However, the usage of monovalent streptavidin does not allow for the attachment of a protein of interest to the platform, as no further binding pockets are available.
- Divalent streptavidin, with the two alive binding pockets being located diagonally, enables a protein of interest to be bound to the platform. Further, having a site-specific fluorescent label in one of the dead binding sites allows for the verification of streptavidin being bound to the platform. Still, unintended binding is a possibility also in this scenario, but presumably less likely than with the use of tetravalent streptavidin.

As a consequence of these considerations, the biotin labeling strategy was implemented directly on bilayer systems with either the usage of tetrameric streptavidin (proof of principle, see section 7.4.2) or site-specifically labeled divalent streptavidin (attachment of the scFv, see section 7.4.3).

### Other modifications

Several other modifications are available for oligos which can be used to attach ligands to a DNA origami platform. Due to the vast number of modifications available, only the modifications tested during the work for this thesis will be described briefly. However, only click chemistry and biotin modifications were finally used for the presented experiments.

The HaloTag protein (34 kDA) is a genetically engineered derivative of a dehalogenase and can be fused at either the N- or C-terminus to proteins of interest. By forming a covalent bond with various synthetic HaloTag ligands, it can be used to attach essentially any protein of interest to a DNA strand [228]. Here, a commercial bromohexyl modification was used to produce the substrate for the HaloTag domain. Preliminary experiments were carried out using a Halo-tagged GFP.

A different method routinely used in labeling DNA oligonucleotides with different functionalities is click chemistry [229]. This two-step process utilizes quantitative chemical reactions of alkyne and azide moieties to create covalent carbon-heteroatom bonds between biochemical species. Using copper(I) as a catalyst, a 1,2,3-triazole between an azide and a terminal alkyne is formed. Click chemistry reactions proceed rapidly and tend to be highly selective for a single product, making them a suitable method for labeling oligonucleotides.

A further possibility for oligonucleotide labeling is the usage of thiol groups. These groups can be used to attach an oligo to a variety of fluorescent and non-fluorescent moieties, but are mainly used for the coupling of oligonucleotides to solid supports. As thiol modifiers are shipped in their oxidized form, they require a chemical reduction prior to use.

### 7.4.2 Modification with antibodies

Antibodies are a powerful tool used in many biological applications and the most commonly used antibodies are commercially available. In general, they are used

to identify and locate intracellular and extracellular proteins. The possibility to attach antibodies to the DNA origami platform makes it a universally applicable system, which can be tailored to specific problems.

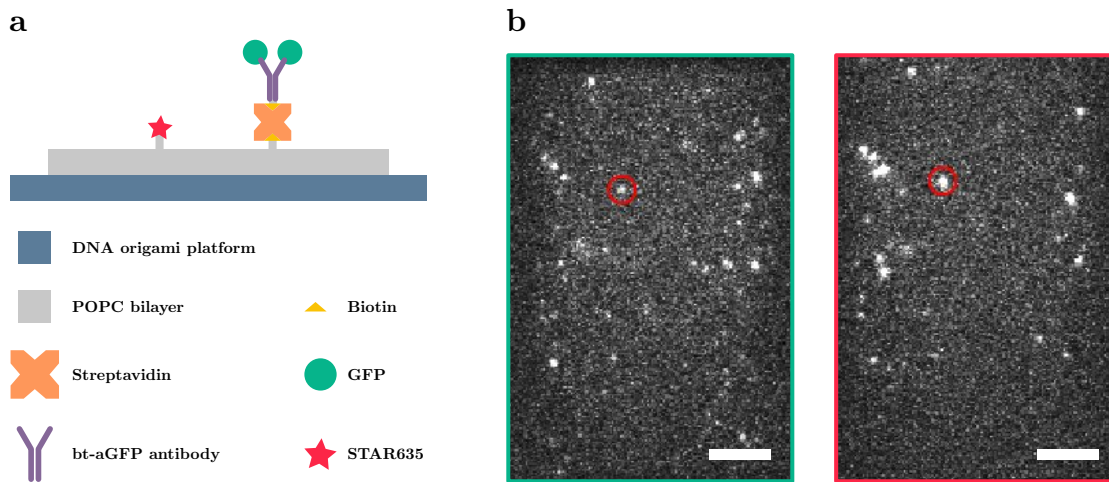


**Figure 7.10:** *The attachment of antibodies to DNA origami platforms demonstrates their deployability to study biological systems at the nanoscale. (a) The experimental layout consists of a POPC bilayer with DNA platforms attached via cholesterol anchors. These platforms are decorated with four STAR635 fluorophores and 4 biotin-TEG modifications. Streptavidin functions as a linker for the binding of a biotinylated aGFP antibody. This allows GFP to be attached to the DNA origami platform. (b) Colocalization as well as co-diffusion are used qualitatively for experimental verification of the attachment of GFP to the DNA origami platform. A colocalized signal is highlighted in the GFP channel (green) and in the STAR635 channel (red). Scalebars are 5 μm.*

As a proof of principle, we attached a biotinylated antibody against GFP to the platform in order to capture GFPs. The experimental design consists of a DNA origami platform diffusing on a lipid bilayer (see Figure 7.10a). This platform is simultaneously decorated with four fluorophores and four biotin modification sites. Via its biotin modification, streptavidin can be bound to the platform. First tests with fluorescently labeled streptavidin confirmed the attachment of streptavidin to the platform. For further experiments, regular tetrameric streptavidin was used. Biotinylated antibodies—in this case an antibody against GFP—can be attached to unoccupied binding pockets of these streptavidin molecules. These antibodies are able to bind GFPs to specific lo-

cations on the DNA origami platform. Colocalization of the fluorophore signal and the GFP signal can be used as a proof of principle that DNA origami platforms can be decorated with antibodies using a biotin-streptavidin linkage (see Figure 7.10b). A detailed description of the sample preparation and the measurement parameters can be found in section 9.3.4.

Although antibodies are widely used in biological applications and attachment of antibodies to a DNA origami platform introduces many experimental possibilities, it is not possible to use this system to probe the influence of spatial organization of ligands on T cell activation. The reasons for this are twofold. First, antibodies possess two antigen binding sites. Second, tetrameric streptavidin is related to several issues, including the possibility to bind up to three biotinylated antibodies. Taken together, the system as presented here is too undefined to probe different ligand arrangements. An experimental approach, involving the usage of a single chain antibody fragment together with divalent streptavidin, can be used to circumvent these problems and is described in the following section.

### 7.4.3 Modification with the single chain antibody fragment

In order to study the influence of nanoscale spatial organization of the TCR $\beta$ -reactive single chain antibody fragment (scFv) site-specifically labeled with AF555 [230] on T cell activation, the DNA origami platform is decorated with scFv and embedded—together with co-stimulatory molecules and adhesion proteins—on a planar glass-supported lipid bilayer (see Figure 7.11a).

Although DNA origami offer the possibility to control the position of ligands with nm-precision, we decided to propose a more general experimental approach and to focus on the role of clustering in T cell activation. Two different sets of ligand distributions on this platform will be compared, a batch-platform where 20 scFvs can be clustered in the center of the platform, and an individual-platform where four scFvs are distributed evenly. These scenarios will be compared with freely diffusing scFv. Figure 7.11b-d depicts these three measurement scenarios for future experiments. By using different concentrations of these platforms on the bilayer, the overall concentration of ligands can—in principle—be kept constant and the influence of spatial organization can be singled out. However, preparing

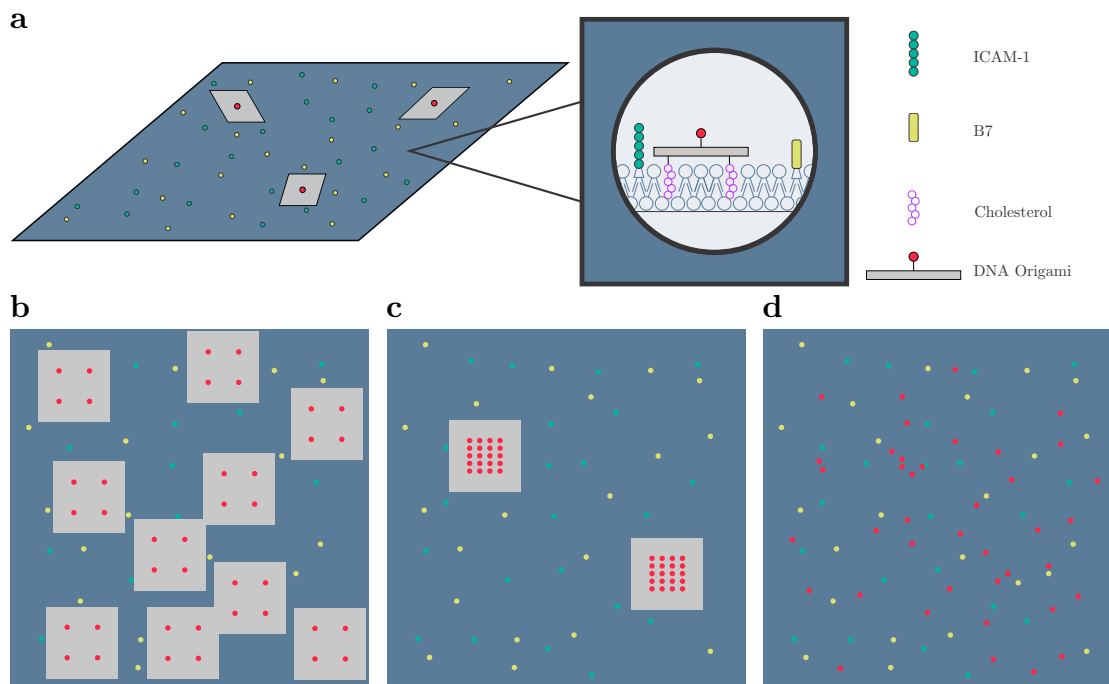


**Figure 7.11:** *The experimental layout is set out to probe the influence of three different ligand distributions on T cell activation. (a) A lipid bilayer system with DNA origami decorated with the scFv and adhesion proteins is used to imitate an APC. Different origami layouts can be incubated to test different spatial organizations of ligands with the overall ligand density remaining constant. (b) An origami platform decorated with four scFvs separates them spatially and guarantees for a specific minimum distance between the ligands. (c) A DNA origami platform with 20 scFvs can be used to simulate ligand clustering. (d) Instead of an origami platform, streptavidin can be bound to the bilayer using polyhistidine tags. scFv bound to the bilayer in this way is free to diffuse and is not subjected to a specific layout.*



biological samples on a lipid bilayer to an exact concentration is a nearly impossible endeavor. Hence, the ligand density needs to be determined in a separate experiment and compared with the level of activated T cells. Ideally, in future experiments ligand density is determined by comparing the brightness of a single ligand with the total brightness and activation is determined by performing calcium imaging. However, also microcluster formation can be used as an indication for activated T cells.

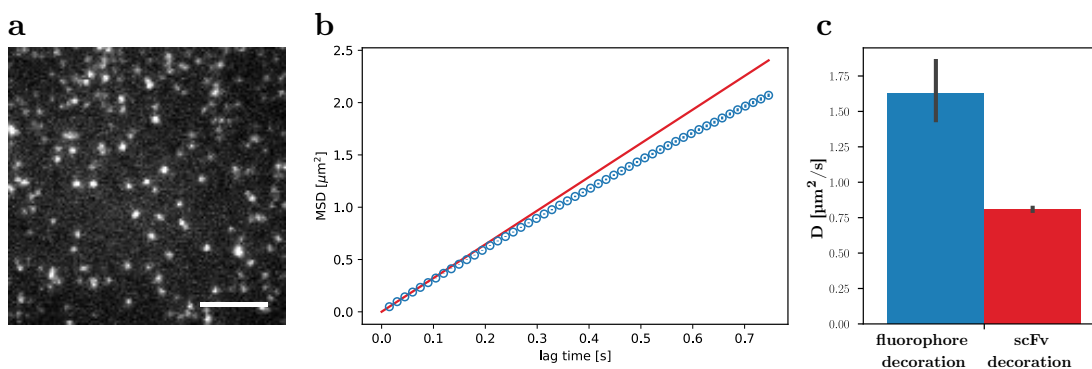


**Figure 7.12: Diffusion analysis of functional DNA origami on a lipid bilayer.** (a) Exemplary image of the DNA origami platform decorated with 20 scFvs-AF555 on a POPC bilayer. Scalebar is 5  $\mu\text{m}$ . (b) MSD plot for the platform is shown in panel a. Here, the diffusion coefficient  $D$  is 0.80  $\mu\text{m}^2/\text{s}$  and the positional accuracy  $PA$  is 15 nm. (c) Comparison of the diffusion coefficients of the fluorophore-decorated DNA origami platform to the platform with fluorophores as well as scFv attached.

Preliminary experiments were performed to show the feasibility of this experimental design. For these experiments, DNA origami decorated with 4 STAR635 fluorophores together with either four or twenty AF555-scFv are incubated on lipid bilayer which also harbors additional proteins necessary for T cell activation. Further details on sample preparation can be found in section 9.3.5. Colocalization analysis was used to confirm correct sample preparation (data not shown), and SPT was performed to compare the diffusion behavior of these origami platforms to the initially used DNA origami platforms decorated only with fluorophores (see Figure 7.12). MSD analysis from five independent experiments with a DNA origami platform decorated with twenty modification sites for scFv attachment gives a diffusion coefficient  $D$  of  $0.8 \pm 0.01 \mu\text{m}^2/\text{s}$  and a positional accuracy  $PA$  of  $21 \pm 4 \text{ nm}$ . The diffusion coefficient of this platform is



about half of the diffusion coefficient decorated with only fluorophores. This difference in behavior could be caused by the additional cargo on the DNA origami platform or by the additional proteins present on the lipid bilayer.

Further experiments are needed to obtain the desired results. Although, the DNA origami platform is designed to probe different designs, occupancy of the platform still needs confirmation. Unfortunately, issues with the transgenic mice strain limited the supply with mouse T cells and prevented seeding cells on these samples.



# Chapter 8

## Conclusion and outlook

Recently, a variety of techniques have been developed that aim at controlling the spatial organization of molecules in cells, each with its individual advantages. DNA nanostructures can serve as custom tools tailored to specific tasks, e.g. to manipulate the interactions with and between target proteins. DNA nanostructures are atomically defined designs. Therefore, DNA nanostructures can be used as scaffolds to specifically place modifications.

However, only few techniques employing precisely designed DNA nanostructures for specific tasks have passed the proof-of-concept stage. Next to the field's young age, also conceptional challenges such as an undetected structural heterogeneity might be the reason for this. Improving quality control could result in an increase in experimental reproducibility, if small but critical differences in folding quality can be determined.

One goal of this thesis was to develop a system to control the spatial organization of ligands. To this end, a general approach for the construction of a virtually unlimited number of platforms was established. The DNA origami platforms were shown to be capable of featuring fluorophores, antibodies and TCR $\beta$ -reactive scFv. Furthermore, these DNA origami can be adapted to serve as mobile platforms and are thereby able to imitate cellular systems more closely.

This system can be used to address and answer central questions in T cell immunology: the role of TCR clustering in the course of T cell activation, but also the role of accessory or inhibitory proteins in this process and their spatial arrangement. Extending the existing design to 3d structures could be used to investigate the kinetic-segregation model of T cell activation, which is based on size-sensitivity for the molecules involved [231]. Ultimately, a better understand-

ing of the TCR recognition process of MHC molecules loaded with antigenic peptides might help elucidate the subsequent steps in T cell activation. Additionally, the influence of the reorganization of ligands on the immune response can be singled out. DNA nanotechnology with its immense potential for single molecule studies and for structure evaluation with near atomic resolution, enables to face these challenges.

# Chapter 9

## Materials and methods

### 9.1 DNA-templated design

General	
Lattice type	square
DNA geometry	
Axial rise per base-pair	0.34 nm
Helix diameter	2.25 nm
Crossover spacing	10.5 bp
DNA mechanical properties	
Axial stiffness	1100 pN
Bending stiffness	230 pN nm <sup>2</sup>
Torsional stiffness	460 pN nm <sup>2</sup>
Nick stiffness factor	0.01

**Table 9.1:** *Submission parameters for the CanDo analysis of the DNA origami platform.*

## 9.2 Folding, purification and labeling

### 9.2.1 Folding protocol

The folding process was conducted in a PCR machine (BIO-RAD CFX Connect Real-Time PCR Detection System) and started with fast heating to 90 °C and remaining at this temperature for 15 min. This denaturation step was a requisite for a successful folding, as it melted unspecific base pairings and thereby prevented undesired side products. After the melting process, slow and stepwise cooling from 90 °C to 20 °C with a rate of 1 °C per min led to the controlled hybridization of the DNA origami platform. The folded DNA platform can be stored for at least 1 d at 4 °C, or for up to 6 months at −20 °C.

### 9.2.2 Folding mix

A total final volume of 100 µl folding mix was prepared in a PCR tube, containing 10 µl of 100 nM scaffold solution, 10 µl of 10× folding buffer and 12.5 µl of 100 mM MgCl<sub>2</sub> solution. The volumes of the master mixes were aimed at a 10× excess for the unmodified oligonucleotides in relation to the scaffold strand concentration. The aimed total volume of 100 µl of the folding mix was achieved by adding H<sub>2</sub>O. The specific volumes are given in Table 9.2.

The 10× folding buffer for DNA origami structures contains 50 mM Tris (pH 8), 500 mM NaCl and 10 mM EDTA and it can be stored for up to 6 months at room temperature. The M13mp18 scaffold strand was purchased from New England Biolabs. Staple strands were purchased from Eurofins-MWG-Biotech, IBA and IDT-DNA. Unmodified staple strands were ordered in desalting purification grade, whereas modified staples were ordered in HPLC purification grade. Further, unmodified staples were ordered diluted in H<sub>2</sub>O to a fixed concentration in a 96-well-plate to facilitate handling. Modified staple strands were ordered lyophilized, as they are more stable and their concentration can be adjusted to specific needs.

Component	Amount [ $\mu\text{l}$ ]	Final concentration
Scaffold, 100 nM	10	10 nM
Folding buffer, 10 $\times$	10	1 $\times$
MgCl <sub>2</sub> , 100 mM	12.5	12.5 mM
Unmodified oligos (54 staples, 925.93 nM per staple)	10.8	100 nM each staple
Yellow mix (10 staples, 5000 nM per staple)	2	100 nM each staple
Red mix (4 staples, 12 500 nM per staple)	0.8	100 nM each staple
Green mix (20 staples, 2500 nM per staple)	4	100 nM each staple
H <sub>2</sub> O	49.9	
Total	100	

**Table 9.2: Composition of the folding mix.** All components were combined in a PCR tube with a 10 $\times$  excess of the unmodified oligonucleotides. The final total volume of 100  $\mu\text{l}$  of the folding mix was achieved by adding H<sub>2</sub>O.

### 9.2.3 Purification of DNA origami structures

#### Spin column filtration

The purification with centrifugal filters followed a protocol described by Schmied et al. [206]. Amicon Ultra 0.5 ml, 100K centrifugal filters were used to purify the folded DNA structures. After putting the centrifugal filter into an affiliated tube, it is filled with 400  $\mu$ l folding buffer followed by 100  $\mu$ l DNA origami solution. Then, the filter is spun for 10 min at 15 000 g and 4 °C. The tube containing the folding buffer together with the unbound oligonucleotides is emptied, and the process is repeated three times by filling 400  $\mu$ l of folding buffer into the filter each time. Next, the filter is flipped and put into a new, unused tube. For retrieval of the DNA origami structures it is centrifuged for 2 min at 1000 g and 4 °C. Storage at  $-20$  °C.

#### PEG precipitation

The purification protocol using PEG precipitation was adapted from Stahl et al. [232]. In short, the assembled DNA nanostructures were mixed 1:1 (vol) with PEG precipitation buffer containing 15% PEG 8000 (w/v), 5 mM Tris, 1 mM EDTA and 505 mM NaCl. The solution was mixed by tube inversion and spun for 25 min at 16 000 g and room temperature using a microcentrifuge. The supernatant was removed carefully using a pipette. The pellet was dissolved in target buffer, i.e.  $1\times$  folding buffer with 12.5 mM  $MgCl_2$  and incubated for approximately 20 h at room temperature.

### 9.2.4 Labeling of DNA origami structures

The external labeling procedure followed closely the protocol described by Schmied et al. [206]. After purification, the DNA origami solution was diluted in  $1\times$  folding buffer to a total final volume of 100  $\mu$ l. The modified labeling strand with the complementary sequence to the extended staple strands on the DNA structure were added in  $\geq 5\times$  molar excess over the binding staples. This solution was incubated for 2 h at 37 °C. Then, the solution is again purified by PEG precipitation.



## 9.3 Characterization of the DNA origami platform

### 9.3.1 Agarose gel electrophoresis

Electrophoresis of the folded DNA origami structures was carried out in 1% agarose gels containing electrophoresis buffer (1× TAE buffer with 12.5 mM MgCl<sub>2</sub> added). Gel loading dyes were mixed with the DNA samples before loading. Then, the samples were electrophoresed for two hours at 70 V in a gel box filled with electrophoresis buffer. For staining, the gel ethidium bromide was used. The samples were illuminated using a UV lamp and yields were compared qualitatively.

### 9.3.2 Atomic force microscopy

#### Sample preparation

DNA origami structures were immobilized on a mica surface using electrostatic interactions. First, a mica sheet was fixed to a coverslip using UV glue. Due to the hexagonal sheet-like arrangement of its atoms, mica can be cleaved nearly perfectly. This is achieved by sticking a piece of adhesive tape on the mica sheet. When removing the tape, the upmost mica layer is removed resulting in a clean, nearly atomically planar surface which is negatively charged. This step was repeated until the surface is smooth and free of damage. The mica surface was preincubated with AFM imaging buffer containing 40 mM Trizma base, 2 mM EDTA and 12.5 mM MgCl<sub>2</sub> (pH = 8) for 5 min. Then the DNA sample was added (1 μl in 10 μl for PEG purified samples) and incubated for 5 min. It is recommended to wait for 15 min before imaging to minimize thermal drift. Additional AFM imaging buffer may be added so that the sample is always fully covered during imaging.

#### AFM imaging

For imaging, a NanoWizard 3 (JPK Instruments) was used in tapping mode together with a MSNL-E (Bruker) cantilever. First, the working amplitude was tuned close to the resonance frequency of the cantilever. For a first sample overview, a region of 5 μm<sup>2</sup> was chosen and the set point (force) was at the lowest

possible value to minimize sample damage. For further imaging, a specific region of DNA origami structures was selected and scanned. In general, increasing the scanning speed when decreasing the scan region improved results. For post-processing, a polynomial surface was subtracted and subsequently a linear fit from each scan line was subtracted independently.

### 9.3.3 Diffusion analysis

#### Sample preparation

Lipid vesicles were needed in order to form a SLB. For this, 10  $\mu\text{l}$  of POPC 10 mg /ml were put in a glass eprouvette. If necessary, the desired amount of 1,2-dioleoyl-sn-glycero-3-[N(5-amino-1-carboxypentyl) iminodiacetic acid]succinyl[nickel salt] (DGS-NTA(Ni)) (Avanti Polar Lipids) 0.1 mg /ml can be added at this step. The lipids were dried under  $\text{N}_2$  for 15 min, until all solvent residues were evaporated. 1 ml phosphate-buffered saline (PBS) was added to the lipids and the solution was mixed thoroughly. After closing the eprouvette with parafilm, the lipid solution was sonicated in the ultrasonic bath for 10 min. Finally, the lipid vesicle solution was transferred to a plastic container.

For the formation of a SLB, a glass cover slip (#1.5, 24 $\times$ 60 mm, Menzel) was plasma cleaned in a Harrick Plasma Cleaner for 10 min. The glass slide was glued to a Lab-Tek chamber (Nunc) using Twinsil (Picodent) glue. 120  $\mu\text{l}$  of the 10-fold PBS-diluted lipid suspension was pipetted into each well and left for 20 min for bilayer formation. Each chamber was carefully rinsed with 15 ml PBS. Extra care needs to be taken that the bilayer is never exposed to air and always submerged in buffer. After filling the well all the way with PBS, 330  $\mu\text{l}$  were removed, resulting in 350  $\mu\text{l}$  being left in the well. If necessary, 50  $\mu\text{l}$  of the cocktail containing His-tagged diluted in PBS or the DNA strands with the cholesterol modification can be added to each well. Following an incubation of 60 min at room temperature in the dark, the bilayer was again rinsed twice with 15 ml PBS. Further details on the preparation of SLB can be found in [161].

For the attachment of DNA origami structures to a POPC bilayer, 0.2  $\mu\text{l}$  of 0.1 mM Chol-TEG-Z strands were incubated for 30 min at room temperature. After washing, 0.2  $\mu\text{l}$  DNA origami platforms were incubated for 60 min at room temperature. After a final washing step, the sample could be used for experiments.

## Microscopy

TIRF microscopy experiments were performed on a home-built system based on a modified inverted microscope (Zeiss Axiovert 200) equipped with a 100 $\times$  oil-immersion objective (Zeiss Apochromat NA1.46, Germany). For colocalization and diffusion experiments, a 640 nm diode laser (imaging of STAR635; Coherent) and a 532 nm diode-pumped solid state laser (imaging of DYE549, Millennia X, Spectra Physics) were used. Emission light was filtered using appropriate filter sets (Chroma) and recorded on an iXon DU 897-DV EM-CCD camera (Andor). TIRF illumination was achieved by shifting the excitation beam in parallel to the optical axis with a mirror mounted on a motorized movable table. In total, 5000 frames were recorded per tracking movie with an illumination time of 1 ms and a delay of 6 ms.

## Analysis

For the determination of single molecule positions, an in-house-developed Python algorithm was used. This implementation of 3D-DAOSTORM [225], which is a fast Gaussian fitting algorithm based on maximum likelihood estimation, does several rounds of feature finding and fitting, in order to fit even features which are close together. The corresponding ROIs in both color channels were selected. Beads images were used to correct for chromatic aberrations. Therefore, the corresponding localizations in the selected ROIs were matched and affine transformations for the x and y coordinates were calculated by a linear least squares fit of the embedding of the affine space into a higher dimensional vector space. According to these transformations, the red channel was corrected and was overlaid with the green channel and all positions in both channels were matched. In particular, for every localization in one channel, all localizations in the other channel occurring in the same frame, that are in a square of length 2 px around it, are considered and then the closest one is picked.

For determination of the percentage of colocalization, only the first 15 frames of each movie were considered. Due to differences in the total number of signals in the two channels, the percentage of colocalization was determined separately for both channels relative to the other channel.

For diffusion analysis, the tracks to which colocalized pairs belong to were matched. The minimum fraction of matched localizations that have to belong

to the same pair of tracks was set to 0.98. Then, the ensemble mean square displacements from this tracking data were calculated. The function  $msd(t) = 4Dt + 4PA^2$  was fit to the tag-vs.-MSD graph, where  $D$  is the diffusion coefficient and  $PA$  is the positional accuracy (uncertainty). Only the first two lag times were used for fitting. The positional accuracy was corrected for motion during exposure.

### 9.3.4 Antibody modification setup

The DNA origami platform for the antibody modification experiment was modified with four Y'-strands used for the attachment of STAR635-Y-strands and four X'-strands used for the attachment of four biotin-TEG-X-strands. The folded platforms were PEG purified and labeled, followed by another purification step.

POPC bilayer formation and incubation of the DNA origami platform on the bilayer followed the same protocol as described in section 9.3.3. Streptavidin (AppliChem) was added to the bilayer system at a concentration of 50  $\mu\text{g}/\text{ml}$  and after 30 min the bilayer was washed to remove excess streptavidin. Further, 10  $\mu\text{g}/\text{ml}$  biotinylated aGFP (Novus) was incubated on the bilayer for 30 min and subsequently unbound antibody was washed away. Finally, 10  $\mu\text{g}/\text{ml}$  GFP (gift from J. Piehler, Univ. Osnabrück) was added to the bilayer, and incubated for 20 min followed by a washing step. TIRF microscopy was performed using the same parameters as for the diffusion analysis.

### 9.3.5 Single chain antibody fragment modification setup

Two different DNA origami platforms were used in the scFv modification experiment, with either four or twenty Y'-strands which were used for the attachment of the AF555 labeled scFv (provided by J. Huppa, Medical Univ. Vienna) linked to TCOPEG-Y-strands. In both cases, four X'-strands were used for the attachment of STAR635-X-strands.

POPC+2% DGS-NTA(Ni) bilayer formation and incubation of the DNA origami platform on the bilayer followed the same protocol as described in section 9.3.3. Formed planar supported lipid bilayers were incubated with His-tagged proteins ICAM2 and B7-1 for 75 min at room temperature and then rinsed with PBS.

Details on the microscopy setup as well as colocalization and diffusion analysis have been described in section 9.3.3.



## Part III

# TCR micropatterning to study ZAP70 kinetics



Die approbierte gedruckte Originalversion dieser Dissertation ist an der TU Wien Bibliothek verfügbar.  
The approved original version of this doctoral thesis is available in print at TU Wien Bibliothek.



# Chapter 10

## Introduction

Cell signaling processes at the plasma membrane are often initiated by interactions between a membrane protein and a cytosolic interaction partner. Although this general principle holds true for many ligand-receptor pairs, methods to characterize and quantify such interactions are few and far between. In order to obtain a complete understanding of such signaling processes—in particular of the interaction kinetics of the involved proteins—, prevalent techniques such as FRAP have to be carefully reassessed and refined.

Commonly used methods for the quantification of intracellular binding kinetics, i.e. the extraction of kinetic parameters, are single molecule imaging methods [233, 234] and FRAP [45, 234–237]. In particular FRAP, first introduced in 1976 [238], is widely used for probing the dynamic properties of proteins and lipids such as their mobility and localization in different organelles [239, 240]. In most studies, FRAP is used together with confocal microscopy. However, due to the small penetration depth of the evanescent field, TIRF microscopy is particularly suited to investigate processes at the plasma membrane. FRAP has been applied with both confocal and TIRF microscopy to study interaction kinetics between a membrane protein and a fluorescently tagged cytoplasmic protein [45, 234–237, 241–243]. Still, in most cases quantification of such interactions in living cells is far from straightforward and experiments are often hampered by non-specific contributions to the fluorescence recovery signal. Sophisticated experimental protocols as well as analysis approaches need to be used to overcome these issues [235, 244–247].

Micropatterning of proteins in the plasma membrane of living cells is a widely-used technique to investigate different protein-protein and protein-lipid interac-

tions [237, 248–253]. It is based on the spatially controlled immobilization of a large amount of ligands in defined areas and the rearrangement of a large portion of interaction partners in the cell. A combination of micropatterning and FRAP allows for the creation of specific detection and reference areas within a single cell, each being either enriched or depleted in TCR, allowing for the isolation of the interaction partners in a straight-forward manner. This approach has been previously introduced to probe the binding kinetics of the micropatterned transmembrane protein CD4 and the palmitoylated tyrosine kinase Lck [250]. In this thesis, this method is extended and characterized for the quantitative analysis of the interaction kinetics of a cytosolic protein and its target protein at the plasma membrane.

The interaction of ZAP70, a cytoplasmic Syk family kinase, and the TCR is an important step in the course of T cell activation. On this experimental system, this approach—based on protein micropatterning that allows the elimination of such non-specific contributions and considerably simplifies analysis of FRAP data—is exemplified in Jurkat T cells [45, 234, 236] and compared to a conventional FRAP approach.

### **Structure of this part**

This part consists of four major chapters, including this introduction.

In chapter 11, the theory behind the combined approach of micropatterning together with FRAP is described. It is split into three distinct parts. First, the determination of kinetic parameters using FRAP will be introduced. Then, the general principles of protein micropatterning with focus on its applications in cell biology will be described. Finally, an in-depth view on the interaction between ZAP70 and the TCR will be provided.

Chapter 12 focuses on the actual implementation of this approach. Here, the different experimental systems will be described in detail and the obtained results are discussed.

Materials and methods used in this part are described in chapter 14.

### **About this part**

Most of the work presented in this part was published in [254].

# Chapter 11

## Theoretical background

A complete understanding of the interaction kinetics in between proteins, as well as of their diffusion behavior relies heavily on the profound knowledge of the applied methods. In particular, complex systems such as the TCR with its interaction partners require a particular attention to detail when designing experiments. Here, we use FRAP, a commonly used method for the quantification of intracellular binding kinetics, and extend it by combining it with a micropatterning approach, which allows for the creation of specific detection and reference areas within a single cell. This approach is exemplified on the interaction of ZAP70 and the TCR, in order to elucidate their role in T cell activation. While understanding the methodology is a prerequisite, a broad knowledge base on the investigated system is of utmost importance.

The first focus of this chapter lies on the experimental methods used, in particular the FRAP approach and the micropatterning approach. Further, ZAP70 and its interaction with the TCR will be examined. Thereby, this chapter should provide a foundation for understanding the obtained results described in a later chapter.

### 11.1 Fluorescence recovery after photobleaching

FRAP is a frequently used technique for in vivo analysis of dynamic molecular interactions in cellular processes. The obtained FRAP data—properly interpreted—yields information on binding interactions of fluorescently labeled molecules, in-

cluding the number of binding states and the binding strength of each state. However, appropriate models for the processes underlying a FRAP recovery are hard to come by and demand an in-depth review of the technique as well as a continued development of the approach.

While the fundamental principles of FRAP experiments are already described in section 3.1.4, this section presents a more sophisticated review of the analysis of FRAP experiments, including a qualitative as well as a quantitative interpretation. This section is mainly based on [247].

### 11.1.1 The influence of diffusion and binding

Both, interaction kinetics and cytosolic diffusion properties affect the results of a FRAP experiment. The influence of binding interactions manifests itself in a retarded FRAP recovery compared to a diffusion-only scenario. By comparing a FRAP recovery of an inert, non-binding molecule of comparable size to the FRAP recovery of the protein of interest, it can be determined whether binding interactions are involved in the recovery process. Commonly, this is achieved by comparing the recovery behavior of unconjugated GFP to that of a GFP fusion of the protein of interest. Binding is implicated, if the FRAP recovery of the protein of interest is slower than that of its non-binding counterpart, with the degree of slowdown being a measure of the binding strength. In general, GFP recovery takes places in less than a second, whereas binding interactions can slow down the recovery of GFP fusion proteins to require many seconds or even longer. These differences cannot be attributed to the increase in mass alone, but suggest that binding is retarding the FRAP recovery of the fusion protein. However, to exclude size-dependent effects completely, using size-matched markers would allow for a better comparison and would therefore facilitate the identification of binding effects.

If both diffusion and binding are present in a system, their respective contribution to the recovery curve needs to be determined. Depending on the relative speed of the diffusion compared to the binding, i.e. the diffusion time compared to the inverse association rate, different regimes can be distinguished (see Figure 11.1). Diffusion-coupled and -uncoupled FRAP recoveries yield distinct behaviors and require completely different qualitative and quantitative interpretations. For a sophisticated analysis of FRAP data, an assessment of which of these regimes is appropriate can be helpful. This can be achieved by either

measuring the fluorescence recovery in various areas of the bleached zone [255], or alternatively by using different spot sizes for bleaching and by determining whether the FRAP recovery changes [256]. However, using the FRAP technique together with TIRF microscopy, compared to confocal microscopy, complicates the variation of bleaching spot sizes. Following, these two behaviors will be discussed separately.

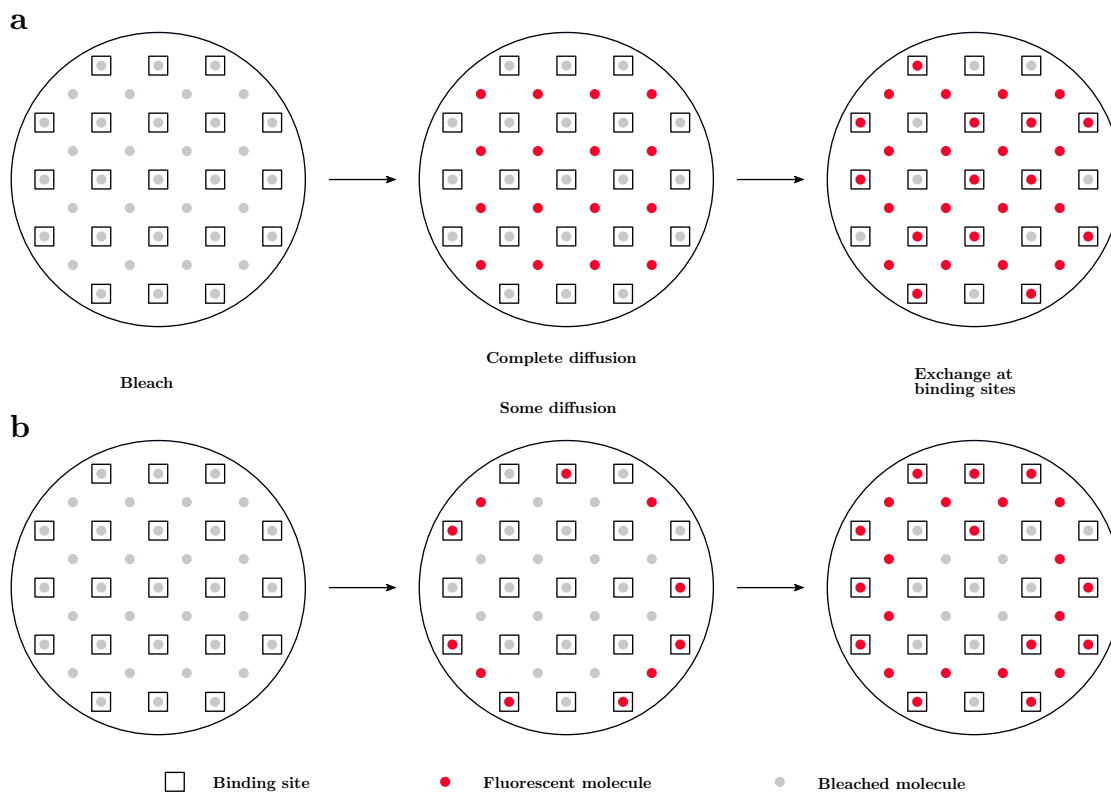


**Figure 11.1: Simplified depiction of different FRAP behaviors.** (a) In the case of diffusion-uncoupled behavior, fluorescent molecules rapidly diffuse into the bleach spot and only bound bleached molecules remain at their binding sites. After dissociation, fluorescent molecules can bind to vacant binding sites. (b) For diffusion-coupled systems, diffusing fluorescent molecules associate with the first binding site they encounter. Gradually, the interior of the bleach spot gets populated with fluorescent molecules. Illustration adapted from [247].

### 11.1.2 Diffusion-uncoupled FRAP

A diffusion-uncoupled recovery curve is characterized by a much shorter diffusion time compared to the time to begin binding. This separates the recovery into two distinct phases, a short initial diffusive phase followed by a much longer binding phase. This second phase directly reflects all binding interactions, be it a single or several different binding states with distinct binding affinities.

In general, analysis of FRAP recovery curves focuses on the immobile fraction and on the speed of the recovery, i.e. protein mobility and binding interactions. In order to quantify experiments and to ensure the accuracy of this qualitative interpretation, these quantitative parameters can either be determined numerically, or by fitting the normalized FRAP curve  $I(t)$  with mathematical models. The simplest case of a single binding state is described by the inverse of an exponential decay (see also section 3.1.4) [256–259]. This allows for the direct estimation of both the off rate of binding and the immobile fraction.

Still, this approach only takes into account a single binding state. If two independent binding states are present, the FRAP recovery curve can be described using two exponential terms from which the binding parameters for each individual binding state can be determined [256, 260, 261]. However, fitting a sum of exponentials needs an extra degree of caution and is described in more detail in section 11.1.4.

In the presence of multiple, dependent binding states, these relatively simple formulas do not properly describe the recovery behavior. Alternatively, a set of ordinary differential equations describing the binding interactions can be solved numerically [262, 263] and fitted to the FRAP data using various techniques [255, 264] to determine binding parameters.

### 11.1.3 Diffusion-coupled FRAP

If the diffusion time for the protein of interest is comparable or slower than its association time, diffusion and binding are intertwined and the recovery curve cannot be separated in the respective phases. Since both diffusion and binding contribute to the recovery curve, extracting binding information is far more difficult compared to the diffusion-uncoupled situation. Still, solutions for simple cases exist and computer algorithms have been developed for even more complex situation [264].

The diffusion-coupled mode is not described in detail, since the decoupling of diffusion and binding is being achieved by applying a micropatterning approach. This simplifies data analysis massively, as in general, the equations describing a diffusion-coupled FRAP are far more complex than those used to describe diffusion-uncoupled FRAP and cannot be solved without several simplifying assumptions.

### 11.1.4 Fitting FRAP recovery curves

If an appropriate model has been found, it can be fitted to the data. For the analysis of most photobleach-recovery events, the perturbation-relaxation theory is used, which is based on the kinetic theory of physical-chemical processes. In a FRAP experiment, the bleach pulse causes a perturbation in the cell and the relaxation to equilibrium, i.e. the fluorescence recovery, is monitored. A basic approach to fit this recovery curve is by an exponential function

$$F(t) = F_{\infty} - (F_{\infty} - F_i)e^{-t/\tau} \quad (11.1)$$

$$F(t) = (F_{\infty} - F_i)[1 - e^{-t/\tau}] + F_i \quad (11.2)$$

with  $F(t)$ ,  $F_i$ ,  $F_{\infty}$  being the fluorescence recovery at time  $t$  during recovery, the initial fluorescence, and the final fluorescence, respectively, and  $\tau$  is a time constant. The characteristic half-time of recovery,  $t_{1/2}$ , is related to the time constant  $\tau$  via

$$t_{1/2} = \tau \ln 2. \quad (11.3)$$

In order to take different contributions to the recovery curve into account, additional exponential terms can be added to the model. For models consisting of a sum of exponential functions, special attention needs to be paid to the quality of the fit. Several consistency checks can be applied to confirm fit quality.

#### Fit of a sum of exponential functions

The error in analyzing FRAP curves depends crucially on the accuracy of the fits. Unfortunately, the fit of data by a sum of exponentials and in particular by real exponents may be a very ill-conditioned problem of numerical analysis, where small changes in the data can cause large changes in the best-fit parameters [265,

266].

$$y(t) = \alpha + \sum_{i=1}^p \beta_i e^{\lambda_i t} \quad (11.4)$$

In 1975, Osborne introduced a modified Prony algorithm [267]. In Prony's method, a sum of exponential functions is interpolated through a series of data values at equally-spaced points, and a system of linear equations is solved for the coefficients of a difference equation satisfied by the exponential functions. Then, the exponential functions can be obtained from the roots of the polynomial with these coefficients.

In this thesis, standard non-linear least squares were used to fit the data. Minimization was performed using a Trust Region Reflective algorithm, which is a robust method particularly suited for large sparse problems with bounds. Fit results were compared to parameters determined by an algorithm based on modified Prony's method and no significant deviations were found.

### Goodness of Fit

The goodness of fit is a measure for how well a statistical model describes a set of observations and typically summarizes the discrepancy between the observed and expected values [268–270]. Pearson's chi-squared test establishes whether an observed frequency distribution differs from a theoretical distribution, and thereby evaluates how likely it is that any observed difference between those sets arose by chance. This can be written as

$$\chi^2 = \sum_{i=0}^{N-1} \frac{(O_i - E_i)^2}{E_i} \quad (11.5)$$

where  $O_i$  and  $E_i$  are the observed and expected values. To be more specific, if data points  $(x_i, y_i)$  are fit by a model equation reading  $y(x) = y(x; a_0 \dots a_{M-1})$ , then the maximum likelihood estimate of the equation parameters is obtained by minimizing the chi-square

$$\chi^2 = \sum_{i=0}^{N-1} \frac{(y_i - y(x_i; a_0 \dots a_M))^2}{\sigma} \quad (11.6)$$

Using this result, the chi-square distribution for  $\nu = N - M$  degrees of freedom can be calculated using incomplete gamma function. The probability  $Q$  that the



chi-squared should exceed a particular chi-square by chance is then given by

$$Q(\chi^2 | \nu) = Q\left(\frac{\chi^2}{2} \mid \frac{\nu}{2}\right) = 1 - P(\chi^2 | \nu) = 1 - P\left(\frac{\chi^2}{2} \mid \frac{\nu}{2}\right) \quad (11.7)$$

with  $N$  being the number of fitted points and  $M$  is the number of parameters within equation to fit.  $Q > 0.1$  suggests a good fit and  $Q > 0.01$  a moderately good fit. However, if  $Q < 0.01$  either the applied model or the experimental data need to be reevaluated.

### Lomb-Scargle periodogram

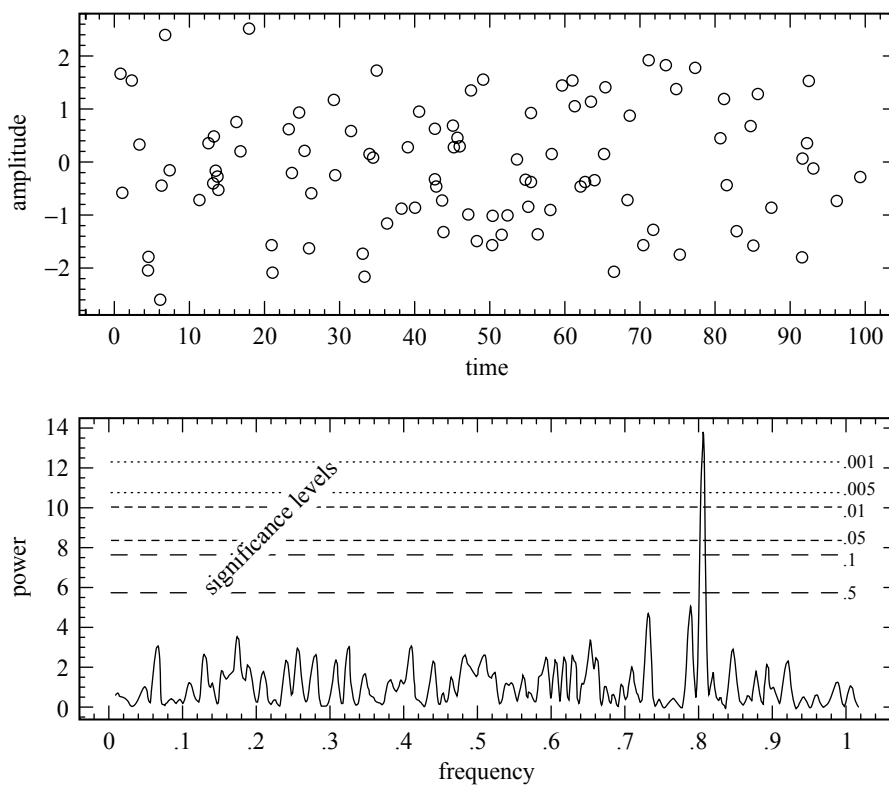


**Figure 11.2:** *Example of the Lomb algorithm.* The sinusoidal component for these 100 data points (upper figure) is readily uncovered (lower figure) in the Lomb-Scargle periodogram, although there is no visible aliasing into the Nyquist range for these unevenly spaced points. Image taken from [271].

When comparing  $Q$  values for different fit models, it is noticeable that they often do not differ by much. An additional method to characterize the quality of

the fit is based on the spectral analysis of unevenly sampled data. This approach was developed by Lomb [272], and additionally elaborated by Scargle [273], and is called a Lomb-Scargle periodogram. In general, the Lomb-Scargle periodogram is an algorithm for detecting and characterizing periodic signals in unevenly-sampled data and it yields an estimate of the Fourier power as a function of period of oscillation. [271] In the case of determining the quality of fit, it is used to detect the periodic component in the residuals by generating a power spectrum. When analyzing fit quality in this work however, no individual frequency could be identified using the Lomb-Scargle periodogram, neither for the mono- nor for the biexponential fit. Therefore, this method could not be used to determine the superior fit function.

## 11.2 Protein micropatterning

The investigation of different protein-protein and protein-lipid interactions is often hampered by non-specific contributions to the signal of interest. Micropatterning of proteins in the plasma membrane of living cells is a technique based on the generation of specific interaction areas, which allow for isolation of the specific signal and hence the elimination of non-specific contributions. Thereby simplifying the analysis of experimental data, such as obtained by FRAP experiments.

In this section, protein micropatterning will be described in general, with particular focus on its applications in cell biology. First, a brief overview of the fundamentals of the immobilization of proteins to surfaces will be given, starting with a description of the different types of immobilization. Then, different strategies to generate protein patterns on planar surfaces will be reviewed, focusing on micropatterning—the technique used in this thesis.

### 11.2.1 Types of immobilization

Several types of immobilization can be distinguished by the involved interaction. In order to generate the structures used in this work, several different immobilization approaches were combined. Here, their fundamental principles will be described.

## Physical adsorption

Physical adsorption is the simplest type of immobilization of proteins to a surface which is based on non-covalent interactions, mainly electrostatic, van der Waals, and dehydration of hydrophobic interfaces. In this physical process, the surface coverage depends largely on the mutual attraction between the solid surface and the protein and displays varying levels of reversibility.

Commonly used surfaces for this method include hydrophobic polymers, such as polydimethylsiloxane (PDMS), cationic surfaces like polylysine-coated glass slides and glass or silicon substrates chemically modified to acquire hydrophobic surface properties [274]. In contrast, protein adsorption is dramatically reduced on hydrophilic substrates, such as hydrophilic polymers, for example agarose or PEG. Fibronectin and bovine serum albumin (BSA) are also known to inhibit protein adsorption and are commonly used as blocking agents [275]. In this thesis, fibronectin was used to prevent unwanted protein adsorption.

## Covalent binding

Protein immobilization via covalent binding is based on the formation of a chemical bond between the solid surface and the protein, and is a more stable method compared to physical adsorption. Proteins display a variety of functional groups, which can be used to attach them to surfaces with complementary chemical groups. One of the most commonly used bonds is an amide linkage, formed between amino- and carboxyl-modified surfaces with the amino groups of proteins [274].

## Biorecognition

Biorecognition is based on a high-affinity ligand pair, which provides a stable interaction similar in strength to covalent binding. The two most commonly used pairs are biotin-avidin and antigen-antibody pairs which both were used in this thesis.

Avidin is a protein found in egg whites and its interaction with biotin is one of the strongest non-covalent affinities known. Streptavidin, isolated from *Streptomyces avidinii*, is another biotin binding protein. Both avidin and streptavidin contain four identical subunits, each with a single biotin binding site. However,

streptavidin has a much lower isoelectric point compared to avidin and shows considerably less non-specific binding than avidin. [276, 277]

Antibodies have the ability to recognize a specific antigen via the Fab's variable region. They consist of two identical antigen-binding sites and a tail, the Fc region. Full binding capacity can only be reached if the antibodies are immobilized in an oriented manner, such that the antigen-binding site is available for recognition. [278]

### 11.2.2 Lithography techniques

Microfabrication is the process of fabricating structures with dimensions of 0.1  $\mu\text{m}$  to 100  $\mu\text{m}$ . The trend of going towards smaller and smaller structures, makes fabrication a challenging task. Lithography, in general, is the process of structuring a material. In the context of biotechnology, this applies to all printing or stamping procedures of biomolecules. However, in conventional lithography, including photolithography and beam (electron or ion) lithography, the substrate is covered with a layer of photoresist, which gets locally exposed to radiation. After subsequent development, the desired pattern is created on the substrate. [279, 280]

#### Photolithography

In photolithography, a photomask is placed above a substrate which is covered with a photoresist, i.e. a radiation-sensitive polymer (see Figure 11.3). By using the photomask, only selected areas are exposed to the radiation. Depending on the use of a positive or a negative photoresist, the exposed part becomes either soluble or insoluble in a developer solution, and thus gets removed or remains on the substrate after development. The remaining resist on the substrate can subsequently be used as a mask in etching or deposition steps.

The resolution obtained in photolithography is defined by the wavelength of the radiation and the mask used. Typically, UV light with a wavelength of 365 nm to 436 nm is used. By using radiation with a lower wavelength, e.g. X-rays, an even better resolution can be achieved. [279, 280]

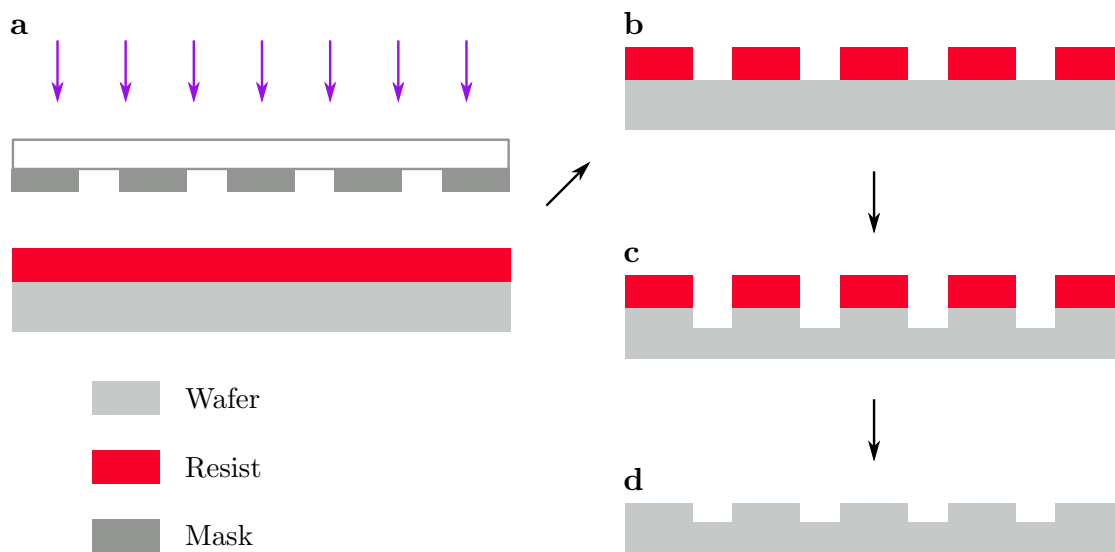


**Figure 11.3:** *General principle of proximity photolithography.* (a) A resist-coated wafer is exposed to UV light with a mask placed on top limiting exposure through the holes in the mask. (b) Development removes the exposed parts, thereby creating a resist pattern on the wafer. (c) During etching, the resist acts as a mask itself. (d) Finally, the resist is removed, resulting in a wafer with the etched mask pattern.

## Scanning beam lithography

In contrast to photolithography, scanning beam lithography is a maskless procedure, but the general process is similar. A substrate covered by an electron or ion sensitive resist layer is scanned by a focused electron or ion beam. In this direct writing process, the resist is selectively exposed to a focused beam. Although scanning beam methods can achieve smaller resolutions compared to photolithography, they are much slower. This is due to the fact that scanning beam lithography techniques are serial methods, whereas photolithography is a parallel technique. However, scanning beam lithography is usually used for the production of photomasks for photolithography. [280–282]

### 11.2.3 Soft lithography

Soft lithography is often seen as an unconventional lithography technique, since it is based on pattern transfer rather than radiation exposure. In general, soft lithography techniques are based on molding, replication and pattern transfer by the use of organic, soft materials.

Commonly in soft lithography techniques, a mold is formed from a master template, thereby replicating the inverse features of the master (see Figure 11.4a). In this process, a liquid precursor, usually a prepolymer mixture, is cast into the master. This master exhibits different topographical features and is usually made of silicon. Then, the mold is cured and solidifies. Finally, it can be removed from the master and used in subsequent patterning steps. The molds allow for a high throughput because of parallel patterning, but without the need for expensive equipment. Still, the master is commonly fabricated with conventional lithography techniques with a high resolution, but also with high costs and a slow throughput. However, once a master is created, it can be used multiple times. [19, 281]

Although nomenclature in this area is not fully established, soft lithography techniques can be grouped in three categories [283]:

- Replica molding
- Embossing
- Printing

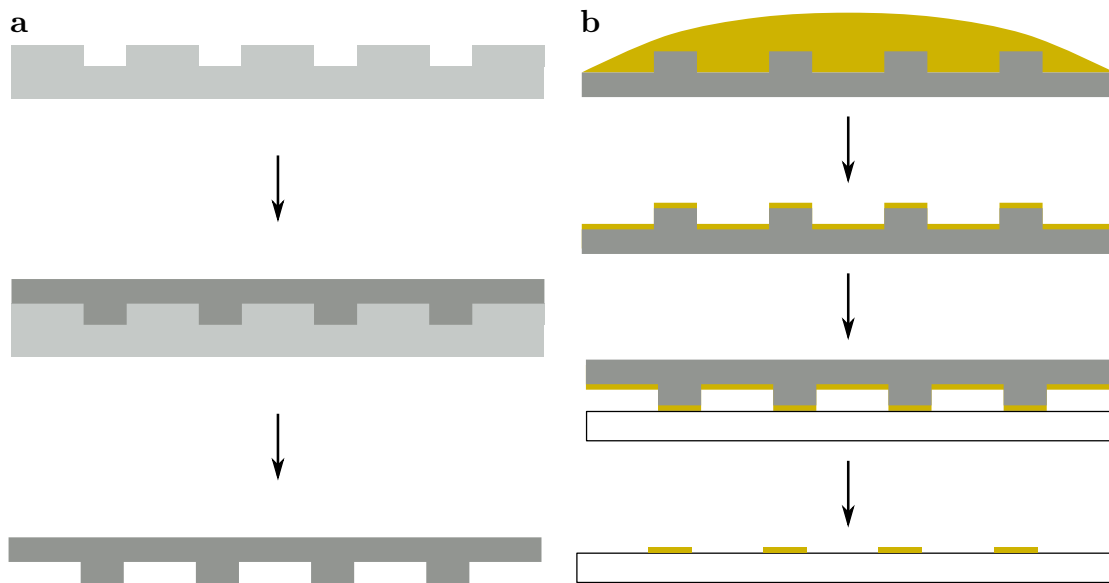


**Figure 11.4: Fabrication of polymer stamps for soft lithography and their usage in microcontact printing.** (a) A master (light gray) fabricated by conventional lithography techniques functions as a basis. This master is coated with a liquid precursor (dark gray), usually a prepolymer mixture, and then cured to make it solid. After release, the mold can be used in subsequent patterning steps. (b) In microcontact printing, a stamp is inked with the material to be transferred (yellow). After removal of excess material, a contact between the protruding features of the stamp with the substrate is formed. The material transferred from the stamp to the substrate generates the desired pattern.

In this thesis, printing techniques, in particular microcontact printing, were applied to generate structured surfaces. Therefore, microcontact printing will be described in more detail.

### Microcontact printing

Microcontact printing is a technique based on the material transfer from the mold to the substrate (see Figure 11.4b). In this method, a patterned elastomeric stamp is inked with the material to be transferred, e.g. antibodies or streptavidin. After removal of excess material, the stamp is placed in contact with the substrate to be printed. Ideally, material is only transferred from the stamp to the substrate where the protruding features of the stamp are in contact with the substrate, thereby creating the desired pattern. In order to ensure conformal contact between the stamp and the substrate, the material of the stamp has to be elastomeric. In microcontact printing, one master can be used to produce several identical stamps. Conveniently, each of these stamps can again be used multiple times.

In general, soft lithography techniques use elastomers, i.e. crosslinked amorphous polymers that are used at temperatures above their glass transition temperature. PDMS is the most widely used flexible elastomer used in microcontact printing.

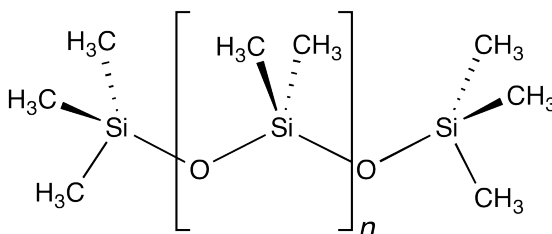


**Figure 11.5:** *Chemical structure of PDMS.*

PDMS consists of an inorganic siloxane backbone with organic methyl groups attached to it (see Figure 11.5). It can be used in a wide temperature range and is inert, non-toxic, optically transparent and biocompatible. Further, it is thermally and electrically insulating. With its low surface energy, PDMS can be removed easily from structures. Curing of PDMS can either be done at room temperature, or more rapidly at temperatures up to 120 °C. [283–285] In principle, PDMS is



hydrophobic due to its methyl groups. However, plasma treatment creates silanol groups and removes methyl groups, thereby creating a hydrophilic surface. [285, 286] Further properties of PDMS are summarized in Table 11.1.

Stability temperatures	$-50\text{ }^{\circ}\text{C}$ to $200\text{ }^{\circ}\text{C}$
Durometer hardness, Shore A	50
Tensile strength	7.1 MPa
Elongation at break	1.4
Young's modulus (tensile modulus)	1 MPa to 5 MPa
Surface energy	low, approximately $21.6\text{ mJ /m}^2$
Linear coefficient of thermal expansion	$310\text{ ppm /}^{\circ}\text{C}$
Hydrophobicity	hydrophobic
Permeability to gases	high
Optical properties	optically transparent down to 300 nm
Viscosity (prior to curing)	medium viscosity, at $23\text{ }^{\circ}\text{C}$ $4000\text{ mPa s}$
Elastic modulus	1.8 MPa
Compressibility	high, $2\text{ N /mm}^2$
Shear modulus	$\leq 1\text{ GPa}$
Work of adhesion	$10^{-7}\text{ J /mm}^2$

**Table 11.1:** *The properties of PDMS after curing.* Values taken from [282, 283, 287–291]

Although PDMS has appropriate mechanical properties for microcontact printing, printing accurate sub-micrometer patterns is challenging. In particular, features with a high aspect ratio tend to pair together due to the softness and mechanical flexibility of the material. Further, PDMS is prone to shrinkage during curing, leading to distortion. Also, adhesive forces during separation of the master and stamp can cause distortion of the features. These properties limit the usage of PDMS for the generation of patterns in the nanometer regime. [288, 290]

In principle, the adsorption of a protein on a surface is simple to perform. However, biological activity of the immobilized proteins might be lost or significantly altered. In particular in microcontact printing this issue occurs twice, during inking the stamp and during the transfer to the substrate [292]. In order to transfer the protein to the substrate, the adhesion of the protein with the

substrates must be higher than that of the protein with the stamp. Further, printing can also introduce mechanical stress on the protein, leading to conformational changes. However, various different proteins have been tested and their activity after printing compared to adsorption from solution [293]. Whereas antibodies and streptavidin are very robust against loss of function, enzymes are more susceptible to denaturation.

### 11.2.4 Application in cell biology

Protein micropatterns are used for a vast number of applications. In cell biology, these patterned protein surfaces are mainly used to interact with cell surface proteins in their native environment and composition. This technique was first used for tissue engineering and the creation of specific microenvironments by controlling the shape or adhesion geometries, e.g. to study cell growth in response to specific patterns [294–300]. Micropatterning also allows for the arrangement of receptors and other cell surface proteins into the desired shape. This can be achieved by printing an antibody against an extracellular domain of the cell surface protein of interest. Cells seeded onto such patterned surfaces will exhibit a redistribution of the specific surface protein according to the antibody pattern. The micropatterning technique has been used to study cell adhesion and phagocytosis [301, 302], signaling [303, 304], protein-ligand interactions [253, 305], and cellular protein-protein interactions [237, 250, 251, 306, 307].

## 11.3 ZAP70

The kinase ZAP70 and its interaction kinetics with the TCR will be discussed in more detail, as it is the central protein of this part. However, ZAP70 was already introduced in the context of T cell immunobiology and its role in T cell activation was described in section 2.2.1. In this section, the structure of ZAP70 will be described in more detail and models of its binding dynamics to the TCR will be presented.

### 11.3.1 Discovery of ZAP70

ZAP70 and its key role in T cell activation and development was discovered in 1994. ZAP70 is a protein tyrosine kinase of 70 kDa, primarily expressed in

T cells and NK cells [39, 308]. Due to its homology to porcine Syk, it was defined as a member of the Syk/ZAP70 kinase family [309]. Mutations in the ZAP70 have been reported to lead to a severe immunodeficiency, with the most of these identified mutation occurring in the catalytic domain of ZAP70 [310–312]. In mice lacking ZAP70, neither CD4 nor CD8-single positive T cells can be developed [313]. An essential step in T cell development is the encounter between the TCR and a MHC molecule bearing a self-peptide [43]. Further propagation includes positive and negative selection, i.e. T cells responding to antigens, but not as strongly as to be autoreactive, respectively. ZAP70-deficient mice lack this checkpoint [313, 314]. This leads to the proposed pathogenic mechanism for severe immunodeficiency in humans, that a complete lack of ZAP70 results in deficient TCR signaling capacity during early T cell development, which in turn leads to low numbers of CD8+ cytotoxic T cells and normal numbers of non-functional CD4+ helper T cells [315, 316].

### 11.3.2 Structure of ZAP70

ZAP70 is composed of two tandem SH2 domains, linked by an interdomain A (see Figure 11.6a). The second SH2 domain is linked to the carboxy-terminal (C-terminal) catalytic region via another linker region, the interdomain B [39, 317].

ZAP70 interacts with the double-phosphorylated ITAMs of the TCR  $\zeta$ -chain via its tandem SH2 domain [318], as depicted in Figure 11.6b. The amino-terminal (N-terminal) SH2 domain only has an incomplete phosphotyrosine binding pocket by itself, but it can be completed by the surface of the C-terminal SH2 domain [42, 43]. The current model suggests that first the C-terminal SH2 domain binds to the N-terminal phosphotyrosine of an ITAM. This allows for the binding of the C-terminal phosphotyrosine after proper alignment of the C- and N-terminal SH2 domains. The interdomain A is believed to mediate this conformational change. The interdomain B is the most important regulatory substructure of ZAP70. It contains three tyrosine residues, Y292, Y315 and Y319, which get phosphorylated by Lck following TCR stimulation [319]. The inactive state of ZAP70 is constituted by an auto-inhibited conformation, which is maintained by a close association between the distal surface of the kinase domain and the interdomains A and B. This results in a distorted conformation of the tandem SH2 domain, such that it is unable to bind to the ITAMs [320]. Mainly

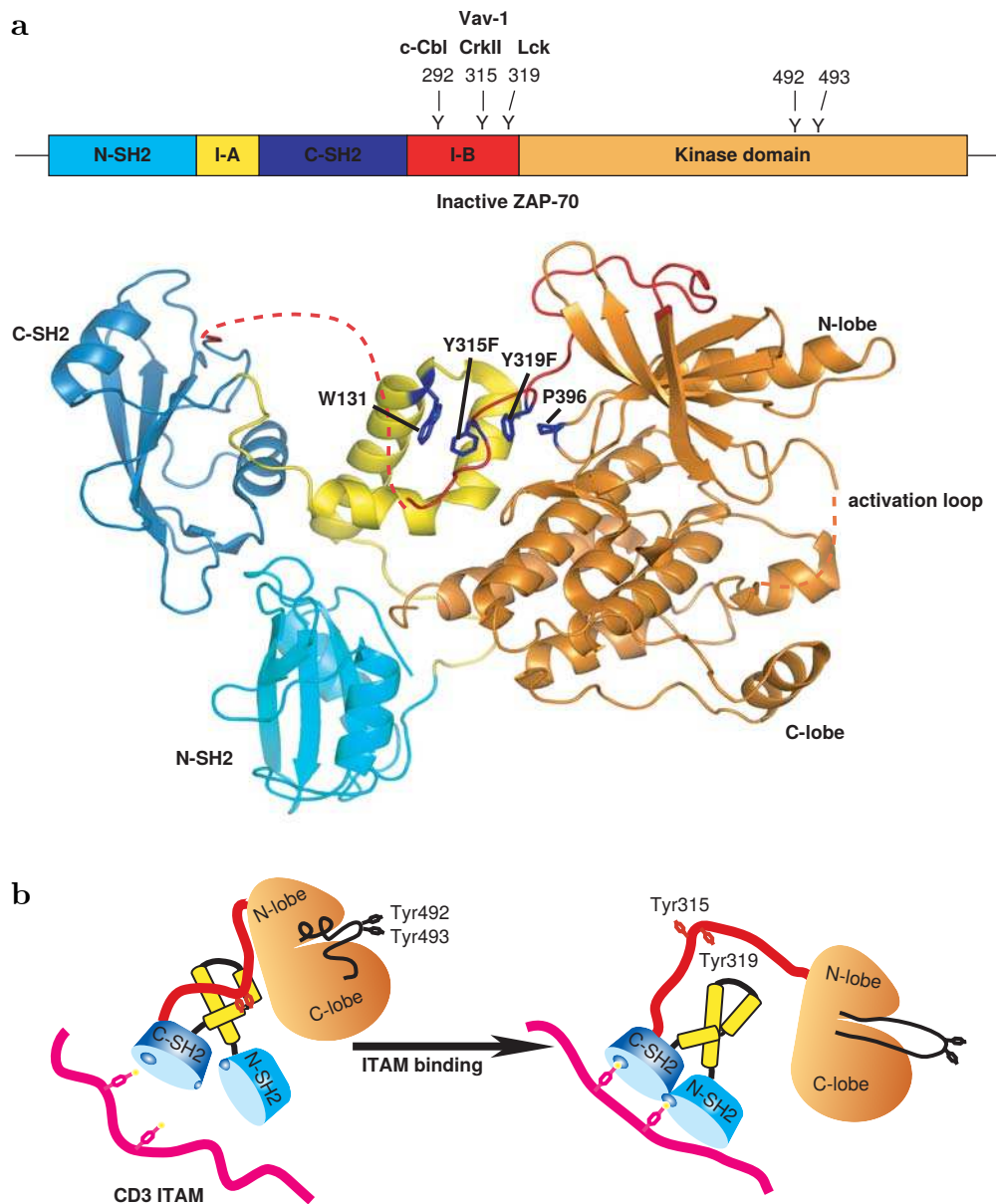


**Figure 11.6: Structural organization of autoinhibited ZAP70, and model of autoinhibition.** (a) The domain structure of ZAP70 and phosphorylated tyrosine residues with binding molecules (top), together with the crystal structure of autoinhibited ZAP70 (bottom). Here, the amino- and carboxy-terminal SH2 domains, the A and B interdomains as well as the kinase domain are shown in different colors. Important side chains of residues are highlighted. Dotted lines represent disordered regions. (b) Model for the activation of ZAP70 after binding to the doubly phosphorylated ITAMs (pink). ITAM binding introduces conformational changes in ZAP70 which leads to the exposure of tyrosines in interdomain B, resulting in their phosphorylation that further destabilizes the interface. Image taken from [41].

the Y315 and Y319 residues inside the interdomain B, but also the proline P147 residue which interacts with Y597 and Y598 in the C-lobe of the kinase domain, are responsible for this auto-inhibitory behavior [320].

### 11.3.3 ZAP70 in the TCR pathway

After Lck phosphorylates the tyrosines in the ITAMs of the CD3 and  $\zeta$ -chain of the TCR complex, ZAP70 is recruited to the plasma membrane and interacts with these phosphotyrosines [308, 321]. This leads to the release from its auto-inhibited conformation and the Y315 and Y319 residues inside the interdomain B are either autophosphorylated by ZAP70 or phosphorylated by Lck [317, 322, 323]. This subsequently destabilizes the auto-inhibited conformation of ZAP70 [320]. Following, the Y493 residue located inside the activation loop of the kinase domain of ZAP70 is phosphorylated by Lck, which leads to the subsequent auto-phosphorylation of Y492 by ZAP70 itself [324, 325]. This leads to a conformational change, displacing the activation loop from the catalytic site which activates the tyrosine kinase function of ZAP70 [42, 326]. Finally, ZAP70 is able to phosphorylate the transmembrane adapter protein LAT, which is involved in further downstream signaling pathways [327].

Different mutational studies highlight the role of different residues in ZAP70 on the TCR signaling pathway. For example, Y292 in the interdomain B plays a negative regulatory role for ZAP70 activation [328], and Y319 is involved in the  $\text{Ca}^{2+}$  mobilization and subsequent IL-2 secretion [322, 323]. In contrast, phosphorylated Y315 plays a regulatory role for the remodeling of the actin cytoskeleton [329]. Further, Y315 also participates in T cell adhesion via the integrin LFA1 [330, 331]. Through both mechanisms, ZAP70 influences the formation of the immunological synapse between T cells and APCs [332]. As ZAP70 activity is required for the internalization and degradation of TCR-CD3 complexes [333], it is also involved in TCR downregulation following antigen encounter.

Studies on Y315F-Y319F and Y315A-Y319A ZAP70 mutants show how conformational changes control the association and activity of ZAP70 to the TCR, in order to achieve maximal kinase and cellular activity. This led to the development of a model on a kinetic proofreading mechanism, based on multiple conformational and receptor-binding equilibria for the control of ZAP70 activity (see Figure 11.8). Here, TCR binding or phosphorylation of ZAP70 triggers a transition from a closed, autoinhibited conformation to an open conformation.

Ultimately, stabilized binding of ZAP70 to the TCR results in catalytic activity. [236]

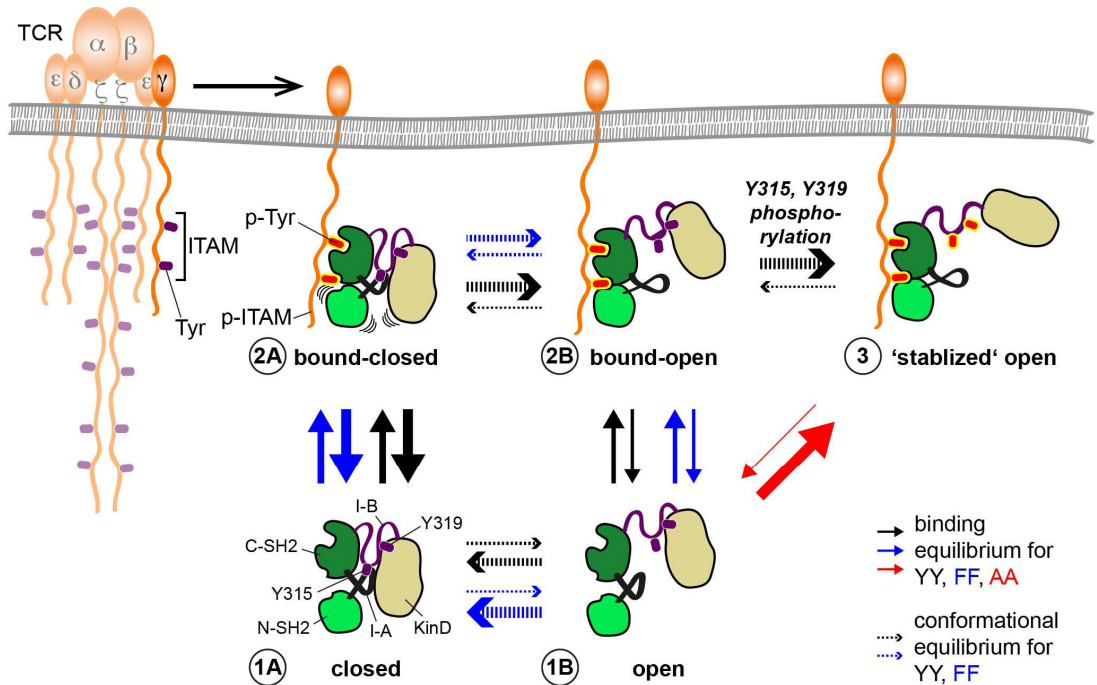


**Figure 11.7: Model of ZAP70 TCR-binding dynamics and activation.** Binding (continuous) and conformation equilibria (dotted) for wild-type ZAP70 (black) and different mutants (blue, red). While cytosolic ZAP70 is in a dynamic equilibrium between the autoinhibited and the open conformations (1A and 1B), binding leads to either a bound-closed or a bound-open complex (2A and 2B). Phosphorylation of Y315 and Y319 results in prolonged TCR association, as it stabilizes the open conformation (3). Arrow thickness depicts the reaction rate. Image taken from [236].

### 11.3.4 The dynamics of signaling complexes

Signaling complexes change in composition as certain proteins dissociate and reassociate. In particular, ZAP70 has been shown to remain associated with laterally immobile TCR clusters for 20 min and more. However, photobleaching studies reveal that ZAP70 dissociates from and reassociates with these signaling complexes. While the extent of fluorescence recovery decreases with increasing



spreading time, the time to half-maximal recovery remains in the range of 7.5 s to 10 s. Different underlying mechanisms could explain the reduced extent of fluorescence recovery. Either TCRs become incapable of rebinding ZAP70, or free ZAP70 becomes incapable of rebinding the TCR. Another possibility is that existing TCR-ZAP70 complexes are prohibited from dissociating. [45] Still, further studies are needed in order to confirm and refine this model.

Further studies investigating the recruitment, activation and release of ZAP70 at phosphorylated TCRs suggest a dynamic model with a catch-and-release mechanism. This model describes how ZAP70 is recruited to phosphorylated TCR-CD3 complexes via its SH2 domains, activated by phosphorylation and released into the plane of the plasma membrane (see Figure 11.8). Additional ZAP70 molecules can bind to the vacant TCR sites, thereby turning the TCR into a catalytic unit that amplifies antigenic stimuli. [234]

These studies give insights on the dynamics of the TCR-ZAP70 interaction. However, the role of ZAP70 in T cell activation is far from being understood, and further research is needed in order to obtain complete understanding of all involved mechanisms. Further, live cell experiments are often challenging to perform and include a superposition of different processes. Using sophisticated experimental designs helps to disentangle these processes.

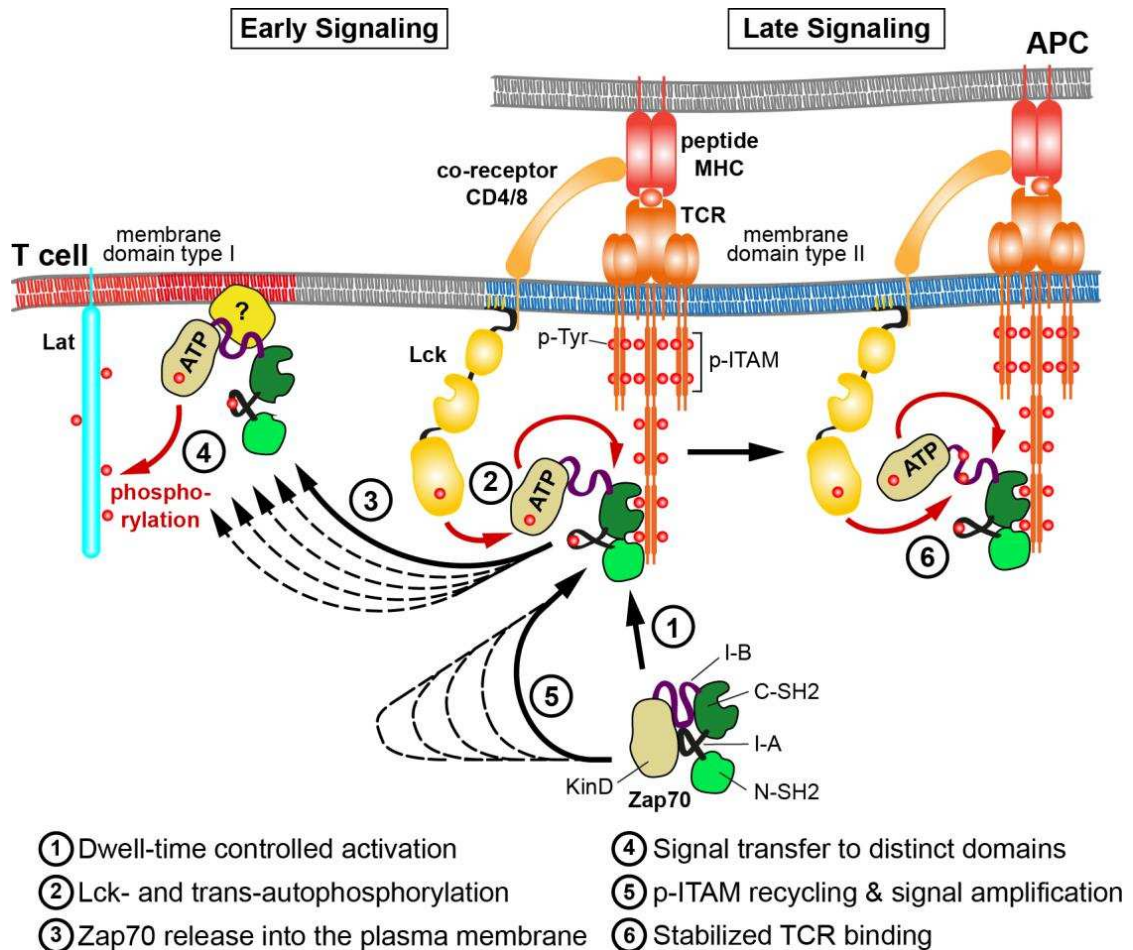


**Figure 11.8:** *TCR signal amplification and dispersion via a catch-and-release model in early and late ZAP70 signaling.* In early signaling, ZAP70 is phosphorylated on Y126, activated and binds ATP. ZAP70's release from the TCR into the plane of the plasma membrane creates a vacated p-ITAM which in turn is able to recruit, activate and release additional ZAP70 proteins. During late signaling, ZAP70 remains stably associated with the TCR. Image taken from [234].



# Chapter 12

## Results

Quantification of the intracellular binding kinetics between a membrane protein and a cytosolic interaction partner is rarely a simple task. Although FRAP experiments are commonly used to obtain kinetic parameters on protein interactions in living cells, they are often subject to non-specific contributions to the fluorescence recovery signal. Here, we combine this method with a protein micropatterning assay to eliminate such non-specific contributions and to considerably simplify analysis of FRAP data. This approach is applied to study the interaction between the TCR and the kinase ZAP70.

The experimental results described in this section have been published in [254].

### 12.1 Jurkat T cell activation on OKT3 micropatterns

An activating antibody against the CD3 $\epsilon$ -subunit of the TCR complex (OKT3) was microstructured into distinct patterns in order to capture the TCR at defined sites in living Jurkat T cells expressing ZAP70-GFP (see Figure 12.1). The protocol used for surface preparation has been previously described in [334]. In order to promote cell adhesion, the interspaces between the 1  $\mu$ m-sized OKT3 dots were filled with fibronectin. Jurkat T cells seeded onto patterned surfaces showed fast activation upon surface contact, together with the recruitment of ZAP70-GFP to OKT3-containing sites (see Figure 12.2).

Intracellular calcium levels were measured using the ratiometric calcium-sensitive dye Fura-2 AM, in order to ensure proper Jurkat T cell activation

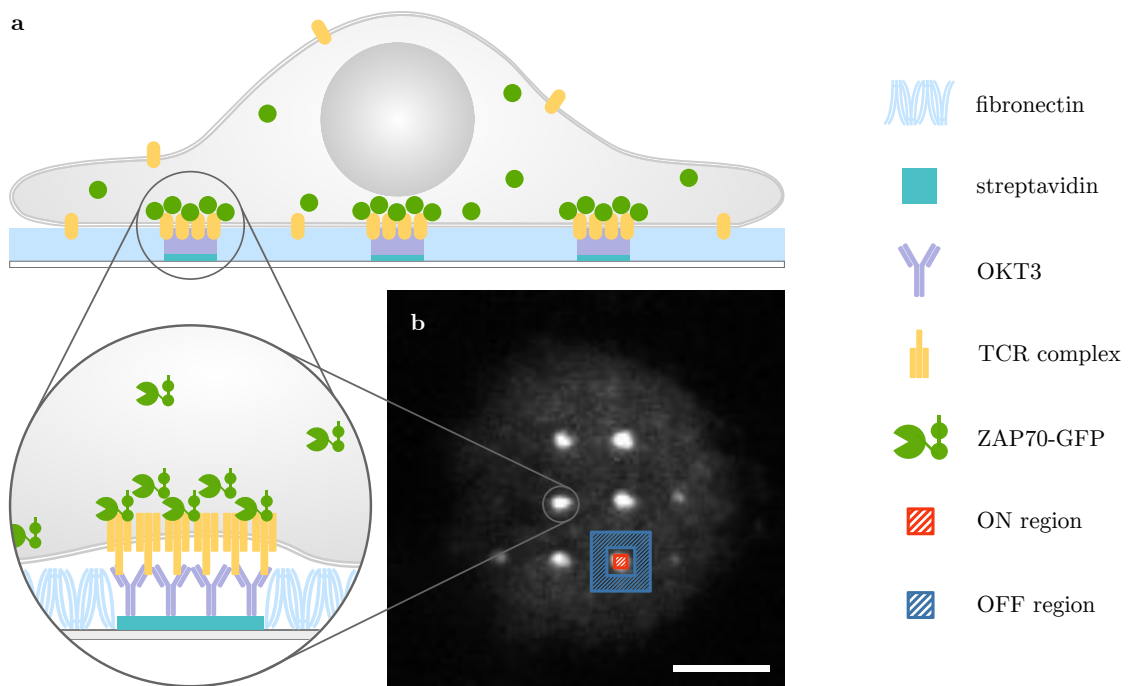


**Figure 12.1: A Jurkat T cell on patterned OKT3 antibody surface.** (a) Living Jurkat T cells are seeded onto OKT3 antibody patterns. Thereby TCR get enriched and immobilized at specific sites at the plasma membrane, and subsequently ZAP70 is recruited to these sites. (b) A typical cell showing enrichment of ZAP70-GFP at micropatterned OKT3/TCR sites. Selection masks for TCR-enriched (ON) and -depleted (OFF) areas are highlighted in red and blue, respectively. Scale bar is 5  $\mu\text{m}$ .

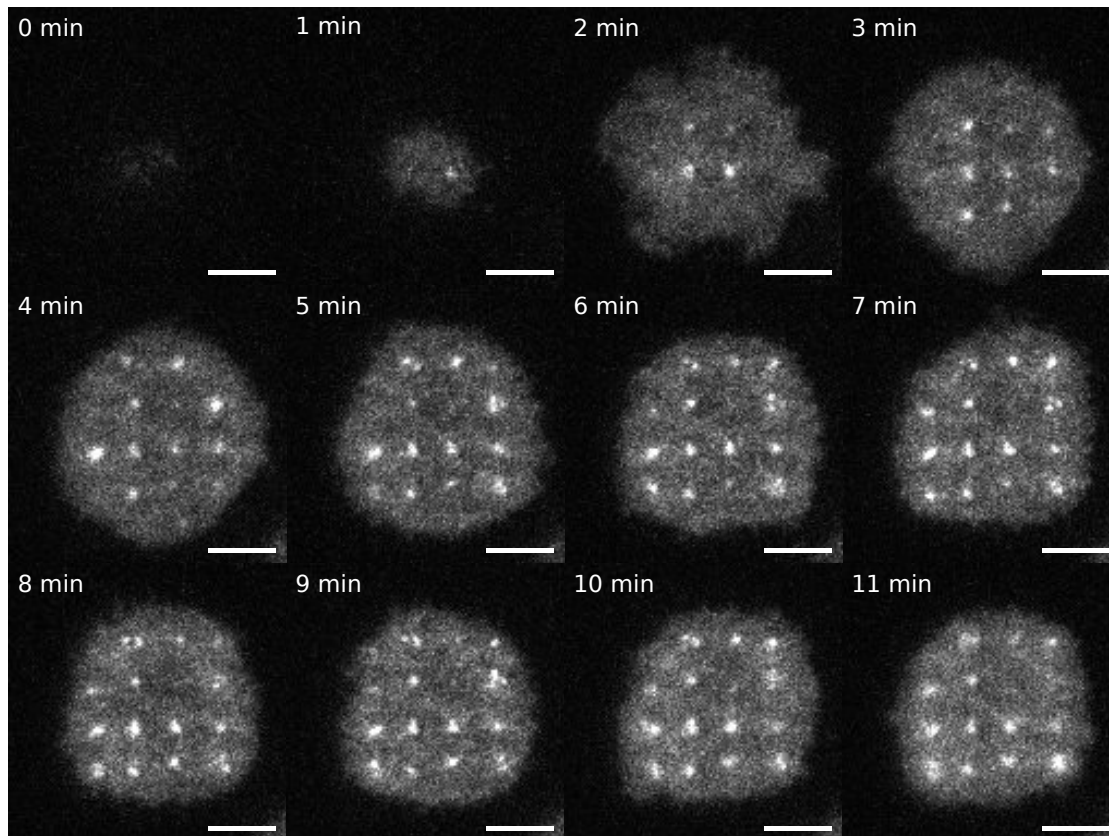


**Figure 12.2:** *Time course of ZAP70-GFP recruitment to OKT3 sites. The time course of a representative cell seeded onto a micropatterned OKT3 surface at  $t = 0$  min shows cell attachment as well as the formation of ZAP70-GFP pattern. Scale bar is  $5\ \mu\text{m}$ .*

on the microstructured surfaces. 64% of cells activated on micropatterned surfaces within 5 min after seeding, which is slightly less compared to cells seeded on surfaces homogeneously coated with OKT3 (see Figure 12.3a). This reduced activation may be attributed to the lower overall OKT3 density on patterned surfaces, since ~90% of the area does not contain OKT3. However, the local OKT3 density in the ON areas was similar to surfaces fully coated with OKT3 (see Figure 12.4). In contrast, on fibronectin-coated surfaces only ~15% of cells activated, similar to previously described values [335]. As expected, surfaces homogeneously coated with OKT3 induced microcluster formation over the whole cell area, whereas on patterned surfaces, ZAP70-GFP was enriched at OKT3/TCR sites (see Figure 12.3b for ZAP70-GFP distribution in representative cells on different surfaces).

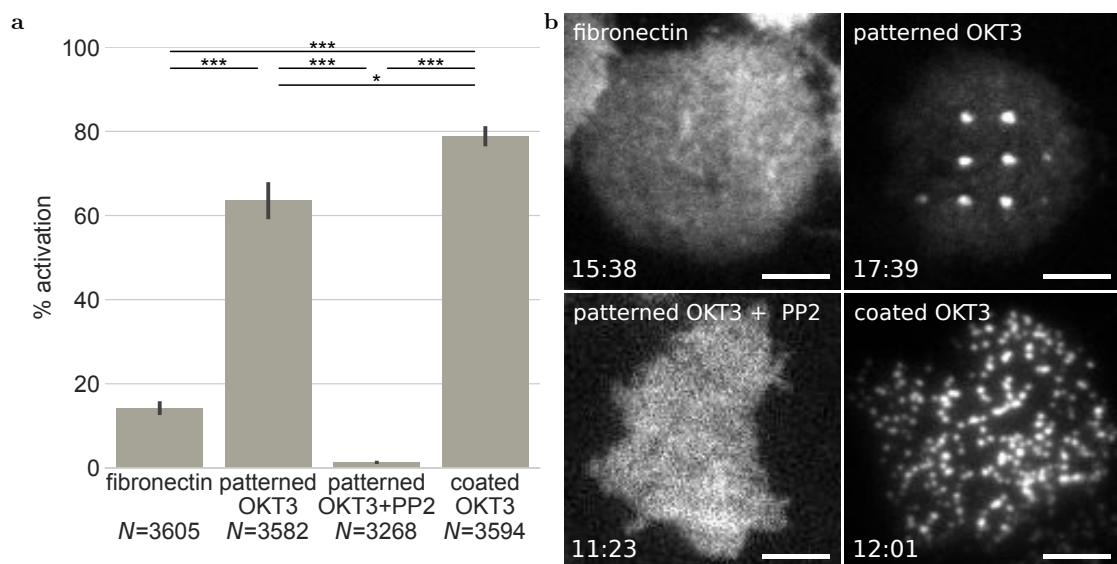


**Figure 12.3: Jurkat T cell activation on the different surfaces.** (a) Mean percentage of activated cells measured via the increase of intracellular  $Ca^{2+}$  levels ( $*P < 0.05$  and  $***P < 0.005$  (two-tailed unpaired *t*-test)). Error bars show the SEM in 3 or more different experiments. *N* indicates the total number of measured cells. (b) The ZAP70-GFP distribution in representative cells on different surfaces. The timepoint of image capture after cell seeding is shown in the bottom left corner. Scale bar is 5  $\mu$ m.

To confirm the specificity of ZAP70-GFP enrichment in CD3 ON areas, we investigated the recruitment behavior using patterns with different antibodies.

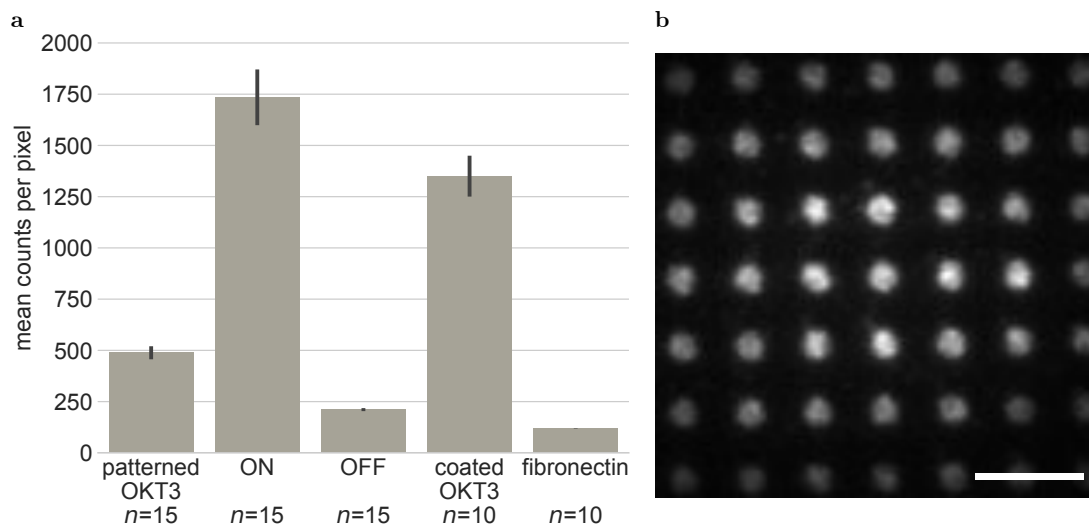


**Figure 12.4: Relative OKT3 antibody densities on patterned and homogeneously coated OKT3 surfaces.** (a) The relative densities of OKT3 antibodies labeled with Zenon Alexa Fluor 647 Mouse IgG2a Fab fragments given by the fluorescence intensities. Data from three independent experiments (average  $\pm$  SEM); the number of measured areas is indicated as  $n$ . (b) A patterned OKT3 surface labeled with Zenon Fab fragments. Scale bar is  $5\mu\text{m}$ .

While surfaces patterned with the CD3 $\epsilon$  antibody clone MEM-57 resulted in ZAP70-GFP patterning, no ZAP70-GFP pattern formation was observed for a non-specific antibody (see Figure 12.5).

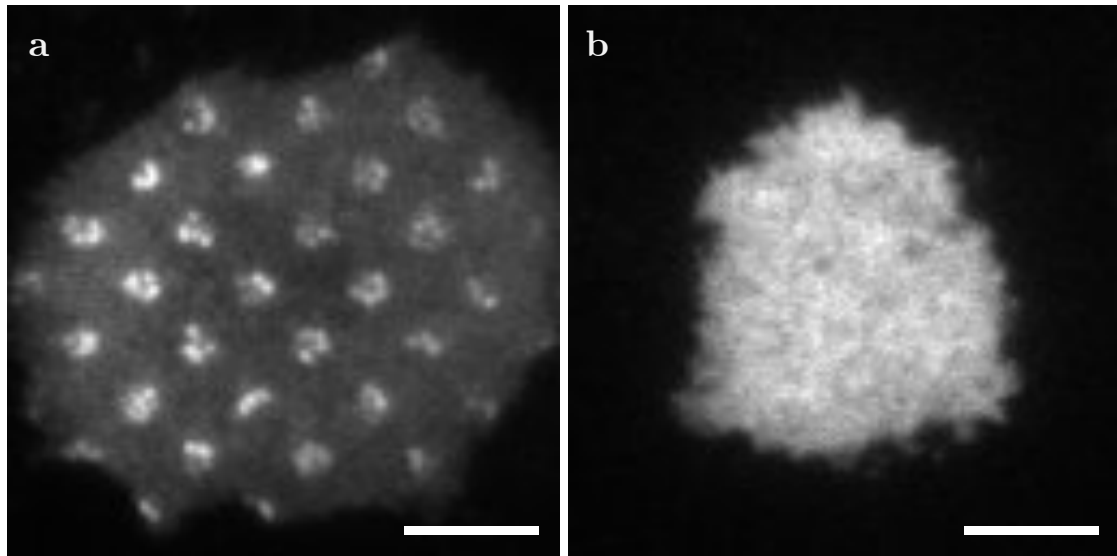


**Figure 12.5:** *Specificity of ZAP70-GFP recruitment to aCD3 ON areas. (a) Cells seeded onto micropatterned surfaces featuring antibodies against the CD3 $\epsilon$  epitope MEM-57 show the recruitment of ZAP70-GFP to the ON areas. (b) In contrast, a micropatterned antibody against an HA-tag did not lead to a redistribution of ZAP70-GFP. Cells were allowed to adhere to the surface for 10 min before image capture. Scale bar is 5  $\mu$ m.*

The Src kinase inhibitor PP2 has been shown to block ZAP70 recruitment to the activated TCR on anti-CD3 substrates [45, 54, 336]. T cell activation, as well as ZAP70-GFP pattern formation was abolished in the presence of 40  $\mu$ M PP2, which further ascertains that the appearance of patterns was a consequence of ZAP70-GFP recruitment to the TCR in the course of T cell activation (see Figure 12.3).

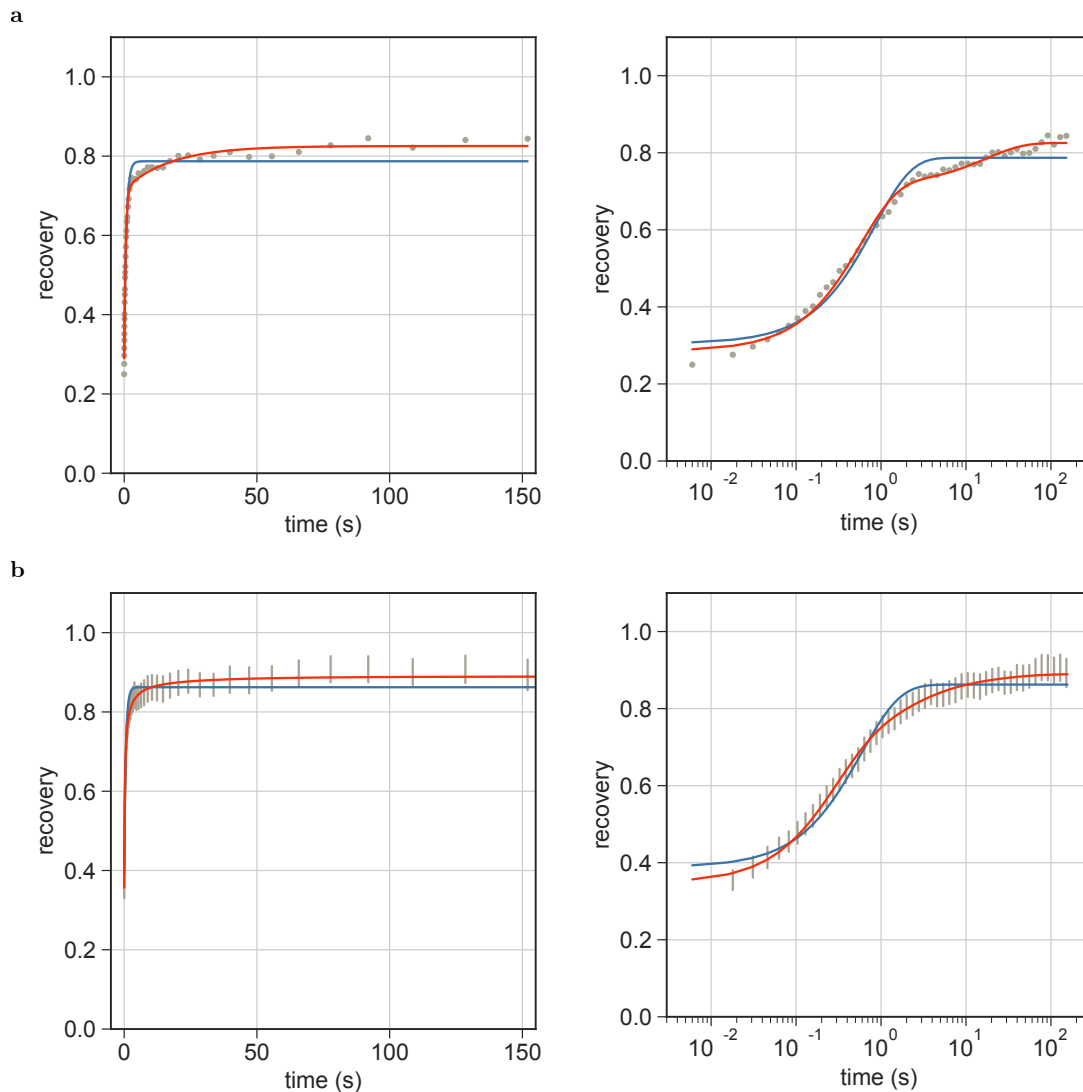


**Figure 12.6: FRAP experiments on non-activated Jurkat T cells.** (a) A representative FRAP curve of ZAP70-GFP measured in a cell seeded onto a fibronectin-coated surface shown using a linear (left) and a logarithmic (right) scale on the x axis. A biexponential fit (see Equation 12.2, shown in red) yielded  $\tau_1 = 0.57\text{ s}$ ,  $\tau_2 = 17.4\text{ s}$ ,  $F_\infty = 0.83$ ,  $F_i = 0.29$  and  $c = 0.80$ . As a reference, a monoexponential fit (see Equation 12.1) is shown in blue. (b) The averaged FRAP curves of ZAP70-GFP measured in cells on a fibronectin-coated surface obtained from three independent experiments with 17 different cells. The 95 % confidence interval is shown. Mean values  $\pm$  SE from cells fitted individually with Equation 12.2 were:  $\tau_1 = 0.29 \pm 0.03\text{ s}$ ,  $\tau_2 = 12.6 \pm 3.9\text{ s}$ ,  $F_\infty = 0.89 \pm 0.02$ ,  $F_i = 0.35 \pm 0.01$  and  $c = 0.67 \pm 0.03$ . The average of all fit curves is shown in red.



## 12.2 Complex recovery behavior of ZAP70-GFP in non-activated Jurkat T cells

In a typical FRAP experiment, ideally all fluorescent molecules in a defined region of interest within the cell are bleached by a short and powerful laser pulse. Then, the recovery of fluorescence in this region is monitored over time. In order to understand ZAP70-TCR binding kinetics, we decided to first establish a baseline by measuring the ZAP70-GFP recovery behavior in non-activated cells (see Figure 12.6). After seeding cells on homogeneously coated fibronectin surfaces, we performed FRAP experiments with a modified timing protocol—the intense bleach pulse is followed by a logarithmically timed illumination protocol, in order to effectively capture the fast recovery of ZAP70-GFP from the cytosol, but minimize photobleaching at later time points (for details see the Methods chapter 14).

After recording, the measured recovery curves were normalized and corrected for bleaching during image acquisition and depletion caused by the bleach pulse as described in the Methods chapter 14. Although the penetration depth of the TIRF field ( $\sim 100$  nm to 200 nm) is rather small compared to the height of the cell, the bleach pulse causes a significant depletion of the cytosolic pool of ZAP70-GFP. By applying an alternative FRAP protocol, we were able to determine this depletion to be  $\sim 12\%$  (see Figure 12.7), and to subsequently correct for it.

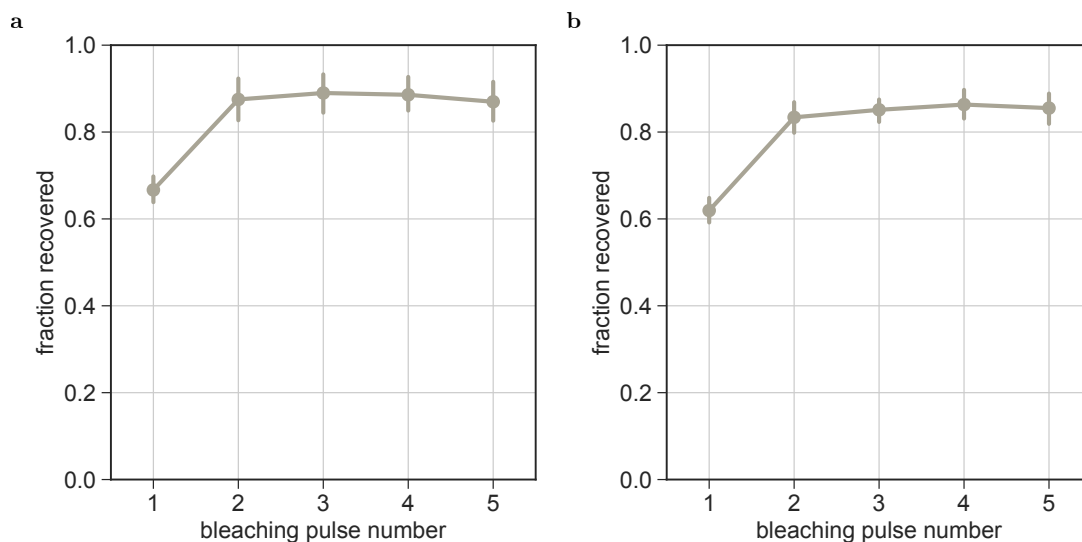
The analysis of the recovery behavior of ZAP70-GFP in cells on fibronectin-coated coverslips revealed substantial deviations from the monophasic recovery behavior. Figure 12.6 shows the recovery curves of a representative cell (panel a) as well as pooled recovery curves for all cells measured (panel b). In order to approximate these recovery curves, we fitted them with an empirical model consisting of one (Equation 12.1), or a sum of two exponential functions (Equation 12.2).

$$F(t) = (F_{\infty} - F_i)[1 - e^{-t/\tau}] + F_i \quad (12.1)$$

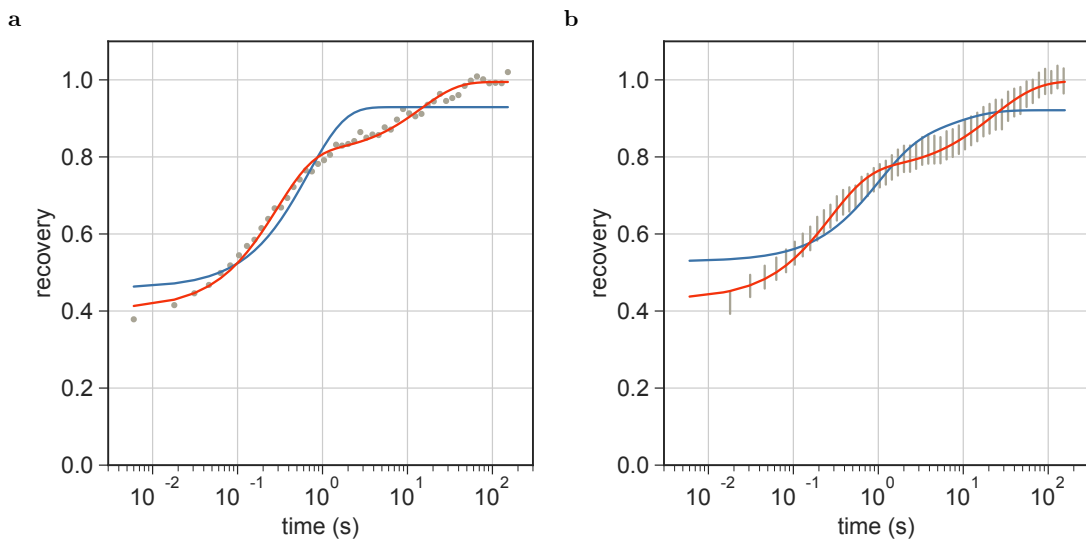
$$F(t) = (F_{\infty} - F_i)[1 - ce^{-t/\tau_1} - (1 - c)e^{-t/\tau_2}] + F_i \quad (12.2)$$

Here,  $\tau$ ,  $\tau_1$  and  $\tau_2$  are the exponential time constants and  $F_{\infty}$  is the mobile fraction.  $F_i$  is a factor accounting for incomplete bleaching, ZAP70-GFP recovery from the cytosol during the 500 ms bleach pulse and before the first recovery





**Figure 12.7: Recovering fraction of ZAP70-GFP after repetitive bleach pulses.** Five consecutive images were recorded 1 s after the end of a 500 ms bleach pulse each and then normalized to the corresponding pre-bleach image. The short time interval between bleach pulses only allows for the recovery of the fast fraction of ZAP70-GFP, not however for the slower fraction. The recovering fraction increases with successive bleach pulses to level out at  $\sim 88\%$  (a) and  $\sim 85\%$  (b), indicating that the depletion of the cytosolic pool of ZAP70-GFP caused by the bleach pulse amounts to  $\sim 12\%$  and  $\sim 15\%$  at  $22^\circ\text{C}$  and  $37^\circ\text{C}$ , respectively. Data are from two independent experiments with 50 (a) and 21 (b) different cells (average + 95% confidence interval shown).



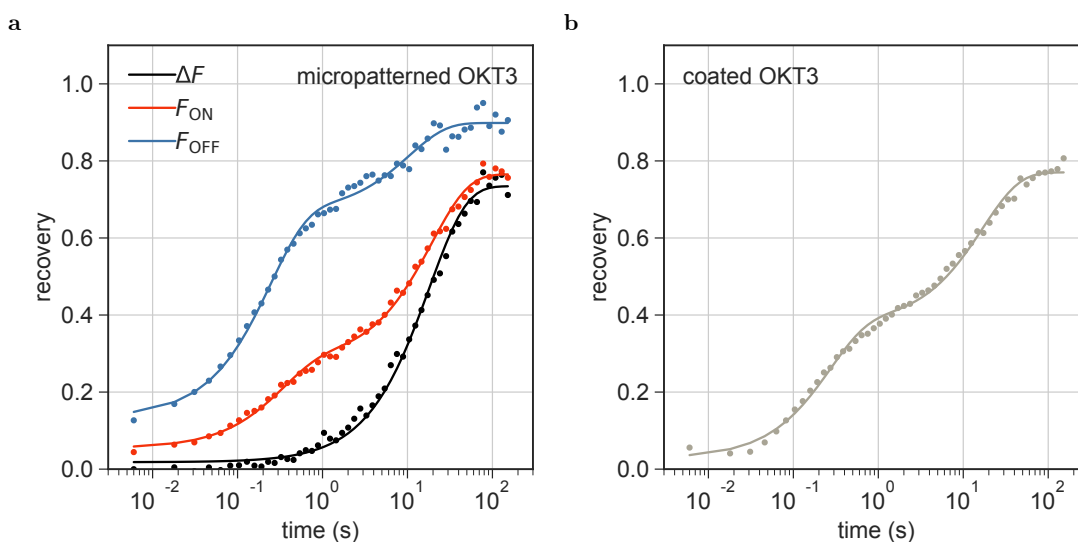
**Figure 12.8: FRAP data recorded in cells expressing cytosolic GFP on a fibronectin-coated surface.** (a) A FRAP curve of cytosolic GFP measured in a representative cell on a fibronectin-coated surface. A biexponential fit (see Equation 12.2, shown in red) yielded  $\tau_1 = 0.29$  s,  $\tau_2 = 14.46$  s,  $F_\infty = 0.99$ ,  $F_i = 0.40$  and  $c = 0.68$ . A mono-exponential fit is shown in blue as a reference. (b) The averaged FRAP curves of cytosolic GFP measured in cells on a fibronectin-coated surface obtained from three independent experiments with 29 different cells. The 95 % confidence interval is shown. Mean values  $\pm$  SE from cells expressing cytosolic GFP fitted individually with Equation 12.2 were:  $\tau_1 = 0.28 \pm 0.02$  s,  $\tau_2 = 25.4 \pm 2.4$  s,  $F_\infty = 1.00 \pm 0.01$ ,  $F_i = 0.43 \pm 0.01$  and  $c = 0.59 \pm 0.02$ . The average of all fit curves is shown in red.

image was taken at  $t = 6$  ms.  $c$  is the fraction of the first component in the biexponential fit.

This more slowly recovering fraction of ZAP70-GFP could have different origins. In principle, it could be a consequence of cell activation, as  $\text{Ca}^{2+}$  experiments showed that a small percentage of cells ( $\sim 15\%$ ) is activated even under per se non-activating conditions. However, this explanation seems rather unlikely, as the slow component was observed not only in a subset but in every measured cell. Further, ZAP70-GFP could experience transient trapping in membrane ruffles or within the cortical actin or microtubule network. This molecular sieving effect would cause a size-dependent retardation of cytoplasmic molecules [247]. Another explanation is based on the fact that the bleach pulse creates a gradient in the bleached cytosolic pool of ZAP70-GFP, resulting in a prolonged diffusional recovery [235]. Finally, it is also possible that ZAP70 transiently binds to one or more unknown membrane proteins or directly to the plasma membrane via its SH2 domain [44], and that this membrane-associated fraction recovers more slowly. In order to investigate these different options, we applied the same FRAP protocol to Jurkat cells expressing cytosolic GFP which again resulted in biphasic recovery curves (see Figure 12.8). In comparison, most fit parameters were quantitatively similar for ZAP70-GFP and GFP with differences in the mobile fraction ( $\sim 11\%$  of ZAP70-GFP did not recover, while cytosolic GFP fully recovered) as well as in the slow recovery rate  $\tau_2$ , which was smaller for ZAP70-GFP and showed a larger cell-to-cell variability. These results suggest that this complex biphasic recovery behavior in non-activated cells at least partly arises from cellular structures and/or diffusion during the bleach pulse with possible contributions from a membrane-bound fraction of ZAP70. Interestingly, a similar diffusional recovery from the cytosol with a slow late component has been described for clathrin light and heavy chains [235].

### 12.3 Micropatterning to specifically probe ZAP70-TCR binding kinetics

In order to investigate ZAP70-TCR binding kinetics, we focused on activated Jurkat T cells next. Here, the recovery behavior of ZAP70-GFP is expected to contain all contributions present in non-activated cells, but with at least one



**Figure 12.9: ZAP70-GFP recovery in cells on micropatterned and coated OKT3 surfaces.** (a) Recovery of fluorescence over time in ON and OFF areas in a representative micropatterned cell is shown in red and blue, respectively. Fitting with Equation 12.2 yielded  $\tau_1 = 0.2$  s,  $\tau_2 = 10.5$  s,  $F_\infty = 0.90$ ,  $F_i = 0.14$  and  $c = 0.7$  for the OFF curve, and  $\tau_1 = 0.3$  s,  $\tau_2 = 19.4$  s,  $F_\infty = 0.77$ ,  $F_i = 0.05$  and  $c = 0.32$  for the ON curve. The relative recovery of fluorescence  $\Delta F$  over time is shown in black and was fit with Equation 12.1 yielding  $\tau = 18.1$  s,  $F_\infty = 0.73$ ,  $F_i = 0.02$ . (b) Recovery of fluorescence over time in a representative cell on a homogeneously coated OKT3 surface fitted with Equation 12.2 yielding  $\tau_1 = 0.26$  s,  $\tau_2 = 17.0$  s,  $F_\infty = 0.77$ ,  $F_i = 0.03$  and  $c = 0.47$ .

additional component reflecting its dissociation from the TCR. An exemplary recovery curve for an activated cell on micropatterned (panel a) and on homogeneously coated (panel b) OKT3 surfaces can be seen in Figure 12.9. Due to the micropatterning approach we were able to analyze the recovery behavior in the ON and OFF areas separately. For this, we again used a biexponential fit (see Equation 12.2) as an empirical approximation to describe the recovery curves. Interestingly, the recovery curves in OFF regions (Figure 12.9a, blue) feature a slow late component, that is even more pronounced than in non-activated cells. This is particularly intriguing with respect to the proposed catch-and-release model described in section 11.3, in which ZAP70 is released from the TCR into the plasma membrane via binding to an unknown partner in early TCR signaling [234]. It is therefore quite possible, that for activated T cells an additional membrane-bound fraction of ZAP70 contributes to the recovery curve.

In contrast to OFF areas, even more effects contribute to the recovery curves of ZAP70-GFP in activated Jurkat T cells in ON areas or on homogeneously coated OKT3 surfaces, which makes their analysis particularly challenging. However, in this experimental design, the micropatterning approach allows us to isolate contributions specific to the TCR binding in a straight-forward manner. The OKT3-free OFF areas of micropatterned cells can serve as reference areas to correct the fluorescence recovery in the detection (OKT3 ON) areas (Figure 12.9a, blue and red, respectively), as in the OFF area fluorescence recovery of ZAP70-GFP is governed by cytosolic diffusion plus other non-specific contributions only. Ideally, the relative recovery of fluorescence in the ON areas compared to OFF areas,  $\Delta F = F_{\text{ON}} - F_{\text{OFF}}$ , only contains the contribution of ZAP70-GFP binding to the TCR (Figure 12.9a, black). Then, it was observed that  $\Delta F$  exhibits an exponential behavior and it was thus fit with Equation 12.1.

The key FRAP parameters (recovered fraction and unbinding time constant) from the relative fluorescence recovery curve obtained using the micropatterning approach were compared with the analogous parameters extracted from cells on homogeneously coated OKT3 surfaces using Equation 12.2. Bunnell et al. as well as Katz et al. reported a dependence of the mobile fraction of ZAP70 on the measurement time point after seeding [45, 234]. Furthermore, experiments showed a certain degree of cell-to-cell variability due to different expression levels of the TCR and proteins involved in the signaling cascade such as Lck and CD45. Therefore, the recovery curve for each cell was fit individually and the obtained

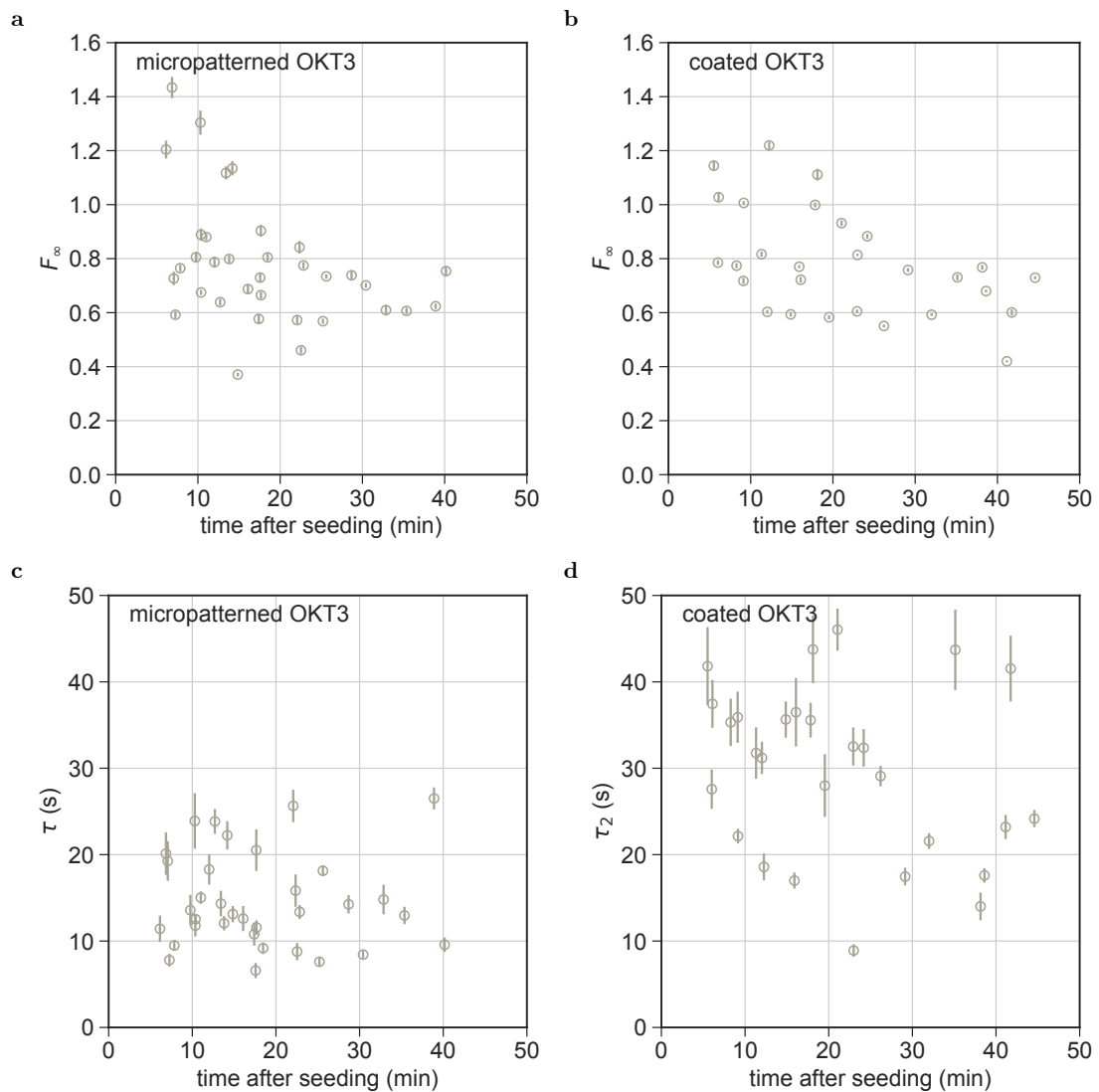


**Figure 12.10:** Comparison of several FRAP parameters for cells on micropatterned and homogeneously coated OKT3 surfaces at 22°C. The fraction of mobile ZAP70-GFP  $F_{\infty}$  ((a), (b)) and the unbinding time constants  $\tau$  and  $\tau_2$  ((c), (d)) are plotted over time after seeding for cells on micropatterned ( $N = 34$ ) ((a), (c)) and homogeneously coated ( $N = 28$ ) ((b), (d)) OKT3 surfaces. Error bars show the SE of the fit.

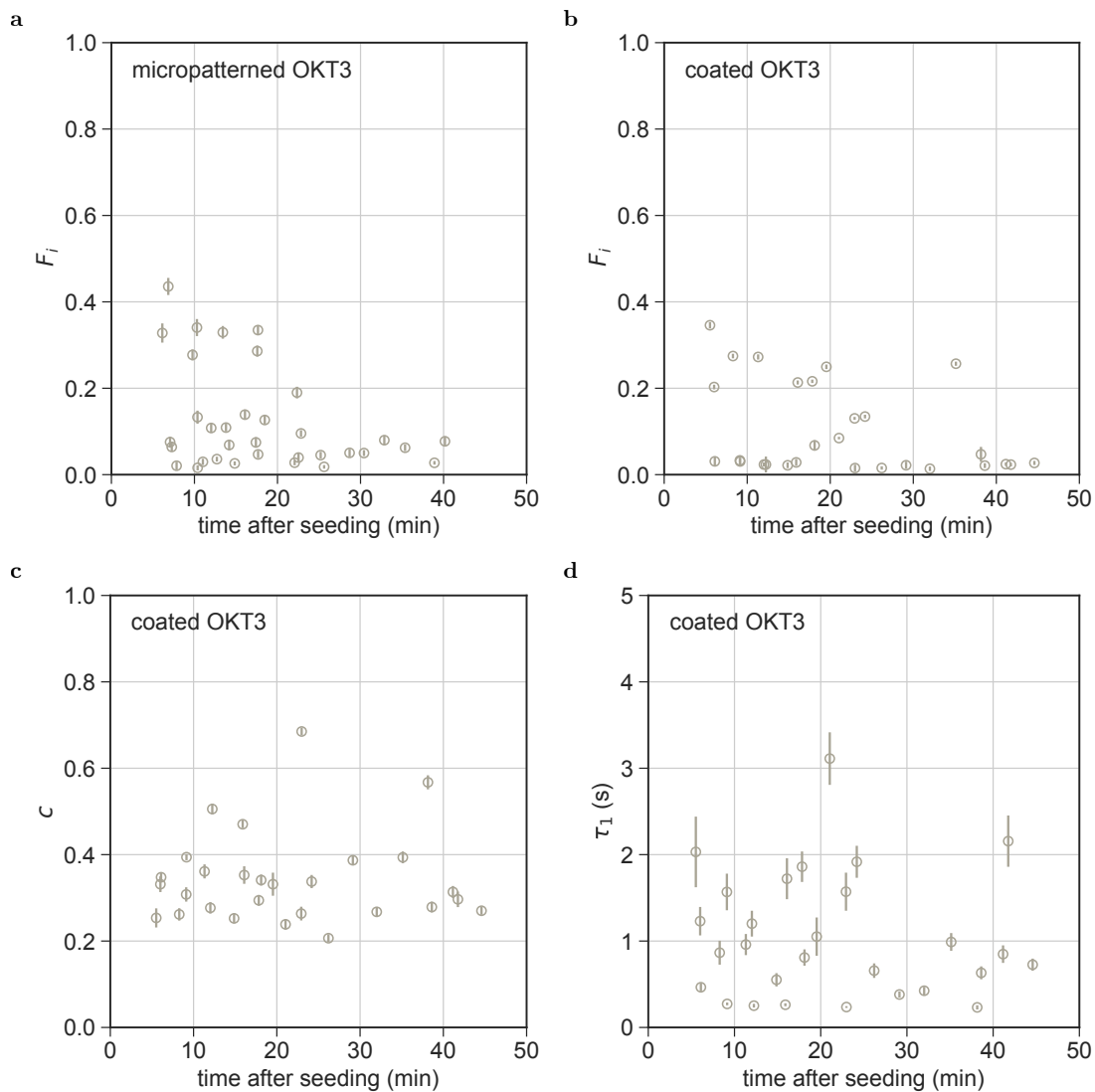


**Figure 12.11:** Comparison of several other FRAP parameters for cells on micropatterned and homogeneously coated OKT3 surfaces at 22°C. The fitting parameters  $F_i$ ,  $c$  and  $\tau_1$  are plotted over time after seeding for cells on micropatterned ( $N=34$ , 3 independent experiments) ((a)) and homogeneously coated ( $N=28$ , 4 independent experiments) ((b)-(d)) OKT3 surfaces. Error bars show the SE of the fit.

key FRAP parameters were plotted as a function of the measurement time point (see Figure 12.10). For completeness, figure 12.11 shows FRAP parameters of minor interest ( $\tau_1$ ,  $F_i$  and  $c$ ), plotted as a function of time, and a listing of all extracted averaged parameters is given in Table 12.1. In the following sections, data and fit results obtained from cells on micropatterned and homogeneously coated OKT3 surfaces will be compared.

T	min after seeding	surface	$\tau_1$ (s)	$\tau_2/\tau$ (s)	$F_\infty$	$F_i$	$c$	$N$
22 °C	5-45	pattern	—	14.6±1.0	0.78±0.04	0.12±0.02	—	34
		coating	1.0±0.1	29.7±1.9	0.78±0.04	0.10±0.02	0.34±0.02	28
37 °C	5-15	pattern	—	6.7±1.1	0.68±0.03	0.07±0.01	—	8
		coating	1.6±0.3	15.6±3.7	0.76±0.04	0.21±0.05	0.33±0.07	7
	25-45	pattern	—	4.7±0.90	0.57±0.04	0.05±0.01	—	8
		coating	1.2±0.2	20.7±5.3	0.57±0.05	0.17±0.04	0.43±0.05	8

**Table 12.1: Parameters extracted from FRAP curves.** Cells seeded onto micropatterned and homogeneously coated OKT3 surfaces were fit individually with Eq. 1 and Eq. 2, respectively. Mean fit values  $\pm$  SEM are listed for  $\tau_1$ ,  $\tau_2$ ,  $F_\infty$ ,  $F_i$  and  $c$ . For cells measured at 22 °C, all cells shown in Figure 12.10 were included. For data recorded at 37 °C, cells were grouped according to the timepoints of their measurement (5-15 minutes and 25-45 minutes after seeding).  $N$  indicates the number of cells in the time group. Data were recorded in at least 2 independent experiments.

## 12.4 Mobile fraction

In both cases, a mobile fraction  $F_\infty$  of 78 % was observed in cells measured at 22 °C (see Table 12.1 and Figure 12.10). Interestingly, at early measurement time points after seeding, some cells showed a recovery of fluorescence intensity above 100 %. This behavior is attributed to the fact that in these cells one or more dots or microclusters, which appeared rather dim in the prebleach image, increased in brightness during the recovery process. This can be explained by either the new recruitment of ZAP70-GFP to sites of immobilized TCR additionally to the exchange of previously bound ZAP70 or additional accumulation of TCR at



these sites. As not all cells make surface contact at the same time, there might be some uncertainty on the time axis. Apart from that, no correlation of the mobile fraction  $F_\infty$  with the time point after cell seeding was observed.

TCR signaling can be split in early signaling (directly after contact is established) and late signaling (after 30 min), with previous studies conducted at 37 °C suggesting that a conformation of ZAP70 becomes dominant in the late signaling regime that is more stably associated with the TCR and does not recover on the timescale of 2 min. In particular, the mobile fraction of ZAP70 in the first 10 min after cell seeding was reported to range from ~65 to 85 % and decreased to ~30 % after 30 min [45, 234]. At room temperature, T cell activation happens much slower in comparison to 37 °C, therefore it is possible that late signaling stages are not reached within the 45 min of our experiments. In order to address this point in more detail, we conducted our experiments also at 37 °C. Similarly to published results, a pronounced time dependence of the mobile ZAP70-GFP fraction in cells on patterned and homogeneously coated OKT3 surfaces was found (see Figure 12.12 and Table 12.1). In the early signaling regime (in the first 15 min after cell seeding), the fluorescence recovery was 68 and 76 %, on patterned and coated OKT3 surfaces, respectively, but both of these values decreased to 57 % after 25 min. A quantitative comparison of values with previously published data is difficult to accomplish due to the different treatment of the offset of the recovery curves (taken here into account as  $F_i$  in Equations 12.1 and 12.2, but not in earlier work [45, 234]). Figure 12.13 shows the FRAP parameters  $\tau_1$ ,  $F_i$  and  $c$  as a function of the timepoint after seeding for cells measured at 37 °C.

## 12.5 Interaction times

Next, we investigated ZAP70-TCR interaction times. While ZAP70-GFP unbinding time constants extracted from patterned cells at 22 °C were not dependent on the time after seeding (see Figure 12.10c,d), a minor dependence was observed at 37 °C. In particular, time constants were by a factor of 2–2.5 lower at 37 °C than at 22 °C. In contrast to mobile fractions, ZAP70-GFP unbinding time constants differed between cells on micropatterned and those on OKT3-coated surfaces (see Table 12.1 and Figures 12.10c,d and 12.12c,d). Time constants extracted from cells on micropatterned OKT3 surfaces were in general lower and

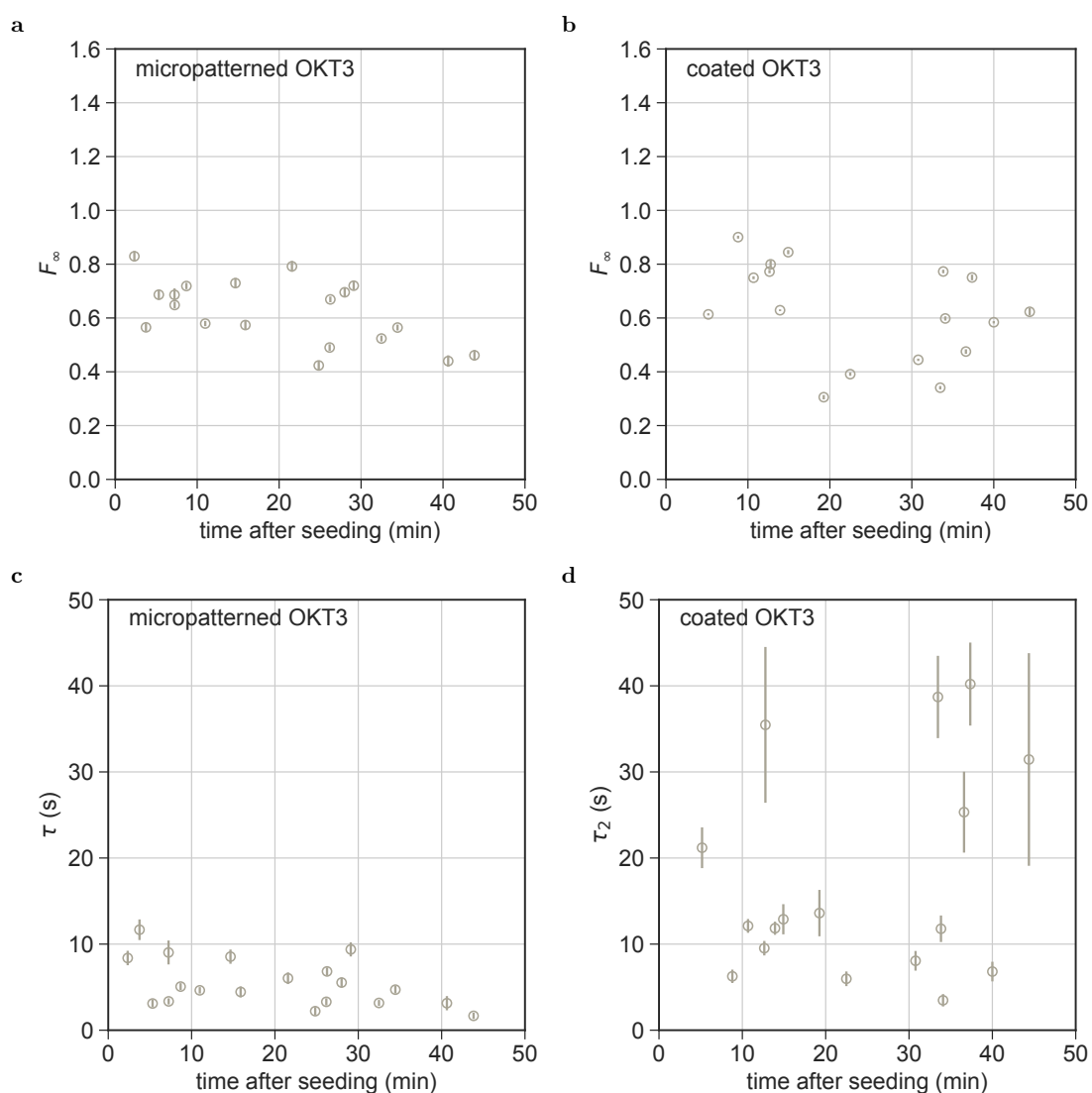


**Figure 12.12: Comparison of several FRAP parameters for cells on micropatterned and homogeneously coated OKT3 surfaces at 37°C.** Cells seeded onto micropatterned and homogeneously coated OKT3 surfaces were fit individually with Equation 12.1 and Equation 12.2, respectively. Mean fit values  $\pm$  SEM are listed for  $\tau_1$ ,  $\tau_2$ ,  $F_{\infty}$ ,  $F_i$  and  $c$ . For cells measured at 22°C, all cells shown in Figure 12.10 were included. For data recorded at 37°C, cells were grouped according to the timepoints of their measurement (5 min to 15 min and 25 min to 45 min after seeding).  $N$  indicates the number of cells in the time group. Data were recorded in at least 2 independent experiments.

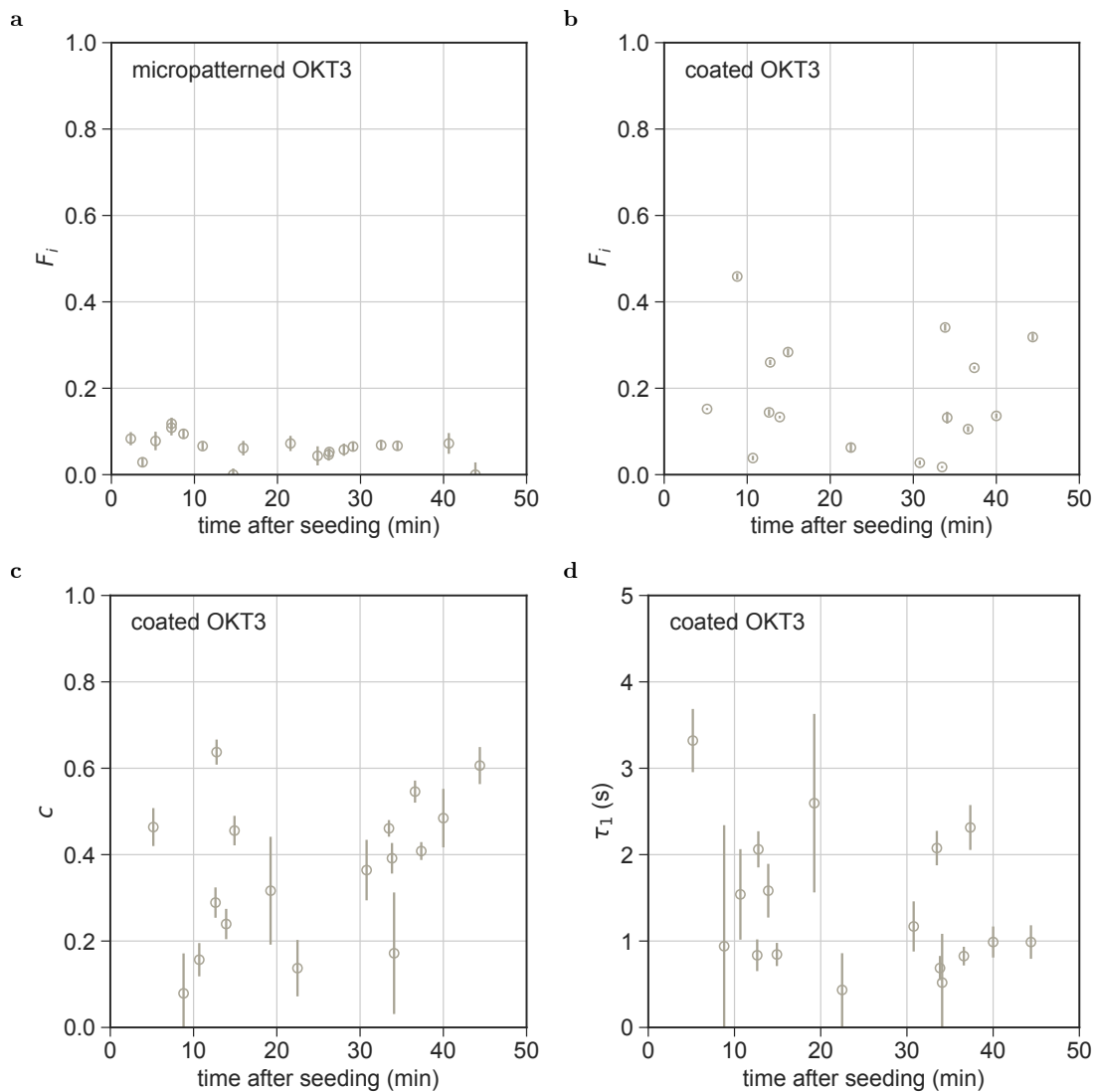


**Figure 12.13:** Comparison of FRAP parameters for cells on micropatterned and homogeneously coated OKT3 surfaces at 37°C. The fitting parameters  $F_i$ ,  $c$  and  $\tau_1$  are plotted over time after seeding for cells on micropatterned ( $N=19$ , 2 independent experiments) ((a)) and homogeneously coated ( $N=17$ , 2 independent experiments) ((b)-(d)) OKT3 surfaces. Error bars show the SE of the fit.

showed less variability than on homogeneously coated OKT3 surfaces. As already mentioned in section 11.1.4, fitting a sum of exponentials, especially to rather noisy data such as single cell FRAP curves, is known to be an ill-conditioned problem and thus prone to yield erroneous fit parameters [265]. This aspect certainly contributes to the heterogeneity observed for cells on coated OKT3 surfaces, whereas the situation is further complicated by the fact that an exponential function itself does not correctly describe the fast recovery from the cytosol.

Non-specific contributions compromising the ZAP70-GFP recovery data recorded for cells on homogeneously coated OKT3 surfaces most likely lead to an overestimation of the unbinding time constants. Indeed, this effect was previously observed in TIR-FRAP measurements of clathrin heavy and light chain exchange in clathrin-coated pits [235], in which the authors found that fluorescence recovery in pits was not exponential, and the recovery outside of pits had a late slow-rising component. Correction of their FRAP data in clathrin-coated pits using an approach similar to protein micropatterning lead to diffusion-corrected curves that could be approximated well by a monoexponential function. When compared to those previously reported in the literature, their extracted time constants were smaller by a factor of 2, which the authors attributed to diffusion artifacts. Compared to our observations for ZAP70-GFP, these findings are surprisingly similar. Previously reported unbinding half-times for ZAP70-GFP at 37 °C are  $\sim 22$  s [234] and 7.5 s to 10 s [45], corresponding to  $\tau \sim 32$  s and  $\tau \sim 11$  s to 14 s, respectively. While these values are consistent with the  $\tau_2$  values we extracted from cells on homogeneously coated OKT3 surfaces (16 s to 21 s), they are higher than the values we determined on patterned OKT3 surfaces at 37 °C ( $\sim 5$  s to 7 s). Apart from unspecific contributions from cytosolic diffusion, a fraction of slowly diffusing membrane-bound ZAP70-GFP could additionally contribute to the recovery curve for cells on coated OKT3, surfaces but would be eliminated in the micropatterning approach.

# Chapter 13

## Conclusion and outlook

Combining FRAP with protein micropatterning results in a versatile method for specifically determining binding kinetics between a cytosolic protein and a transmembrane interaction partner. Application and validation of this approach was done on ZAP70 binding to the TCR with the result that non-specific contributions to the fluorescence recovery signal can indeed be removed. The hereby corrected recovery curves only reflect the interaction times of the two involved proteins, and can therefore be fit with a monoexponential function in a straightforward manner to obtain key parameters such as the interaction time or the mobile fraction. In the case of the ZAP70-TCR interaction, formation of immobile TCR microclusters simplifies FRAP analysis. However, the employed micropatterning approach can be particularly useful for measuring the interaction of a cytosolic protein and an otherwise mobile membrane protein.



# Chapter 14

## Materials and methods

### 14.1 Cells and reagents

The plasmid DNA for hZAP70-eGFP was kindly provided by B. Lillemeier (Salk Institute for Biological Studies) and the plasmid for cytosolic GFP was a gift from H. Stockinger (Medical University of Vienna). Both constructs were re-cloned into the retrovirus vector backbone pBMN-Z. Phoenix packaging cells were co-transfected with the vector and pCL-eco using TurboFect Transfection Reagent (Invitrogen Life Technologies). After 2 days of virus production, the supernatant was mixed with 10 µg/ml polybrene (Sigma-Aldrich), added to Jurkat E6-1 T cells from the American Type Culture Collection, followed by spin infection. Cells were cultured in RPMI 1640 medium supplemented with 10 % fetal bovine serum (FBS), 2 mM L-glutamine, 1000 U/ml penicillin–streptomycin (all from Sigma-Aldrich) in a humidified atmosphere at 37 °C and 5 % CO<sub>2</sub>. For microscopy, we used an imaging buffer consisting of HBSS (Lonza, Switzerland) supplemented with 2 % FBS. For kinase inhibition, cells were incubated in imaging buffer with 40 µM PP2 (Sigma-Aldrich) for 5 min before and during the experiment. Biotinylated monoclonal antibody against CD3ε (clone: OKT3) and biotinylated anti-HA.11 Epitope Tag antibody (clone: 16B12) were purchased from BioLegend. Monoclonal biotinylated anti-CD3ε antibody (clone: MEM-57) was purchased from Sigma-Aldrich.

## 14.2 Surface preparation

Micropatterned OKT3 surfaces were produced following a previously published protocol [334]. Briefly, polymer stamps featuring circular pillars with a diameter of  $1\ \mu\text{m}$  and a center-to-center distance of  $3\ \mu\text{m}$  (EV group) were cleaned with absolute ethanol and  $\text{dH}_2\text{O}$ , then incubated with  $50\ \mu\text{g}/\text{ml}$  streptavidin (AppliChem) in PBS (Sigma-Aldrich) for 15 min, rinsed with  $\text{dH}_2\text{O}$ , and dried in a  $\text{N}_2$  flow. After drying, the stamp was placed on an epoxy-coated coverslip (Schott), pressed to ensure good contact and incubated for 30 min at  $22\ ^\circ\text{C}$ . After removal of the stamp, a Secure-Seal hybridization chamber (Grace Biolabs) was placed on top of the pattern and  $10\ \mu\text{g}/\text{ml}$  fibronectin (Sigma-Aldrich) in PBS with 1% BSA (Sigma-Aldrich) was added. After 30 min incubation, the structures were rinsed with PBS and incubated with biotinylated antibody at a concentration of  $10\ \mu\text{g}/\text{ml}$  in PBS with 1% BSA. After 15 min, samples were rinsed thoroughly with PBS. Homogeneously coated OKT3 surfaces were produced by placing a Secure-Seal hybridization chamber onto an epoxy-coated coverslip and adding OKT3 antibody at a concentration of  $10\ \mu\text{g}/\text{ml}$  in PBS into the chamber. After 15 min, samples were rinsed thoroughly with PBS. Fibronectin-coated surfaces were produced by placing a Secure-Seal hybridization chamber on an epoxy-coated coverslip and adding  $10\ \mu\text{g}/\text{ml}$  fibronectin in PBS into the chamber. After 30 min incubation, samples were rinsed thoroughly with PBS.

## 14.3 Total internal reflection fluorescence microscopy

TIRF microscopy experiments were performed on a home-built system based on a modified inverted microscope (Zeiss Axiovert 200) equipped with a  $100\times$  oil-immersion objective (Zeiss Apochromat NA1.46). For FRAP experiments, a 488 nm diode laser (Toptica ibeam-smart) was used. Emission light was filtered using appropriate filter sets (Chroma) and recorded on an iXon DU 897-DV EM-CCD camera (Andor). TIRF illumination was achieved by shifting the excitation beam in parallel to the optical axis with a mirror mounted on a motorized movable table. For experiments performed at  $37\ ^\circ\text{C}$ , the temperature was maintained by means of an in-house-built incubator box equipped with a heating unit and an objective heater (PeCon). For characterization of patterned and coated OKT3



surfaces, prepared slides were incubated with the Zenon Alexa Fluor 647 Mouse IgG2a Labeling Kit (Molecular Probes) according to the manufacturer's protocol and imaged with a 640 nm diode laser (Coherent, Obis). To determine the antibody densities, the mean bulk brightness of the different surfaces was compared. For patterned surfaces, selection masks defining ON and OFF regions were applied.

## 14.4 Ratiometric $\text{Ca}^{2+}$ Imaging

For ratiometric  $\text{Ca}^{2+}$  imaging, cells were incubated with 5  $\mu\text{g}/\text{ml}$  Fura-2, AM (Thermo Fisher Scientific) in imaging buffer for 20 min at 22 °C and washed twice with imaging buffer. For each experiment, cells were resuspended in imaging buffer at  $5 \times 10^6$  cells/ml, and 50  $\mu\text{l}$  were deposited in a Secure-Seal hybridization chamber, which was mounted on the microscope. Image acquisition was started immediately. Fura-2-AM was excited using a monochromatic light source (Polychrome V, TILL Photonics), coupled to a Zeiss Axiovert 200 M equipped with a 20 $\times$  objective (Olympus) and an Andor iXon Ultra. Imaging was performed at 340 nm or 380 nm at an illumination time of 50 ms or 10 ms, respectively. The total recording time was 10 min at 1 Hz. ImageJ was used to generate the ratio images. Cells were segmented and tracked using a sum image of both channels, using an in-house Matlab algorithm based on published literature [337]. Cellular positions and tracks were stored and used for intensity extraction based on the ratio image. Intensity traces were normalized to the starting value at time point zero. A cell was considered as activated if a threshold set at 0.4 was exceeded.

## 14.5 FRAP experimental procedure

All cell measurements were carried out in HBSS supplemented with 2% FBS at 22 °C unless stated otherwise. Experiments were carried out 5 min to 45 min after cell seeding. A prebleach image (exposure time: 5 ms) was acquired, followed by a bleach pulse of 500 ms duration. Imaging was performed at low laser power (150  $\text{W}/\text{cm}^2$ ) to minimize photobleaching; bleach pulses were performed at 4000  $\text{W}/\text{cm}^2$ . 50 postbleach images were taken with delays between consecutive images being evenly spaced on a logarithmic scale, with the first postbleach image taken at 6 ms after the end of the bleach pulse (see Figure 14.1).

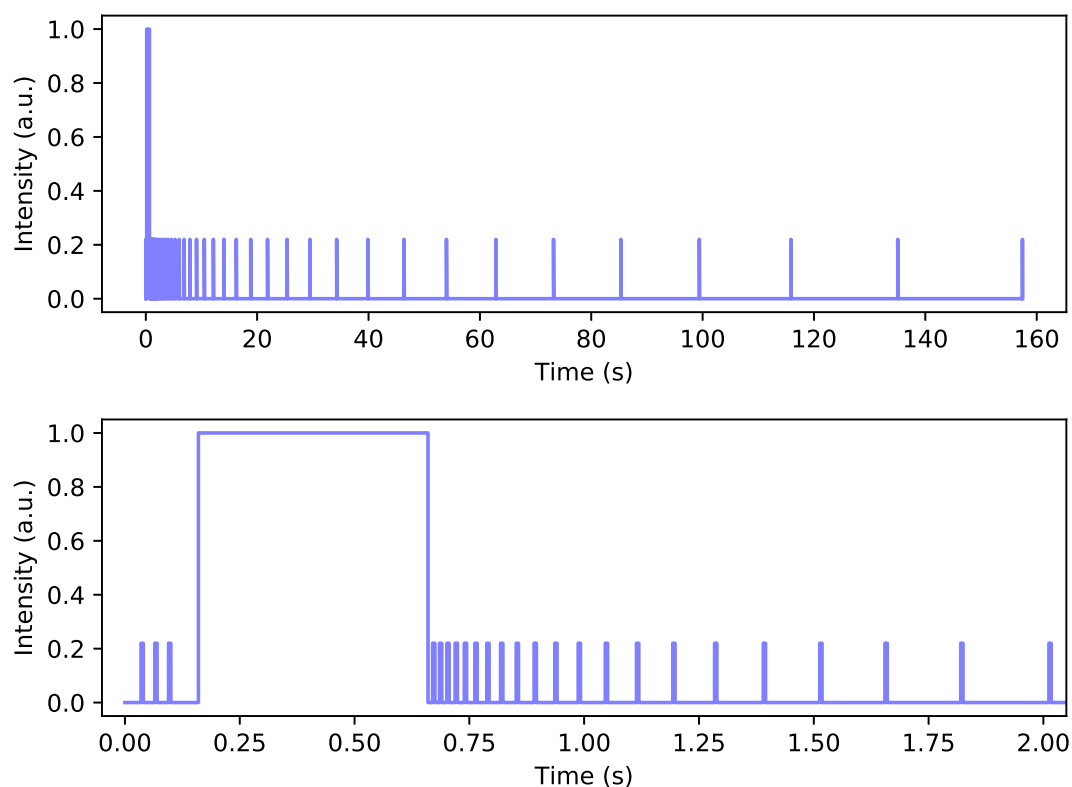


**Figure 14.1:** *Illumination protocol used for FRAP experiments. Postbleach images are evenly spaced on a logarithmic scale to effectively capture the fast recovering fraction of ZAP70-GFP, but minimize photobleaching at later time points (upper panel). The lower panel shows the first 2 s of the protocol in detail, with 3 prebleach images, a 500 ms bleach pulse of high intensity as well as the beginning of the postbleach image acquisition sequence.*

Control experiments to determine the amount of photobleaching during image acquisition were performed using the same timing protocol as used for the FRAP experiments and replacing the bleach pulse with a standby time of the same duration. Since the recovery curves of ZAP70-GFP as well as cytosolic GFP contained contributions other than pure cytosolic diffusion of unknown origin, we chose to determine the extent of depletion during the bleach pulse by applying an alternative FRAP protocol. Cells expressing ZAP70-GFP seeded onto fibronectin-coated surfaces were subjected to repetitive 500 ms bleach pulses separated by 1.5 s to isolate the fast recovering component. Images were read out 1 s after the end of each bleach pulse. To determine the extent of depletion, the basal plasma membrane of a cell (excluding cell edges) was selected as a region of interest and the relative change of the background corrected mean pixel intensity values for each region between pre- and post-bleach image was calculated. For each cell, the intensity change caused by the first bleach pulse was discarded and the mean recovering fraction was calculated from the subsequent four bleach pulses. Values were determined separately for cells at 22 °C and 37 °C.

## 14.6 FRAP analysis

For analysis of FRAP curves on patterned cells, selection masks were created from the pre-bleach image using ImageJ and applied to all postbleach images. For ON regions, a rectangular ROI inside the ZAP70-GFP dot was selected; for the corresponding OFF region, a rectangular annulus around ON regions was selected as shown in Fig. 12.1. The background corrected mean pixel intensity values for each region,  $F_{\text{ON}}$  and  $F_{\text{OFF}}$ , were used for further analysis. Only dots with a minimal contrast of 0.4 were included in the analysis, with the contrast being defined as  $\frac{F_{\text{ON}} - F_{\text{OFF}}}{F_{\text{ON}}}$ . The number of ROIs measured in each cell was strongly dependent on the cell size, with a mean of  $6.7 \pm 0.51$  (SEM) ROIs for all patterned cells. There was no correlation between the number of ROIs and either  $f_m$  or  $\tau$ . For cells on homogeneously coated surfaces, the basal plasma membrane of a cell (excluding cell edges) was selected as a region of interest in ImageJ. The following steps in the analysis of FRAP data were implemented using Python (Python Software Foundation).  $\Delta F = F_{\text{ON}} - F_{\text{OFF}}$  in micropatterned cells was determined separately for each dot of the pattern by subtracting the mean pixel intensity value of each OFF area region from the mean pixel intensity

value of the respective ON region. All dots in a cell were combined to generate a FRAP curve. Then, FRAP curves were normalized to the pre-bleach value of the respective pulse train. To correct for photobleaching during image acquisition, each datapoint of a FRAP curve was divided by the respective datapoint of the control curve (recorded as described in the previous section). Further, to correct for depletion of the fluorescent ZAP70-GFP pool by the bleach pulse, each postbleach datapoint of a FRAP curve was divided by the determined depletion correction value of 0.88 and 0.85 for data collected at 22 °C and 37 °C, respectively. We used the `scipy.optimize.curve_fit` function for performing non-linear least squares to fit Eq. 12.1 and Eq. 12.2 to the data. A Trust Region Reflective algorithm was used for optimization. FRAP data were fit separately for each cell.

# Part IV

## EBID nanostructuring



Die approbierte gedruckte Originalversion dieser Dissertation ist an der TU Wien Bibliothek verfügbar.  
The approved original version of this doctoral thesis is available in print at TU Wien Bibliothek.

# Chapter 15

## Introduction

As nanostructured and biofunctionalized surfaces gain more and more importance in the bio-sciences, the number of techniques developed for these purposes is increasing. Well-defined arrays at the nanoscale can be used to feature a high density of reaction sites and offer control over the spatial distribution of activating biomolecules at the nanoscale. Further, the much smaller sample volume compared to micropatterns can potentially translate into a higher sensitivity, improved kinetics, as well as faster reaction times. Ultimately, well-defined nanoarrays can pave the way to immobilize individual proteins at specific sites. [338]

Here, a biofunctionalization platform consisting of carbon-containing nanofeatures is created using electron-beam-induced deposition (EBID) [24, 85]. In this technique, a focused electron-beam is scanned over a sample leading to the localized decomposition of hydrocarbons. Therefore, this technique is a direct-write process which is inherently limited by its low throughput. However, EBID offers the possibility to create custom patterns with sub-10 nm resolution. More precisely, in this approach the size of the target areas can be controlled with nanometer-scale precision [339] and their lateral distances can be freely chosen. These structures can be decorated with functional biomolecules with the potential to probe the influence of spatial organization of individual proteins on cellular systems.

### Structure of this part

This part is divided into three main sections. First, the generation of the used patterns is described, then the direct and indirect utilization of the patterns will

be described. In the direct approach, patterns were decorated with antibodies. Since the production of large scale EBID structures is not feasible in a reasonable amount of time, a single cell was attached to a coated AFM cantilever and positioned on the structured area. For the indirect approach, EBID structuring was combined with the DNA origami technique. Here, specifically designed DNA nanostructures can bind in defined stoichiometry or molecular orientation on the individual arrays [340–343] and inherently offer excellent control over ligand positioning (see part II) [21, 191, 344, 345].

However, the used EBID structured slides were produced by project partners and only a limited number of slides could be supplied during the project. Therefore, only preliminary experiments could be performed. For the sake of completeness even these fragmentary results will be described.



## Chapter 16

# The generation of carbon nanostructures

We used EBID patterning to create nanostructured bio-functionalized surfaces. For this, a high-resolution scanning electron microscope (SEM) with a beam blanker and an attached control unit for e-beam lithography is used to write nanostructures composed of carbon on a transparent sample. Here, the electron dose can be varied in order to control shape, diameter and height of the designed nanostructures. Then, the created carbon nanostructures are selectively coated with biomolecules.

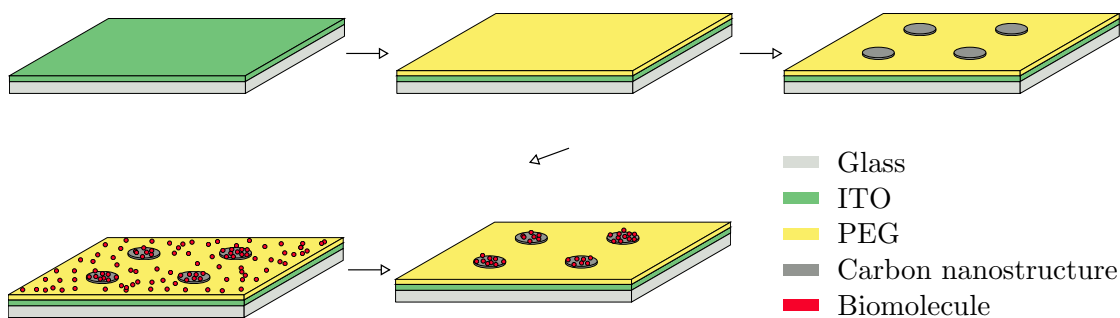


**Figure 16.1:** *The generation of biomolecular nanopatterns via EBID. First, the indium tin oxide (ITO)-glass substrate undergoes polyethylene glycol (PEG)-silanization, then carbon nanostructures of defined geometry are generated via EBID. Incubation with biomolecules and subsequent rinsing leads to the selective decoration of the nanostructures with biomolecules.*

The process for the generation of biomolecular nanopatterns via EBID can

be outlined as a sequence of distinct steps (see Figure 16.1) and will now be described in detail. The first step is the polyethylene glycol (PEG)-silanization of an indium tin oxide (ITO) coated glass substrate in order to create a dense, self-assembled monolayer (SAM) of PEG. The 17 nm thick ITO film is used to prevent electrostatic charging of the substrate as ITO dissipates electrical current during the e-beam writing. Further, it is optically transparent and thereby allows for the optical assessment of adsorbed biomolecules. [346] ITO was subjected to chemical surface modification to convey a PEG film, which was found to have the expected physical and chemical properties, in particular excellent passivation properties. [347] Here, PEG is used to prevent the non-specific binding of biomolecules to non-target areas surrounding the nanostructures. Exposing this PEG film to a focused e-beam leads to the decomposition of organic residues in the SEM chamber atmosphere and subsequent deposition near the irradiated substrate surface. [85] Mainly secondary electrons with energies  $<100$  eV, which are created by the primary e-beam in the topmost layer of the substrate, but also backscattered electrons from the excitation volume are responsible for this deposition process ultimately resulting in the formation of nanodeposits consisting mostly of carbon. [24, 85] This EBID approach allows for the precise control over the lateral position of the nanostructures, as well as their lateral size and height. Above a certain threshold, higher electron doses correspond to an increase in height. Upon incubation, biomolecules physisorb to the created carbon deposits, whereas the surrounding PEG surface suppresses their non-specific adsorption. After washing, biomolecules are arranged according to the shape and geometry of the underlying EBID features. By varying the electron dose, the surface density of biomolecules per nanostructure can be tuned as higher structures lead to a larger amount of bound biomolecules. [347, 348]

Although the e-beam focus of a typical field emitter SEM is less than 1 nm wide, feature broadening effects—mainly attributed to secondary electron emission from both the substrate and the EBID features themselves—lead to lateral feature sizes of a few 10 nm. [85, 349] However, by using a scanning transmission electron microscope (STEM) together with a well-defined precursor atmosphere, EBID features in the range of 1 nm can be produced. [339]

AFM is commonly used to confirm the successful writing of the designed EBID features. However, a root mean square (RMS) roughness of 1 nm [346] of the ITO surface makes AFM analysis of features at the same scale difficult.

To circumvent this, EBID features can be written on atomically flat silicon to allow for AFM imaging. Still, one has to be aware that there might be slight differences in the samples.

In this thesis, two different geometric arrangements of EBID nanostructures were used with different functionalizations dependent on their application. These two distinct patterns are described separately in their respective sections. However, in both cases the first functionalization step included the incubation of avidin. Due to its positive charge ( $pI = 10.5$ ), avidin selectively coats the negatively polarized carbon deposits. [348, 350] Since avidin has an approximate size of  $4 \times 5 \times 6$  nm, it is possible that several avidin molecules are bound to an individual nanostructure. Avidin-coated nanostructures can be used to either immobilize biotinylated proteins via biorecognition or to electrostatically bind negatively charged DNA origami plates ( $pI = 1.5$ ). In the first case, hereafter also called direct approach, biotinylated proteins can be directly attached, whereas the other case in which avidin serves as an electrostatic adhesive to bind DNA plates to the nanostructures (indirect approach) represents a hierarchical two-layer assembly. In prospective experiments, these DNA plates can be modified to display few to individual protein molecules on their top.

Further details on the lithography system and the other methods can be found in section 20.



# Chapter 17

## Pick-and-place manipulation

The structuring of biofunctionalized surfaces offers a myriad of experimental opportunities to probe various properties of biological system. Whereas with some structuring methods, such as micropatterning, it is possible to structure large areas in a reasonable amount of time, some more sophisticated methods come with the main disadvantage of low throughput. In order to still take advantage of custom designed surface structuring with methods such as EBID, we implemented a pick-and-place manipulation approach.

In this approach, an individual cell is attached to a functionalized AFM cantilever and can be positioned precisely on the biofunctionalized surface. This approach offers not only spatial control over the cell, but also temporal control, as the moment when the cell establishes contact to the surface is not only known but can be chosen deliberately.

In this section, this pick-and-place manipulation approach will be described together with a proof of concept. More precisely, an individual Jurkat T cell is attached to a cantilever and placed on an aOKT3 micropatterned surface. Here, not only the generation of micropatterned areas inside the cell could be monitored, also calcium imaging was performed. Placing cells on spatially confined structures poses additional problems, as the functionalized pattern needs to be found after attaching the cell to the cantilever. Here, we demonstrate this by placing a cell on a face-pattern created via EBID.

## 17.1 Attaching cells to the cantilever

In a typical single cell force spectroscopy (SCFS) experiment, an individual cell is attached to a cantilever in order to test its adhesion to a sample substrate or to another, adherent cell. Here, the first step in this procedure, i.e. the attachment of the cell to the cantilever, will be described.

### 17.1.1 Cantilever choice

When performing SCFS experiments, the cell bound to the cantilever makes contact with the surfaces and compresses as the cantilever deflects. Since cells are in general very soft, the cantilever to which they are bound should be very flexible, i.e. have a low spring constant in the range of 0.01 N/m to 0.06 N/m. Tipless cantilevers are more suitable for these experiments, as the presence of a tip at the end of the cantilever can disrupt the measurements. In order to facilitate the adhesion of a cell to the cantilever, it must be functionalized in advance. Cantilever modification techniques are described in the next section.

### 17.1.2 Cantilever modification

The binding of the cell to the cantilever is a critical step when conducting SCFS experiments. In order to achieve this, several different coating methods are being used.

- The lectin **Concanavalin A (ConA)** which binds D-glucose and  $\alpha$ -D-mannose sugar moieties at the cell surface is the most commonly used approach as it gives non-specific, strong binding between cell and cantilever. However, cells of the immune system will activate very effectively when binding to sugar moieties. Therefore, this approach cannot be used.
- Alternatively, the cantilever can be modified with **antibodies** by simple adsorption for short contact time experiments with low interaction forces or by covalent attachment.
- Functionalization of the cantilever with **fibronectin** is appropriate for attaching cells that have a strong interaction with fibronectin (i.e. invasive cancerous cell lines, fibroblasts). Two different approaches can be used for coating the cantilever with fibronectin. Either it is adsorbed onto the

cantilever by incubating the cantilever in a fibronectin solution and used immediately after washing, or the cantilever is silanized and activated with glutaraldehyde before the addition of fibronectin, if a stronger adhesion is required.

Here, we used fibronectin adsorption to attach cells to the cantilever. Prior to tip functionalization, the cantilever was plasma cleaned to remove any organic material.

### 17.1.3 Harvesting cells

In order to attach cells to a cantilever, a cell suspension must be prepared. Suspension cells can be added straight into the sample chamber. However, if the cells of interest are in 2D culture, they must be released from the culture dishes first. After harvesting by centrifugation, the cells are resuspended in imaging buffer and allowed to recover for several minutes.

In general cells are sticky and tend to bind rather to the substrate than to the cantilever, especially when using coated substrates. This makes the cell capture procedure challenging. Therefore, part of the substrate was passivated by a homogeneous PEG coating. To be able to separately treat two parts of the substrate with the different coatings, i.e. the PEG coating and the biofunctionalized surface area, a chamber with two adjacent cavities was designed and used (see section 17.2 for details).

### 17.1.4 Attaching cells by performing a force curve

In principle, the cantilever should be calibrated before attaching the cell. This step can be omitted since we are not interested in performing classical SCFS experiments, however it is considered advisable to do it anyway as a reference. Still, since cantilever calibration requires recording a force curve with a relatively large setpoint (at least 1 V) to determine the sensitivity, it should be performed only once as the coating would suffer from several force distance cycles. Further, the approach of the cantilever to the surface should also be done only once and with a low setpoint in order to preserve the coating of the cantilever.

The suspended cells are introduced by lifting the AFM head and pipetting the cell suspension directly into the sample chamber. PEG coating of the sample

chamber prevents adhesion to the substrate, such that cells will prefer to adhere to the cantilever. In principle, transfer of the cell between two distinct sample chambers is not possible, since the surface tension of the medium will detach the cell from the cantilever as soon as the cell leaves the buffer solution. We developed a chamber design to simplify cell transfer (see section 17.2).

For the actual attachment process, the cantilever is oriented above the cell using an optical microscope. Then, a force curve is performed to press the cantilever onto the selected cell. Using the head positioning screws during the approach period, the cantilever can be carefully moved to orient it exactly above the cell. Depending on the cell type, the setpoint should be around 0.5 nN and the contact time around 2 s to 5 s. Hydrodynamic forces could push the cell out from under the cantilever, therefore the cantilever should not be moved faster than 5  $\mu\text{m/s}$  during the approach. The pulling length should be as long as possible to ensure that the cell and the sample surface are completely separated. Ideally, the cantilever with the cell attached is retracted to the piezo retracted position with the retract speed over the whole distance. Moving with higher speed can result in the loss of the cell. Then, the cell should be allowed to recover and to form a strong interaction with the coated cantilever over a period of at least 5 min before starting the first experiments.

## 17.2 Cell transfer

The two different parts of a pick-and-place experiment require fundamentally different surface conditions. For the pick, the surface should be as passive as possible and for the place, it needs to feature the designed structures. However, in a pick-and-place experiment these two distinct surfaces need to be combined. For this purpose, a special sample chamber was designed.

The chamber features two adjacent cavities which are separated by a small barrier and surrounded by a larger barrier (see Figure 17.1). By using this approach, cells can be seeded in the cavity featuring the passivated surface with the small barrier preventing them from diffusing to the biofunctionalized patterns. Since this middle barrier is lower than the surrounding barrier, buffer solution can be added to the system until it connects both cavities. Then, a cell can be attached to a cantilever and transferred between the two cavities without leaving the buffer solution, such that no surface tension needs to be overcome and the



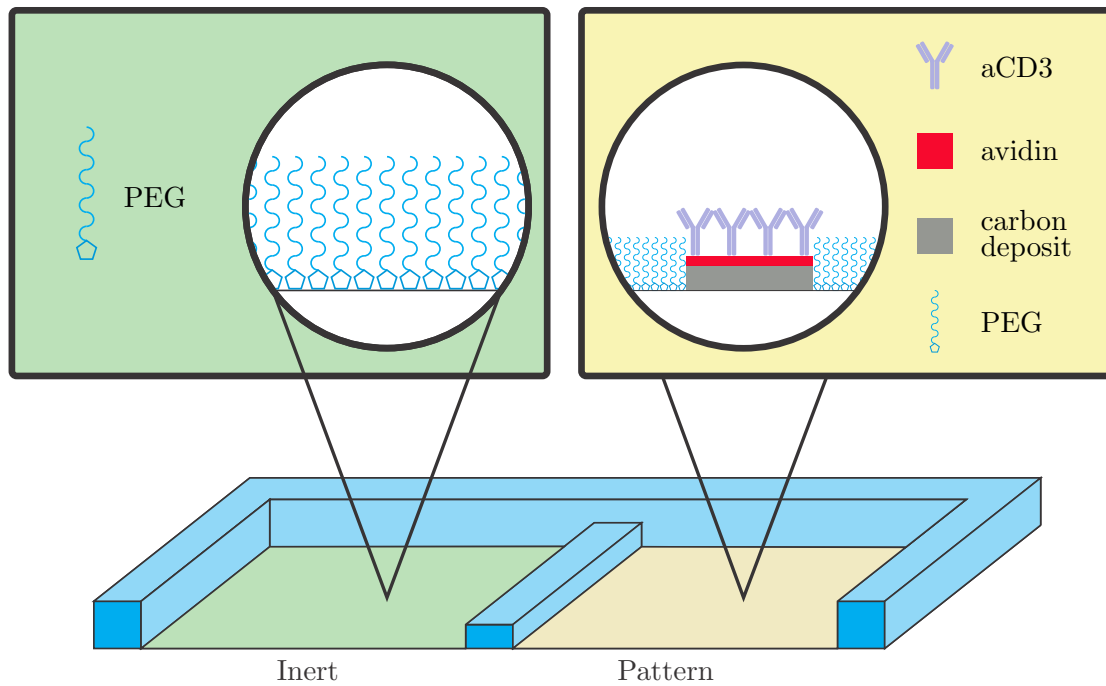


**Figure 17.1:** *The chamber design features two adjacent cavities. In the green cavity, PEG is used to passivate the substrate. Here, cells are added to the chamber and can be attached to a cantilever. The yellow cavity features the biofunctionalized areas to which the cell should be transferred. The barrier in between those two cavities is lower than the surrounding barrier such that the buffer solution can connect them.*

cell remains attached to the cantilever. Finally, this allows for the placement of a single cell on the desired location without other cells being in the measurement cavity.

In order to produce this sample chamber, an inverse mold was printed with a 3D printer. This mold can be filled with Twinsil glue in order to make a single sample chamber. The mold can be reused and a clean chamber can be created for each experiment. For further details see section 20.3.

### 17.3 Single cell delivery

Following the attachment of the cell to the cantilever and waiting for a recovery period of several minutes, the cell can be delivered to the functionalized measurement area. This section discusses how appropriate experimental parameters are set.

The setpoint and the contact time determine the adhesion force and contact area between the cell and substrate. The setpoint is chosen in such a way to be high enough to induce adequate adhesion, but also sufficiently low to reduce the pressure applied to the cell. Commonly, setpoints of several hundreds of pN are used.

In SCFS experiments the contact time is a crucial factor. In general, the longer the contact time, the stronger the adhesion. At some point, the adhesion may even exceed the binding strength of the coating and the cell is pulled off the cantilever. Since the purpose of our approach is not to conduct classic SCFS experiments, this is not of much concern.

Another important parameter is the cantilever speed which in general should not exceed  $5 \mu\text{m/s}$  in order to avoid excessive hydrodynamic drag.

When the cantilever is lowered onto the substrate and the cell makes contact with the surface, either the force or the piezo height can be kept constant during the contact time. In this regard, thermal drift of the cantilever needs to be considered. This effect is crucial when using silicon nitride cantilevers, which are very susceptible for thermal drift. Longer contact times increase the influence of drift on the measurement. In constant height mode, the height will be maintained for the whole contact time. During this time any changes in cantilever deflection will be measured but will trigger no response.

When a cell is brought into contact with the surface, it elastically deforms on

contact and then it will relax in the manner of a viscous material. This relaxation pulls the cantilever toward the surface and reduces the force applied to the cell.

After successful delivery of the cell to the intended sample position, experiments including calcium imaging or fluorescence microscopy can be performed.

## 17.4 Results

The described method was implemented using Jurkat T cells together with a surface structured with OKT3 antibodies similar to the micropatterning approach described in part III. The goal of the presented pick-and-place manipulation technique was to place cells on defined areas of nanostructured samples. However, these could not be produced at a large scale. We thus transferred cells to micropatterned surfaces first. Thereafter, a single cell was also placed on a structure created via EBID as a proof of concept.

### 17.4.1 Micropatterned surfaces

Surface micropatterning of proteins is a technique mainly used to investigate the interactions of cell surface proteins with their interaction partners. Micropatterning has already been described in detail in section 11 and the generation of micropatterned surfaces as well as the experimental techniques which will be used in this section have also been already described in section 14. Here, micropatterns are used as a tool—on the one hand to create an activating surface for calcium experiments and on the other hand to be able to observe the recruitment of proteins to these patterns upon cell placement.

#### Calcium imaging

In a first experiment, Jurkat T cells expressing ZAP70-GFP were seeded on the PEG-coated side of the measurement chamber and a single cell was attached to a fibronectin-coated cantilever (see Figure 17.2a). Then, this cell was transferred to the micropatterned side of the measurement chamber and lowered until it made contact with the surface. At the same time, we performed ratiometric calcium imaging in order to look for proper activation, even if the cell is attached to the cantilever. And indeed cells showed increased intracellular calcium levels as shown for an exemplary cell in Figure 17.2b. This method offers the additional

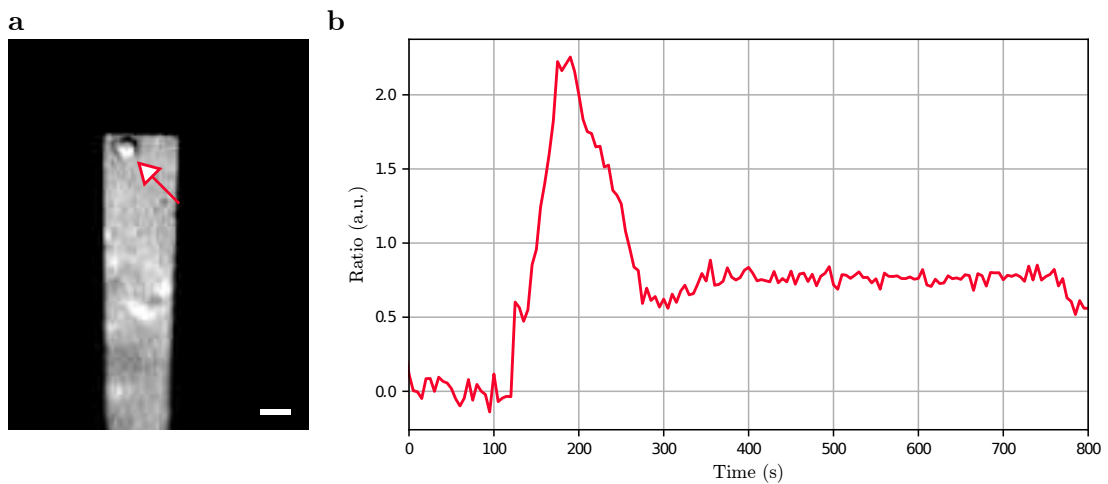


**Figure 17.2:** *Calcium imaging of a single cell attached to a tipless cantilever. (a) Bright-field image of a cell (red arrow) attached to a cantilever which is in contact with the sample surface. Scalebar is  $10\ \mu\text{m}$ . (b) An exemplary calcium trace of a single cell on a micropatterned surface. At timepoint zero the cell attached to a cantilever first establishes contact with the surface. After a short amount of time the intracellular calcium level increases rapidly as the cell activates.*

benefit that the exact time point when the cell makes contact with the surface is known. In principle, this allows the determination of the exact time span until calcium flux occurs. However, as only a single cell can be measured at a time, this method has a low throughput and acquiring enough cells for good statistics would require quite some time and effort.

### Fluorescence imaging

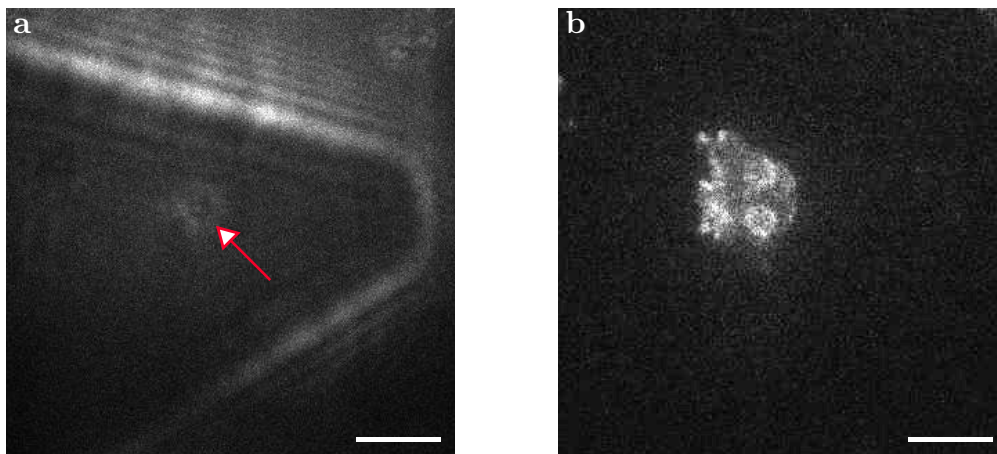


**Figure 17.3:** *The recruitment of ZAP70-GFP after placing a cell attached to a cantilever on a micropatterned surface. (a) Bright-field image of a cell (red arrow) attached to a cantilever when lowering it down to the sample surface. (b) A typical cell showing enrichment of ZAP70-GFP at micropatterned OKT3 sites while still being attached to a cantilever. Scalebar is  $10\ \mu\text{m}$ .*

Next, cells placed on micropatterned surfaces were imaged using TIRF microscopy. Similar to the experimental procedure for calcium imaging, a single Jurkat T cell expressing ZAP70-GFP was picked by a fibronectin-coated cantilever from a PEG-coated surface (see Figure 17.3a) and placed on a micropatterned OKT3 surface. After making contact with the surface, the cell showed enrichment of ZAP70-GFP at micropatterned OKT3 sites, thereby showing that the same behavior is triggered by this pick-and-place approach compared to traditional seeding. The same advantages and disadvantages hold true for fluorescence imaging as for calcium imaging. The whole time course of the experiment is well defined, however obtaining data from many cells is a time consuming endeavor.

### 17.4.2 EBID structures

Previous experiments showed that the principle of picking a cell and placing it on a micropatterned surface works. Although this approach provides temporal control over the cell in an experiment, the additional benefit of spatial control which the methods also provides is not needed. Due to the low throughput of e-beam lithography techniques, only small surfaces areas can be structured in a reasonable amount of time. In these cases, the pick-and-place manipulation approach can be very useful, as cells can be placed directly on the structured surface areas.

Here, we tested this approach on structures resembling a smiley face. These smiley faces were written on a PEGylated ITO-slide via EBID and they have a nominal linewidth of  $0.5\ \mu\text{m}$  and a diameter of  $5\ \mu\text{m}$ . The custom-made sample chamber could be glued to this slide. After incubation of the slide with avidin and biotinylated OKT3-antibodies, the quality of the patterns was evaluated using the Zenon antibody-labeling kit and the exact position of the patterns on the slide was marked. This last step is of particular importance, since once a cell is attached to the cantilever, it should be imaged as soon as possible. Then, Jurkat T cells expressing ZAP70-GFP were seeded in the passivated part of the sample chamber and attached to a fibronectin-coated cantilever. Next, the cantilever was positioned at the pattern marker and lowered until the cell can be seen using bright-field microscopy. After fine alignment with the face-structures, the cell is pushed towards the surface until a cantilever deflection can be measured, i.e. the cell makes contact with the surface. As can be seen in Figure 17.4, we were able to position a cell directly on a face-structure using this pick-and-place approach. Although this cell showed some rearrangement of ZAP70-GFP, no clear face-structure can be seen inside the cell. It is noteworthy, that not even the eyes of the smiley face, which show high intensity in the antibody image, led to an accumulation of ZAP70-GFP. However, it is difficult to determine the reason for this behavior, since we only had one sample slide and could perform this experiment only once. In principle, this lack of ZAP70 could be caused by an insufficient antibody density on the pattern or by the cell itself.

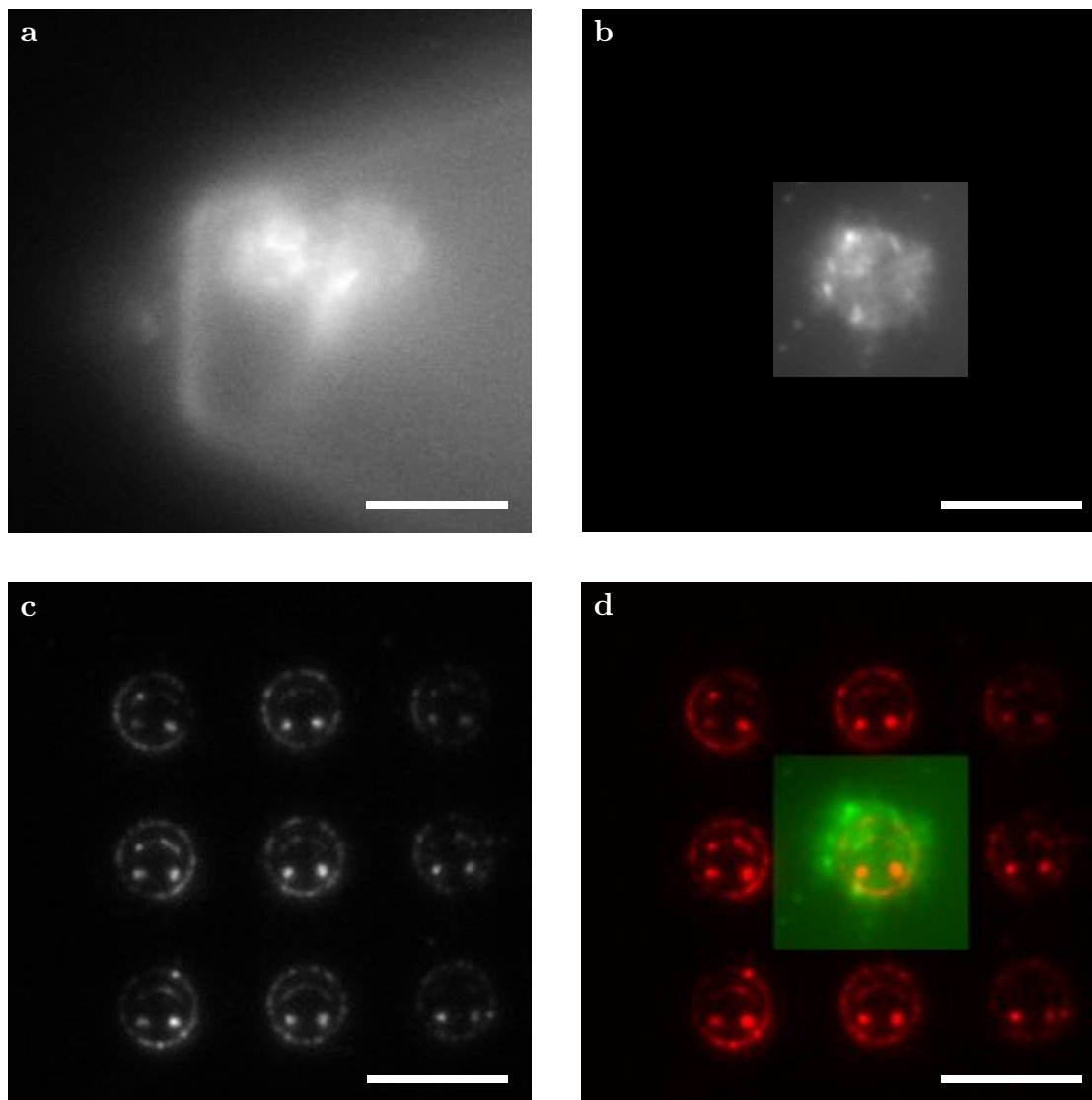


**Figure 17.4:** *The delivery of cells to EBID patterned surfaces. (a) Bright-field image of an exemplary cell attached to a cantilever. (b) After placing the cell on the patterned substrate, a time series showing the rearrangement of ZAP70-GFP in the cell was recorded in TIRF microscopy. The average intensity of the recorded images is shown. (c) The underlying antibody pattern produced via EBID is visualized using Zenon Alexa Fluor 647 Mouse IgG2a Fab fragments. (d) An overlay image of the pattern (red) and the cell (green). Scalebar is 10  $\mu\text{m}$ .*





# Chapter 18

## DNA origami on EBID structures

DNA origami allow for the precise control of staple positions and are a suitable tool to arrange molecules, proteins or nanoparticles. The size limitation of DNA origami in the range of 100 nm, as well as the precise positioning of single structures in an ensemble hamper their usage for widespread, hierarchical arrangements with addressability at the nanometer scale. In general, several polymerization methods [205, 221, 351] or a larger scaffold [352] are used to generate larger structures. With the help of lithographic fabrication processes, patterns with higher order structures can be produced, allowing for the precise arrangement of DNA nanostructures.

Here, we used EBID to generate 100 nm-wide carbon nanoislands. On these islands positively charged avidin proteins and negatively charged DNA origami nanoplates are immobilized, while undesired adsorption to surrounding non-target areas is suppressed. By immobilizing DNA origami nanoplates on the islands, the number of capturing sites for other proteins can be adjusted. Such arrays represent a first step towards single-molecule protein arrays.

In order to utilize such arrays, a thorough characterization is of utmost importance. Therefore, we used fluorescently labeled DNA origami nanoplates composed of a single-duplex layer with nominal dimensions of  $2 \times 50 \times 50$  nm. Stepwise photobleaching analysis was used to determine the number of fluorescently labeled origami nanoplates per nanoisland.

## 18.1 Results

To facilitate detection of the DNA origami nanoplates with fluorescence microscopy, four Alexa532-modified oligonucleotides were hybridized to the corners of the plates. Figure 18.1 shows the binding of these fluorophore-tagged DNA nanoplates to the avidin-coated nanoislands. Analysis of single arrays revealed a wide spread of the number of islands which were covered with DNA nanoplates. For arrays written at 2.9 pC,  $54.75 \pm 14.35\%$  (mean $\pm$ sd,  $n = 4$ ) of all islands showed a fluorescence signal. However, qualitative analysis showed that the binding of DNA nanoplates to the nanoislands is not very specific, as many fluorescent signals can be detected next to the islands.

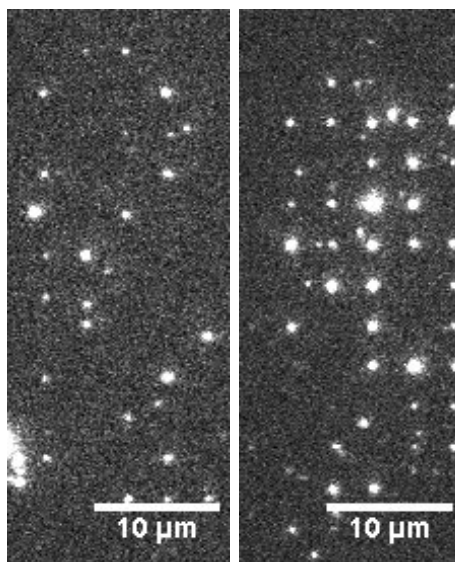


**Figure 18.1:** *Fluorescently labeled DNA origami nanoplates bound to carbon nanoislands coated with avidin. Fluorescence image of an array of nanoislands of  $100 \times 100$  nm written at a dose of 2.9 pC showing a low (left) or high (right) coverage of islands with DNA origami nanoplates.*

In general, surface coverage of islands with DNA plates increases with the electron dose. However, above a certain threshold dose, the number of DNA nanoplates binding per nanoisland did not drastically alter. This suggests that the maximum number is limited by steric exclusion. [350] In order to determine the exact number of DNA nanoplates bound per nanoisland, we used stepwise photobleaching analysis, which has been already described in section 3.

### 18.1.1 Stepwise photobleaching

Due to the quantal nature of single dye fluorescence emission, the bleaching of complexes consisting of several dyes occurs in a stepwise manner. Here, we applied this stepwise photobleaching approach to DNA origami plates immobilized on carbon nanoislands. In the fluorescence intensity trace for each carbon nanoisland, each distinct step represents one photobleaching event of a single dye molecule. If the degree of labeling of the DNA origami nanoplates is known, the number of nanoplates per carbon nanoisland can be determined. The bleach traces of two exemplary carbon nanoislands can be seen in Figure 18.2 with distinct steps clearly visible. However, in some cases the step height in bleach traces was around 20 a.u. (see Figure 18.2a), whereas the bleach traces for other islands showed step height in order of 200 a.u. (see Figure 18.2b). In some cases, a single intensity trace displays steps with height differences in the order of a magnitude. While some difference in step height was to be expected, the variation observed in these experiments are puzzling and too large to draw any conclusion on the number of DNA origami plates per carbon nanoisland.

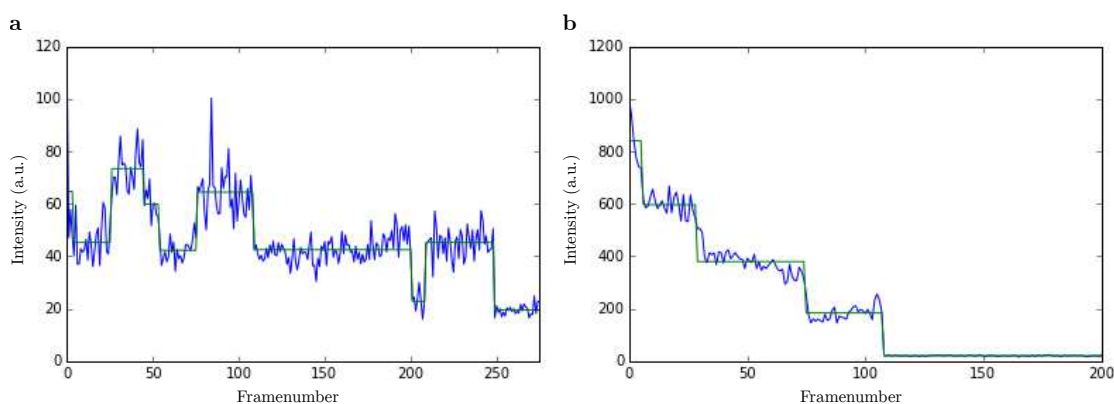


**Figure 18.2:** *Fluorescence intensity traces of two stepwise photobleaching experiments of DNA origami nanoplates immobilized on carbon nanoislands. The resulting step height varied largely between different carbon nanoislands. While some traces showed a step height of  $21.18 \pm 4.07$  a.u. (panel a), others showed a much higher step height of  $173.29 \pm 40.50$  a.u. (panel b).*

## 18.2 Quenching effects of ITO

In order to explain these unexpected results from the stepwise photobleaching experiments, different characteristics of the experimental system were reconsidered. The validity of all fluorescence microscopy data relies on the assumption that carbon nanoislands and PEG-coated ITO areas have no differential influence on fluorescence emission. Even though this equality seemed to be experimentally demonstrated previously [348], a more recent study found distance-dependent quenching effects of ITO on fluorophores [353]. In principle, this finding should have only limited impact, as both the carbon nanoislands and the water-hydrated PEG-layer [354] have the same distance to and height above the ITO substrate of around 3 nm to 4 nm. However, DNA nanoplates being attached to the sides of the island and not only to the top would lead to a broader distribution of the measured single step height, as the distance-dependent quenching of fluorophores by ITO would cause a fluorescence increase with island height, as the physical distance between fluorophore and quencher lowers the energy transfer efficiency and thus restores emission.

# Chapter 19

## Conclusion and outlook

In this part, the utilization of a biofunctionalization platform consisting of EBID nanostructures with two different methods was described.

A pick-and-place manipulation approach was implemented to make use of custom EBID patterns which are usually restricted to a small sample area. A home-built sample chamber was developed, featuring two chambers—one for cell picking and one for cell placing—which are separated by a barrier but can be interconnected. It was demonstrated how a cell can be picked with a coated AFM-cantilever, transferred to a different sample chamber and placed on a nanostructured surface area. On a micropatterned surface, Jurkat T cells expressing ZAP70-GFP showed rearrangement according to the underlying OKT3 patterns. After placing these cells on EBID patterns functionalized with OKT3, no clear rearrangement of ZAP70-GFP could be observed, although it has to be noted that the sample size was very small ( $n = 1$ ). Further experiments are needed in order to draw sophisticated conclusions. Still, the implemented pick-and-place approach can be extended to other systems, in particular when spatial or temporal control of a single cell is needed. Possible scenarios include sequential exposure of cells to either different ligands or different arrangements of the same ligand. Further, also the possibility to expose cells to repeated contact with the surface with user-defined time periods of contact and non-contact gives rise to interesting experimental ideas.

The combination of top-down physical nanopatterns and bottom-up DNA origami nanostructures allows for the generation of nanoislands displaying few to single molecules. Here, we showed how carbon nanoislands produced via EBID can be decorated with DNA origami nanoplates featuring fluorophore decoration.

However, characterization of the number of DNA origami nanoplates per carbon nanoisland proved to be difficult due to quenching effects caused by the ITO substrate used. Still, DNA nanoplates with a matching size compared to the nanoislands can be used to display a defined number of molecules. The approach of using DNA origami nanoplates as masks to cover part of the nanoislands, which results in reduced binding of other ligands on sites not blocked by the DNA plates can be particularly useful for patterning methods that cannot produce nanostructures smaller than 100 nm [355]. Still, a sophisticated characterization of the experimental system is of utmost importance to draw any conclusions. Since fluorescence microscopy techniques are not applicable for this system, other methods such as AFM imaging could be used.

# Chapter 20

## Materials and methods

### 20.1 Sample preparation

#### 20.1.1 PEG-Silanization

ITO-coated glass slides ( $50 \times 24 \times 0.175$  mm) with an ITO thickness of  $17 \pm 2$  nm and a sheet resistance of  $1200 \pm 200 \Omega/\text{sq}$  were obtained from Hans Tafelmaier Dünnschicht-Technik. These slides were cleaned to remove organic contaminants and incubated in 10:90, 50:50, and 90:10 methanol: $\text{CHCl}_3$  for 15 min each in an ultrasonic bath. After sonication, the slides were treated in basic Piranha (1:1:5 mixture of 30 % ammonia and 30 % hydrogen peroxide and water, freshly prepared, incubation for 40 min at  $70^\circ\text{C}$ ), rinsed with deionized water and dried under a stream of nitrogen. Next, the slides were plasma-oxidized in a Plasma System NANO (Diener electronic) at 0.4 mbar for 2 min at 50 W. Me-O-PEG-( $\text{CH}_2$ )<sub>3</sub>-Si(OMe)<sub>3</sub> with a MW of 460–590 D was purchased from ABCR (#SIM6492.7). A layer of PEG silane was grafted onto the ITO surface by immersing the slides in 20 mM PEGsilane in anhydrous toluene containing 5 % triethylamine as catalyst for 18 h at  $60^\circ\text{C}$ . Afterwards, the slides were sonicated in toluene and ethanol for 5 min each to remove loosely bound PEG, rinsed with deionized water and dried in a stream of nitrogen.

#### 20.1.2 Electron-beam-induced deposition

EBID features were written with an e-beam lithography system eLINE Plus (Raith) equipped with a GEMINI field-emitter column that allows for an electron

beam size of 1.6 nm for electron energies  $>3$  keV. The background pressure during lithography is below  $2 \times 10^{-5}$  Torr in the sample chamber, and below  $10^{-9}$  Torr at the cathode. The typical working distance during e-beam was 10 mm. The acceleration voltage was 20 kV and the aperture 10  $\mu\text{m}$ . The e-beam lithography setup was operated in a Class 100 clean room.

### 20.1.3 Biomolecule adsorption

Samples were incubated with a 2  $\mu\text{M}$  solution of avidin in 0.1 $\times$ PBS buffer (both Sigma-Aldrich) for 30 min at RT followed by a thorough washing step with PBS. Next, the samples were incubated either with biotinylated OKT3 antibody at a concentration of 10  $\mu\text{g}/\text{ml}$  in PBS or with 7 nM fluorophore-tagged DNA nanoplates in Tris base-acetic acid-EDTA (TAE) buffer supplemented with 14 mM  $\text{MgCl}_2$  for 30 min. Then samples were again washed with either PBS or TAE buffer with 14 mM  $\text{MgCl}_2$ . DNA nanoplates of 50 $\times$ 50 nm lateral size with Alexa532-modified DNA oligonucleotides in the four corners were supplied by our project partners. For details see [350]. For characterization of OKT3 surfaces, prepared slides were incubated with the Zenon Alexa Fluor 647 Mouse IgG2a Labeling Kit (Molecular Probes) according to the manufacturer's protocol and imaged with a 640 nm diode laser (Coherent, Obis).

## 20.2 Atomic Force Microscopy

A commercial AFM (JPK Instruments) equipped with a CellHesion 200 head was used. MLCT (Bruker) cantilevers were cleaned in a Harrick Plasma Cleaner for 30 s prior to tip functionalization. Subsequently, cantilevers were immersed in 10  $\mu\text{g}/\text{ml}$  fibronectin (Sigma-Aldrich) for 30 min. After washing with PBS, cantilevers were immediately used for experiments. After adjusting the cantilever over the target cell, approach was done by hand in 1  $\mu\text{m}$  steps until cantilever deflection was detected. The contact time between the cantilever and the cell at the surface as well as the pause time after cell attachment were set to 30 s and 5 min, respectively. For cell-sample separation, the z piezo was retracted over its full range of 100  $\mu\text{m}$  at a speed of 5  $\mu\text{m}/\text{s}$ . Then, the AFM head was raised using the three stepper motors until the cantilever was well above the middle barrier of the sample chamber. Next, the sample chamber was moved underneath the AFM



head and the target area was located. Coarse approach was again performed using the stepper motors. Fine approach of the cantilever with the cell was done by z piezo extension in 1  $\mu\text{m}$  steps until the cantilever deflected, indicating contact between the cell and the surface. Contact time varied depending on the type of experiment. Calcium imaging as well as fluorescence imaging were performed as described in chapter 14. All AFM experiments were performed at room temperature.

### 20.3 Chamber design

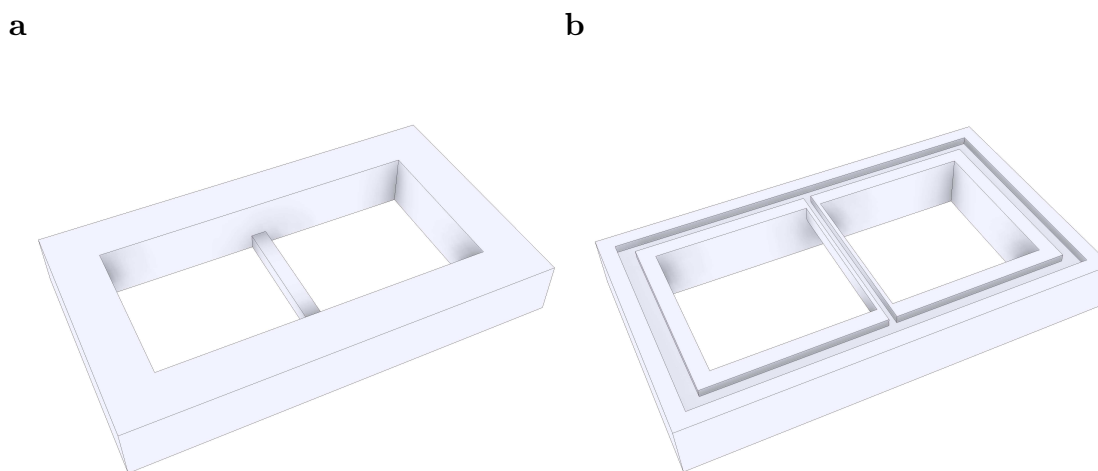


**Figure 20.1:** *Design of the sample chamber featuring two separate cavities. (a) Topview of the sample chamber in which the height difference between the middle and the surrounding barrier can be seen. (b) Bottomview of the sample chamber in which the glue trench can be seen.*

To create the sample chamber, a mold was designed using Autodesk Inventor. This 3d-printed mold was filled using Twinsil (Picodent) glue, resulting in the chamber design depicted in Figure 20.1. The height of the surrounding barrier is 3.5 mm while the height of the inner barrier is only 1 mm. Both cavities have the same size which is 10 $\times$ 10 mm. The bottom of the chamber features trenches which again can be filled with Twinsil glue for attaching the chamber to the glass slide.

## 20.4 Stepwise photobleaching

Fluorescence microscopy experiments were performed on a setup as described in chapter 14. For stepwise photobleaching experiments, a 532 nm diode-pumped solid state laser (Spectra physics Millennia 6s) was used. For image acquisition a sequence of 1000 images was recorded with an illumination time of 30 ms and a delay of 20 ms. Imaging was performed at a laser power of 120 W/cm<sup>2</sup>.

A stepwise bleaching approach was performed [72, 356] on fluorescently labeled DNA origami plates on carbon nanoislands. An oxygen scavenging system (PCA/PCD) was used to maximize fluorescence and reduce photoblinking [68]. Time-series data were fitted using custom-written software in Labview. Smoothing, nonmaximum suppression, and thresholding identified the locations of bright spots. Intensity versus time was plotted, and bleaching steps were identified manually [72, 73].

# Part V

## Outlook and Conclusions



Die approbierte gedruckte Originalversion dieser Dissertation ist an der TU Wien Bibliothek verfügbar.  
The approved original version of this doctoral thesis is available in print at TU Wien Bibliothek.

The quest for understanding the influence of spatial organization of biomolecules in cells on biological systems as a whole has driven the development of a vast number of micro- and nanostructuring techniques. In the context of this thesis, we implemented new approaches to probe the influence of spatial organization on T cell activation, used established methods to facilitate experimental analysis and combined different patterning approaches to improve their applicability.

A system to control the spatial organization of ligands using DNA origami nanostructures was developed with the purpose of its application in T cell biology. To this end, a general approach for the construction of a DNA platform was established, which can be modified in numerous ways. The DNA origami platform was shown to be capable of featuring fluorophores, antibodies and the TCR $\beta$ -reactive scFv. Further, the DNA origami platform can be adapted to serve as a mobile platform and if used together with co-stimulatory proteins is able to closely imitate an APC. This makes the system a custom tool to address and answer central questions in T cell immunology: the role of TCR clustering in T cell activation, the unknown composition of protein complexes in the T cell plasma membrane as well as the mechanisms of their cohesion. Future developments of the system could focus on extending it into the 3d regime. This would allow for the investigation of the kinetic-segregation model of T cell activation which is based on size-sensitivity for the molecules involved.

A combined approach of protein micropatterning together with FRAP was used to specifically determine binding kinetics between a cytosolic protein and a transmembrane interaction partner. This approach was validated on the interaction of ZAP70 with the TCR with the result that non-specific contributions to the fluorescence recovery signal can indeed be removed. Using this technique, the interaction times of the two involved proteins can be extracted from the recovery curves by fitting with a monoexponential function. Key parameters such as the interaction time or the mobile fraction could be determined. The employed micropatterning approach is not limited to measuring the interaction of ZAP70 with the TCR but can also be extended to investigate the interaction of any cytosolic protein and an otherwise mobile plasma membrane protein.

We implemented a pick-and-place manipulation approach to position single cells on custom written EBID patterns. By developing a home-built sample chamber, the experimental process of cell picking and cell delivery could be simplified. While rearrangement of ZAP70 according to the micropatterned sub-

strate could be observed, this could not be verified for EBID patterned substrates, most likely due to insufficient antibody density on structures. The implemented pick-and-place approach offers spatial and temporal control of a single cell and can be extended to other cell systems or different surface modification. A particular intriguing example would be the variation of contact time of T cells with activating surfaces as well as the influence of repeated contact with activating surfaces.

The combination of EBID nanopatterns with DNA origami nanoplates was shown and experimental challenges in characterizing the occupation of the nanoislands with the DNA nanoplates were described. In principle, DNA nanoplates with a matching size compared to the nanoislands can be used to display a defined number of molecules at a defined location. This approach might be practical for patterning methods that cannot produce nanofeatures smaller than 100 nm.

All these examples show different possibilities to employ micro- and nanostructuring techniques for specific tasks in T cell biology. Currently only few techniques have passed the proof-of-concept stage and conceptual challenges need to be overcome. Further, there might be also the need for new methods for improving characterization and quality control. This thesis demonstrated the immense potential of micro- and nanostructuring technology for single molecule studies in T cell biology and lays the foundation for structure evaluation. Ultimately, a better understanding of the influence of spatial organization on biological systems will enable to face of a broad range of challenges in biophysics and molecular biology. Additionally, a deeper understanding of each of the applied structuring techniques will help to improve future experimental designs as well as data analysis.

# Part VI

## Appendix



Die approbierte gedruckte Originalversion dieser Dissertation ist an der TU Wien Bibliothek verfügbar.  
The approved original version of this doctoral thesis is available in print at TU Wien Bibliothek.



# Appendix A

## Sequences

Following the common convention, DNA sequences are written in the 5'-to-3' direction. If modifications are added to single strands, they are written at the respective end of the sequence.

### A.1 Modification strands

Name	Sequence
X	CTTCTGTCTATCTTGGC
X'	GCCAAGATAGACAGAAG
Y	ACATTAGGCTAGTCCAC
Y'	GTGGACTAGCCTAATGT
Z	GGCTAAATATGCTAGGACTCT
Z'	AGAGTCCTAGCATATTTAGCC

**Table A.1:** *Sequences used for adding modifications the DNA origami platform.* These sequences are added to the modification and their respective reverse complement is added to specific staple strands of the DNA platform design. Often, a 4T region or a linker is added between the sequence and the modification. Primed letters denote the reverse complement of the original sequence.

## A.2 Staple strand mixes

The following tables list all staple strand sequences used in the DNA origami platform. Start and End indicate the row and column of the start and end position of a strand in the caDNAno program. General staple strands are grouped in the mastermix, whereas staple strands which can be used to attach modifications are grouped in separated mixes.

The yellow mix is used for attaching cholesterol moieties by using the staple strands with a Z'-4T sequence added to the 5' end. If no added functionality is wanted, the unmodified staples can be used. All staple strands in the red mix can be exchanged by strands with a 4T-X' sequence added to the 3' end and it is mostly used to attach fluorophores to the platform. All staple strands in the green mix can be exchanged by strands with a 4T-Y' sequence added to the 3' end and it is mostly used for attaching functional modifications to the DNA origami platform. To fold the batch-platform, all 20 staple strands in the red mix need to be replaced. Whereas for the individual-platform, only four staple strands—marked in gray in the table—need to be replaced.

### Yellow mix

Start	End	Sequence
2[47]	0[48]	GCGAGCTGAATTCTGCGAACGAGTATGCTGTA
3[128]	5[127]	CAATACTGGACGATAAAAACCAAAAATAATG
6[47]	4[48]	ATAAATTAGAGTAATGTGTAGGTAATACTTTT
7[128]	9[127]	CATTGTGAGCTCATTCAAGTGAATACGCATAGG
10[47]	8[48]	TAAATGTGTTGTAAATCAGCTCAAGCCCCAA
11[128]	13[127]	CAACGGAGGCACCAACCTAAAACGTACAGAGG
14[47]	12[48]	ACGCCAGGCTGTTGGGAAGGGCGATCGCACTC
15[128]	17[127]	ATACCGATAAAATCTCCAAAAAAAACAACCTT
18[47]	16[48]	TGCGTATTGCGTTGCGCTCACTGCCAATTCCA
19[128]	21[127]	AACCCATGTAGTACCGCCACCTCAGTACCAG

**Green mix**

Start	End	Sequence
4[63]	6[64]	ACCCTGTAAAGATTCAAAAAGGGTGTATGATAT
5[80]	6[96]	CGGAGACATTCATCAGTTGAGATTATTACAGG
6[63]	8[64]	TCAACCGTATCGATGAACGGTAATGGTTGATA
7[80]	8[96]	TAGCATGTTAGTAAATTGGGCTTGAAACACC
8[63]	10[64]	ATCAGAAATTTTTTAACCAATAGGCCTGTAGC
8[95]	7[79]	AGAACGAGCAATCATATGTACCCCCGTAAAAC
9[80]	10[96]	CAAAAATAAAAGAGGACAGATGAAGAACTGAC
9[112]	7[111]	AGACCAGGAGGCTTGCCCTGACGAAGATGGTT
10[63]	12[64]	CAGCTTTCGGGCGCATCGTAACCGATCGGCCT
10[95]	9[79]	CAACTTTGATTCGCGTCTGGCCTTAACGCCAT
11[80]	12[96]	CCAGTTTGCTTTGACCCCGAGCGAACACTAAA
11[112]	9[111]	AGCGCGAACAATCATAAGGGAACCCGGTGTAC
12[63]	14[64]	CAGGAAGATCGGTGCGGCCTCTTGCTGCAAG
12[95]	11[79]	ACACTCATAGGGACGACGACAGTTGCATCTG
13[80]	14[96]	CGCCAGCTAAAGACAGCATCGGAAGTCACCCT
13[112]	11[111]	GCAACGGCAAAGAGGCAAAGAATTTATACCA
14[95]	13[79]	CAGCAGCGGGCGAAAGGGGATGTCGCTATTA
15[112]	13[111]	TTTCTTAACCGCTTTTGCGGGATCCGAGGGTA
16[95]	15[79]	GTATCGGTGCTGTTTCCTGTGTGACGTAATCA
17[112]	15[111]	TTTTGCTAAGGCTCCAAAAGGAGCGAGGTGAA

**Red mix**

Start	End	Sequence
2[63]	4[64]	TATTTTCATTAAGCAATAAAGCCTACATTATG
7[112]	5[111]	TAATTTCACTAACGGAACAACATTTAGGAATA
14[63]	16[64]	GCGATTAAGTACCGAGCTCGAATTAATTGTTA
19[112]	17[111]	TAGCAAGCCGATCTAAAGTTTTGTGTATGGGA

## Mastermix

Start	End	Sequence
0[47]	1[31]	GCTCAACATGTTTTAAATATGCAAATAACAGT
0[63]	2[64]	TGAATATAAGATTTAGTTTGACCATTTAGCTA
0[95]	0[64]	TCATTTTTGCGGATGGCTTAGAGCTTAATTGC
0[143]	1[127]	ACAGGTCAGGATTAGAGAGTACCTGAAGCCCG
1[32]	3[31]	TGATTCCCAAAGGTGGCATCAATAATCATAC
1[80]	2[96]	ATTCGCAAGCAAAGCGGATTGCAGACTATTA
1[112]	0[96]	ATTAAGAGTTAATTGCTCCTTTTGATAAGAGG
1[128]	3[127]	AAAGACTTTGACCATAAATCAAAAATAGCGTC
2[95]	1[79]	TAGTCAGAAATGGTCAATAACCTGTTAGATAC
2[143]	0[144]	AACGAGAACAAATATCGCGTTTTAAACTCCA
3[32]	5[31]	AGGCAAGGAGCCTTTATTTCAACGTTTAAATG
3[80]	4[96]	AAAGCTAACAGAGGGGTAATAGTGCAAAAAGA
3[112]	1[111]	TAGACTGGATCAGGTCTTTACCCTTCAAAAAG
4[47]	2[48]	GCGGGAGACAAAGAATTAGCAAAATTTGGGGC
4[95]	3[79]	AGTTTTGCATCGGTTGTACCAAAACAGAGCAT
4[143]	2[144]	TACCAGACCGGAATCGTCATAAATGTTTCAGAA
5[32]	7[31]	CAATGCCTATGCCGAGAGGGTAGTCATTGCC
5[112]	3[111]	CCACATTCATAGCGAGAGGCTTTTAAAATGTT
5[128]	7[127]	CAGATACAACGTTAATAAAACGAACTTTAAT
6[95]	5[79]	TAGAAAGAGTCAAATCACCATCAAAGAAAGGC
6[143]	4[144]	AAAAATCTAACGCCAAAAGGAATCCCTCGTT
7[32]	9[31]	TGAGAGTCAGATTGTATAAGCAAAAATTCGCA
8[47]	6[48]	AAACAGGATGGAGCAAACAAGAGATCTAGCTG
8[143]	6[144]	ACAAAGCTATTACCTTATGCGATTTTGGGAAG
9[32]	11[31]	TTAAATTTAGCGAGTAACAACCCGACCGTAAT
9[128]	11[127]	CTGGCTGAACGAGGCGCAGACGGTACAAAAGTA
10[143]	8[144]	TAGCCGGACCTTCATCAAGAGTAATCAACGTA
11[32]	13[31]	GGGATAGTTTTCCGGCACCCTTCCATTTCAGG
12[47]	10[48]	CAGCCAGCTCACGTTGGTGTAGATATCAACAT
12[143]	10[144]	CTACGAAGATTTGTATCATCGCCTATGTTACT
13[32]	15[31]	CTGCGCAAGTTTTCCAGTCACGAATGCCTGC
13[128]	15[127]	CTTTGAGGTGCAGGGAGTTAAAGGACAGCTTG
14[143]	12[144]	CTGAGGCTACTAAAGACTTTTTTCATAATGCCA
15[32]	17[31]	AGGTGCACACGAGCCGGAAGCATACTAACTCA
15[80]	16[96]	TGGTCATATTATCAGCTTGCTTTCCTTTAATT
16[47]	14[48]	CACAACATTCTAGAGGATCCCCGGGTGGGTA
16[63]	18[64]	TCCGCTCACCGCTTCCAGTCGGGGCCAACGC
16[143]	14[144]	TCACGTTGAGTTGCGCCGACAATGTTCCGGTCC

Start	End	Sequence
17[32]	19[31]	CATTAATTGGGCGCCAGGGTGGTTATTGCCCT
17[80]	18[96]	CGTGCCAGAGTAAATGAATTTTCTCGTCTTTC
17[128]	19[127]	TCAACAGTCTCATAGTTAGCGTAACCAATAGG
18[63]	20[64]	GCGGGGAGGCAGCAAGCGGTCCACTGATGGTG
18[95]	17[79]	CAGACGTTCTGCATTAATGAATCGAAACCTGT
18[143]	16[144]	AGACAGCCTTCAGCGGAGTGAGAATAATTTT
19[32]	21[31]	TCACCGCCATAAATCAAAAGAATAGGAACAAG
19[80]	20[96]	GCCCCAGCAGCCACCACCCTCATTGAACCGCC
20[47]	18[48]	AATCCCTTTGGCCCTGAGAGAGTTAGGCGGTT
20[63]	21[79]	GTTCCGAATCCAACGTCAAAGGGCGAAAAACC
20[95]	19[79]	ACCCTCAGAGGCGAAAATCCTGTTGCTGTTTT
20[143]	18[144]	AGGAGGTTTACCGTAACACTGAGTCATTCCAC
21[32]	20[48]	AGTCCACTATTAAAGAACGTGGACATCGGCAA
21[80]	21[111]	GTCTATCAAGAGAAGGATTAGGATTAGCGGGG
21[112]	19[111]	TTTTGCTCAGAACCGCCACCCTCATTAGGGA
21[128]	20[144]	GCGGATAAGTGCCGTCGAGAGGGTCCGTA

### A.3 M13mp18

1	aatgctacta	ctattagtag	aattgatgcc	accttttcag	ctcgcgcccc	aaatgaaaat
61	atagctaaac	aggttattga	ccatttgcca	aatgatctca	atgggtcaaac	taaatctact
121	cgttcgcaga	attgggaatc	aactgttata	tggaatgaaa	cttccagaca	ccgtacttt
181	gttgcatatt	taaaacatgt	tgagctacag	cattatattc	agcaattaag	ctctaagcca
241	tccgcaaaaa	tgacctctta	tcaaaaggag	caattaaagg	tactctctaa	tcctgacctg
301	ttggagtttg	cttccggctc	ggttcgcttt	gaagctcgaa	ttaaaacgcg	atatttgaag
361	tctttcgggc	ttcctcttaa	tcttttgat	gcaatccgct	ttgcttctga	ctataatagt
421	cagggtaaag	acctgatttt	tgatttatgg	tcattctcgt	tttctgaact	gtttaaagca
481	tttgaggggg	attcaatgaa	tatttatgac	gattccgcag	tattggacgc	tatccagtct
541	aaacatttta	ctattacccc	ctctggcaaa	acttcttttg	caaaagcctc	tcgctatfff
601	ggtttttatac	gtcgtctggt	aaacgagggt	tatgatagtg	ttgctcttac	tatgcctcgt
661	aattcctttt	ggcgttatgt	atctgcatta	gttgaaatgtg	gtattcctaa	atctcaactg
721	atgaatcttt	ctacctgtaa	taatgtttgt	ccgttagttc	gttttattaa	cgtagatttt
781	tcttccaac	gtcctgactg	gtataatgag	ccagttctta	aaatcgcata	aggtaattca
841	caatgattaa	agttgaaatt	aaaccatctc	aagcccaatt	tactactcgt	tctgggtgtt
901	ctcgtcaggg	caagccttat	tactgaatg	agcagctttg	ttacgttgat	ttgggtaatg
961	aatatccggt	tcttgtcaag	attactcttg	atgaaggtca	gccagcctat	gcgctcgtc
1021	tgtacaccgt	tcactgtccc	tctttcaaag	ttggtcagtt	cggttccctt	atgattgacc
1081	gtctgcgcct	cgttccggct	aagtaacatg	gagcaggtcg	cggatttcga	cacaatttat
1141	caggcgatga	tacaaatctc	cgttgtaact	tgtttcgcgc	ttggtataat	cgctgggggt
1201	caaagatgag	tgttttagtg	tattcttttg	cctcttctgt	tttaggttgg	tgctctccta
1261	gtggcattac	gtattttacc	cgtttaatgg	aaacttctc	atgaaaaagt	ctttagtctt
1321	caaagcctct	gtagecgttg	ctaccctcgt	tccgatgctg	tctttcctg	ctgagggtga
1381	cgatcccga	aaagcgcct	ttaactcct	gcaagcctca	gcgaccgaat	atatcggtta
1441	tgctgtgggc	atggttgttg	tcattgtcgg	cgcaactatc	ggtatcaagc	tgtttaagaa

1501	attcacctcg	aaagcaagct	gataaacgca	tacaattaa	ggctcctttt	ggagcctttt
1561	ttttggagat	tttcaacgtg	aaaaaattat	tattcgcaat	tcctttagtt	gttcctttct
1621	attctcactc	cgctgaaact	gttgaaagtt	gtttagcaaa	atcccataca	gaaaattcat
1681	ttactaacgt	ctggaaagac	gacaaaactt	tagatcgтта	cgctaactat	gagggtctgc
1741	tgtggaatgc	tacagcgctt	gtagtttgta	ctggtgacga	aactcagttg	tacggtacat
1801	gggttcctat	tggtcttgct	atccctgaaa	atgagggtgg	tggtctgag	ggtggcggtt
1861	ctgagggtgg	cggttctgag	ggtggcggtg	ctaaacctcc	tgagtacggt	gatacaccta
1921	ttccgggcta	tacttatatc	aacctctcgc	acggcactta	tccgctggt	actgagcaaa
1981	accccgctaa	tcctaatcct	tctcttgagg	agtctcagcc	tcttaatact	ttcatgtttc
2041	agaataatag	gttccgaaat	aggcaggggg	cattaactgt	ttatacgggc	actgttactc
2101	aaggcactga	ccccgttaa	acttattacc	agtacactcc	tgtatcatca	aaagccatgt
2161	atgacgctta	ctggaacggt	aaattcagag	actgcgcttt	ccattctggc	tttaatgagg
2221	atttatttgt	tttgaatat	caaggccaat	cgtctgacct	gcctcaacct	cctgtcaatg
2281	ctggcggcgg	ctctggtggt	ggttctggtg	gcggtctgga	gggtggtggc	tctgagggtg
2341	gcggttctga	gggtggcggc	tctgagggag	gcggttccgg	tggtggctct	ggttccggtg
2401	attttgatta	tgaaaagatg	gcaaacgcta	ataagggggc	tatgaccgaa	aatgccgatg
2461	aaaacgcgct	acagtctgac	gctaaaggca	aacttgattc	tgtcgcctact	gattacgggtg
2521	ctgctatcga	tggtttcatt	ggtgacgttt	ccggccttgc	taatggtaat	ggtgctactg
2581	gtgattttgc	tggtctaat	tcccaaatgg	ctcaagtcgg	tgacggtgat	aattcacctt
2641	taatgaataa	tttccgcaa	tatttacctt	cctccctca	atcggttgaa	tgtcgcctt
2701	ttgtctttgg	cgctggtaaa	ccatatgaat	tttctattga	ttgtgacaaa	ataaacttat
2761	tccgtggtgt	ctttgcgttt	cttttatatg	ttgccacctt	tatgtatgta	ttttctacgt
2821	ttgctaacat	actgcgtaat	aaggagtctt	aatcatgcca	gttcttttgg	gtattccggtt
2881	attattcgct	ttctcgggtt	tccttctggt	aactttgttc	ggctatctgc	ttacttttct
2941	taaaaaggggc	ttcggtaaaga	tagctattgc	tatttcattg	tttctgctc	ttattattgg
3001	gcttaactca	attcttgtgg	gttatctctc	tgatattagc	gctcaattac	cctctgactt
3061	tgttcagggt	gttcagttaa	tttcccgtc	taatgcgctt	ccctgttttt	atgttattct
3121	ctctgtaaag	gctgctattt	tcatttttga	cgtaaacaa	aaaatcgttt	cttatttgga
3181	ttgggataaa	taatatggct	gtttattttg	taactggcaa	attaggtctt	ggaaaagcgc
3241	tcgttagcgt	tggtaaagatt	caggataaaa	ttgtagctgg	gtgcaaaaata	gcaactaatc
3301	ttgatttaag	gcttcaaaac	ctcccgaag	tcgggaggtt	cgctaaaacg	cctcgcgttc
3361	ttagaatacc	ggataagcct	tctatatctg	atttgcttgc	tattgggcgc	ggtaatgatt
3421	cctacgatga	aaataaaaac	ggcttgcttg	ttctcgatga	gtcgggtact	tggtttaata
3481	cccgttcttg	gaatgataag	gaaagacagc	cgattattga	ttggtttcta	catgctcgta
3541	aattagatg	ggatattatt	tttctgttc	aggacttatc	tattgttgat	aaacaggcgc
3601	gttctgcatt	agctgaacat	gttgtttatt	gtcgtcgtct	ggacagaatt	actttacctt
3661	ttgtcggtag	tttatattct	cttattactg	gctcgaaaat	gcctctgcct	aaattacatg
3721	ttggcgttgt	taaatatggc	gattctcaat	taagccctac	tgttgagcgt	tggtttata
3781	ctgtaagaa	tttgataaac	gcatatgata	ctaaacaggc	ttttctagt	aattatgatt
3841	ccggtgttta	ttcttattta	acgccttatt	tatcacacgg	tcggtatttc	aaaccattaa
3901	atttagtca	gaagatgaaa	ttaactaaaa	tatatattgaa	aaagttttct	cgcgttcttt
3961	gtcttgcgat	tggtttgca	tcagcattta	catatagtta	tataaccaa	cctaagccgg
4021	aggttaaaaa	ggtagtctct	cagacctatg	attttgataa	attcactatt	gactctctc
4081	agcgtcttaa	tctaagctat	cgctatgttt	tcaaggattc	taagggaaaa	ttaattaata
4141	gcgacgattt	acagaagcaa	ggttattcac	tcacatatat	tgatttatgt	actgtttcca
4201	ttaaaaaagg	taattcaaat	gaaattgtta	aatgtaatta	atttgtttt	cttgatgttt
4261	gtttcatcat	cttcttttgc	tcaggtaatt	gaaatgaata	atcgcctct	gcgcgatttt
4321	gtaacttggg	attcaaagca	atcaggcgaa	tccgttattg	tttctcccga	tgtaaaaggt
4381	actgttactg	tatattcatc	tgacgttaaa	cctgaaaatc	tacgcaattt	ctttatttct

4441	gttttacgtg	caaataattt	tgatatggta	ggttctaacc	cttcattat	tcagaagtat
4501	aatccaaaca	atcaggatta	tattgatgaa	ttgcatcat	ctgataatca	ggaatatgat
4561	gataattccg	ctccttctgg	tggtttcttt	gttccgcaaa	atgataatgt	tactcaaact
4621	tttaaaatta	ataacgttcg	ggcaaaggat	ttaatacgag	ttgtcgaatt	gtttgtaaag
4681	tctaatactt	ctaaatcttc	aaatgtatta	tctattgacg	gctctaactc	attagtgtt
4741	agtgcctcta	aagatatttt	agataacctt	cctcaattcc	tttcaactgt	tgatttgcca
4801	actgaccaga	tattgattga	gggttgata	tttgaggttc	agcaagggtga	tgcttagat
4861	ttttcatttg	ctgctggctc	tcagcgtggc	actggtgcag	gcggtgttaa	tactgaccgc
4921	ctcacctctg	ttttatcttc	tgctgggtgg	tcgttcggta	ttttaatgg	cgatgtttta
4981	gggctatcag	ttcgcgcatt	aaagactaat	agccattcaa	aaatattgtc	tgtgccacgt
5041	attcttacgc	ttcaggtca	gaagggttct	atctctgttg	gccagaatgt	cccttttatt
5101	actggctcgtg	tgaactggtga	atctgccaat	gtaaataatc	catttcagac	gattgagcgt
5161	caaaatgtag	gtatttccat	gagcgttttt	cctgttgcaa	tggtcggcgg	taatattgtt
5221	ctggatatta	ccagcaaggc	cgatagtttg	agttcttcta	ctcaggcaag	tgatgttatt
5281	actaatcaaa	gaagtattgc	tacaacggtt	aatttgcgtg	atggacagac	tcttttactc
5341	ggtgccctca	ctgattataa	aaacacttct	caggattctg	gcgtaccgtt	cctgtctaaa
5401	atccctttaa	tcggcctcct	gtttagctcc	cgctctgatt	ctaacgagga	aagcacgtta
5461	tacgtgctcg	tcaaagcaac	catagtacgc	gccctgtagc	ggcgcattaa	gcgcggcggg
5521	tgtgggtggt	acgcgcagcg	tgaccgctac	acttgccagc	gccctagcgc	ccgtccttt
5581	cgctttcttc	ccttcctttc	tcgccacgtt	cgccggcttt	ccccgcaag	ctctaaatcg
5641	ggggctccct	ttagggttcc	gatttagtgc	tttacggcac	ctcgaccca	aaaaactga
5701	tttgggtgat	ggttcacgta	gtgggcatc	gccctgatag	acggtttttc	gcccttgac
5761	gttggagtcc	acgttcttta	atagtggact	cttgttccaa	actggaacaa	cactcaaccc
5821	tatctcgggc	tattcttttg	atltataagg	gattttgccg	atctcggaac	caccatcaaa
5881	caggattttc	gcctgctggg	gcaaaccagc	gtggaccgct	tgtcgaact	ctctcagggc
5941	caggcgggtga	agggcaatca	gctgttgcct	gtctcactgg	tgaaaagaaa	aaccacctg
6001	gcgccaata	cgcaaaccgc	ctctcccgc	gcgttgccg	attcattaat	gcagctggca
6061	cgacaggttt	cccactgga	aagcgggcag	tgagcgcac	gcaattaatg	tgagttagct
6121	cactcattag	gcaccccagg	ctttacactt	tatgcttccg	gctcgtatgt	tgtgtggaat
6181	tgtgagcggga	taacaatttc	acacaggaaa	cagctatgac	catgattacg	aattcgagct
6241	cggtaccggg	ggatctctta	gagtcgacct	gcaggcatgc	aagcttgcca	ctggccgtcg
6301	ttttacaacg	tcgtgactgg	gaaaacctg	gcgttacca	acttaatcgc	cttgacgac
6361	atcccccttt	cgccagctgg	cgtaatagcg	aagaggcccg	caccgatcgc	ccttccaac
6421	agttgcgcag	cctgaatggc	gaatggcgtc	ttgcctggtt	tccggcacca	gaagcgggtc
6481	cggaagctg	gctggagtgc	gatcttctcg	aggccgatac	tgtcgtcgtc	ccctcaaact
6541	ggcagatgca	cggttacgat	gcgccatct	acaccaacgt	gacctatccc	attacggtea
6601	atccgcggtt	tgttcccacg	gagaatccga	cggttggtta	ctcgctcaca	tttaatgttg
6661	atgaaagctg	gctacaggaa	ggccagacgc	gaattatttt	tgatggcgtt	cctattggtt
6721	aaaaaatgag	ctgatttaac	aaaaatttaa	tgcgaatttt	aacaaaatat	taacgtttac
6781	aatttaaata	tttgcttata	caatcttctc	gtttttgggg	cttttctgat	tatcaaccgg
6841	ggtacatatg	attgacatgc	tagttttacg	attaccgttc	atcgattctc	ttgtttgctc
6901	cagactctca	ggcaatgacc	tgatagcctt	tgtagatctc	tcaaaaatag	ctaccctctc
6961	cggcattaat	ttatcageta	gaacggttga	atatcatatt	gatggtgatt	tgactgtctc
7021	cggcctttct	cacccttttg	aatctttacc	tacacattac	tcaggcattg	catttaaaat
7081	atatgagggt	tctaaaaatt	tttatccttg	cgttgaaata	aaggcttctc	ccgcaaaagt
7141	attacagggt	cataatgttt	ttggtacaac	cgatttagct	ttatgctctg	aggctttatt
7201	gcttaatttt	gctaattctt	tgcttgcct	gtagatttta	ttgtagtt	



# List of Abbreviations

AFM	atomic force microscope
AGE	agarose-gel electrophoresis
AOM	acousto optic modulator
APC	antigen presenting cell
ATP	adenosine triphosphate
BCR	B cell receptor
BSA	bovine serum albumin
CD	cluster of differentiation
ConA	Concanavalin A
cSMAC	central supramolecular activation complex
DAG	diacylglycerol
DC	dendritic cell
DGS-NTA(Ni)	1,2-dioleoyl-sn-glycero-3-[N(5-amino-1-carboxypentyl) iminodiacetic acid]succinyl[nickel salt]
DNA	deoxyribonucleic acid
dsDNA	double-stranded DNA
dSMAC	distal supramolecular activation complex
DYE549	Dye 549
EBID	electron-beam-induced deposition

---

EDTA	ethylenediaminetetraacetic acid
EMCCD	electron multiplying charge-coupled device
ER	endoplasmic reticulum
FBS	fetal bovine serum
FCS	fluorescence correlation spectroscopy
FRAP	fluorescence recovery after photobleaching
FWHM	full width at half maximum
GFP	Green fluorescent protein
ICAM	intercellular adhesion molecule
IL-2	interleukin-2
IP3	inositol trisphosphate
IS	immunological synapse
ITAM	immunoreceptor tyrosine-based activation motif
ITO	indium tin oxide
LAT	linker of activated T cells
LFA1	leukocyte function-associated antigen 1
MAPK	mitogen-activated protein kinase
MHC	major histocompatibility complex
MSD	mean square displacement
NA	numerical aperture
NFAT	nuclear factor of activated T cells
NK	natural killer
NMR	nuclear magnetic resonance
PALM	photoactivated localization microscopy

PBS	phosphate-buffered saline
PCR	polymerase chain reaction
PDMS	polydimethylsiloxane
PEG	polyethylene glycol
PI 3-kinase	phosphoinositide 3-kinase
PIP2	phosphatidylinositol bisphosphate
PIP <sub>3</sub>	phosphatidylinositol (3,4,5)-trisphosphate
PKC- $\theta$	protein kinase C- $\theta$
PLC- $\gamma$	phospholipase C- $\gamma$
pMHC	peptide major histocompatibility complex
POPC	1-palmitoyl-2-oleoyl-sn-glycero-3-phosphocholine
PPO	poly propylene oxide
PSF	point spread function
pSMAC	peripheral supramolecular activation complex
RMS	root mean square
RNA	ribonucleic acid
ROI	region of interest
SAM	self-assembled monolayer
SCFS	single cell force spectroscopy
scFv	single chain antibody fragment
SDS	sodium dodecyl sulfate
SEM	scanning electron microscope
SH	Src homology
SLB	supported lipid bilayer
SLO	secondary lymphoid organ
SMAC	supramolecular activation complex
SPT	single particle tracking
ssDNA	single-stranded DNA

---

STAR635	AbberiorStar635
STED	stimulated emission depletion
STEM	scanning transmission electron microscope
STORM	stochastic optical reconstruction microscopy
SUV	small unilamellar vesicle
TAE	Tris base-acetic acid-EDTA
TCR	T cell receptor
TEG	tetraethylene glycol
TEM	transmission electron microscope
TIRF	total internal reflection fluorescence
Tris	trishydroxymethylaminomethane
ZAP70	$\zeta$ -chain-associated protein kinase 70

# List of Figures

1.1	Schematic overview of the presented methods for structuring surfaces. . . . .	8
2.1	Composition of the T cell receptor complex. . . . .	16
2.2	The binding of CD4 to an MHC class II molecule. . . . .	17
2.3	Binding of adhesion and co-stimulatory molecules to their ligands.	19
2.4	ITAM phosphorylation is responsible for the recruitment of ZAP70 to the TCR. . . . .	21
2.5	Overview of an immunological synapse (IS). . . . .	23
2.6	Ca <sup>2+</sup> entry activates the nuclear factor of activated T cells (NFAT).	26
3.1	The physical basis of fluorescence. . . . .	30
3.2	Schematic overview of an inverted microscope and the microscopy setup. . . . .	32
3.3	TIRF microscopy allows for the observation of single molecule fluorescence at surfaces and interfaces. . . . .	33
3.4	Fundamental principles of a FRAP experiment. . . . .	35
3.5	Fluorescence intensity of a structure in a typical FRAP experiment.	36
3.6	The central diffraction spot of a point source is called Airy disk.	38
3.7	The fundamental principle of SPT consists of acquisition, localization and tracking. . . . .	41
3.8	Bleaching steps of single fluorescent protein complexes reveal the number of fluorescently labeled subunits. . . . .	43
3.9	Colocalization of spectrally separated fluorophores gives information on the interaction of differentially labeled subunits of complexes.	45
3.10	Basic setup and working principle of an AFM. . . . .	46
3.11	Operating modes in atomic force microscopy. . . . .	48

3.12	Cell-substrate adhesion operating principle. . . . .	53
3.13	EBID is a resistless deposition technique practiced mainly in SEMs. . . . .	55
4.1	This flowchart schematically shows the individual steps of the DNA origami nanostructuring procedure. . . . .	62
5.1	Individual components of DNA and their composition forming a double helix structure. . . . .	65
5.2	A toehold mediated strand displacement reaction is an example for a branch migration process. . . . .	73
5.3	DNA motifs and secondary structure. . . . .	75
5.4	Structures of lipid types and lipid assemblies. . . . .	78
5.5	Interactions of DNA nanostructures with lipid bilayers. . . . .	80
6.1	Various examples for DNA nanostructures. . . . .	84
6.2	Overview of various DNA origami applications. . . . .	86
6.3	Scaffolded DNA origami design concepts. . . . .	88
6.4	Hybridization strategies for modified oligonucleotides to DNA nanoconstructs. . . . .	91
6.5	Thermal annealing of scaffolded DNA nanostructures. . . . .	94
6.6	Gel electrophoresis purification. . . . .	98
6.7	DNA origami purification using Amicon Ultra 100K centrifugal filters. . . . .	100
6.8	DNA origami purification using PEG precipitation. . . . .	101
7.1	Design of the rectangular DNA origami platform. . . . .	107
7.2	Possible positions of modifications on the DNA origami platform. . . . .	109
7.3	Bending of the DNA origami platform. . . . .	110
7.4	Gel electrophoresis of the DNA origami platform. . . . .	113
7.5	AFM overview images of DNA platforms on mica. . . . .	114
7.6	AFM image of a single DNA origami platform on a mica surface measured in liquid. . . . .	115
7.7	Colocalization analysis of the DNA origami platform. . . . .	118
7.8	Single particle tracking analysis of the DNA origami platform. . . . .	120
7.9	Biotin-modified oligos serve as a suitable tool for the attachment of a protein of interest to a DNA origami structure. . . . .	122

7.10	The attachment of antibodies to DNA origami platforms demonstrates their deployability to study biological systems at the nanoscale.	125
7.11	The experimental layout is set out to probe the influence of three different ligand distributions on T cell activation. . . . .	127
7.12	Diffusion analysis of functional DNA origami on a lipid bilayer. . .	128
11.1	Simplified depiction of different FRAP behaviors. . . . .	149
11.2	Example of the Lomb algorithm. . . . .	153
11.3	General principle of proximity photolithography. . . . .	157
11.4	Fabrication of polymer stamps for soft lithography and their usage in microcontact printing. . . . .	159
11.5	Chemical structure of PDMS. . . . .	160
11.6	Structural organization of autoinhibited ZAP70, and model of autoinhibition. . . . .	164
11.7	Model of ZAP70 TCR-binding dynamics and activation. . . . .	166
11.8	TCR signal amplification and dispersion via a catch-and-release model in early and late ZAP70 signaling. . . . .	168
12.1	A Jurkat T cell on patterned OKT3 antibody surface. . . . .	170
12.2	Time course of ZAP70-GFP recruitment to OKT3 sites. . . . .	171
12.3	Jurkat T cell activation on the different surfaces. . . . .	172
12.4	Relative OKT3 antibody densities on patterned and homogeneously coated OKT3 surfaces. . . . .	173
12.5	Specificity of ZAP70-GFP recruitment to aCD3 ON areas. . . . .	174
12.6	FRAP experiments on non-activated Jurkat T cells. . . . .	175
12.7	Recovering fraction of ZAP70-GFP after repetitive bleach pulses. . . . .	177
12.8	FRAP data recorded in cells expressing cytosolic GFP on a fibronectin-coated surface. . . . .	178
12.9	ZAP70-GFP recovery in cells on micropatterned and coated OKT3 surfaces. . . . .	180
12.10	Comparison of several FRAP parameters for cells on micropatterned and homogeneously coated OKT3 surfaces at 22 °C. . . . .	182
12.11	Comparison of several other FRAP parameters for cells on micropatterned and homogeneously coated OKT3 surfaces at 22 °C. . . . .	183
12.12	Comparison of several FRAP parameters for cells on micropatterned and homogeneously coated OKT3 surfaces at 37 °C. . . . .	186

12.13	Comparison of FRAP parameters for cells on micropatterned and homogeneously coated OKT3 surfaces at 37 °C. . . . .	187
14.1	Illumination protocol used for FRAP experiments. . . . .	194
16.1	The generation of biomolecular nanopatterns via EBID. . . . .	201
17.1	The chamber design features two adjacent cavities. . . . .	209
17.2	Calcium imaging of a single cell attached to a tipless cantilever. . . . .	212
17.3	The recruitment of ZAP70-GFP after placing a cell attached to a cantilever on a micropatterned surface. . . . .	213
17.4	The delivery of cells to EBID patterned surfaces. . . . .	215
18.1	Fluorescently labeled DNA origami nanoplates bound to carbon nanoislands coated with avidin. . . . .	218
18.2	Fluorescence intensity traces of two stepwise photobleaching experiments of DNA origami nanoplates immobilized on carbon nanoislands. . . . .	219
20.1	Design of the sample chamber featuring two separate cavities. . . . .	225



# List of Tables

5.1	Properties of ssDNA and dsDNA. . . . .	68
5.2	The thermodynamic parameters for DNA duplex formation at 1 M NaCl. . . . .	70
5.3	Base pair stacking free energy parameters for $\Delta G$ in kcal mol <sup>-1</sup> . . . . .	71
6.1	Comparison of different purification methods for DNA origami. . . . .	102
7.1	A listing of the labeling strands for the DNA origami platform used in this thesis. . . . .	112
9.1	Submission parameters for the CanDo analysis of the DNA origami platform. . . . .	133
9.2	Composition of the folding mix. . . . .	135
11.1	The properties of PDMS after curing. . . . .	161
12.1	Parameters extracted from FRAP curves. . . . .	184
A.1	Sequences used for adding modifications the DNA origami platform. . . . .	233



# Bibliography

1. Morón, J. A. & Devi, L. A. Use of proteomics for the identification of novel drug targets in brain diseases. *Journal of Neurochemistry* **102**, 306–315 (2007).
2. Siwiak, M. & Zielenkiewicz, P. Transimulation-protein biosynthesis web service. *PLoS One* **8**, e73943 (2013).
3. Alberts, B. *et al.* *Molecular Biology of the Cell* (Garland Science, 2014).
4. Bernstein, B. W. & Bamberg, J. R. Actin-ATP hydrolysis is a major energy drain for neurons. *Journal of Neuroscience* **23**, 1–6 (2003).
5. Smrt, S. T., Draney, A. W., Singaram, I. & Lorieau, J. L. Structure and dynamics of membrane proteins and membrane associated proteins with native bicelles from eukaryotic tissues. *Biochemistry* **56**, 5318–5327 (2017).
6. Schneiter, R. & Toulmay, A. The role of lipids in the biogenesis of integral membrane proteins. *Applied Microbiology and Biotechnology* **73**, 1224–1232 (2007).
7. Sevcsik, E. & Schütz, G. J. With or without rafts? Alternative views on cell membranes. *Bioessays* **38**, 129–139 (2016).
8. Shaw, A. *et al.* Spatial control of membrane receptor function using ligand nanocalipers. *Nature Methods* **11**, 841 (2014).
9. Salaita, K. *et al.* Restriction of receptor movement alters cellular response: physical force sensing by EphA2. *Science* **327**, 1380–1385 (2010).
10. Betzig, E. *et al.* Imaging intracellular fluorescent proteins at nanometer resolution. *Science* **313**, 1642–1645 (2006).

11. Hell, S. W. & Wichmann, J. Breaking the diffraction resolution limit by stimulated emission: stimulated-emission-depletion fluorescence microscopy. *Optics Letters* **19**, 780–782 (1994).
12. Fang, Y. Ligand–receptor interaction platforms and their applications for drug discovery. *Expert Opinion on Drug Discovery* **7**, 969–988 (2012).
13. Murphy, K. & Weaver, C. *Janeway's Immunobiology* (Garland Science, 2016).
14. Huppa, J. B. & Davis, M. M. T-cell-antigen recognition and the immunological synapse. *Nature Reviews Immunology* **3**, 973 (2003).
15. Grakoui, A. *et al.* The immunological synapse: a molecular machine controlling T cell activation. *Science* **285**, 221–227 (1999).
16. Monks, C. R., Freiberg, B. A., Kupfer, H., Sciaky, N. & Kupfer, A. Three-dimensional segregation of supramolecular activation clusters in T cells. *Nature* **395**, 82 (1998).
17. James, J. R. *et al.* The T-cell receptor triggering apparatus is composed of monovalent or monomeric proteins. *Journal of Biological Chemistry*, jbc–M111 (2011).
18. James, J. R. *et al.* Single-molecule level analysis of the subunit composition of the T cell receptor on live T cells. *Proceedings of the National Academy of Sciences* **104**, 17662–17667 (2007).
19. Xia, Y. & Whitesides, G. M. Soft lithography. *Angewandte Chemie International Edition* **37**, 550–575 (1998).
20. Hong, F., Zhang, F., Liu, Y. & Yan, H. DNA origami: scaffolds for creating higher order structures. *Chemical Reviews* **117**, 12584–12640 (2017).
21. Rothmund, P. W. Folding DNA to create nanoscale shapes and patterns. *Nature* **440**, 297 (2006).
22. Douglas, S. M. *et al.* Self-assembly of DNA into nanoscale three-dimensional shapes. *Nature* **459**, 414 (2009).
23. Rai-Choudhury, P. *Handbook of microlithography, micromachining, and microfabrication: microlithography* (Iet, 1997).
24. Broers, A., Molzen, W., Cuomo, J. & Wittels, N. Electron-beam fabrication of 80-Å metal structures. *Applied Physics Letters* **29**, 596–598 (1976).

25. Van Dorp, W. F. & Hagen, C. W. A critical literature review of focused electron beam induced deposition. *Journal of Applied Physics* **104**, 081301. eprint: <https://doi.org/10.1063/1.2977587>. <https://doi.org/10.1063/1.2977587> (2008).
26. Huppa, J. B. & Davis, M. M. in *Advances in Immunology* 1–50 (Elsevier, 2013).
27. Den Haan, J. M., Arens, R. & van Zelm, M. C. The activation of the adaptive immune system: cross-talk between antigen-presenting cells, T cells and B cells. *Immunology Letters* **162**, 103–112 (2014).
28. Hivroz, C., Chemin, K., Tourret, M. & Bohineust, A. Crosstalk between T lymphocytes and dendritic cells. *Critical Reviews in Immunology* **32** (2012).
29. Kambayashi, T. & Laufer, T. M. Atypical MHC class II-expressing antigen-presenting cells: can anything replace a dendritic cell? *Nature Reviews Immunology* **14**, 719 (2014).
30. Cooper, M. D. The early history of B cells. *Nature Reviews Immunology* **15**, 191 (2015).
31. LeBien, T. W. & Tedder, T. F. B lymphocytes: how they develop and function. *Blood* **112**, 1570–1580 (2008).
32. Terunuma, H., Deng, X., Dewan, Z., Fujimoto, S. & Yamamoto, N. Potential role of NK cells in the induction of immune responses: implications for NK cell-based immunotherapy for cancers and viral infections. *International Reviews of Immunology* **27**, 93–110 (2008).
33. Huang, J. *et al.* A single peptide-major histocompatibility complex ligand triggers digital cytokine secretion in CD4<sup>+</sup> T cells. *Immunity* **39**, 846–857 (2013).
34. Sakihama, T., Smolyar, A. & Reinherz, E. L. Molecular recognition of antigen involves lattice formation between CD4, MHC class II and TCR molecules. *Immunology today* **16**, 581–587 (1995).
35. Weber, S. & Karjalainen, K. Mouse CD4 binds MHC class II with extremely low affinity. *International Immunology* **5**, 695–698 (1993).
36. Corr, M. *et al.* T cell receptor-MHC class I peptide interactions: affinity, kinetics, and specificity. *Science* **265**, 946–949 (1994).

37. Matsui, K., Boniface, J. J., Steffner, P., Reay, P. A. & Davis, M. M. Kinetics of T-cell receptor binding to peptide/I-Ek complexes: correlation of the dissociation rate with T-cell responsiveness. *Proceedings of the National Academy of Sciences* **91**, 12862–12866 (1994).
38. Krogsgaard, M. *et al.* Evidence that structural rearrangements and/or flexibility during TCR binding can contribute to T cell activation. *Molecular Cell* **12**, 1367–1378 (2003).
39. Chan, A. C., Iwashima, M., Turck, C. W. & Weiss, A. ZAP-70: a 70 kd protein-tyrosine kinase that associates with the TCR  $\zeta$  chain. *Cell* **71**, 649–662 (1992).
40. Sloan-Lancaster, J. *et al.* Regulation of ZAP-70 intracellular localization: visualization with the green fluorescent protein. *Journal of Experimental Medicine* **186**, 1713–1724 (1997).
41. Wang, H. *et al.* ZAP-70: an essential kinase in T-cell signaling. *Cold Spring Harbor Perspectives in Biology* **2**, a002279 (2010).
42. Hatada, M. H. *et al.* Molecular basis for interaction of the protein tyrosine kinase ZAP-70 with the T-cell receptor. *Nature* **377**, 32 (1995).
43. Au-Yeung, B. B. *et al.* The structure, regulation, and function of ZAP-70. *Immunological Reviews* **228**, 41–57 (2009).
44. Park, M.-J. *et al.* SH2 domains serve as lipid-binding modules for pTyr-signaling proteins. *Molecular Cell* **62**, 7–20 (2016).
45. Bunnell, S. C. *et al.* T cell receptor ligation induces the formation of dynamically regulated signaling assemblies. *The Journal of Cell Biology* **158**, 1263–1275 (2002).
46. Norcross, M. *A synaptic basis for T-lymphocyte activation in Annales de l'Institut Pasteur/Immunologie* **135** (1984), 113–134.
47. Paul, W. E. & Seder, R. A. Lymphocyte responses and cytokines. *Cell* **76**, 241–251 (1994).
48. Dustin, M. L. *et al.* A novel adaptor protein orchestrates receptor patterning and cytoskeletal polarity in T-cell contacts. *Cell* **94**, 667–677 (1998).
49. Davis, D. M. & Dustin, M. L. What is the importance of the immunological synapse? *Trends in Immunology* **25**, 323–327 (2004).

50. Ortega-Carrion, A. & Vicente-Manzanares, M. Concerning immune synapses: a spatiotemporal timeline. *F1000Research* **5** (2016).
51. Valitutti, S. & Dupré, L. in *Immunological Synapse* 209–228 (Springer, 2010).
52. Thauland, T. J. & Parker, D. C. Diversity in immunological synapse structure. *Immunology* **131**, 466–472 (2010).
53. Lee, K.-H. *et al.* T cell receptor signaling precedes immunological synapse formation. *Science* **295**, 1539–1542 (2002).
54. Campi, G., Varma, R. & Dustin, M. L. Actin and agonist MHC–peptide complex–dependent T cell receptor microclusters as scaffolds for signaling. *Journal of Experimental Medicine* **202**, 1031–1036 (2005).
55. Yokosuka, T. *et al.* Newly generated T cell receptor microclusters initiate and sustain T cell activation by recruitment of Zap70 and SLP-76. *Nature Immunology* **6**, 1253 (2005).
56. Varma, R., Campi, G., Yokosuka, T., Saito, T. & Dustin, M. L. T cell receptor–proximal signals are sustained in peripheral microclusters and terminated in the central supramolecular activation cluster. *Immunity* **25**, 117–127 (2006).
57. Yokosuka, T. *et al.* Spatiotemporal basis of CTLA-4 costimulatory molecule–mediated negative regulation of T cell activation. *Immunity* **33**, 326–339 (2010).
58. Saito, T. & Yokosuka, T. Immunological synapse and microclusters: the site for recognition and activation of T cells. *Current Opinion in Immunology* **18**, 305–313 (2006).
59. Krummel, M. F., Sjaastad, M. D., Wülfing, C. & Davis, M. M. Differential clustering of CD4 and CD3 $\zeta$  during T cell recognition. *Science* **289**, 1349–1352 (2000).
60. Krummel, M. F. & Davis, M. M. Dynamics of the immunological synapse: finding, establishing and solidifying a connection. *Current Opinion in Immunology* **14**, 66–74 (2002).
61. Hashimoto-Tane, A. & Saito, T. Dynamic regulation of TCR–microclusters and the microsynapse for T cell activation. *Frontiers in Immunology* **7**, 255 (2016).

62. Weiss, A. & Littman, D. R. Signal transduction by lymphocyte antigen receptors. *Cell* **76**, 263–274 (1994).
63. Wange, R. L. & Samelson, L. E. Complex complexes: signaling at the TCR. *Immunity* **5**, 197–205 (1996).
64. Murphy, D. B. & Davidson, M. W. *Fundamentals of Light Microscopy and Electronic Imaging* 2nd ed. (Wiley-Blackwell, 2012).
65. Zeiss, C. *Zeiss Axiovert 200 Brochure* tech. rep. (Zeiss, 2006).
66. Ambrose, E. A surface contact microscope for the study of cell movements. *Nature* **178**, 1194 (1956).
67. Axelrod, D. Cell-substrate contacts illuminated by total internal reflection fluorescence. *The Journal of Cell Biology* **89**, 141–145 (1981).
68. Vogelsang, J. *et al.* Make them blink: Probes for super-resolution microscopy. *ChemPhysChem* **11**, 2475–2490 (2010).
69. Thompson, R. E., Larson, D. R. & Webb, W. W. Precise nanometer localization analysis for individual fluorescent probes. *Biophysical Journal* **82**, 2775–2783 (2002).
70. Manzo, C. & Garcia-Parajo, M. F. A review of progress in single particle tracking: from methods to biophysical insights. *Reports on Progress in Physics* **78**, 124601 (2015).
71. Wieser, S. & Schütz, G. J. Tracking single molecules in the live cell plasma membrane—Do's and Don't's. *Methods* **46**, 131–140 (2008).
72. Ulbrich, M. H. & Isacoff, E. Y. Subunit counting in membrane-bound proteins. *Nature Methods* **4**, 319 (2007).
73. Ulbrich, M. H. in *Far-Field Optical Nanoscopy* 263–291 (Springer, 2011).
74. Binnig, G., Quate, C. F. & Gerber, C. Atomic force microscope. *Physical Review Letters* **56**, 930 (1986).
75. Hansma, A. *et al.* Tapping mode atomic force microscopy in liquids. *Applied Physics Letters* **64**, 1738–1740 (1994).
76. Eaton, P. & West, P. *Atomic force microscopy* (Oxford University Press, 2010).
77. JPK. *Nano Wizard AFM Handbook* 6.0. JPK Instruments AG (July 2018).



78. Martin, Y., Williams, C. & Wickramasinghe, H. K. Atomic force microscope–force mapping and profiling on a sub 100-Å scale. *Journal of Applied Physics* **61**, 4723–4729 (1987).
79. Zhong, Q., Inniss, D., Kjoller, K. & Elings, V. Fractured polymer/silica fiber surface studied by tapping mode atomic force microscopy. *Surface Science Letters* **290**, L688–L692 (1993).
80. JPK. *CellHesion 200* tech. rep. (JPK Instruments AG, 2015).
81. JPK. *Using the CellHesion module- a practical guide* tech. rep. (JPK Instruments AG, 2014).
82. Helenius, J., Heisenberg, C.-P., Gaub, H. E. & Muller, D. J. Single-cell force spectroscopy. *Journal of Cell Science* **121**, 1785–1791 (2008).
83. De Broglie, L. Nouvelle dynamique des quanta. *Rapport et discussions du V e Conseil de Physique Solvay* (1928).
84. Knoll, M. & Ruska, E. Das Elektronenmikroskop. *Zeitschrift für Physik* **78**, 318–339 (1932).
85. Silvis-Cividjian, N., Hagen, C., Kruit, P. v. d., vd Stam, M. & Groen, H. Direct fabrication of nanowires in an electron microscope. *Applied Physics Letters* **82**, 3514–3516 (2003).
86. Oatley, C. W. The early history of the scanning electron microscope. *Journal of Applied Physics* **53**, R1–R13 (1982).
87. Koops, H. W. *et al.* Characterization and application of materials grown by electron-beam-induced deposition. *Japanese Journal of Applied Physics* **33**, 7099 (1994).
88. Kiyohara, S., Takamatsu, H. & Mori, K. Microfabrication of diamond films by localized electron beam chemical vapour deposition. *Semiconductor Science and Technology* **17**, 1096 (2002).
89. Silvis-Cividjian, N. *Electron Beam Induced Nanometer Scale Deposition* PhD thesis (Technical University in Delft, 2002).
90. Chen, J. & Seeman, N. C. Synthesis from DNA of a molecule with the connectivity of a cube. *Nature* **350**, 631 (1991).
91. Winfree, E., Liu, F., Wenzler, L. A. & Seeman, N. C. Design and self-assembly of two-dimensional DNA crystals. *Nature* **394**, 539 (1998).

92. Andersen, E. S. *et al.* Self-assembly of a nanoscale DNA box with a controllable lid. *Nature* **459**, 73 (2009).
93. Dietz, H., Douglas, S. M. & Shih, W. M. Folding DNA into twisted and curved nanoscale shapes. *Science* **325**, 725–730 (2009).
94. Han, D. *et al.* DNA origami with complex curvatures in three-dimensional space. *Science* **332**, 342–346 (2011).
95. Liedl, T., Högberg, B., Tytell, J., Ingber, D. E. & Shih, W. M. Self-assembly of three-dimensional prestressed tensegrity structures from DNA. *Nature Nanotechnology* **5**, 520 (2010).
96. Ke, Y. *et al.* Multilayer DNA origami packed on a square lattice. *Journal of the American Chemical Society* **131**, 15903–15908 (2009).
97. Douglas, S. M., Bachelet, I. & Church, G. M. A logic-gated nanorobot for targeted transport of molecular payloads. *Science* **335**, 831–834 (2012).
98. Marras, A. E., Zhou, L., Su, H.-J. & Castro, C. E. Programmable motion of DNA origami mechanisms. *Proceedings of the National Academy of Sciences* **112**, 713–718 (2015).
99. Ackermann, D. *et al.* A double-stranded DNA rotaxane. *Nature Nanotechnology* **5**, 436 (2010).
100. List, J., Falgenhauer, E., Kopperger, E., Pardatscher, G. & Simmel, F. C. Long-range movement of large mechanically interlocked DNA nanostructures. *Nature Communications* **7**, 12414 (2016).
101. Funke, J. J. & Dietz, H. Placing molecules with Bohr radius resolution using DNA origami. *Nature Nanotechnology* **11**, 47 (2016).
102. Kuzyk, A. *et al.* DNA-based self-assembly of chiral plasmonic nanostructures with tailored optical response. *Nature* **483**, 311 (2012).
103. Langecker, M., Arnaut, V., List, J. & Simmel, F. C. DNA nanostructures interacting with lipid bilayer membranes. *Accounts of Chemical Research* **47**, 1807–1815 (2014).
104. Endo, M., Katsuda, Y., Hidaka, K. & Sugiyama, H. A versatile DNA nanochip for direct analysis of DNA base-excision repair. *Angewandte Chemie International Edition* **49**, 9412–9416 (2010).

105. Endo, M., Katsuda, Y., Hidaka, K. & Sugiyama, H. Regulation of DNA methylation using different tensions of double strands constructed in a defined DNA nanostructure. *Journal of the American Chemical Society* **132**, 1592–1597 (2010).
106. Derr, N. D. *et al.* Tug-of-war in motor protein ensembles revealed with a programmable DNA origami scaffold. *Science* **338**, 662–665 (2012).
107. Rinker, S., Ke, Y., Liu, Y., Chhabra, R. & Yan, H. Self-assembled DNA nanostructures for distance-dependent multivalent ligand–protein binding. *Nature Nanotechnology* **3**, 418 (2008).
108. Jungmann, R. *et al.* Single-molecule kinetics and super-resolution microscopy by fluorescence imaging of transient binding on DNA origami. *Nano Letters* **10**, 4756–4761 (2010).
109. Yurke, B., Turberfield, A. J., Mills Jr, A. P., Simmel, F. C. & Neumann, J.L. A DNA-fuelled molecular machine made of DNA. *Nature* **406**, 605 (2000).
110. Shin, J.-S. & Pierce, N. A. A synthetic DNA walker for molecular transport. *Journal of the American Chemical Society* **126**, 10834–10835 (2004).
111. Simmel, F. C. Processive motion of bipedal DNA walkers. *ChemPhysChem* **10**, 2593–2597 (2009).
112. Green, S., Bath, J. & Turberfield, A. Coordinated chemomechanical cycles: a mechanism for autonomous molecular motion. *Physical Review Letters* **101**, 238101 (2008).
113. Veneziano, R. *et al.* Designer nanoscale DNA assemblies programmed from the top down. *Science* **352**, 1534–1534 (2016).
114. Benson, E. *et al.* DNA rendering of polyhedral meshes at the nanoscale. *Nature* **523**, 441 (2015).
115. Yang, Y. *et al.* Self-assembly of size-controlled liposomes on DNA nanotemplates. *Nature Chemistry* **8**, 476 (2016).
116. Linko, V., Ora, A. & Kostianen, M. A. DNA nanostructures as smart drug-delivery vehicles and molecular devices. *Trends in Biotechnology* **33**, 586–594 (2015).

117. Gopinath, A., Miyazono, E., Faraon, A. & Rothemund, P. W. Engineering and mapping nanocavity emission via precision placement of DNA origami. *Nature* **535**, 401 (2016).
118. Knudsen, J. B. *et al.* Routing of individual polymers in designed patterns. *Nature Nanotechnology* **10**, 892 (2015).
119. Schreiber, R. *et al.* Chiral plasmonic DNA nanostructures with switchable circular dichroism. *Nature Communications* **4**, 2948 (2013).
120. Roller, E.-M. *et al.* DNA-assembled nanoparticle rings exhibit electric and magnetic resonances at visible frequencies. *Nano Letters* **15**, 1368–1373 (2015).
121. Chandrasekaran, R. & Arnott, S. The structure of B-DNA in oriented fibers. *Journal of Biomolecular Structure and Dynamics* **13**, 1015–1027 (1996).
122. Murphy, M., Rasnik, I., Cheng, W., Lohman, T. M. & Ha, T. Probing single-stranded DNA conformational flexibility using fluorescence spectroscopy. *Biophysical Journal* **86**, 2530–2537 (2004).
123. Mills, J. B., Vacano, E. & Hagerman, P. J. Flexibility of single-stranded DNA: use of gapped duplex helices to determine the persistence lengths of Poly (dT) and Poly (dA) 1. *Journal of Molecular Biology* **285**, 245–257 (1999).
124. Tinland, B., Pluen, A., Sturm, J. & Weill, G. Persistence length of single-stranded DNA. *Macromolecules* **30**, 5763–5765 (1997).
125. Gedde, U. W. in *Polymer Physics* 19–38 (Springer, 1999).
126. Marko, J. F. & Siggia, E. D. Stretching dna. *Macromolecules* **28**, 8759–8770 (1995).
127. Franklin, R. E. & Gosling, R. G. Molecular configuration in sodium thymonucleate. *Nature* **171**, 740–741 (1953).
128. Watson, J. D., Crick, F. H., *et al.* Molecular structure of nucleic acids. *Nature* **171**, 737–738 (1953).
129. Leslie, A., Arnott, S., Chandrasekaran, R. & Ratliff, R. Polymorphism of DNA double helices. *Journal of Molecular Biology* **143**, 49–72 (1980).

130. Chandrasekaran, R. *et al.* A re-examination of the crystal structure of A-DNA using fiber diffraction data. *Journal of Biomolecular Structure and Dynamics* **6**, 1189–1202 (1989).
131. Wang, A. *et al.* Left-handed double helical DNA: variations in the backbone conformation. *Science* **211**, 171–176 (1981).
132. Protozanova, E., Yakovchuk, P. & Frank-Kamenetskii, M. D. Stacked–unstacked equilibrium at the nick site of DNA. *Journal of Molecular Biology* **342**, 775–785 (2004).
133. Douglas, S. M., Chou, J. J. & Shih, W. M. DNA-nanotube-induced alignment of membrane proteins for NMR structure determination. *Proceedings of the National Academy of Sciences* **104**, 6644–6648 (2007).
134. Bloomfield, V. & Crothers, D. M. *Nucleic acids: structures, properties and functions* **574.192 B52** (2000).
135. SantaLucia, J. A unified view of polymer, dumbbell, and oligonucleotide DNA nearest-neighbor thermodynamics. *Proceedings of the National Academy of Sciences* **95**, 1460–1465 (1998).
136. SantaLucia, J., Allawi, H. T. & Seneviratne, P. A. Improved nearest-neighbor parameters for predicting DNA duplex stability. *Biochemistry* **35**, 3555–3562 (1996).
137. Wang, J. C. Helical repeat of DNA in solution. *Proceedings of the National Academy of Sciences* **76**, 200–203 (1979).
138. Hunter, C. A. Sequence-dependent DNA structure. *Bioessays* **18**, 157–162 (1996).
139. Wang, M. D., Yin, H., Landick, R., Gelles, J. & Block, S. M. Stretching DNA with optical tweezers. *Biophysical Journal* **72**, 1335–1346 (1997).
140. Baumann, C. G. *et al.* Stretching of single collapsed DNA molecules. *Biophysical Journal* **78**, 1965–1978 (2000).
141. SantaLucia Jr, J. & Hicks, D. The thermodynamics of DNA structural motifs. *Annu. Rev. Biophys. Biomol. Struct.* **33**, 415–440 (2004).

142. Astell, C. R., Chow, M. & Ward, D. Sequence analysis of the termini of virion and replicative forms of minute virus of mice DNA suggests a modified rolling hairpin model for autonomous parvovirus DNA replication. *Journal of Virology* **54**, 171–177 (1985).
143. Iko, A. S. & Hearst, J. E. Identification of a structural hairpin in the filamentous chimeric phage M13Gori1. *Journal of Molecular Biology* **151**, 245–259 (1981).
144. Gacy, A. M., Goellner, G., Juranić, N., Macura, S. & McMurray, C. T. Trinucleotide repeats that expand in human disease form hairpin structures in vitro. *Cell* **81**, 533–540 (1995).
145. Mathews, D. H., Burkard, M. E., Freier, S. M., Wyatt, J. R. & Turner, D. H. Predicting oligonucleotide affinity to nucleic acid targets. *RNA* **5**, 1458–1469 (1999).
146. Nazarenko, I., Pires, R., Lowe, B., Obaidy, M. & Rashtchian, A. Effect of primary and secondary structure of oligodeoxyribonucleotides on the fluorescent properties of conjugated dyes. *Nucleic Acids Research* **30**, 2089–2195 (2002).
147. Srinivas, N. *et al.* On the biophysics and kinetics of toehold-mediated DNA strand displacement. *Nucleic Acids Research* **41**, 10641–10658 (2013).
148. Huss, V. A., Festl, H. & Schleifer, K. H. Studies on the spectrophotometric determination of DNA hybridization from renaturation rates. *Systematic and Applied Microbiology* **4**, 184–192 (1983).
149. Tataurov, A. V., You, Y. & Owczarzy, R. Predicting ultraviolet spectrum of single stranded and double stranded deoxyribonucleic acids. *Biophysical Chemistry* **133**, 66–70 (2008).
150. Zadeh, J. N. *et al.* NUPACK: analysis and design of nucleic acid systems. *Journal of Computational Chemistry* **32**, 170–173 (2011).
151. Zuker, M. Mfold web server for nucleic acid folding and hybridization prediction. *Nucleic Acids Research* **31**, 3406–3415 (2003).
152. Svoboda, P. & Cara, A. D. Hairpin RNA: a secondary structure of primary importance. *Cellular and Molecular Life Sciences CMLS* **63**, 901–908 (2006).

153. McKinney, S. A., Déclais, A.-C., Lilley, D. M. & Ha, T. Structural dynamics of individual Holliday junctions. *Nature Structural and Molecular Biology* **10**, 93 (2003).
154. Seeman, N. C. Nucleic acid junctions and lattices. *Journal of Theoretical Biology* **99**, 237–247 (1982).
155. Parkinson, G. N., Lee, M. P. & Neidle, S. Crystal structure of parallel quadruplexes from human telomeric DNA. *Nature* **417**, 876 (2002).
156. Bochman, M. L., Paeschke, K. & Zakian, V. A. DNA secondary structures: stability and function of G-quadruplex structures. *Nature Reviews Genetics* **13**, 770 (2012).
157. Murat, P. & Balasubramanian, S. Existence and consequences of G-quadruplex structures in DNA. *Current Opinion in Genetics & Development* **25**, 22–29 (2014).
158. Weil, J. *et al.* Stabilization of the i-motif by intramolecular adenine–adenine–thymine base triple in the structure of d (ACCCT). *Acta Crystallographica Section D: Biological Crystallography* **55**, 422–429 (1999).
159. Dong, Y., Yang, Z. & Liu, D. DNA nanotechnology based on i-motif structures. *Accounts of Chemical Research* **47**, 1853–1860 (2014).
160. Day, H. A., Pavlou, P. & Waller, Z. A. i-Motif DNA: structure, stability and targeting with ligands. *Bioorganic & Medicinal Chemistry* **22**, 4407–4418 (2014).
161. Axmann, M., Schütz, G. J. & Huppa, J. B. Single molecule fluorescence microscopy on planar supported bilayers. *Journal of Visualized Experiments: JoVE* (2015).
162. Czogalla, A., Franquelim, H. G. & Schwille, P. DNA nanostructures on membranes as tools for synthetic biology. *Biophysical Journal* **110**, 1698–1707 (2016).
163. Burns, J. R. *et al.* Lipid-bilayer-spanning DNA nanopores with a bifunctional porphyrin anchor. *Angewandte Chemie International Edition* **52**, 12069–12072 (2013).
164. Burns, J. R., Stulz, E. & Howorka, S. Self-assembled DNA nanopores that span lipid bilayers. *Nano Letters* **13**, 2351–2356 (2013).



165. Göpfrich, K. *et al.* Ion channels made from a single membrane-spanning DNA duplex. *Nano Letters* **16**, 4665–4669 (2016).
166. Göpfrich, K. *et al.* Large-conductance transmembrane porin made from DNA origami. *ACS Nano* **10**, 8207–8214 (2016).
167. Krishnan, S. *et al.* Molecular transport through large-diameter DNA nanopores. *Nature Communications* **7**, 12787 (2016).
168. Langecker, M. *et al.* Synthetic lipid membrane channels formed by designed DNA nanostructures. *Science* **338**, 932–936 (2012).
169. Czogalla, A. *et al.* Amphipathic DNA origami nanoparticles to scaffold and deform lipid membrane vesicles. *Angewandte Chemie International Edition* **54**, 6501–6505 (2015).
170. Perrault, S. D. & Shih, W. M. Virus-inspired membrane encapsulation of DNA nanostructures to achieve in vivo stability. *ACS Nano* **8**, 5132–5140 (2014).
171. Kocabey, S. *et al.* Membrane-assisted growth of DNA origami nanostructure arrays. *ACS Nano* **9**, 3530–3539 (2015).
172. Suzuki, Y., Endo, M. & Sugiyama, H. Lipid-bilayer-assisted two-dimensional self-assembly of DNA origami nanostructures. *Nature Communications* **6**, 8052 (2015).
173. Suzuki, Y., Endo, M. & Sugiyama, H. Mimicking membrane-related biological events by DNA origami nanotechnology. *ACS Nano* **9**, 3418–3420 (2015).
174. Czogalla, A. *et al.* Switchable domain partitioning and diffusion of DNA origami rods on membranes. *Faraday Discussions* **161**, 31–43 (2013).
175. Khmelinskaia, A., Franquelim, H. G., Petrov, E. P. & Schwille, P. Effect of anchor positioning on binding and diffusion of elongated 3D DNA nanostructures on lipid membranes. *Journal of Physics D: Applied Physics* **49**, 194001 (2016).
176. List, J., Weber, M. & Simmel, F. C. Hydrophobic actuation of a DNA origami bilayer structure. *Angewandte Chemie International Edition* **53**, 4236–4239 (2014).



177. Chan, Y.-H. M., van Lengerich, B. & Boxer, S. G. Effects of linker sequences on vesicle fusion mediated by lipid-anchored DNA oligonucleotides. *Proceedings of the National Academy of Sciences*, pnas-0812356106 (2009).
178. Dave, N. & Liu, J. Programmable assembly of DNA-functionalized liposomes by DNA. *ACS Nano* **5**, 1304–1312 (2011).
179. Rodríguez-Pulido, A. *et al.* Light-triggered sequence-specific cargo release from DNA block copolymer–lipid vesicles. *Angewandte Chemie* **125**, 1042–1046 (2013).
180. Huang, Y.-F. *et al.* Molecular assembly of an aptamer–drug conjugate for targeted drug delivery to tumor cells. *ChemBioChem* **10**, 862–868 (2009).
181. Koyfman, A. Y., Braun, G. B. & Reich, N. O. Cell-targeted self-assembled DNA nanostructures. *Journal of the American Chemical Society* **131**, 14237–14239 (2009).
182. Felgner, P. L. *et al.* Lipofection: a highly efficient, lipid-mediated DNA-transfection procedure. *Proceedings of the National Academy of Sciences* **84**, 7413–7417 (1987).
183. Pozharski, E. & MacDonald, R. C. Thermodynamics of cationic lipid–DNA complex formation as studied by isothermal titration calorimetry. *Biophysical Journal* **83**, 556–565 (2002).
184. Gromelski, S. & Brezesinski, G. DNA condensation and interaction with zwitterionic phospholipids mediated by divalent cations. *Langmuir* **22**, 6293–6301 (2006).
185. McManus, J. J., Rädler, J. O. & Dawson, K. A. Does calcium turn a zwitterionic lipid cationic? *The Journal of Physical Chemistry B* **107**, 9869–9875 (2003).
186. Ainalem, M.-L. *et al.* DNA binding to zwitterionic model membranes. *Langmuir* **26**, 4965–4976 (2009).
187. Sobczak, J.-P. J., Martin, T. G., Gerling, T. & Dietz, H. Rapid folding of DNA into nanoscale shapes at constant temperature. *Science* **338**, 1458–1461 (2012).

188. Ke, Y., Bellot, G., Voigt, N. V., Fradkov, E. & Shih, W. M. Two design strategies for enhancement of multilayer–DNA-origami folding: underwinding for specific intercalator rescue and staple-break positioning. *Chemical Science* **3**, 2587–2597 (2012).
189. Martin, T. G. & Dietz, H. Magnesium-free self-assembly of multi-layer DNA objects. *Nature Communications* **3**, 2095 (2012).
190. Mao, C., Sun, W. & Seeman, N. C. Designed two-dimensional DNA Holliday junction arrays visualized by atomic force microscopy. *Journal of the American Chemical Society* **121**, 5437–5443 (1999).
191. Zheng, J. *et al.* From molecular to macroscopic via the rational design of a self-assembled 3D DNA crystal. *Nature* **461**, 74 (2009).
192. Acuna, G. *et al.* Fluorescence enhancement at docking sites of DNA-directed self-assembled nanoantennas. *Science* **338**, 506–510 (2012).
193. Pfitzner, E. *et al.* Rigid DNA beams for high-resolution single-molecule mechanics. *Angewandte Chemie International Edition* **52**, 7766–7771 (2013).
194. Wei, R., Martin, T. G., Rant, U. & Dietz, H. DNA origami gatekeepers for solid-state nanopores. *Angewandte Chemie* **124**, 4948–4951 (2012).
195. Bell, N. A. *et al.* DNA origami nanopores. *Nano Letters* **12**, 512–517 (2011).
196. Hernández-Ainsa, S. *et al.* DNA origami nanopores for controlling DNA translocation. *ACS Nano* **7**, 6024–6030 (2013).
197. Wei, B., Dai, M. & Yin, P. Complex shapes self-assembled from single-stranded DNA tiles. *Nature* **485**, 623 (2012).
198. Ke, Y., Ong, L. L., Shih, W. M. & Yin, P. Three-dimensional structures self-assembled from DNA bricks. *Science* **338**, 1177–1183 (2012).
199. Castro, C. E. *et al.* A primer to scaffolded DNA origami. *Nature Methods* **8**, 221 (2011).
200. Douglas, S. M. *et al.* Rapid prototyping of 3D DNA-origami shapes with caDNAno. *Nucleic Acids Research* **37**, 5001–5006 (2009).
201. Kim, D.-N., Kilchherr, F., Dietz, H. & Bathe, M. Quantitative prediction of 3D solution shape and flexibility of nucleic acid nanostructures. *Nucleic Acids Research* **40**, 2862–2868 (2011).

202. Woo, S. & Rothemund, P. W. Self-assembly of two-dimensional DNA origami lattices using cation-controlled surface diffusion. *Nature Communications* **5**, 4889 (2014).
203. Aghebat Rafat, A., Pirzer, T., Scheible, M. B., Kostina, A. & Simmel, F. C. Surface-Assisted Large-Scale Ordering of DNA Origami Tiles. *Angewandte Chemie International Edition* **53**, 7665–7668 (2014).
204. Gerling, T., Wagenbauer, K. F., Neuner, A. M. & Dietz, H. Dynamic DNA devices and assemblies formed by shape-complementary, non-base pairing 3D components. *Science* **347**, 1446–1452 (2015).
205. Jungmann, R. *et al.* DNA origami-based nanoribbons: assembly, length distribution, and twist. *Nanotechnology* **22**, 275301 (2011).
206. Schmied, J. J. *et al.* DNA origami-based standards for quantitative fluorescence microscopy. *Nature Protocols* **9**, 1367 (2014).
207. Pinheiro, A. V., Han, D., Shih, W. M. & Yan, H. Challenges and opportunities for structural DNA nanotechnology. *Nature Nanotechnology* **6**, 763 (2011).
208. Snodin, B. E. *et al.* Direct simulation of the self-assembly of a small DNA origami. *ACS Nano* **10**, 1724–1737 (2016).
209. Bai, X.-c., Martin, T. G., Scheres, S. H. & Dietz, H. Cryo-EM structure of a 3D DNA-origami object. *Proceedings of the National Academy of Sciences* **109**, 20012–20017 (2012).
210. Privalov, P., Ptitsyn, O. & Birshtein, T. Determination of stability of the DNA double helix in an aqueous medium. *Biopolymers: Original Research on Biomolecules* **8**, 559–571 (1969).
211. Dominguez, K. & Ward, W. S. A novel nuclease activity that is activated by Ca<sup>2+</sup> chelated to EGTA. *Systems Biology in Reproductive Medicine* **55**, 193–199 (2009).
212. Gopinath, A. & Rothemund, P. W. Optimized assembly and covalent coupling of single-molecule DNA origami nanoarrays. *ACS Nano* **8**, 12030–12040 (2014).
213. Chopra, A., Krishnan, S. & Simmel, F. C. Electrotransfection of polyamine folded DNA origami structures. *Nano Letters* **16**, 6683–6690 (2016).

214. Lin, C., Perrault, S. D., Kwak, M., Graf, F. & Shih, W. M. Purification of DNA-origami nanostructures by rate-zonal centrifugation. *Nucleic Acids Research* **41**, e40–e40 (2012).
215. Martin, T. G. *Functional Synthetic DNA Nanostructures* PhD thesis (Technische Universität München, 2013).
216. Voigt, N. V. *et al.* Single-molecule chemical reactions on DNA origami. *Nature Nanotechnology* **5**, 200 (2010).
217. Dutta, P. K. *et al.* DNA-directed artificial light-harvesting antenna. *Journal of the American Chemical Society* **133**, 11985–11993 (2011).
218. Stein, I. H., Steinhauer, C. & Tinnefeld, P. Single-molecule four-color FRET visualizes energy-transfer paths on DNA origami. *Journal of the American Chemical Society* **133**, 4193–4195 (2011).
219. Kuzyk, A., Laitinen, K. T. & Törmä, P. DNA origami as a nanoscale template for protein assembly. *Nanotechnology* **20**, 235305 (2009).
220. Saccà, B. *et al.* Orthogonal protein decoration of DNA origami. *Angewandte Chemie International Edition* **49**, 9378–9383 (2010).
221. Woo, S. & Rothmund, P. W. Programmable molecular recognition based on the geometry of DNA nanostructures. *Nature Chemistry* **3**, 620 (2011).
222. Li, Z., Wang, L., Yan, H. & Liu, Y. Effect of DNA hairpin loops on the twist of planar DNA origami tiles. *Langmuir* **28**, 1959–1965 (2011).
223. Scheible, M., Jungmann, R. & Simmel, F. C. in *Nano-Biotechnology for Biomedical and Diagnostic Research* 87–96 (Springer, 2012).
224. Pastré, D. *et al.* Adsorption of DNA to mica mediated by divalent counterions: a theoretical and experimental study. *Biophysical Journal* **85**, 2507–2518 (2003).
225. Babcock, H., Sigal, Y. M. & Zhuang, X. A high-density 3D localization algorithm for stochastic optical reconstruction microscopy. *Optical Nanoscopy* **1**, 6 (2012).
226. Johnson-Buck, A., Jiang, S., Yan, H. & Walter, N. G. DNA-cholesterol barges as programmable membrane-exploring agents. *ACS Nano* **8**, 5641–5649 (2014).

227. Laitinen, O., Hytönen, V., Nordlund, H. & Kulomaa, M. Genetically engineered avidins and streptavidins. *Cellular and Molecular Life Sciences CMLS* **63**, 2992–3017 (2006).
228. Los, G. V. *et al.* HaloTag: a novel protein labeling technology for cell imaging and protein analysis. *ACS Chemical Biology* **3**, 373–382 (2008).
229. Kolb, H. C., Finn, M. & Sharpless, K. B. Click chemistry: diverse chemical function from a few good reactions. *Angewandte Chemie International Edition* **40**, 2004–2021 (2001).
230. Huppa, J. B. *et al.* TCR–peptide–MHC interactions in situ show accelerated kinetics and increased affinity. *Nature* **463**, 963 (2010).
231. Davis, S. J. & van der Merwe, P. A. The kinetic-segregation model: TCR triggering and beyond. *Nature Immunology* **7**, 803 (2006).
232. Stahl, E., Martin, T. G., Praetorius, F. & Dietz, H. Facile and scalable preparation of pure and dense DNA origami solutions. *Angewandte Chemie International Edition* **53**, 12735–12740 (2014).
233. Mashanov, G. I., Tacon, D., Peckham, M. & Molloy, J. E. The spatial and temporal dynamics of pleckstrin homology domain binding at the plasma membrane measured by imaging single molecules in live mouse myoblasts. *Journal of Biological Chemistry* **279**, 15274–15280 (2004).
234. Katz, Z. B., Novotná, L., Blount, A. & Lillemeier, B. F. A cycle of Zap70 kinase activation and release from the TCR amplifies and disperses antigenic stimuli. *Nature Immunology* **18**, 86–95 (2017).
235. Loerke, D., Wienisch, M., Kochubey, O. & Klingauf, J. Differential control of clathrin subunit dynamics measured with EW-FRAP microscopy. *Traffic* **6**, 918–929 (2005).
236. Klammt, C. *et al.* T cell receptor dwell times control the kinase activity of Zap70. *Nature Immunology* **16**, 961 (2015).
237. Lanzerstorfer, P. *et al.* Quantification and kinetic analysis of Grb2-EGFR interaction on micro-patterned surfaces for the characterization of EGFR-modulating substances. *PLoS One* **9**, e92151 (2014).
238. Axelrod, D., Koppel, D., Schlessinger, J., Elson, E. & Webb, W. W. Mobility measurement by analysis of fluorescence photobleaching recovery kinetics. *Biophysical Journal* **16**, 1055–1069 (1976).

239. Kenworthy, A. K. *et al.* Dynamics of putative raft-associated proteins at the cell surface. *The Journal of Cell Biology* **165**, 735–746 (2004).
240. Lippincott-Schwartz, J., Altan-Bonnet, N. & Patterson, G. H. Photo-bleaching and photoactivation: following protein dynamics in living cells. *Nature Cell Biology*, S7–14 (2003).
241. Pochynyuk, O., Staruschenko, A., Bugaj, V., LaGrange, L. & Stockand, J. D. Quantifying RhoA facilitated trafficking of the epithelial Na<sup>+</sup> channel toward the plasma membrane with total internal reflection fluorescence-fluorescence recovery after photobleaching. *Journal of Biological Chemistry* **282**, 14576–14585 (2007).
242. Ghosh, D., Segal, A. & Voets, T. Distinct modes of perimembrane TRP channel turnover revealed by TIR-FRAP. *Scientific Reports* **4**, 7111 (2014).
243. Ghosh, D. *et al.* VAMP7 regulates constitutive membrane incorporation of the cold-activated channel TRPM8. *Nature Communications* **7**, 10489 (2016).
244. Tannert, A., Tannert, S., Burgold, S. & Schaefer, M. Convolution-based one and two component FRAP analysis: theory and application. *European Biophysics Journal* **38**, 649–661 (2009).
245. Tannert, A., Voigt, P., Burgold, S., Tannert, S. & Schaefer, M. Signal amplification between G $\beta\gamma$  release and PI3K $\gamma$ -mediated PI (3, 4, 5) P3 formation monitored by a fluorescent G $\beta\gamma$  biosensor protein and repetitive two component total internal reflection/fluorescence redistribution after photobleaching analysis. *Biochemistry* **47**, 11239–11250 (2008).
246. Kang, M., Day, C. A., DiBenedetto, E. & Kenworthy, A. K. A quantitative approach to analyze binding diffusion kinetics by confocal FRAP. *Biophysical Journal* **99**, 2737–2747 (2010).
247. Sprague, B. L. & McNally, J. G. FRAP analysis of binding: proper and fitting. *Trends in Cell Biology* **15**, 84–91 (2005).
248. Fülöp, G., Brameshuber, M., Arnold, A. M., Schütz, G. J. & Sevcsik, E. Determination of the Membrane Environment of CD59 in Living Cells. *Biomolecules* **8**, 28 (2018).
249. Sevcsik, E. *et al.* GPI-anchored proteins do not reside in ordered domains in the live cell plasma membrane. *Nature Communications* **6**, 6969 (2015).



250. Schwarzenbacher, M. *et al.* Micropatterning for quantitative analysis of protein-protein interactions in living cells. *Nature Methods* **5**, 1053–1060 (2008).
251. Löchte, S., Waichman, S., Beutel, O., You, C. & Piehler, J. Live cell micropatterning reveals the dynamics of signaling complexes at the plasma membrane. *J Cell Biol* **207**, 407–418 (2014).
252. Shen, K., Thomas, V. K., Dustin, M. L. & Kam, L. C. Micropatterning of costimulatory ligands enhances CD4<sup>+</sup> T cell function. *Proceedings of the National Academy of Sciences* **105**, 7791–7796 (2008).
253. Dirscherl, C., Palankar, R., Delcea, M., Kolesnikova, T. A. & Springer, S. Specific Capture of Peptide-Receptive Major Histocompatibility Complex Class I Molecules by Antibody Micropatterns Allows for a Novel Peptide-Binding Assay in Live Cells. *Small* **13**, 1602974 (2017).
254. Motsch, V., Brameshuber, M., Baumgart, F., Schütz, G. J. & Sevcsik, E. A micropatterning platform for quantifying interaction kinetics between the T cell receptor and an intracellular binding protein. *Scientific Reports* **9**, 3288 (2019).
255. Phair, R. D., Gorski, S. A. & Misteli, T. in *Methods in Enzymology* 393–414 (Elsevier, 2003).
256. Sprague, B. L., Pego, R. L., Stavreva, D. A. & McNally, J. G. Analysis of binding reactions by fluorescence recovery after photobleaching. *Biophysical Journal* **86**, 3473–3495 (2004).
257. Belgareh, N. *et al.* An evolutionarily conserved NPC subcomplex, which redistributes in part to kinetochores in mammalian cells. *The Journal of Cell Biology* **154**, 1147–1160 (2001).
258. Bulinski, J. C., Odde, D. J., Howell, B. J., Salmon, T. D. & Waterman-Storer, C. M. Rapid dynamics of the microtubule binding of ensconsin in vivo. *Journal of Cell Science* **114**, 3885–3897 (2001).
259. Yumura, S. Myosin II dynamics and cortical flow during contractile ring formation in *Dictyostelium* cells. *The Journal of Cell Biology* **154**, 137–146 (2001).

260. Kimura, H. & Cook, P. R. Kinetics of core histones in living human cells: little exchange of H3 and H4 and some rapid exchange of H2B. *The Journal of Cell Biology* **153**, 1341–1354 (2001).
261. Molk, J. N. *et al.* The differential roles of budding yeast Tem1p, Cdc15p, and Bub2p protein dynamics in mitotic exit. *Molecular Biology of the Cell* **15**, 1519–1532 (2004).
262. Presley, J. F. *et al.* Dissection of COPI and Arf1 dynamics in vivo and role in Golgi membrane transport. *Nature* **417**, 187 (2002).
263. Dundr, M. *et al.* A kinetic framework for a mammalian RNA polymerase in vivo. *Science* **298**, 1623–1626 (2002).
264. Slepchenko, B. M., Schaff, J. C., Macara, I. & Loew, L. M. Quantitative cell biology with the Virtual Cell. *Trends in Cell Biology* **13**, 570–576 (2003).
265. Wiscombe, W. & Evans, J. Exponential-sum fitting of radiative transmission functions. *Journal of Computational Physics* **24**, 416–444 (1977).
266. Ruhe, A. & Wedin, P. Å. Algorithms for separable nonlinear least squares problems. *SIAM Review* **22**, 318–337 (1980).
267. Osborne, M. R. & Smyth, G. K. A modified Prony algorithm for fitting functions defined by difference equations. *SIAM Journal on Scientific and Statistical Computing* **12**, 362–382 (1991).
268. Chernoff, H. & Lehmann, E. L. in *Selected works of EL Lehmann* 541–549 (Springer, 2012).
269. Plackett, R. L. Karl Pearson and the chi-squared test. *International Statistical Review/Revue Internationale de Statistique*, 59–72 (1983).
270. Gelman, A. A Bayesian formulation of exploratory data analysis and goodness-of-fit testing. *International Statistical Review* **71**, 369–382 (2003).
271. Press, W. H., Teukolsky, S. A., Vetterling, W. T. & Flannery, B. P. *Numerical recipes 3rd edition: The art of scientific computing* (Cambridge university press, 2007).
272. Lomb, N. R. Least-squares frequency analysis of unequally spaced data. *Astrophysics and Space Science* **39**, 447–462 (1976).



273. Scargle, J. D. Studies in astronomical time series analysis. II-Statistical aspects of spectral analysis of unevenly spaced data. *The Astrophysical Journal* **263**, 835–853 (1982).
274. Müller, U. R. & Nicolau, D. V. *Microarray technology and its applications* (Springer, 2005).
275. Bernard, A., Michel, B. & Delamarche, E. Micromosaic immunoassays. *Analytical Chemistry* **73**, 8–12 (2001).
276. Hermanson, G. Avidin-biotin systems. *Bioconjugate Techniques* **2**, 914 (1996).
277. Gonzales, M. *et al.* Interaction of biotin with streptavidin. *J. Biol. Chem* **272**, 11288–11294 (1997).
278. Hermanson, G. T. Antibody modification and conjugation. *Bioconjugate Techniques*, 456–493 (1996).
279. Franssila, S. *Introduction to microfabrication* (John Wiley & Sons, 2010).
280. Ventra, M., Evoy, S. & Heflin, J. R. *Introduction to nanoscale science and technology* (Springer Science & Business Media, 2006).
281. Xia, Y., Rogers, J. A., Paul, K. E. & Whitesides, G. M. Unconventional methods for fabricating and patterning nanostructures. *Chemical Reviews* **99**, 1823–1848 (1999).
282. Gates, B. D. *et al.* New approaches to nanofabrication: molding, printing, and other techniques. *Chemical Reviews* **105**, 1171–1196 (2005).
283. Gates, B. D., Xu, Q., Love, J. C., Wolfe, D. B. & Whitesides, G. M. Unconventional nanofabrication. *Annu. Rev. Mater. Res.* **34**, 339–372 (2004).
284. Sperling, L. H. *Introduction to physical polymer science* (John Wiley & Sons, 2005).
285. McDonald, J. C. & Whitesides, G. M. Poly (dimethylsiloxane) as a material for fabricating microfluidic devices. *Accounts of Chemical Research* **35**, 491–499 (2002).
286. Ng, J. M., Gitlin, I., Stroock, A. D. & Whitesides, G. M. Components for integrated poly (dimethylsiloxane) microfluidic systems. *Electrophoresis* **23**, 3461–3473 (2002).

287. Armani, D., Liu, C. & Aluru, N. *Re-configurable fluid circuits by PDMS elastomer micromachining in Technical Digest. IEEE International MEMS 99 Conference.* (1999), 222–227.
288. Choi, K. M. & Rogers, J. A. A photocurable poly (dimethylsiloxane) chemistry designed for soft lithographic molding and printing in the nanometer regime. *Journal of the American Chemical Society* **125**, 4060–4061 (2003).
289. Odom, T. W., Love, J. C., Wolfe, D. B., Paul, K. E. & Whitesides, G. M. Improved pattern transfer in soft lithography using composite stamps. *Langmuir* **18**, 5314–5320 (2002).
290. Schmid, H. & Michel, B. Siloxane polymers for high-resolution, high-accuracy soft lithography. *Macromolecules* **33**, 3042–3049 (2000).
291. Hui, C., Jagota, A., Lin, Y. & Kramer, E. Constraints on microcontact printing imposed by stamp deformation. *Langmuir* **18**, 1394–1407 (2002).
292. Delamarche, E. Microcontact printing of proteins. *Nanobiotechnology: Concepts, Applications and Perspectives*, 31–52 (2004).
293. Bernard, A. *et al.* Printing patterns of proteins. *Langmuir* **14**, 2225–2229 (1998).
294. Xu, X. *et al.* A patterned recombinant human IgM guides neurite outgrowth of CNS neurons. *Scientific Reports* **3**, 2267 (2013).
295. Falconnet, D., Csucs, G., Grandin, H. M. & Textor, M. Surface engineering approaches to micropattern surfaces for cell-based assays. *Biomaterials* **27**, 3044–3063 (2006).
296. Satav, T., Huskens, J. & Jonkheijm, P. Effects of variations in ligand density on cell signaling. *Small* **11**, 5184–5199 (2015).
297. Théry, M. Micropatterning as a tool to decipher cell morphogenesis and functions. *J Cell Sci* **123**, 4201–4213 (2010).
298. Barthes, J. *et al.* Cell microenvironment engineering and monitoring for tissue engineering and regenerative medicine: the recent advances. *BioMed Research International* **2014** (2014).
299. Kane, R. S., Takayama, S., Ostuni, E., Ingber, D. E. & Whitesides, G. M. in *The Biomaterials: Silver Jubilee Compendium* 161–174 (Elsevier, 1999).

300. Khademhosseini, A., Langer, R., Borenstein, J. & Vacanti, J. P. Microscale technologies for tissue engineering and biology. *Proceedings of the National Academy of Sciences* **103**, 2480–2487 (2006).
301. Cavalcanti-Adam, E. A. *et al.* Lateral spacing of integrin ligands influences cell spreading and focal adhesion assembly. *European Journal of Cell Biology* **85**, 219–224 (2006).
302. Freeman, S. A. *et al.* Integrins form an expanding diffusional barrier that coordinates phagocytosis. *Cell* **164**, 128–140 (2016).
303. Mossman, K. D., Campi, G., Groves, J. T. & Dustin, M. L. Altered TCR signaling from geometrically repatterned immunological synapses. *Science* **310**, 1191–1193 (2005).
304. Wu, M., Holowka, D., Craighead, H. G. & Baird, B. Visualization of plasma membrane compartmentalization with patterned lipid bilayers. *Proceedings of the National Academy of Sciences* **101**, 13798–13803 (2004).
305. Gandor, S. *et al.* A Protein-Interaction Array Inside a Living Cell. *Angewandte Chemie International Edition* **52**, 4790–4794 (2013).
306. Weghuber, J. *et al.* in *Methods in Enzymology* 133–151 (Elsevier, 2010).
307. Wedeking, T. *et al.* Single cell GFP-trap reveals stoichiometry and dynamics of cytosolic protein complexes. *Nano Letters* **15**, 3610–3615 (2015).
308. Chan, A. C., Irving, B. A., Fraser, J. D. & Weiss, A. The zeta chain is associated with a tyrosine kinase and upon T-cell antigen receptor stimulation associates with ZAP-70, a 70-kDa tyrosine phosphoprotein. *Proceedings of the National Academy of Sciences* **88**, 9166–9170 (1991).
309. Taniguchi, T. *et al.* Molecular cloning of a porcine gene syk that encodes a 72-kDa protein-tyrosine kinase showing high susceptibility to proteolysis. *Journal of Biological Chemistry* **266**, 15790–15796 (1991).
310. Meinel, E. *et al.* Differential requirement of ZAP-70 for CD2-mediated activation pathways of mature human T cells. *The Journal of Immunology* **165**, 3578–3583 (2000).
311. Noraz, N. *et al.* Alternative antigen receptor (TCR) signaling in T cells derived from ZAP-70-deficient patients expressing high levels of Syk. *Journal of Biological Chemistry* **275**, 15832–15838 (2000).

312. Turul, T. *et al.* Clinical heterogeneity can hamper the diagnosis of patients with ZAP70 deficiency. *European Journal of Pediatrics* **168**, 87 (2009).
313. Negishi, I. *et al.* Essential role for ZAP-70 in both positive and negative selection of thymocytes. *Nature* **376**, 435 (1995).
314. Kadlecsek, T. A. *et al.* Differential requirements for ZAP-70 in TCR signaling and T cell development. *The Journal of Immunology* **161**, 4688–4694 (1998).
315. Fischer, A. *et al.* ZAP70: a master regulator of adaptive immunity in *Seminars in immunopathology* **32** (2010), 107–116.
316. Perlmutter, R. M. Zapping T-cell responses. *Nature* **370**, 249 (1994).
317. Brdiccka, T., Kadlecsek, T. A., Roose, J. P., Pastuszak, A. W. & Weiss, A. Intramolecular regulatory switch in ZAP-70: analogy with receptor tyrosine kinases. *Molecular and Cellular Biology* **25**, 4924–4933 (2005).
318. Bu, J.-Y., Shaw, A. S. & Chan, A. C. Analysis of the interaction of ZAP-70 and syk protein-tyrosine kinases with the T-cell antigen receptor by plasmon resonance. *Proceedings of the National Academy of Sciences* **92**, 5106–5110 (1995).
319. Zhao, Q., Williams, B. L., Abraham, R. T. & Weiss, A. Interdomain B in ZAP-70 regulates but is not required for ZAP-70 signaling function in lymphocytes. *Molecular and Cellular Biology* **19**, 948–956 (1999).
320. Deindl, S. *et al.* Structural basis for the inhibition of tyrosine kinase activity of ZAP-70. *Cell* **129**, 735–746 (2007).
321. Iwashima, M., Irving, B. A., Van Oers, N., Chan, A. C. & Weiss, A. Sequential interactions of the TCR with two distinct cytoplasmic tyrosine kinases. *Science* **263**, 1136–1139 (1994).
322. Di Bartolo, V. *et al.* Tyrosine 319, a newly identified phosphorylation site of ZAP-70, plays a critical role in T cell antigen receptor signaling. *Journal of Biological Chemistry* **274**, 6285–6294 (1999).
323. Williams, B. L. *et al.* Phosphorylation of Tyr319 in ZAP-70 is required for T-cell antigen receptor-dependent phospholipase C- $\gamma$ 1 and Ras activation. *The EMBO journal* **18**, 1832–1844 (1999).

324. Chan, A. *et al.* Activation of ZAP-70 kinase activity by phosphorylation of tyrosine 493 is required for lymphocyte antigen receptor function. *The EMBO journal* **14**, 2499–2508 (1995).
325. Neumeister, E. N. *et al.* Binding of ZAP-70 to phosphorylated T-cell receptor zeta and eta enhances its autophosphorylation and generates specific binding sites for SH2 domain-containing proteins. *Molecular and Cellular Biology* **15**, 3171–3178 (1995).
326. Wange, R. L. *et al.* Activating and inhibitory mutations in adjacent tyrosines in the kinase domain of ZAP-70. *Journal of Biological Chemistry* **270**, 18730–18733 (1995).
327. Zhang, W., Sloan-Lancaster, J., Kitchen, J., Tribble, R. P. & Samelson, L. E. LAT: the ZAP-70 tyrosine kinase substrate that links T cell receptor to cellular activation. *Cell* **92**, 83–92 (1998).
328. Zhao, Q. & Weiss, A. Enhancement of lymphocyte responsiveness by a gain-of-function mutation of ZAP-70. *Molecular and Cellular Biology* **16**, 6765–6774 (1996).
329. Gelkop, S. & Isakov, N. T cell activation stimulates the association of enzymatically active tyrosine-phosphorylated ZAP-70 with the Crk adapter proteins. *Journal of Biological Chemistry* **274**, 21519–21527 (1999).
330. Epler, J. A., Liu, R., Chung, H., Ottoson, N. C. & Shimizu, Y. Regulation of  $\beta$ 1 integrin-mediated adhesion by T cell receptor signaling involves ZAP-70 but differs from signaling events that regulate transcriptional activity. *The Journal of Immunology* **165**, 4941–4949 (2000).
331. Goda, S., Quale, A. C., Woods, M. L., Felthouser, A. & Shimizu, Y. Control of TCR-mediated activation of  $\beta$ 1 integrins by the ZAP-70 tyrosine kinase interdomain B region and the linker for activation of T cells adapter protein. *The Journal of Immunology* **172**, 5379–5387 (2004).
332. Blanchard, N., Di Bartolo, V. & Hivroz, C. In the immune synapse, ZAP-70 controls T cell polarization and recruitment of signaling proteins but not formation of the synaptic pattern. *Immunity* **17**, 389–399 (2002).
333. Dumont, C. *et al.* TCR/CD3 down-modulation and  $\zeta$  degradation are regulated by ZAP-70. *The Journal of Immunology* **169**, 1705–1712 (2002).

334. Schütz, G. J., Weghuber, J., Lanzerstorfer, P. & Sevcsik, E. in *Proteomics* 261–270 (Springer, 2017).
335. Santos, A. M. *et al.* Capturing resting T cells: the perils of PLL. *Nature Immunology* **19**, 203 (2018).
336. Hanke, J. H. *et al.* Discovery of a novel, potent, and Src family-selective tyrosine kinase inhibitor Study of Lck-and FynT-dependent T cell activation. *Journal of Biological Chemistry* **271**, 695–701 (1996).
337. Gao, Y. & Kilfoi, M. L. Accurate detection and complete tracking of large populations of features in three dimensions. *Optics Express* **17**, 4685–4704 (2009).
338. Taylor, Z. R. *et al.* Fabrication of protein dot arrays via particle lithography. *Langmuir* **25**, 10932–10938 (2009).
339. Van Dorp, W. F., Van Someren, B., Hagen, C. W., Kruit, P. & Crozier, P. A. Approaching the resolution limit of nanometer-scale electron beam-induced deposition. *Nano Letters* **5**, 1303–1307 (2005).
340. Scheible, M. B., Pardatscher, G., Kuzyk, A. & Simmel, F. C. Single molecule characterization of DNA binding and strand displacement reactions on lithographic DNA origami microarrays. *Nano Letters* **14**, 1627–1633 (2014).
341. Kershner, R. J. *et al.* Placement and orientation of individual DNA shapes on lithographically patterned surfaces. *Nature Nanotechnology* **4**, 557 (2009).
342. Hung, A. M. *et al.* Large-area spatially ordered arrays of gold nanoparticles directed by lithographically confined DNA origami. *Nature Nanotechnology* **5**, 121 (2010).
343. Hung, A. M., Noh, H. & Cha, J. N. Recent advances in DNA-based directed assembly on surfaces. *Nanoscale* **2**, 2530–2537 (2010).
344. Wollman, A. J., Sanchez-Cano, C., Carstairs, H. M., Cross, R. A. & Turberfield, A. J. Transport and self-organization across different length scales powered by motor proteins and programmed by DNA. *Nature Nanotechnology* **9**, 44 (2014).
345. Saccà, B. & Niemeyer, C. M. Functionalization of DNA nanostructures with proteins. *Chemical Society Reviews* **40**, 5910–5921 (2011).



346. Schlapak, R., Armitage, D., Saucedo-Zeni, N., Hohage, M. & Howorka, S. Dense passivating poly (ethylene glycol) films on indium tin oxide substrates. *Langmuir* **23**, 10244–10253 (2007).
347. Schlapak, R., Caruana, D., Armitage, D. & Howorka, S. Semipermeable poly (ethylene glycol) films: the relationship between permeability and molecular structure of polymer chains. *Soft Matter* **5**, 4104–4112 (2009).
348. Schlapak, R. *et al.* Painting with biomolecules at the nanoscale: biofunctionalization with tunable surface densities. *Nano letters* **12**, 1983–1989 (2012).
349. Hübner, U., Plontke, R., Blume, M., Reinhardt, A. & Koops, H. On-line nanolithography using electron beam-induced deposition technique. *Microelectronic Engineering* **57**, 953–958 (2001).
350. Hager, R. *et al.* Co-Immobilization of Proteins and DNA Origami Nanoplates to Produce High-Contrast Biomolecular Nanoarrays. *Small* **12**, 2877–2884 (2016).
351. Li, Z. *et al.* Molecular behavior of DNA origami in higher-order self-assembly. *Journal of the American Chemical Society* **132**, 13545–13552 (2010).
352. Zhang, H. *et al.* Folding super-sized DNA origami with scaffold strands from long-range PCR. *Chemical Communications* **48**, 6405–6407 (2012).
353. Moerland, R. J. & Hoogenboom, J. P. Subnanometer-accuracy optical distance ruler based on fluorescence quenching by transparent conductors. *Optica* **3**, 112–117 (2016).
354. Ren, C.-l., Schlapak, R., Hager, R., Szleifer, I. & Howorka, S. Molecular and thermodynamic factors explain the passivation properties of poly (ethylene glycol)-coated substrate surfaces against fluorophore-labeled DNA oligonucleotides. *Langmuir* **31**, 11491–11501 (2015).
355. Hager, R., Halilovic, A., Burns, J. R., Schäffler, F. & Howorka, S. Arrays of Individual DNA Molecules on Nanopatterned Substrates. *Scientific Reports* **7**, 42075 (2017).
356. Leake, M. C. *et al.* Stoichiometry and turnover in single, functioning membrane protein complexes. *Nature* **443**, 355 (2006).





# Danksagung

Sehr geehrter Herr Professor Schütz, lieber Gerhard, vielen Dank für die Möglichkeit in deiner Gruppe frei forschen zu dürfen. Ebenso möchte ich mich für die weitreichende Unterstützung und die freundschaftliche Art der Zusammenarbeit bedanken.

Mein Dank gebührt natürlich auch Eva für die wunderbare Zusammenarbeit und Unterstützung. Ich hätte mir keine bessere Betreuung vorstellen können und weiß nicht, wo ich ohne dich wäre.

Ohne einzelne Personen hervorzuheben, vielen Dank an das gesamte Schützlab für die Unterstützung, die meist gute Arbeitsatmosphäre und den Spaß im Alltag.

Um jetzt doch noch einzelne Personen hervorzuheben, besonderen Dank an Lukas, Martin und Ali, für die Unterstützung bei wissenschaftlichen und weniger wissenschaftlichen Problemen.

Danke Christian, für deine Geduld und Unterstützung über all die Jahre und insbesondere für dein Verständnis in diesen letzten Monaten.

Zu guter Letzt möchte ich meiner Familie danken, meinen Eltern die mich ermutigt haben meinen Interessen zu folgen und mich dabei immer unterstützt haben.



# Curriculum Vitae

## Viktoria Motsch

Date of birth February 24<sup>th</sup>, 1988  
Place of birth Vienna, Austria  
Nationality Austria

### Education

1994-1998 Volksschule Weikendorf, Austria  
1998-2006 Highschool Konrad Lorenz Gymnasium Gänserndorf, Austria  
2006-2010 Bachelor Studies of Technical Physics, TU Wien  
2010-2013 Master Studies of Technical Physics, TU Wien  
Diploma thesis under the supervision of Prof. Schattschneider:  
*Diagonalization of the Mixed Dynamic Form Factor  
for mapping orbital information*  
2013-2019 Doctoral Studies of Technical Sciences, TU Wien  
Doctoral thesis under the supervision of Gerhard Schütz:  
*Micro- and nanostructured surfaces for studying T cell activation*